Session 1

Remote sensing based derivation of biophysical indicators

Remote Sensing Based Assessment of Biophysical Indicators for Land Degradation and Desertification

S.L. Ustin[a,b], S. Jacquemoud[c], A. Palacios-Orueta[a,d], L. Li[e] and M.L. Whiting[a]

[a] California Space Institute Center of Excellence, University of California
Davis, CA 95616, USA, email: slustin@ucdavis.edu
[b] Department of Geography and Environmental Science, University of Auckland, New Zealand
[c] Institut de Physique du Globe de Paris, Géodésie & Gravimétrie, 4 Place Jussieu,
75252 Paris Cedex 5, France
[d] Departamento de Silvopascicultura, Universidad Politécnica de Madrid, Spain
[e] Department of Geology, Indiana University-Purdue University, Indianapolis, IN USA

ABSTRACT

Desert ecosystems spanning moisture conditions from dry grasslands to barren hyper-arid landscapes are the largest terrestrial biome with more than 40% of the terrestrial landmass. Remote sensing data provide an efficient cost-effective means to assess biophysical indicators of land degradation and desertification, providing that essential ecosystem properties can be monitored. We review the spectral characteristics of plants and soils that are detectable using optical sensors and methods to identify and quantify properties that have potential for monitoring arid ecosystem processes. Vegetation indexes have little sensitivity at low leaf area, particularly when the soil background is highly variable, as is characteristic of many arid systems. Additionally, accumulated dry plant material on the soil surface challenges measurement. Although the absorption characteristics of the major biochemical constituents of plants and soils are generally understood, the methods to retrieve this information from reflectance data and to understand the significance of how the structural organization alters the absorption features remains an area of active research. The overlapping absorption features of plants and soils preclude direct assessment of many biogeochemicals of interest. New biophysical methods that take the full spectral shape into account, including the effect of one compound on the spectral absorption of another, are needed to reduce uncertainty in their estimates. As a result, despite significant progress in developing fundamental understanding of ecosystem processes and optical properties, more research is needed before fully predictable quantitative methods are available.

Keywords: spectral indexes, biophysical indicators, radiative transfer, reflectance models

1 INTRODUCTION: DESERTS AND DESERTIFICATION

Desert and dryland ecosystems, including hyperarid, arid, semiarid, and dry subhumid areas are the largest terrestrial biome, about 41% of the terrestrial landmass [1]. Extremely arid deserts have at least 12 consecutive months without precipitation, while arid lands have less than 250 mm annual rainfall, and semiarid lands have mean annual precipitation between 250 and 500 millimeters [2]. Deserts evolved into their modern distributions in response to Quaternary climate conditions, superimposed on local environmental factors. Desert expansion today is attributed to land degradation from land use, land use change, and climate change [1]. There is growing evidence that human activities are creating unprecedented rates of ecosystem change such that novel combinations of climate and disturbance factors may exceed the capacity of current ecosystems to adapt. Desert ecosystems are typically fragile and even small perturbations can have long-lasting impacts on the distribution of vegetation and on functionality [3-4]. Vegetation changes may feedback to climate, accelerating further change [5]. Conversely, within the historic climate range, vegetation distributions tend to be stable, despite large inter-annual variability [6].

Dregne [7] identified three processes that promote desertification: 1) deterioration of vegetation cover from overgrazing, wood cutting and burning; 2) wind and water erosion from improper land management; and 3) salinization from improper irrigation management. Desertification affects all continents (except Antarctica), and 10-20% of global arid systems are believed to be degraded. Because nearly one-third of the human population lives in arid regions, the threat of desertification ranks among the most important environmental problems and has significant impacts on meeting human well-being.

Many interacting factors affect ecosystem sustainability and resistance to degradation (Figure 1). Maintenance of the biotic composition, diversity, and cover is essential to sustainable productivity. In addition to plant factors, maintenance of soil processes, including soil texture, biogeochemical cycles, soil microorganisms and biological crust, and resistance to wind and water borne erosion is also essential to sustaining the health of the ecosystem. Changes in vegetation characteristics and shifts in phonological cycles may accelerate impacts from climate variability and land use. To protect arid lands from accelerated desertification and reduce the potential for feedbacks that may accelerate global climate changes, it is important to understand integrated ecosystem responses.

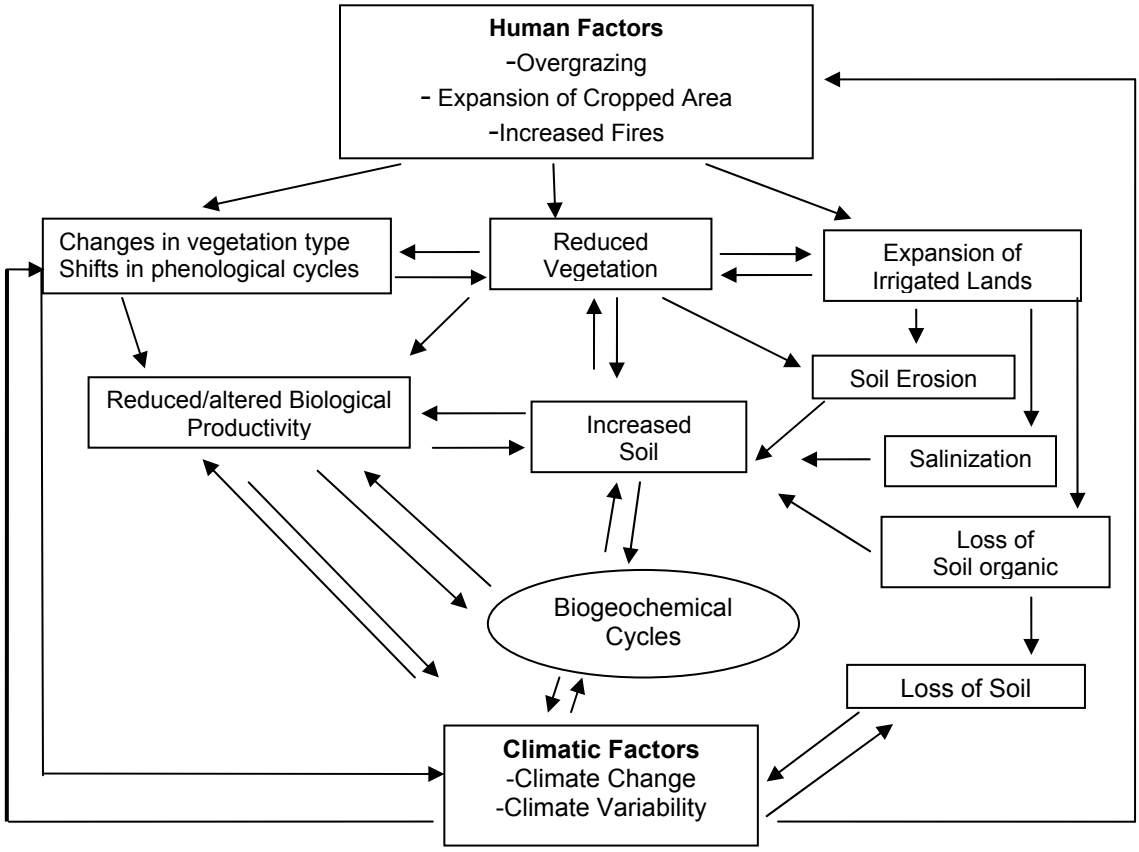

Figure 1. Interactions among climate and human activities that affect functioning of arid ecosystems.

2 RETRIEVING BIOPHYSICAL SPECTRAL INFORMATION

2.1 Biophysical Information from Living Plants

Desert species have developed convergences in the types of leaf structures they have evolved. Similarly, grasses and drought-tolerant shrubs show convergence of growth forms converge. Numerous studies have shown a strong linear relationship between plant cover, biomass, and leaf area in response to water availability [6]. Typically, leaf traits include small thick leaves, with thick cuticles and pubescence, sunken stomata, and small mesophyll cells with thick cell walls and small air spaces. The reflectance and transmittance of leaves is a function of both the concentration of light absorbing compounds (chlorophyll, water, dry plant matter, etc.) and the surface/internal scattering of light that is not efficiently absorbed (Figure 2). Leaf absorbance is reduced by pubescence, and leaves appear more reflective after hairs have dried [8]. As the properties of xeromorphic plant leaves change, e.g., they become more schlerophyllous (drought hardened) or desiccated, and reflectance and transmittance changes in predictable directions [9]. These wavelength specific absorption and scattering produces potentially diagnostic optical patterns of vegetation conditions in deserts. A number of analytical methods have been developed for

directly estimating biochemical composition and structural characteristics. An extensive review of the literature and available optical models are available online at (http://www.multimania.com/opticleaf/).

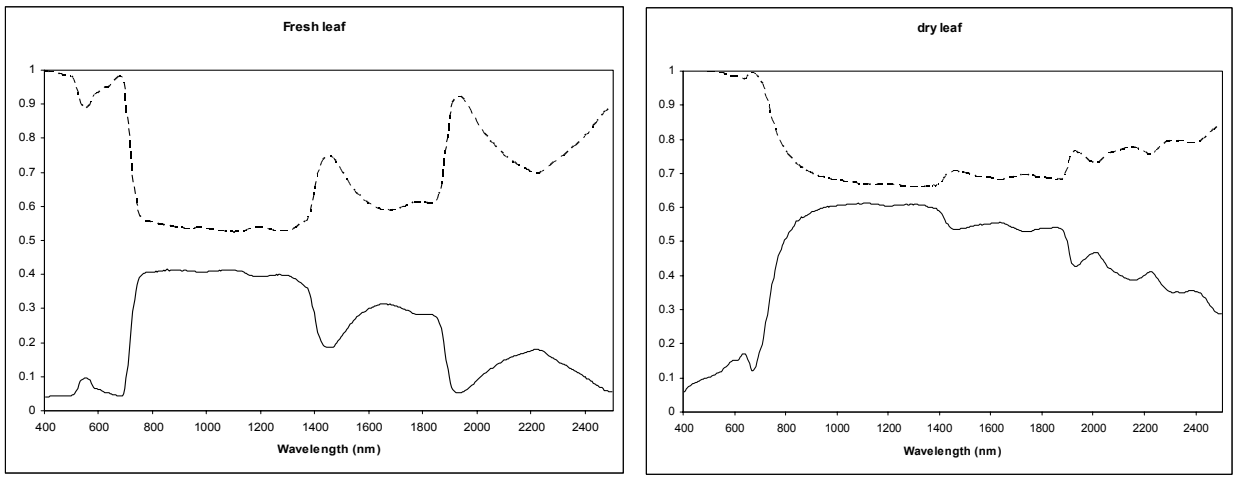

Figure 2. Reflectance (solid line) and transmittance (dashed line) of (left) fresh leaf and (right) dry leaf of a semiarid species, *Quercus pubescens*. Note that the leaf in Figure 2b was dried rapidly since strong chlorophyll absorption and red-edge features remain in the 400-700 nm region.

There is strong interest in developing techniques to detect and quantify individual pigments [10]. The absorption of light by photosynthetic pigments dominates green leaf properties [11] in the visible (VIS) spectrum (400 - 700 nm), with a minimum at 550 nm (Figure 3a-c). Leaf inversion models, e.g., PROSPECT [12-14] predict total pigment concentration (μg cm^{-2}), by assuming that they are entirely composed of chlorophyll (Figure 3a). Characterization of *in vitro* absorption coefficients for other photosynthetic pigments, e.g., xanthophylls, anthocyanins, caroteins and even chlorophyll b could further improve leaf radiative transfer models (Figure 3b). *In vitro* absorption spectra for chlorophylls and several accessory photosynthetic pigments (e.g., carotenoids, xantophylls) are available [15]. However, the pigment spectrum shifts with the solvent used for extraction, so the *in vivo* configuration of plant pigments remains uncertain. Biochemical absorptions that have overlapping wavelengths make individual identifications challenging.

Carotenoids effectively expand the wavelength range for energy absorption by photosynthesis. Xanthophylls, a class of carotenoids, are involved in photoregulation by dissipating excess absorbed energy thus avoiding oxidative damage to the photocenter [16]. Under excess light, violaxanthin is converted to zeaxanthin in the xanthophyll cycle, which increases leaf reflectance. Gamon, Penuelas, and colleagues [17-20] have extensively investigated the use of these spectral differences to develop a normalized ratio termed the Photosynthetic Reflectance Index (PRI) which is sensitive to changing xanthophyll cycle pigments. They successfully used this method to estimate photosynthetic efficiency. Anthocyanins are water-soluble red pigments which are not involved in photosynthesis but occur widely in flowers, fruits and leaves [21-22]. They have a single absorption peak around 529 nm. Phycobilins (Figure 3c), specifically phycoerytherin (red) and phycocyanin (blue) are water-soluble photosynthetic pigments that are only found in the cytoplasm of Cyanobacteria (formerly termed blue-green algae. Because cyanobacteria are the nitrogen fixing component in lichens, these are important constituents of biological soil crust.

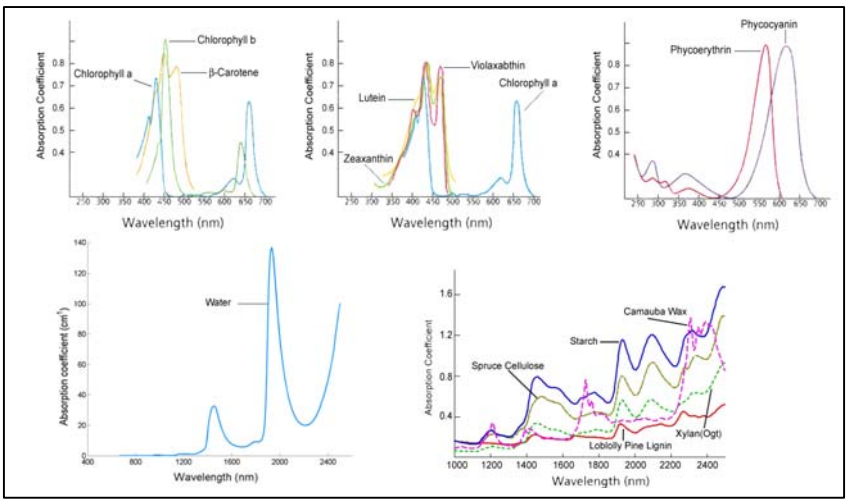

Figure 3. Specific absorption coefficients for upper left, chlorophyll a and b and β-carotene middle, chlorophyll a and xanthopyll pigments: leutin, violaxanthin and zeathanthin, upper right, phycoerythrin and phycocyanin, lower left water (after [40]) and lower right, five common biochemical compounds found in leaves.

Minimal biochemical absorptions occur in the near-infrared (NIR, 700 - 1100 nm) region which are contributed by compounds characteristic of dry leaves, primarily cellulose, lignin and other structural carbohydrates. Reflectance in this region is affected by multiple scattering from internal leaf structure, including the fraction of air spaces, and refraction at air-water interfaces. As intercellular air spaces and cell sizes decrease, overall leaf reflectance or albedo declines. Eller and Willi [23] showed that pubescence mainly affects the visible range, because the increase in reflectance in the infrared is offset by a decrease in transmittance.

Reflectance and transmittance in the shortwave-infrared (SWIR, 1100 - 2500 nm) are dominated by water absorption in green leaves (Figure 3d). The specific absorption coefficients for pure liquid water were first observed by Curcio and Petty [24] and have been extensively studied (see [25]). The primary and secondary absorptions by water in leaf reflectance occur at 1450, 1940, and 2500 nm with important secondary absorptions at 980 nm, and 1240 nm [11].

The spectral signatures of biochemical absorptions in the SWIR region are complex. Even when substances are composed of well-characterized repeating units such as starch, sugar, and cellulose, their molecular weights vary, while other families of biochemical substances are not precisely defined or have not been isolated with their molecular structure intact (e.g., proteins, lignins). In dry leaves, reflectance and transmittance (Figure 3d,e) are controlled by dry carbon-based compounds like cellulose, lignin, and sugars, and nitrogen-based molecules such as proteins and enzymes. For example, nitrogen (N-H bonds) has a first harmonic overtone at 1510 nm and a series of combination bands at 1980, 2060, and 2180 nm [26]. Because many plant and soil macromolecules contain common chemical bonds (-H, C-N, C-O, and N-O bonds, and C=O, O=H, and N=H) they create overlapping absorption features [27-28] that have resisted specific biochemical identification.

2.2 Biophysical Information from Dry Plants

Remote sensing studies often group dry plant material as a class, termed non-photosynthetic vegetation (NPV), which are composed of all the non-green plant parts, including dry leaves, bark, and wood. NPV are spectrally variable, especially when considering a range of species [29-31]. In dry leaves, reflectance forms a more monotonic spectral shape from 400 to 1500 nm. If some green foliage remains then a minor red-edge can be observed. The red-edge is a narrow spectral region between 700-725 nm at the long-wavelength edge of the chlorophyll absorption feature. It is absent in rocks, soils, and most dry plant materials. High spectral resolution studies have concentrated on identifying dry plant materials which are indistinguishable in broadband data. Baret et al. [32] showed that the position of the red-edge inflexion point was not influenced by the soil background or by the atmosphere. Elvidge et al. [33] noted that the problem in detecting trace quantities (< 10% cover) of green vegetation in arid and semiarid region could be solved by measuring the red-edge. Anecdotally, because the red-edge is considered a biosignature of green vegetation, it has become a new avenue of research for astronomers searching for life on extrasolar planets [34]!

Lignin and cellulose are usually present in plant residues in an intimate mixture, and have fundamental absorptions in the SWIR infrared, which produce several combination and overtone bands between 2000 and 2500 nm (Figure 3e). Lignin has a strong absorption in the ultraviolet at 280 nm with an absorption wing across VIS and NIR, observable after pigments have degraded in dry leaves. The combination of cellulose and lignin have two diagnostic bands around 2090 and 2300 nm (Figure 3d) which are not observable in live green vegetation [26].

Since lignin is more resistant to decay than cellulose, as plant residues decompose they become enriched in lignin and the ultraviolet absorption becomes more distinct. Thus, reflectance curves change significantly during decomposition. Nagler et al. [35] developed a Cellulose Absorption Index (CAI) using band depth at 2100 nm. Most soils do not absorb at this wavelength while plant residues do. Additionally, they found that CAI changed with soil moisture and that CAI of wet litter was significantly brighter (higher reflectance) than CAI of wet soil, and therefore, distinguishable.

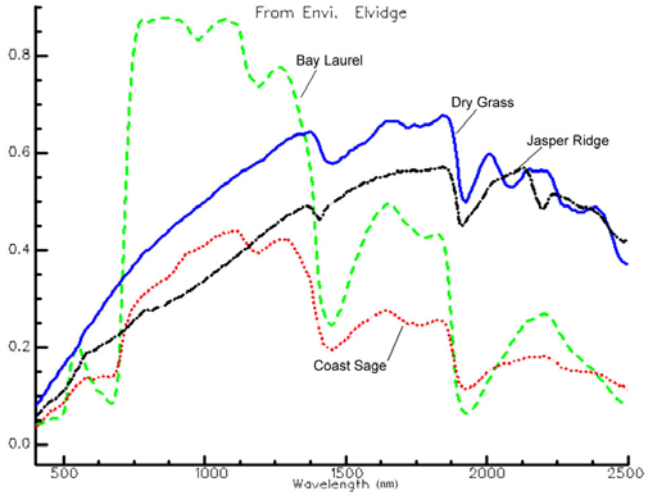

Figure 4. Typical spectra of a fresh green leaf from bigberry manzanita, two stages of dry leaf weathering, and bare soil (bulano sandstone) from Jasper Ridge Biological Preserve, California, showing spectral differences used to differentiate. Note that the *Quercus pubescens* leaf in Figure 2b was dried rapidly since a strong chlorophyll absorption remained in the 400 - 700 nm region. The dry grass residue here lacks a red-edge feature.

As non-photosynthetic vegetation (NPV) decomposes, significant mixing with soil occurs until eventually, cellulose decomposes and only lignin residues remain. Over time, absorption features from decomposition resistant components come to dominant the spectrum. Thus in soil, lignin features develop over time. Surface residues continue to be highly variable in reflectance until decomposition progresses to the point that it becomes indistinguishable from soil [36].

2.3 Biophysical Information from Biological Soil Crusts

Biological soil crusts (BSC) occur on every continent [37] and are a major biological component of arid ecosystems. Although they occur only the first few millimeters of the soil surface they have a key role in arid ecosystem dynamics. BSC typically account for up to 70% of the live cover in arid deserts, therefore account for much of the surface reflectance. BSC are physical and chemical associations between soil particles and microphytic mixtures of lichen, moss, fungi, cyanobacteria, and free-living algae [38-39]. BSC markedly contribute to the high spectral variability in arid regions depending on their active or dormant states and their composition. BSC provide critical ecological functions, including stabilizing soil, nitrogen fixation, water and nutrient retention, carbon fixation, and a seed bed for germination [37]. BSC are typically darker than surrounding bare soil thus loss increases surface albedo [40]. In contrast to BSC, abiotic physical soil crusts and chemical weathering processes are light colored, have low permeability, and are generally much thinner, often less than 1 mm. Bechtel et al. [41] and Buffoni-Hall et al. [42] showed that lichen have low transmittance, making it difficult to estimate spectral properties of the underlying rocks or soils.

2.4 Soil structural crust

In contrast to BSC, soil structural or physical crust is a thin layer (1 mm) formed by kinetic energy of rain drop impact over bare soils. The rain drops contacting the bare soil rearranges a thin surface layer by physical disintegration of the soil particles and dispersion of soil clays which migrate with water in the first few mm of soil. As a result of crust formation, infiltration decreases markedly and runoff and erosion is accentuated [43-44]. Studies show that effects are directly related to the rainfall energy so this contributes to degradation in arid regions with severe storm events and low vegetation cover. In contrast to BSC and desert varnish formation, crust formation is fast and highly dynamic, happening nearly instantaneously after a storm.

Soil crusts alter reflectance because of increased albedo, due to smaller particle size distribution [45-47], orientation of the particles [48], and enhancement of the 2200 nm absorption band by sorting montmorillonite and illite clays onto the surface. Generally there is no significant change in the carbonate 2330 nm band, because it becomes concentrated in the silt or sand fractions. Since soil crust contains higher clay content than the bulk soil, it can bias soil classifications [44]. Albedo and absorptions at 1833 and 2143 nm (no specific absorption feature) have

the best correlation with raindrop energy and infiltration rate, indicating that scattering processes govern these effects [44],[49] with different soils (clay vs. sandy) producing different spectral behaviors [50]. Goldshleger et al. [50] tracked crust formation using reflectance at 1700 nm as an indicator of albedo and the first derivative of absorption at 2200 nm, which represented absorption of clay minerals. They found that a clay-particle relationship was a better indicator than particle size alone.

2.5 Desert Pavement and Varnish

Although little studied for spectral characteristics, desert pavements are important in erosion control and ecosystem stability and represent an early stage of biologic weathering in arid landscapes. Desert pavements are ancient mosaics of rock fragments embedded in sediments [51] that occur on a wide range of undisturbed arid and semiarid landforms. The presence of desert pavement indicates that an area has been undisturbed for (10,000s of years [52]. As pavement ages the rock surfaces become smoother with few protruding fragments. Exposed surfaces are coated with thicker varnishes, which are black or brown coatings formed by bacteria interacting with clay minerals (~70%) and iron or manganese oxides [52-54]. Spectrally, desert pavement and varnish lower surface albedo relative to younger soil and rock surfaces. Loss of the pavement increases albedo by exposing native fine materials, gravel and cobbles. Disturbance may turn over pavement and expose less weathered (oxidized) rocks of different colors, or which have a different mineralogy (less clay and manganese for example). Varnish can be mechanically removed by wind and scraping or water erosion, exposing the less weathered gravel surfaces.

2.6 Biophysical Information from Soils

The weathering process that soils undergo in arid and semiarid regions are related primarily to high temperatures and low and/or irregular availability of water. Thus, salt dissolution combined with high evaporation can precipitate alkaline salts to form hardpans and caliche layers at the wetting front. Important soil surface processes are due to the combination of irregular precipitation, shallow soil development, and scarce vegetative cover which create low infiltration capacity and high runoff. The combination of biotic and abiotic processes produces highly heterogeneous soils that require synoptic coverage over large regions with sufficient spatial and spectral resolution to quantify soil patterns.

Many soils only differ in brightness in red and NIR, which form a linear relationship that is represented in spectral space as a soil brightness vector [55]. The position of a given soil on the soil line depends on factors that affect the albedo such as shadows, moisture content, and roughness [56-57]. The slope of the line depends on the relative position between the R and NIR bands and therefore depends on the intrinsic soil properties such as iron or organic matter content. Also it can be affected by atmosphere and sensor properties such that it becomes soil and scene-dependent. The width of the soil line expresses variable soil properties in these wavelengths (e.g., moisture or organic matter). The soil line has been used to estimate vegetation cover by measuring the perpendicular to a soil line defined by bare soil pixels. The problem in using this index is that the high soil heterogeneity makes it difficult to define a unique soil line. Fox et al [58] proposed an automated soil line identification routine. The soil line only represents a two dimensional spectral space so it only shows the general shape of the spectrum in the VIS-NIR space. Most soil biological and physicochemical properties have information contained in a large number of other wavelengths that make it necessary to use more complex methodologies to study soil properties.

The most widely used semi-analytical technique to determine mineral absorption strength is the continuum removal [60-61]. The continuum removal calculates the normalized band depths by interpolating reflectance between two local reflectance maxima (the shoulders of the absorption feature) then calculates the band depth, area, and asymmetry within the wavelength interval (Figure 5). The mineral type is determined by the wavelength positions at the minima and the feature asymmetry [61]. However other studies [62] have demonstrated that the spectral shape results from all interactions affecting absorption and scattering. Water broadens and shifts the wavelength positions of specific absorption features to longer wavelengths.

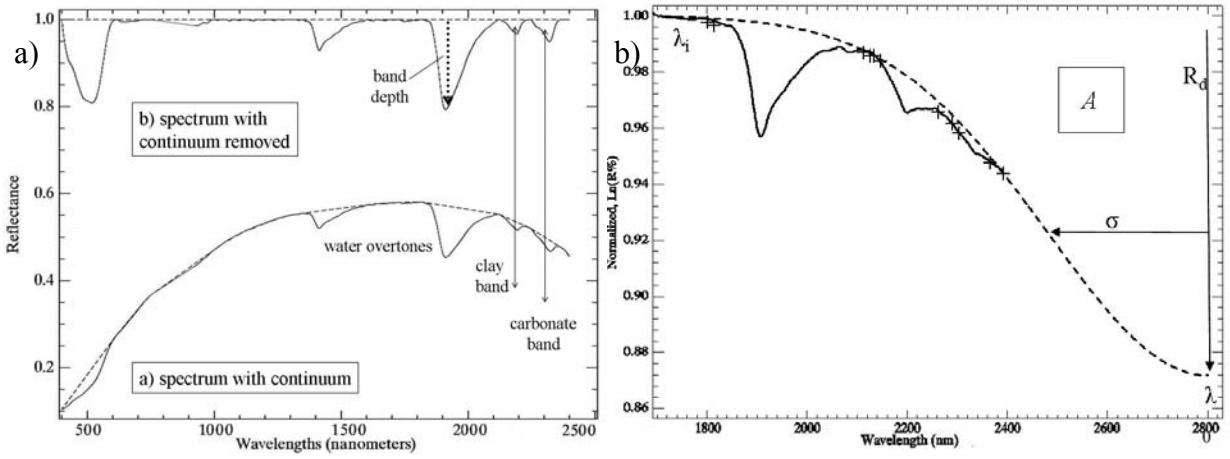

Figure 5. a) Upper, soil spectrum with continuum removed, normalizing absorption features. Lower, soil reflectance spectrum with continuum shown as dashed line. **b**) Soil Moisture Gaussian Model, fit to a soil spectrum from water fundamental at 2800 nm. The shoulders of the absorption features used for continuum removal are shown as crosses [59]. The Gaussian curve is fit from the wavelength (λ) absorption maximum to λ_i, R_d is depth at λ, σ is the full width half max, and *A* is the area.

Moisture is the main source of temporal variability in soil reflectance. Soil reflectance is greatly affected by slight differences in water content [63], reducing the spectral contrast needed for identifying minerals and organic matter absorption depths [64]. The change in band depth is non-linear with water content [65], which requires knowing the light absorption characteristics of the soil for all pixels in an image. Several researchers have successfully modeled soil moisture using 1450 and 1900 nm bands [65-67]. Unfortunately, these absorption bands also absorb water vapor in the atmosphere, confounding soil quantification in image data. Whiting et al. [59] extrapolated the general shape of the SWIR spectrum to the fundamental water absorption at 2800 nm by fitting the convex hull to a Gaussian function and reported that the area under the Gaussian curve is correlated with soil moisture content (r^2=0.90). The Soil Moisture Gaussian Model (SMGM) was highly correlated to the soil water content, up to the water holding capacity of the soil without dependence on specific water absorption bands.

Soil salinity is one of the main consequences of soil degradation. Salinization not only affects the growth of vegetation, but destruction of soil structure due to clay dispersion and subsequent decrease in infiltration and aeration. Reflectance of saline soils results from the spectral properties of salt and surface roughness, presence of crust, soil color and moisture, which have a combined effect on albedo [68]. A good review of spectral characteristics of soil salinity is found in Metternicht and Zinck [68]. Most soil salts (i.e., halite, calcium carbonate, sodium sulfate and gypsum) are highly reflective in the VIS-NIR and show distinct absorption features in the SWIR. Hydrated salts like gypsum have a significant decrease in reflectance toward longer wavelengths and sharp absorptions at the water bands, while salts like halite are highly reflective in this region of the spectrum. As a result most saline areas have high albedo except highly alkaline soils which are dark black due to distillation of organic matter. Roughness and moisture are the two factors affecting albedo. For example the presence of saline crust decreases roughness and increases albedo, while moisture dissolves salt crusts so albedo decreases. Since these properties are highly dynamic their variability makes assessment difficult. While high salt concentrations are easily identifiable, low levels present more difficulty for detection because spectral features are weak and the presence of salt-tolerant vegetation dominates the soil signal. Hypersaline soils have little or no vegetation on them but may have BSC if moisture is available.

Roughness is the primary factor affecting soil reflectance and it is also highly variable in arid soils. Surface roughness is influenced by the size and distribution of soil aggregates and by the density and distribution of any vegetation cover. The effect of roughness on albedo is on the distribution of shadows [69], which affect the spectral contrast and reduce discrimination of spectral features. However, several studies have demonstrated that bi-directional reflectance distribution is distinct on desert surfaces [70]. Thus, Shosany et al. [71] demonstrated that most soils in the Australian desert were anisotropic with a dominant backscattering component. Cierniewski and Karnielli [72] simulated reflectance on four virtual surfaces (desert pavement, BSC, sands and playa) under different illumination conditions and showed that forward scattering and backscattering properties significantly affected spectral contrasts between surfaces. For example, contrast between sand and playa was greatest in the backscattering directions for a specific view and zenith angles, while for crust and desert pavement, the contrast was best in the forward scattering direction.

Erosion is important in arid regions. Common indicators of erosion are a decrease of organic matter, appearance of lower soil horizons at the surface, and presence of rocks. Eroded soil surfaces can have high levels of iron oxides or carbonates from the B or C horizon. Whiting (unpublished) mapped carbonates in the Tomelloso area of Spain where the underlying carbonate layer (caliche) was exposed on the surface. The eroded soil has high albedo and a strong carbonate absorption feature while the floodplain soil has stronger clay absorption. De Jong [45] used imaging spectroscopy to map erosion based on iron and carbonates and Palacios-Orueta et al. [73] mapped organic matter and iron.

3 MAPPING PLANT AND SOIL PROPERTIES USING BIOPHYSIOLOGICAL INDEXES

A wide range of spectral indexes have been developed that take advantage of specific absorption features of plants and soils relative to spectral bands where the materials do not absorb [74]. These methods are quasi-quantitative in that specific chemicals absorb energy at specific wavelengths, thus we know *a priori* where these features occur. However, the absorption depth is not linear with concentration and the presence of other materials with overlapping absorption features will confound quantification. Some chemicals of interest are actually families of related molecules (e.g., organic matter) rather than a specific molecule (e.g., H_2O) which results in inconsistent identification of the wavelength location of absorption features, thus limiting index methods.

Vegetation indexes are sensitive to plant cover and provide an estimate of the "greenness" of an area. Newer indexes identify specific pigments, water content, cellulose, lignin, and nitrogen. Tables 1 and 3 list 36 widely used indexes in four basic types: pigment, foliar water, foliar chemistry, (Table I) and soil indexes (Table 3). Not all of these indexes are independent. Obviously the multiple indexes estimating chlorophyll content will be correlated. Additionally, correlations between physiological characteristics lead to further correlations between indexes. For example, the water indexes and nitrogen index are highly correlated to NDVI. This is because nitrogen increases with water as does the photosynthetic machinery, resulting in higher NDVI. Conditions where indexes become uncorrelated or partially uncorrelated may provide evidence for stress conditions.

3.1 Vegetation indexes

Vegetation indexes (VI) take advantage of the strong contrast between red and NIR reflectance produced by green foliage (related to vigor and amount of vegetation). In desert environments, VIs must be able to discriminate vegetation at low cover, from zero up to about 50%, and to extract information about vegetation properties, while minimizing soil, atmosphere, and sun and view angle effects. In arid environments soil is the most significant contribution to scene variance therefore, a correction for soil background effects is necessary.

3.2 Pigment indexes

Pigment indexes focus on photosynthetic pigments, primarily chlorophyll the dominant photosynthetic pigment of green vegetation. However, some like the PRI identify xanthophyll cycle pigments, which are important in regulating light absorption in high light intensity environments. Leaves possess a range of accessory photosynthetic pigments, including carotenoids and xanthophylls that serve functions to regulate and increase photosynthetic performance.

3.3 Foliar water indexes

Water absorbs strongly throughout the SWIR wavelengths [19]. Most narrow-band indexes use the 970 or 1240 nm water absorption features, although broad band indexes have been used (e.g., Landsat bands 4, 5 and 7).

3.4 Foliar chemistry indexes

Several leaf chemistry indexes have been proposed. The normalized difference nitrogen index (NDNI) was successfully used by Serrano et al. [75] on AVIRIS data to estimate nitrogen concentration in a semiarid shrubland. Nonetheless, other studies have found it difficult to extract this data from two band indexes. Pinzon et al. [76] used singular value decomposition to accurately estimate leaf nitrogen from leaf samples in laboratory data. Later, Smith et al. [77] used partial least squares to relate field measured leaf nitrogen to canopy nitrogen in AVIRIS hyperspectral data. The cellulose absorbance index (CAI; [35]), estimates the cellulose content of senescent plant matter, emphasizing the distinctions between soil and plant litter. This index may be useful in arid and semi-arid regions where green vegetation is seasonally sparse and much of the biomass is in undecomposed plant litter and stems.

3.5 Soil indexes

Table 1. Vegetation Indexes Developed as Biophysical Indicators.

Index[a]	Formula	Details	Source[b]
Pigment			
SR	R_{NIR} / R_R	Index of green vegetation cover. Wavelengths, depending on sensor, e.g., NIR=845nm, R=665nm.	1
NDVI	$(R_{NIR} - R_R)/(R_{NIR} + R_R)$	Index of green vegetation cover. Wavelengths, depending on sensor., e.g., NIR=845nm, R=665nm.	1
mNDVI	$(R_{750} - R_{705})/(R_{750} + R_{705})$	Leaf chlorophyll content	2
SGR	$\sum_{n=500}^{599} R_n$	Index of green vegetation cover.	2
PRI	$(R_{531} - R_{570})/(R_{531} + R_{570})$	Xanthophyll light response ~ photosynthetic efficiency. Sensitive to carotenoid/chlorophyll ratio	3
RGR	$(R_{600-699})/(R_{500-599})$	Anthocyanins/chlorophyll	2
NPCI	$(R_{680} - R_{430})/(R_{680} + R_{430})$	Total pigments/chlorophyll	4
SRPI	R_{430} / R_{680}	Carotenoid/chlorophyll *a* content	5
NPQI	$(R_{415} - R_{435})/(R_{415} + R_{435})$	Chlorophyll degradation, detects early stress	5
SIPI	$(R_{800} - R_{445})/(R_{800} - R_{680})$	Carotenoid/chlorophyll *a* concentrations	5
PI1	R_{695} / R_{420}	Plant stress status	5
PI2	R_{695} / R_{760}	Plant stress status	5
PI3	R_{440} / R_{690}	Vegetation health index, chlorophyll fluorescence ratios	6
PI4	R_{440} / R_{740}	Vegetation health, chlorophyll fluorescence ratios	6
Water			
NDWI	$(R_{860} - R_{1240})/(R_{860} + R_{1240})$	Leaf water content	7
WBI	R_{900} / R_{970}	Leaf water content	8
Foliar chemistry			
NDNI	$\left[\log\left(1/R_{1680}\right)\right] / \left[\log\left(1/R_{1680} R_{1510}\right)\right]$	Foliar nitrogen concentration	9
NDLI	$\left[\log\left(1/R_{1680}\right)\right] / \left[\log\left(1/R_{1680} R_{1754}\right)\right]$	Foliar lignin concentration	9
CAI	$0.5(R_{2020} + R_{2220}) - R_{2100}$	Cellulose & lignin absorption features, discriminates plant litter from soils	10

[a] **SR**: Simple Ratio; **NDVI**: Normalized Difference Vegetation Index; **mNDVI**: Modified NDVI; **SGR**: Summed green reflectance; **PRI**: Photochemical Reflectance Index; **RGR**: Red/Green ratio; **NPCI**: Normalized Pigments; **CRI**: Chlorophyll Ratio Index; **SRPI**: Simple Ratio Pigment Index; **NPQI**: Normalized Phaeophytinization Index; **SIPI**: Structure Intensive Pigment Index; **PI**: Pigment Index; **NDWI**: Normalized Difference Water Index; **WBI**: Water Band Index; **NDNI**: Normalized Difference Nitrogen Index; **NDLI**: Normalized Difference Lignin Index; **CAI**: Cellulose Absorption Index. [b] 1,[80]; 2, [81]; 3, [17]; 4, [19]; 5, [82]; 6, [83]; 7,[84]; 8, [29]; 9, [75]; 10, [35]

To observe desert conditions and desertification it is critical to map soils with low amounts of vegetation. The soil line, related to soil brightness in red and NIR bands, has already been introduced. Although soil spectra lack strong absorption bands, several soil indexes (Table 3) related to soil color have been developed [78-79]. The latter found high correlation between the Helmholtz definition of color and Thematic Mapper indexes in an arid environment. Redness indexes are important for characterizing soil weathering and oxidation. Color is important for assessing soil quality and is closely related to surface processes and types of chemical weathering. Soil color is defined by parent material, weathering, and topography which are related to soil biophysical properties, therefore, color might be used as an indicator of erosion or deposition or as an indicator of surface organic matter. If soil variability is high, as in many desert environments, there will not be a unique soil line and the width of the soil line becomes critical for defining soil properties.

4 LEAF REFLECTANCE AND TRANSMITTANCE MODELS

Over the past decade, sophisticated radiative transfer models have been developed to account for leaf properties and changes in reflectance/transmittance due to changing leaf biochemistry and structure. The simplest models consider the leaf as a single scattering and absorbing plane-parallel layer while the most complicated models consider the full three-dimensional structure and biochemistry of the cells and tissues that form the leaf. At a minimum, physically realistic models require information about the refractive index and the specific absorption coefficients of leaf constituents (Figure 3). Computer-based leaf models can be categorized into different classes, arranged in order of increasing complexity (Figure 6).

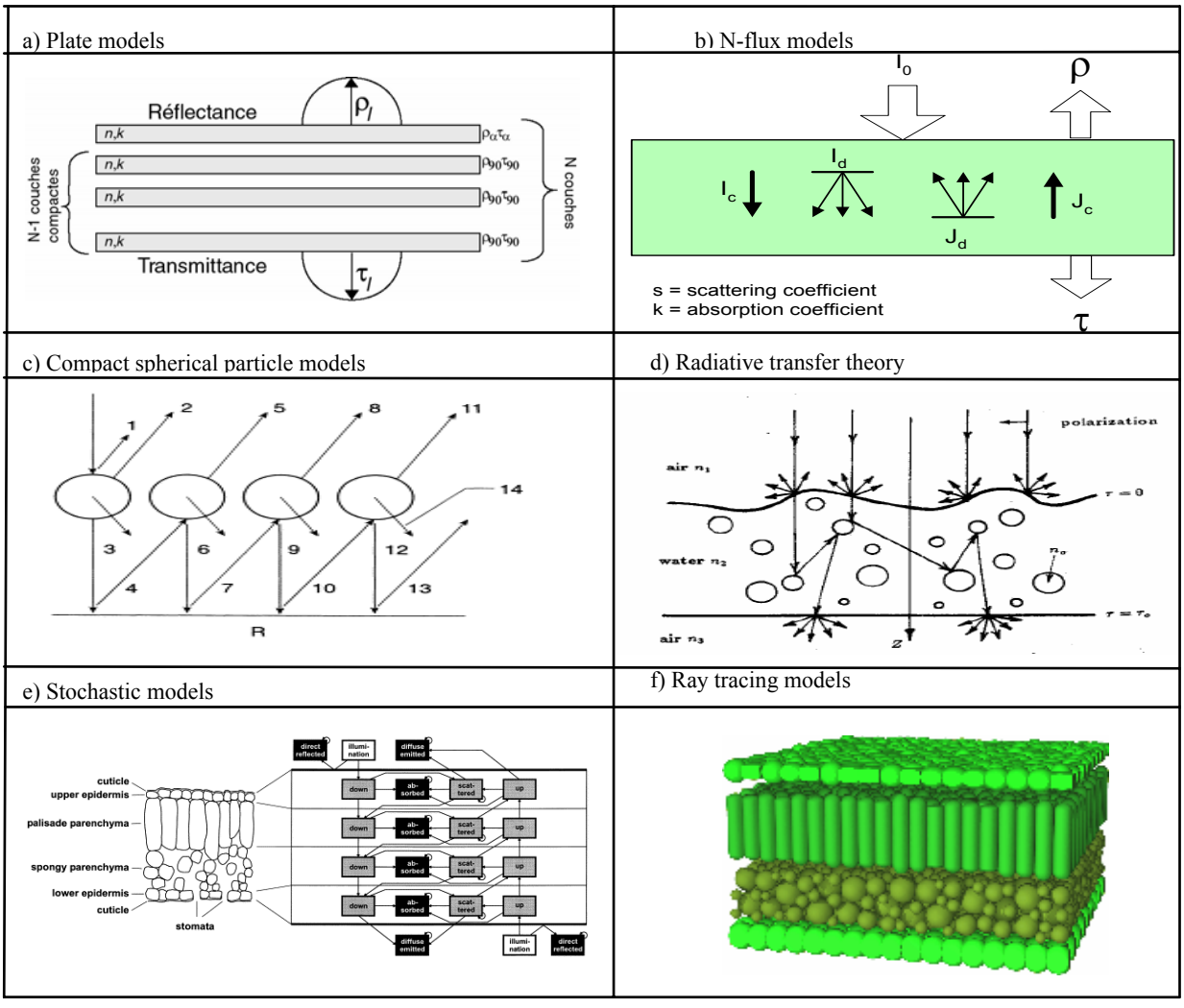

Figure 6. Major classes of models simulating leaf optical properties.

4.1 PLATE MODELS

Figure 6a: Allen et al. [85] were the first to represent a compact leaf as an absorbing plate with rough surfaces producing diffusion. This approach was extended to non-compact leaves by regarding them as layers of plates separated by N–1 air spaces [86]. The parameter N provides an internal structure for scattering. The widely used PROSPECT model (Leaf Optical Properties Spectra) [12] was designed to accurately simulate the hemispherical reflectance and transmittance of various types of plant leaves (fresh monocot and dicot leaves, senescent and dry leaves) over the solar spectrum from 400 to 2500 nm. The original model was improved significantly by optimization of input parameters [13-14]; [87-88]. Its four input parameters today are the leaf structure parameter, chlorophyll a+b concentration, equivalent water thickness, and dry matter content. Recent studies [89-90] have quantified the contribution of these parameters to the PROSPECT model outputs, as well as their interactions (Figure 7), demonstrating that most foliar absorptions are accounted for in the current model, with the gray line the sum of these contributions. Clearly there is potential to improve the model in both the VIS and SWIR regions.

PROSPECT provides good estimates of leaf water content (equivalent water thickness) in fresh leaves, illustrated in Table 2 using data from the LOPEX experiment [92]. Likewise dry matter estimated from dry leaves is well predicted although poorly estimated from fresh leaves. For the *Quercus pubescens* example shown in Figure 2, Table 2 provides a comparison between measured and predicted chemistry. Chuvieco et al. [91] have empirically solved this problem for wildfire risk in Mediterranean ecosystems by using multi-temporal data and combining the dry biomass estimate from the driest part of the annual period with water content from all other dates. Because total ecosystem biomass changes slowly, this method provides better estimates than direct model inversions.

4.2 N-flux models

Figure 6b: Derived from the Kubelka-Munk theory these models consider the leaf as a slab of diffusing and absorbing materials. Different parameters are allowed in each layer and the model estimates leaf reflectance and transmittance. Leaf biochemistry was introduced by Conel et al. [93] who used a two-flux model to evaluate the influence of water, protein, cellulose, lignin, and starch on leaf reflectance, however their model was not validated.

4.3 Compact spherical particle models

Figure 6c: Dawson et al. [94] adapted Melamed's theory of light interaction with suspended powders and designed the LIBERTY model (Leaf Incorporating Biochemistry Exhibiting Reflectance and Transmittance Yields) specifically to calculate the optical properties of both dried and fresh stacked conifer (particularly pine) needles. By treating the leaf as an aggregation of cells, with multiple scattering, output reflectance and transmittance are a function of three structural parameters (cell diameter, intercellular air space, and leaf thickness) and the combined absorption coefficients for chlorophyll, water, lignin and cellulose, and nitrogen.

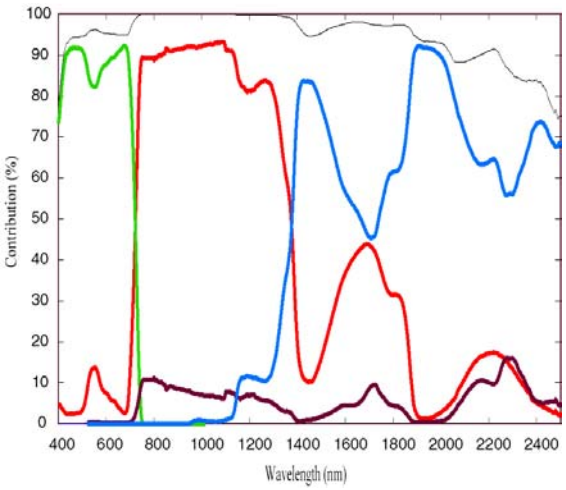

Figure 7. Contribution to leaf transmittance simulated by PROSPECT for chlorophyll concentration Cab (green), water content Cw (blue), dry matter content Cm (brown) and the structure parameter N (red) (Pavan, unpublished).

4.4 Radiative transfer equation

Figure 6d: Few leaf models directly use the radiative transfer equation because essential information about internal leaf structure and biochemical distributions is lacking, leading to major simplifications. Ma et al. [95] described the leaf as a slab of water with an irregular surface containing randomly distributed spherical particles. Ganapol et al. [96] developed LEAFMOD (Leaf Experimental Absorptivity Feasibility MODel), which models the leaf as a homogeneous mixture of biochemicals which scatter and absorb light. The homogeneity simplification ignores the obvious cellular organization of leaf chemistry. Nonetheless, Johnson [97] used this model to predict leaf nitrogen from several laboratory datasets.

4.5 Stochastic models

Figure 6e: Tucker and Garatt [98] proposed a stochastic model in which radiation transfer is simulated by a Markov chain. The leaf is partitioned into palisade parenchyma and spongy mesophyll tissues with four radiation states (solar, reflected, absorbed, and transmitted) with defined the transition probabilities. The SLOP (Stochastic model for Leaf Optical Properties) model [99] is a recent improvement in which the leaf is partitioned into four tissues.

4.6 Ray tracing models

Figure 6f: Only ray tracing techniques account for the full three dimensional complexity of internal leaf structure as it appears in a photomicrograph. This technique requires a detailed description of individual cells and their unique arrangement inside tissues and the optical properties of leaf materials (cell walls, cytoplasm, pigments, air cavities, etc.) must be defined. Using the laws of reflection, refraction, and absorption, the propagation of individual photons incident on the leaf surface can be simulated. Once a sufficient number of rays have been simulated, statistically valid estimates of the radiation transfer in a leaf can be predicted.

Leaf Properties	LOPEX Chemistry	Fresh Leaf Predictions	Dry Leaf Prediction
N		1.38	2.97
Cab (µg/cm^2)	42.7	42.2	28.1
Brown pigments (µg/cm^2)	--	30.2	105.7
Cw (g/cm^2)	0.00825	0.00750	0.00063
Cm (g/cm^2)	0.00604	0.00604	0.00604

Table 2. Leaf chemistry measured in the LOPEX dataset [92] and chemistry predictions from the PROSPECT model for an average of *five Quercus pubescens* leaf measurements.

Govaerts et al. [100] used a three-dimensional ray tracing model, RAYTRAN [101], and developed a virtual three-dimensional leaf, to characterize the light environment, including absorption, scattering and transmission, within and between cells. Cells of variable size, cell wall thicknesses, chemistry, and air spaces were modeled to simulate realistic leaf tissues and the implications for absorption profiles, light harvesting, and photosynthesis was successfully investigated [102]. The model simulated the leaf anatomy of a typical mesic dorsiventral dicot leaf. In general, we lack sufficient information about leaf anatomy and biochemistry to apply this model to a wider range of morphological types, e.g., xeromorphic leaves. However, if anatomical and morphological data were available, it would be possible to simulate a range of environmental conditions and improve our understanding of biophysical measurements in arid ecosystems.

4.7 Next Generation of Leaf Models

Despite decades of research, more work is required before we will accurately model leaf optical properties. Progress on the next generation of optical models requires new understanding of cell and leaf anatomy for leaves with adaptations to a range of environments. Perhaps new approaches to modeling may lead to fundamental improvements, e.g., the ABM (Algorithmic BDF Model) or FSM (Foliar Scattering Model), used to study the interaction of light and plant leaves for image synthesis [103]. Further, more understanding of the relationships between structure and function at the leaf level are clearly needed to drive model improvements. Lastly, better optical characterization of more biochemical compounds is needed to expand the range of biochemistry that can be detected. One reason for needing more information is that a direct interpretation of chlorophyll only estimates potential carbon fixation and does not measure actual state of photosynthetic activation.

A small but measurable fraction of the radiation reflected and transmitted by leaves is actually fluorescence emission [104-105] by polyphenols in the blue and chlorophyll a in the red and NIR as shown in Figure 8. Passive sensing of chlorophyll fluorescence in the oxygen bands emerges as a promising approach for monitoring vegetation health. However, the interpretation of this signal depends both on the leaf environment (incoming light quality and intensity, temperature, etc.) and on intrinsic parameters (physiological state, species, biochemical composition, etc.). In the FluorMOD project (Development of a Vegetation Fluorescence Canopy Model), a leaf fluorescence model has been developed that predicts reflectance and transmittance of a fresh leaf including chlorophyll fluorescence [106-107]. Beside the classical input variables for PROSPECT, fluorescence quantum yield, PSII/PSI ratio, temperature, species, and incident PAR are required. Figure 8 shows the first results of the FLUORMODLEAF for a typical dicot leaf. Although the model is still at an early stage of validation, these results are encouraging.

Many studies have demonstrated a direct relationship between photosynthetic rates, light absorbance, chlorophyll content, leaf nitrogen, and dry matter production are all related to leaf area (e.g., [108-109]. There appears to be a linear dependence of maximum photosynthetic capacity on leaf nitrogen [110] which is partially species specific. Leaf nitrogen exhibits a linear relationship with specific leaf mass, the reciprocal of specific leaf area (1/specific leaf area) [111], and a property inversely related to dry biomass estimated by PROSPECT.

As described earlier, hairy and/or waxy leaves are typical of plants in arid regions. Specific surface optical properties of these leaves are poorly known. For instance, a thick cuticle, which may protect leaves from desiccation or insects acts as a mirror, preferentially reflecting light in the specular direction. In contrast, hairs tend to scatter light in all directions. This duality between specular and Lambertian surfaces is characteristic of the leaf bidirectionnal reflectance distribution function (BRDF). Leaf BRDF was recently acquired for several species using a goniophotometer at 400 wavelengths and 98 viewing angles [112]. These measurements (Figure 8) have been successfully estimated with a specular reflection model (Cook-Torance) coupled with prospect to simulate the diffuse fraction.

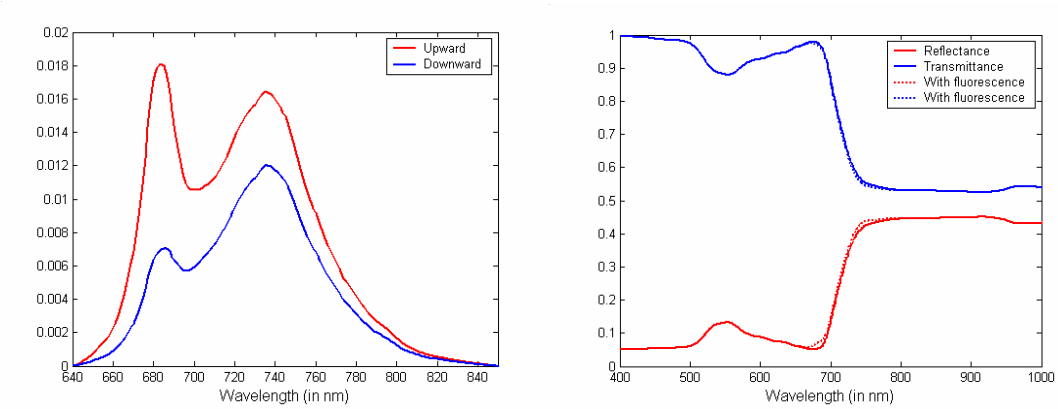

Figure 8. Simulation of the adaxial and abaxial chlorophyll fluorescence (on the left) and of the reflectance and transmittance with and without fluorescence (on the right) using FLUORMODLEAF. Structure parameter: N = 1.5, chlorophyll a+b content: C_{ab} = 33 µg cm^{-2}, equivalent water thickness: C_w = 0.025 cm, dry matter content: C_m = 0.01 g cm^{-2}, fluorescence quantum yield: Φ = 0.04, temperature: T = 20ºC, species: green bean, PSII/SPI ratio: Sto = 2.0.

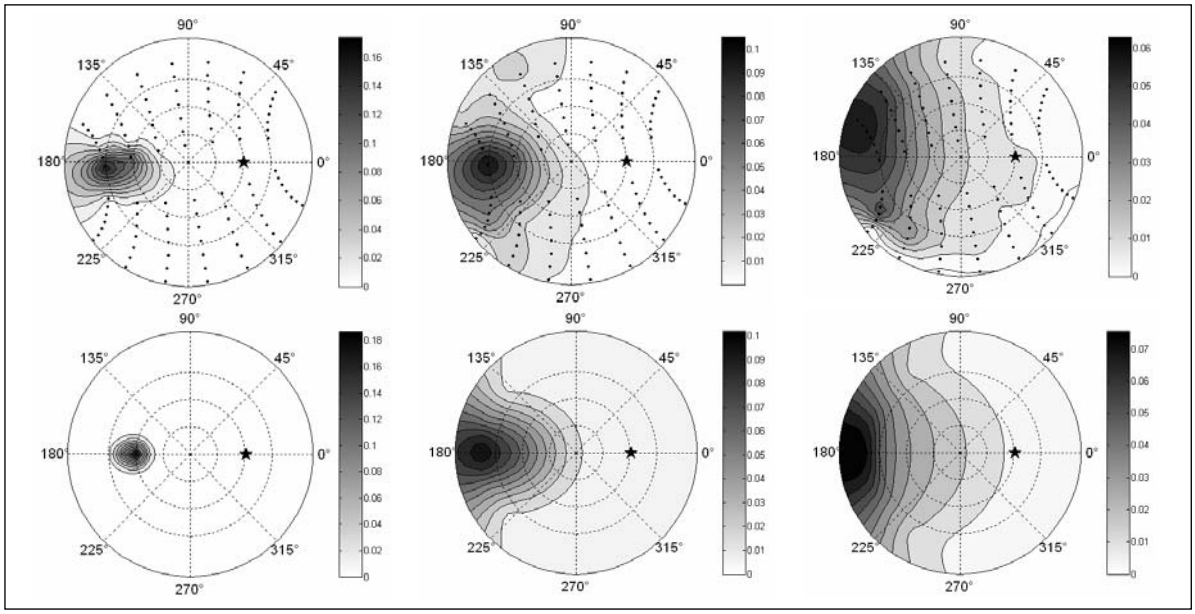

Figure 9. Measured (top) and modeled (bottom) BRDF for θ_s = 41° at wavelengths of minimum reflection (after [112]).

4.8 Extending biophysical measurements to canopy models

Heterogeneous and open plant canopies, characteristic of desert environments, preclude the use of simple 1-D radiative transfer models that rely on an assumption of homogenous turbid media [113]. On such surfaces, the

interactions between light and objects (for instance, shrubs, grasses, BSC, bare soil), which are distributed in clumped patches rather than uniformly distributed, generate a higher level of complexity that requires 3-D models [114]. Esteve et al. [115] used the DART (Discrete Anisotropic Radiative Transfer) model [116], to simulate radiative transfer in heterogeneous arid 3-D landscape comprised of trees, shrubs, grass, soil, etc. They inverted DART on a temporal series of Landsat MSS acquired in Burkina Faso, and determined the woody cover allowing them to follow its degradation over time. Zarco-Tejada et al. [117] followed changing leaf water content over the summer drought in semiarid southern California using a MODIS time series analyzed with a linked PROSPECT and SAILH canopy model. Some information about surface heterogeneity, which may change fast when land degradation occurs, can also be inferred using multi-angular reflectance data. Widlowski et al. [118] generated various 3-D vegetation canopy representations, from homogeneous to heterogeneous, at the nominal ground resolution of the MISR instrument and simulated their reflectance using RAYTRAN. They showed that the reflectance anisotropy could be obtained by inversion of a simple parametric model.

5 SOIL REFLECTANCE MODELS

Most soil mapping has been related to the fraction of exposed soil or more precisely, the fraction of green vegetation cover, assuming that non-vegetated surfaces are soil. To date the identification of soil biogeochemical components from reflectance measurements have been largely limited to regression models that are valid only for specific locations. Greater use of multivariate statistical models, e.g., neural nets or support vector machines, will provide techniques that increase accuracy of soil quantities and portability across larger regions. Wider use of classification and regression tree (CART) models, partial least-squares, and general additive model (GAM) methods may also improve local regression models by including more spatial data in the analysis, and provide the templates for applying methods in other soil regions. These regression models may also benefit from the inclusion of hierarchical partitioning the surface reflectance components as a means of stratifying the image region to improve the local spectral model, just as much as landscape partitioning improves the accuracy.

The greater task, although highly promising for producing more robust models, is in developing radiative transfer models that can identify the presence and abundance of soil components in the context of intimate mixtures and surface geometry. Knowledge gained in recent years in extending radiative transfer modeling to a wider range of vegetation and soil backgrounds will restart soil modeling efforts begun in 1990's. The identification of absorption coefficients for soil minerals, organic matter, and water are needed to develop radiative transfer models that will measure mineral abundance through spectral curve fitting.

6 CONCLUSION

The geographic extent and remote locations of arid ecosystems and the harsh climate characteristic of arid ecosystems create challenges to effectively monitoring desertification. Furthermore monitoring must be done over long periods to fully observe the stochastic behavior of deserts in a globally changing context. The potential to use remote sensing for cost-effective monitoring has long been recognized, although the extensive heterogeneity of geologic parent material and soils combined with low vegetative cover, rapid biologic responses to wet and dry rainfall pulses, has limited our ability to fully monitor the condition of these ecosystems. Furthermore, infrequent precipitation leads to extended dormancy with short unpredictable periods of biological activity. We reviewed the spectral characteristics of plants and soils that are detectable using optical sensors and current methods to identify and quantify properties that have potential for monitoring arid ecosystem processes. The wealth of existing information on the reflectance and transmittance of desert plants, soils, and other materials, combined with new modeling and index approaches will lead to improved capability for monitoring global desert environments.

A wide range of plant biochemicals are detectable or potentially detectable in hyperspectral data, e.g., chlorophyll, photosynthetic accessory pigments, water, and soil constituents e.g., clays, carbonate, iron, and organic matter. Biophysical methods may improve detection and monitoring of inter-plant spaces composed of bare soil crust, biological soil crust, or dead plant material. The expanded use of absorption features in the VIS and SWIR has produced a large number of spectral index-based methods to identify specific compounds or properties. As we move toward more quantitative predictive models, it is clear that the overlapping structure of many absorption features of plants and soils precludes direct assessment of their concentration. New biophysical methods that take the full spectral shape into account, including the effect of one compound on the spectral absorption of another, are needed to reduce uncertainty in their estimates. Over the past decade several radiative transfer models have been developed based on physical absorption and scattering processes using principles of spectroscopy and information over the entire spectrum. Other models take advantage of new types of data like passive fluorescence or thermal-infrared emissions or bidirectional reflectance.

Table 3. Soil Indexes Developed as Biophysical Indicators.

Index[a]	Formula	Details	Source[b]
NDI	$(R_{840} - R_{1650})/(R_{840} + R_{1650})$	Discriminates soil and dry matter	1
SACRI	$\frac{\alpha(R_{840} - \alpha R_{1650} - \beta)}{R_{1650} - \alpha R_{840} - \alpha\beta}$	Improved NDI discrimination	2
CRIM			3
	TM Indices	**HRV Indices**	
BI	$BI = \sqrt{(TM1^2 + TM2^2 + TM3^2)/3}$	$BI = \sqrt{(XS1^2 + XS2^2)/2}$	4
SI	$SI = (TM3 - TM1)/(TM3 + TM1)$		5
HI	$HI = (2 \times TM3 - TM2 - TM1)/(TM2 - TM1)$		5
CI	$CI = (TM3 - TM2)/(TM3 + TM2)$	$CI = (XS2 - XS1)/(XS2 + XS1)$	6, 7
RI	$RI = TM3^2/(TM1 \times TM2)$	$RI = XS2^2 / XS1^3$	7
RI		$RI = XS2^2 / XS1^4$	4

[a]**NDI**: Normalized Index; **SACRI**: Soil Adjusted Crop Residue Index; **CRIM**: Crop Residue Index Multiband; **BI**: Brightness Index -average soil reflectance; **SI**: Saturation Index-spectral slope; **HI**: Hue Index- dominant wavelength; **CI**: Coloration Index- hematite/ hematite+geothite ratio; **RI**: Redness Index -Hematite Content. [b]1, [119]]; 2, 3 [120]; 4, [121]; 5, [122]; 6, [123]; 7, [124].

ACKNOWLEDGEMENTS

A significant part of this review was done while the first author was on sabbatic at the Department of Geography and Environmental Sciences, University of Auckland, New Zealand. The authors wish to thank Margaret Andrew for her help in assembling the index information and references for Table I and Dr. David Riaño for help in preparing some figures. We wish to thank Van Lay for help in formatting the document and references and preparation of other figures.

REFERENCES

[1] MILLENNIUM ECOSYSTEM ASSESSMENT, 2005: Ecosystems and Human Well-Being: Desertification Synthesis, Desertification synthesis. U.N. Convention to Combat Desertification (UNCCD).

[2] MEIGS, P., 1953: World distribution of arid and semi-arid homoclimates. In: Reviews of research on arid zone hydrology. pp. 203-209. Paris, United Nations Educational, Scientific, and Cultural Organization, Arid Zone Programme-1.

[3] SCHLESINGER, W.H., REYNOLDS, J.F., CUNNINGHAM, G.L., HUENNEKE, L.F., JARRELL, W.M., VIRGINIA, R.A. AND WHITFORD, W.G., 1990: Biological Feedbacks in Global Desertification. *Science 247*, pp. 1043-1048.

[4] OKIN, G.S., MAHOWALD, N., CHADWICK, O.A. AND ARTAXO, P., 2004: Impact of desert dust on the biogeochemistry of phosphorus in terrestrial ecosystems. *Global Biogeochem. Cy. 18,* Art. No. GB2005.

[5] SCHEFFER, M., HOLMGREN, M., BROVKIN, V. AND CLAUSSEN, M., 2005: Synergy between small- and large-scale feedbacks of vegetation on the water cycle. *Glob. Change Biol. 11*, pp. 1003-1012.

[6] BEATLEY, J.C., 1980: Fluctuations and Stability in Climax Shrub and Woodland Vegetation of the Mojave, Great Basin and Transition Deserts of Southern Nevada. *Israel J. Bot. 28*, pp. 149-168.

[7] DREGNE, H.E., 1986: Desertification of arid lands, in Physics of desertification. In: El-Baz, F. and Hassan, M.H.A., (eds.): Physics of Desertification. Dordrecht, The Netherlands: Martinus, Nijhoff.

[8] EHLERINGER, J.R. AND MOONEY, H.A., 1978: Leaf hairs: effects on physiological activity and adaptive value to a desert shrub. *Oecologia 37,* pp. 183-200.

[9] ROTONDI, A., ROSSI, F., ASUNIS, C. AND CESARACCIO, C., 2003: Leaf xeromorphic adaptions of some plants of a coastal Mediterranean macchia ecosystem. *J. Mediterranean Ecol. 4*, pp. 25-35.

[10] USTIN, S.L., ROBERTS, D.A., GAMON, J.A., ASNER, G.P. AND GREEN, R.O., 2004: Using Imaging Spectroscopy to Study Ecosystem Processes and Properties. *Bioscience 54*, pp. 523-534.

[11] CARTER, G.A., 1991: Primary and secondary effects of water content on the spectral reflectance of leaves. *Am. J. Bot. 78,* pp. 916-924.

[12] JACQUEMOUD, S. AND BARET, F., 1990: PROSPECT: a model of leaf optical properties spectra. *Remote Sens. Environ. 34*, pp. 75-91.
[13] JACQUEMOUD S., USTIN S.L., VERDEBOUT J., SCHMUCK G., ANDREOLI G., AND HOSGOOD B., 1996: Estimating leaf biochemistry using the PROSPECT leaf optical properties model. *Remote Sens. Environ. 56*, pp. 194-202.
[14] JACQUEMOUD S., BACOUR C., POILVE H. AND FRANGI J.-P., 2000: Comparison of four radiative transfer models to simulate plant canopies reflectance–Direct and inverse mode. *Remote Sens. Environ. 74*, pp. 471-481.
[15] LICHTENTHALER, H.K., 1987: Chlorophylls and carotenoids: pigments of photosynthetic biomembranes. *Methods Enzymol. 148*, pp. 350-382.
[16] DEY, P. M. AND HARBORNE, J.B., 1997: Plant Biochemistry. Academic Press Inc.
[17] GAMON, J.A., PENUELAS, J. AND FIELD, C.B., 1992: A narrow-waveband spectral index that tracks diurnal changes in photosynthetic efficiency. *Remote Sens. Environ. 41*, pp. 35-44.
[18] GAMON, J.A., SERRANO, L. AND SURFUS, J.S., 1997: The photochemical reflectance index: an optical indicator of photosynthetic radiation use efficiency across species, functional types, and nutrient levels. *Oecologia 112*, pp. 492-501.
[19] PENUELAS, J., BARET, F. AND FILELLA, I., 1995a: Semi-empirical indexes to assess carotenoids/chlorophyll a ratio from leaf spectral reflectance. *Photosynthetica 31*, pp. 221-230.
[20] SIMS, D.A. AND GAMON, J.A., 1999: Estimating anthocyanin, chlorophyll, and carotenoid concentrations using hyperspectral reflectance. Poster, Ecol. Soc. Ann. Meet., 1999.
[21] NEILL, S. AND GOULD, K.S., 1999: Optical properties of leaves in relation to anthocyanin concentration and distribution. *Can. J. Bot. 77*, pp. 1777-1782.
[22] HOCH W.A., ZELDIN, E.L. AND MCCOWN, B.H., 2001: Physiological significance of anthocyanins during autumnal leaf senescence. *Tree Physiol 21,* pp. 1-8.
[23] ELLER, B.M. AND WILLI, P., 1977: The significance of leaf pubescence for the absorption of global radiation by *Tussilago farfara L. Oecologia 29,* pp. 179-187.
[24] CURCIO, J.A. AND PETTY, C.C., 1951: The near infrared absorption spectrum of liquid water. *J. Opt. Soc. Am. 41,* pp. 302-304.
[25] PRAHL, S., 2001: Optical absorption of water. Oregon Medical Laser Center. http://omlc.ogi.edu/spectra/water/
[26] WESSMAN, C.A. 1990. Evaluation of canopy biochemistry. In: Hobbs R.J. and H.A. Mooney (eds.): Remote Sensing of Biosphere Functioning. pp. 135-156. Springer-Verlag, New York.
[27] GROSSMAN, Y.L., USTIN, S.L., SANDERSON, E., JACQUEMOUD, S., SCHMUCK, S. AND VERDEBOUT J., 1996: Critique of Stepwise Multiple Linear Regression for the Extraction of Leaf Biochemistry Information from Leaf Reflectance Data. *Remote Sens. Environ. 56*, pp. 182-193.
[28] BARTON, F.E., II, HIMMELSBACH, D.S., DUCKWORTH, J.H. AND SMITH, M.J., 1992: Two-dimensional vibration spectroscopy: correlation of mid- and near-infrared regions. *Appl. Spectrosc. 46*, pp. 420-429.
[29] ELVIDGE, C.L., 1990: Visible and NIR reflectance characteristics of dry plant materials. *Int. J. Remote Sens. 2*, pp. 1775-1795.
[30] ASNER, G.P., 1998: Biophysical and biochemical sources of variability in canopy reflectance. *Remote Sens. Environ. 64*, pp. 234-253.
[31] ROBERTS, D.A., USTIN, S.L., OGUNJEMIYO, S., GREENBERG, J., DOBROWSKI, S.Z., CHEN, J. AND HINCKLEY, T.M., 2004: Spectral and structural measures of northwest forest vegetation at leaf to landscape scale. *Ecosystems 7*, pp. 545-562.
[32] BARET, F., JACQUEMOUD, S., GUYOT, G. AND LEPRIEUR, C., 1992: Modeled analysis of the biophysical nature of spectral shifts and comparison with information content of broad bands. *Remote Sens. Environ. 41*, pp. 133-142
[33] ELVIDGE, C.D., CHEN, Z.K. AND GROENEVELD, D.P., 1993: Detection of trace quantities of green vegetation in 1990 AVIRIS data. *Remote Sens. Environ. 44*, pp. 271-279.
[34] SEAGER, S., TURNER, E.L., SCHAFER, J. AND FORD, E.B., 2005: Vegetation's red edge: a possible spectroscopic biosignature of extraterrestrial plants. *Astrobiology 5*, pp. 372-390.
[35] NAGLER, P.L., DAUGHTRY, C.S.T. AND GOWARD, S.N., 2000: Plant litter and soil reflectance. *Remote Sens. Environ. 71*, pp. 207-215.
[36] BAUMGARDNER, M.F., SILVA, L.F. BIEHL, L.L. AND STONER, E.R., 1985: Reflectance properties of soils. *Adv. Agron. 38*, pp. 1-44.
[37] BELNAP, J., BUDEL, B. AND LANGE, O.L., 2001a: Biological soil crusts: Characteristics and distribution, In: Belnap, J. and Lange, O.L. (eds.): Biological Soil Crusts: Structure, Function, and Management. pp. 3-30. Springer-Verlag, Berlin.
[38] BELNAP, J., 2001a: Comparative structure of physical and biological soil crusts. In: Belnap, J. and Lange, O.L. (eds.): Biological Soil Crusts: Structure, Function, and Management. pp. 177-192. Springer-Verlag, Berlin.
[39] BELNAP, J., 2001b: Biological soil crust and wind erosion. In: Belnap, J. and Lange, O.L. (eds.): Biological Soil Crusts: Structure, Function, and Management. pp. 339-348. Springer-Verlag, Berlin.

[40] BELNAP, J. AND ELDRIDGE, D.J., 2001: Disturbance and recovery of biological soil crusts. In: Belnap, J. and Lange, O.L. (eds.): Biological Soil Crusts: Structure, Function, and Management. pp. 363-384. Springer-Verlag, Berlin.
[41] BECHTEL, R., RIVARD, B. AND SANCHEZ-AZFEIFA, 2002: Spectral properties of foliose and crustose lichens based on laboratory experiments. *Remote Sens. Environ. 82*, pp. 389-396.
[42] BUFFONI HALL, R.S., BORNMAN, J.F. AND BJÖRN, L.O., 2002: UV-induced changes in pigment content and light penetration in the fruticose lichen *Cladonia* arbuscula ssp. *mitis*. *J. Photochemistry and Photobiology. B, Biology 66,* pp. 13-20.
[43] MCINTYRE, D.S. 1958: Permeability measurement of soil crust formed by raindrop impact. *Soil Sci. 85*, pp. 158-189.
[44] GOLDSHLEGER, N., BEN-DOR, E., BENYAMINI, Y., BLUMBERG D. AND AGASSI, M., 2002: Spectral properties and hydraulic conductance of soil crusts formed by raindrop impact. *Int. J. Remote Sens.23*, pp. 3909–3920.
[45] DE JONG, S.M., 1992: The analysis of spectroscopical data to map soil types and soil crusts of mediterranean eroded soils. *Soil Technol. 5*, pp. 199-211.
[46] GOLDSHLEGER, N., BEN-DOR, E., BENYAMINI, Y., AGASSI, M. AND BLUMBERG ,D.G., 2001: Characterization of soil's structural crust by spectral reflectance in the SWIR region (1.2±2.5 μm). *Terra Nova*, 13, pp. 12-17.
[47] ESHEL, G., LEVY, G.J. AND SINGER, M.J., 2004: Spectral reflectance properties of crusted soils under solar illumination. *Soil Sci. Soc. Am. J.68*, pp. 1982-1991.
[48] COURAULT, D., BERTUZZI, P. AND GIRARD , M.C., 1993:. Monitoring surface changes of bare soils due to slaking using spectral measurements. *Soil Sci. Soc. Am. J.*, 57:1595-1601.
[49] BEN-DOR, E., GOLDLSHLEGER, N., BENYAMINI, Y., AGASSI, M. AND BLUMBERG, D.G., 2003: The spectral reflectance properties of soil structural crusts in the 1.2- to 2.5-mu m spectral region. *Soil Sci. Soc. Am. J. 67*, pp. 289-299.
[50] GODSCHLEGER, N., BEN-DOR, E., BENYAMINI, Y., AGASSI, M., 2004: Soil reflectance as a tool for assessing physical crust arrangement of four typical soils in Israel. *Soil Sci. 169*, pp. 677-687.
[51] COOKE, R.U. AND WARREN, A., 1973: Geomorphology in deserts. London: B.T. Batsford Ltd., p. 120.
[52] DORN, R.I. AND OBERLANDER, T.M., 1981: Microbial origin of desert varnish. *Science 213*, pp. 1245-1247.
[53] POTTER, R.M. AND ROSSMAN, G.R., 1979: Mineralogy of manganese dendrites and coatings. *Am. Mineral. 64*, pp. 1219-1226.
[54] DORN, R.I. AND OBERLANDER, T.M., 1982: Rock Varnish. *Progress in Phys. Geograph. 6,* pp. 317-367.
[55] RICHARDSON, A.J. AND WIEGAND, C.L.1977: Distinguishing Vegetation from Soil Background Information. *Photogram. Eng and Remote Sens.43*, pp. 1541-1552.
[56] ELVIDGE, C. D. AND CHEN, Z. K., 1995: Comparison of Broad-Band and Narrow-Band Red and Near-Infrared Vegetation Indices. *Remote Sens. Environ. 54*, pp.38-48.
[57] BARET, F., JACQUEMOUD, S. AND HANOCQ, J. F., 1993: The soil line concept in remote sensing. *Remote Sens. Rev. 7*, pp.65-82.
[58] FOX, G. A., SABBAGH, G.J., SEARCY, S.W. AND YANG, C., 2004. An automated soil line identification routine for remotely sensed images. *Soil Sci. Soc. Am. J. 68*, pp. 1326-1331.
[59] WHITING, M.L., LI, L. AND USTIN, S.L., 2004: Predicting Water Content Using Gaussian Model on Soil Spectra. *Remote Sens. Environ., 89*, pp. 535-552.
[60] KOKALY, R.F. AND CLARK, R.N., 1999: Spectroscopic determination of leaf biochemistry using band-depth analysis of absorption features and stepwise multiple linear regression. *Remote Sens. Environ. 67*, pp. 267-287.
[61] VAN DER MEER, F., 2004: Analysis of spectral absorption features in hyperspectral imagery. *Int. J. Appl. Earth Observ. Geoinform. 5*, pp. 55-68.
[62] PALACIOS-ORUETA, A. AND USTIN, S.L., 1998: Remote sensing of soil properties in the Santa Monica mountains: I. Spectral analysis. *Remote Sens. Environ. 65*, pp. 170-183.
[63] CLARK, R.N., 1999: Spectroscopy of rocks and minerals, and principles of spectrocopy. In: Rencz, A.N. (ed.), Remote Sensing for the Earth Sciences: Manual of Remote Sensing. pp. 3-58. New York: John Wiley & Sons, Inc.
[64] BOWERS, S.A. AND HANKS, R.J., 1965: Reflection of radiant energy from soils. *Soil Sci. 100*, pp. 130-138.
[65] LOBELL, D.B. AND ASNER, G.P., 2002: Moisture effects on soil reflectance. *Soil Sci. Soc. Am. J. 66*, pp. 722-727.
[66] LIU, W., BARET, F., GU, X., TONG, Q., ZHENG, L. AND ZHANG, B., 2002: Relating soil surface moisture to reflectance. *Remote Sens. Environ. 81*, pp. 238-246.
[67] DALAL, R.C. AND HENRY, R.J., 1986: Simultaneous determination of moisture, organic carbon and total nitrogen by near infrared reflectance spectroscopy. *Soil Sci. Soc. Am. J.50*, pp. 120-123.
[68] METTERNICHT, G.I. AND ZINCK, J.A., 2003: Remote sensing of soil salinity: potentials and constraints. *Remote Sens. Environ. 85,* pp. 1-20.

[69] MATTHIAS, A.D, FIMBRES, A., SANO, E.E., POST, D.F., ACCIOLY, L., BATCHILY, A.K. AND FERREIRA, L.G., 2000: Surface roughness effects on soil albedo. *Soil Sci. Soc. Am. J. 64*, pp. 1035-1041.
[70] DEERING, D.W., ECK, T.F. AND OTTERMAN, J., 1990. Bidirectional reflectances of selected desert surfaces and their three-parameter soil characterization. *Agr. Forest Meteorol. 52*, pp. 71-93.
[71] SHOSHANY, M., 1993: Roughness-reflectance relationship of bare desert terrain, an empirical study. *Remote Sens. Environ. 45*, pp. 15-27.
[72] CIERNIEWSKI, J. AND KARNIELLI, A., 2002: Virtual surfaces simulating the bi-directional reflectance of semi-arid soils. *Int. J. Remote Sensing 23*, pp. 4019-4037.
[73] PALACIOS-ORUETA, A., PINZON, J.E., USTIN, S.L. AND ROBERTS, D.A., 1999: Remote sensing of soil properties in the Santa Monica Mountains. II. Hierarchical foreground and background analysis. *Remote Sens. Environ. 68*, pp. 138-151.
[74] HUETE, A.R., LIU, H.Q., BATCHILY, K. AND VAN LEEUWEN, W., 1997: A comparison of vegetation indices global set of TM images for EOS-MODIS. *Remote Sens. Environ. 59*, pp. 440-451.
[75] SERRANO, L., PENUELAS, J. AND USTIN, S.L., 2002: Remote sensing of nitrogen and lignin in Mediterranean vegetation from AVIRIS data: decomposing biochemical from structural signals. *Remote Sens. Environ. 81*, pp. 355-364.
[76] PINZÓN, J.E., USTIN, S.L., CASTAÑNEDA, C.M. AND SMITH, M.O., 1998: Investigation of leaf biochemistry by hierarchical foreground/background analysis. *IEEE Trans. Geosci. and Remote Sens. 36*, pp. 1-15.
[77] SMITH, M-L., OLLINGER, S.V., MARTIN, M.E., ABER, J.D., HALETT, R.A. AND GOODALE, C.L., 2002: Direct estimation of aboveground forest productivity through hyperspectral remote sensing of canopy nitrogen. *Ecol. Appl. 12*, pp. 1286-1302.
[78] MADEIRA, J., BEDIDI, A., CERVELLE, B., POUGET, M. AND FLAY, N. 1997: Visible spectrometric indices of hematite (Hm) and goethite (Gt) content in lateritic soils: the application of a Thematic Mapper (TM) image for soil-mapping in Brasilia, Brazil. *Int. J. Remote Sens. 18*, pp. 13,2835-13,2852.
[79] MATHIEU, R., POUGET, M., CERVELLE, B. AND ESCADAFAL, R., 1998: Relationships between satellite-based radiometric indices simulated using laboratory reflectance data and typic soil color of an arid environment. *Remote Sens. Environ. 66* , pp. 17-28
[80] TUCKER, C.J., 1979: Red and photographic infrared linear combinations for monitoring vegetation. *Remote Sens. Environ*. *8*, pp. 127-150.
[81] FUENTES, D.A., J.A. GAMON, J.A , QIU, H.L., SIMS, D.A. AND ROBERTS, D.A., 2001: Mapping Canadian boreal forest vegetation using pigment and water absorption features derived from the AVIRIS sensor. *J. Geophys. Res. 106*, pp. 33565-33577.
[82] ZARCO-TEJADA, P.J., 1998: Optical indexes as bioindicators of forest sustainability. Graduate Programme in Earth and Space Science. Toronto, York University.
[83] LICHTENTHALER, H.K., LANG, M., SOWINSKA, M., HEISEL, F. AND MIEHE, J.A., 1996: Detection of vegetation stress via a new high resolution fluorescence imaging system. *J. Plant Physiol. 148*, pp. 599-612.
[84] GAO, B.-C., 1996: NDWI - A normalized difference water index for remote sensing of vegetation liquid water from space. *Remote Sens. Environ. 58,* pp. 257-266.
[85] ALLEN, W.A., GAUSMAN, H.W., RICHARDSON, A.J. AND THOMAS, J.R., 1969: Interaction of isotropic light with a compact leaf. *J. Opt. Soc. Am. 59*, pp. 1376-1379.
[86] ALLEN, W.A., GAUSMAN, H.W. AND RICHARDSON, A.J., 1970: Mean effective constants of cotton leaves. *J. Opt. Soc. Am. 60*, pp. 542-547.
[87] BARET, F. AND FOURTY, T.H., 1997: Estimation of leaf water content and specific leaf weight from reflectance and transmittance measurements. *Agronomie 17*, pp. 455-464.
[88] FOURTY, TH. AND BARET, F., 1998: On spectral estimates of fresh leaf biochemistry. *Int. J. Remote Sens.19,* pp. 1283-1297.
[89] CECCATO, P., FLASSE, S., TARANTOLA, S., JACQUEMOUD, S. AND GRÉGOIRE, J.M., 2001: Detecting vegetation water content using reflectance in the optical domain. *Remote Sens. Environ.* 77, pp. 22-33.
[90] BACOUR, C., JACQUEMOUD, S., TOURBIER, Y., DECHAMBRE, M. AND FRANGI, J.P., 2002: Design and analysis of numerical experiments to compare four canopy reflectance models. *Remote Sens. Environ. 79*, pp. 72-83.
[91] CHUVIECO, E., VENTURA, G., MARTIN, M.P. AND GOMEZ, I., 2005: Assessment of multitemporal compositing techniques of MODIS and AVHRR images for burned land mapping. *Remote Sens. Environ. 94*, pp. 450-462.
[92] HOSGOOD, B., JACQUEMOUD, S., ANDREOLI, G., VERDEBOUT, J., PEDRINI, A. AND SCHMUCK, G., 1994: The JRC Leaf Optical Properties Experiment (LOPEX'93), European Commission, Directorate-General XIII Telecommunications, Information Market and Exploitation of Research L-2920, Luxembourg CL-NA-16095-ENC.
[93] CONEL, J.E., VAN DEN BOSCH, J. AND GROVE, C.I., 1993: Application of a two-stream radiative transfer model for leaf lignin and cellulose concentrations from spectral reflectance measurements. Parts 1 & 2. In: R.O.

Green (ed): Proc. 4th Annual JPL Airborne Geoscience Workshop. Vol. 1. AVIRIS Workshop 25-29 October 1993, Washington (DC), NASA-JPL Publication 93-26, pp. 39-51.
[94] DAWSON T.P., CURRAN P.J. AND PLUMMER S.E., 1998: LIBERTY - Modelling the effects of leaf biochemical concentration on reflectance spectra. *Remote Sens. Environ*. *65*, pp. 50-60.
[95] MA, Q., ISHIMARU, A., PHU, P. AND KUGA, Y., 1990: Transmission, reflection, and depolarization of an optical wave for a single leaf. *IEEE Trans. Geosci. Remote Sens 28*, pp. 865-872.
[96] GANAPOL, B., JOHNSON, L., HAMMER, P., HLAVKA, C. AND PETERSON, D., 1998: LEAFMOD: a new within-leaf radiative transfer model. *Remote Sens. Environ. 6*, pp. 182-193.
[97] JOHNSON, L.F., 2001: Nitrogen influence on fresh-leaf NIR spectra. *Remote Sens. Environ,* 78: pp. 314-320.
[98] TUCKER, C.J. AND GARRATT, M.W., 1977: Leaf optical properties as a stochastic process. *Appl. Opt.16*, pp. 635-642.
[99] MAIER, S.W., LÜDEKER, W. AND GÜNTHER, K.P., 1999: SLOP: A revised version of the stochastic model for leaf optical properties. *Remote Sens. Environ*. *68*, pp. 273-280.
[100] GOVAERTS, Y.M., JACQUEMOUD, S., VERSTRAETE, M.M. AND USTIN, S.L., 1996: Three-dimensional radiation transfer modeling in a dicotyledon leaf. *Appl. Opt. 35,* pp. 6585-6598.
[101] GOVAERTS, Y.M. AND VERSTRAETE, M.M., 1998: Raytran: A Monte Carlo ray-tracing model to compute light scattering in three-dimensional heterogeneous media. *IEEE Trans. Geosci. Remote Sens. 36*, pp. 493-505.
[102] USTIN S.L., JACQUEMOUD, S. AND GOVAERTS, Y.M., 2001. Simulation of photon transport in a three-dimensional leaf: Implication for photosynthesis. *Plant Cell Environ. 24*, pp. 1095-1103.
[103] BARANOSKI, G.V.G AND ROKNE, J.G., 2004: Light interaction with plants. A Computer Graphics Perspective, Horwood Publishing.
[104] ZARCO-TEJADA P.J., PUSHNIK J.C., DOBROWSKI S. AND USTIN S.L., 2003a: Steady-state Chlorophyll a fluorescence detection from canopy derivative reflectance and double-peak effects. *Remote Sens. Environ*. *84*, pp. 283-294.
[105] DOBROWSKI, S.Z., PUSHNIK, J.C., ZARCO-TEJEDA, P.J. AND USTIN, S.L., 2005: Simple reflectance indicesindexes track heat and water stressed induced changes in steady state chlorophyll fluorescence at the canopy scale. *Remote Sens. Environ*. *97*, pp. 403-414.
[106] MILLER, J.R., BERGER M., GOULAS Y., JACQUEMOUD S., LOUIS J., MOISE N., MOHAMMED G., MORENO J., MOYA I., PEDRÓS R., VERHOEF W. AND ZARCO-TEJADA P.J., 2005: Development of a Vegetation Fluorescence Canopy Model, ESTEC Contract No. 16365/02/NL/FF, Final Report, May 2005 (http://www.ias.csic.es/fluormod/)
[107] PEDRÓS R., GOULAS Y., JACQUEMOUD S., LOUIS J. AND MOYA I., 2005: A new leaf fluorescence model. Part 1: Fluorescence excitation & Part 2: Fluorescence emission, *Remote Sens. Environ.*, forthcoming.
[108] GOND, V., FONTES, J. AND LOUDJANI, J.P., 1997: African biomes dynamic by remote sensing temporal analysis. *Comptes Rendus De L'Academie Des Sciences Serie III-Sciences De La Vie-Life Sciences 320*, 179-188
[109] ALT C., STUTZEL, H. AND KAGE, H., 2000: Optimal nitrogen content and photosynthesis in cauliflower (*Brassica oleracea L. botrytis).* Scaling up from leaf to whole plant. *Ann. Bot.-London 85*, pp. 779-787.
[110] FIELD, C. AND MOONEY, H.A., 1986. The photosynthesis-nitrogen relationship in wild plants. In: Givinsh, T.J. (ed.): On the economy of form and function, pp. 25–55. Cambridge University Press, Cambridge,
[111] GARNIER, E., SALAGER, J.L., LAURENT, G. AND SONIE, L., 1999: Relationships between photosynthesis, nitrogen and leaf structure in 14 grass species and their dependence on the basis of expression. *New Phytol. 143*, pp. 119-129.
[112] BOUSQUET, L., LACHERADE, S., JACQUEMOUD, S. AND MOYA, I., 2005: Leaf BRDF measurement and model for specular and diffuse component differentiation. *Remote Sens. Environ.* (in press).
[113] LUQUET, D., BEGUE, A., DAUZAT, J., NOUVELLON, Y. AND REY, H., 1998. Effect of the vegetation clumping on the BRDF of a semi-arid grassland: comparison of the SAIL model and ray tracing method applied to a 3D computerized vegetation canopy, in Proc. Geoscience and Remote Sensing Symposium (IGARSS '98), 6-10 July 1998, pp. 791-793.
[114] PINTY, B., VERSTRAETE, M.M., IAQUINTA, J. AND GOBRON, N., 1996: Advanced modelling and inversion techniques for the quantitative characterization of desertification. In: Hill, J. and Peter, D. (Eds): Proc. The use of remote sensing for land degradation and desertification monitoring in the Mediterranean bassin, EN, Valencia (Spain), 13-15 June 1994, European Commission, Vol. EUR 16732, pp. 79-93.
[115] ESTEVE, P., FONTES, J. AND GASTELLU-ETCHEGORRY, J.P., 1998: Tropical dry ecosystems modelling and monitoring from space. *Ecol. Model. 108*, pp. 175-188.
[116] GASTELLU-ETCHEGORRY, J.-P., DEMAREZ, V., PINEL, V. AND ZAGOLSKI, F., 1996: Modeling radiative transfer in heterogeneous 3-D vegetation canopies. *Remote Sens. Environ. 58*, pp. 131-156.
[117] ZARCO-TEJADA, P.J., RUEDA, C.A. AND USTIN, S.L., 2003: Water content estimation in vegetation with MODIS reflectance data and model inversion methods. *Remote Sens. Environ. 85*: pp. 109-124.

[118] WIDLOWSKI, J.L., PINTY, B., GOBRON, N., VERSTRAETE, M.M. AND DAVIS, A.B., 2001: Characterization of surface heterogeneity detected at the MISR/TERRA subpixel scale. *Geophys. Res. Lett. 28*, pp. 4639-4642.
[119] MCNAIRN, H., AND PROTZ, R. 1993: Mapping corn residue cover on agricultural fields in Oxford County, Ontario, using Thematic Mapper. *Can. J. Remote Sens. 19*, pp. 152-159.
[120] BIARD, F. AND BARET, F., 1997: Crop residue estimation using multiband reflectance. *Remote Sens. Environ.* 59, pp. 530-536.
[121] ESCADAFAL, R., BELGHITH, A. AND BEN MOUSSA, H. 1994: Indices spectraux pour la degradation des milieux naturels en Tunisie aride. 6éme Symp. Int. Mesures Physiques et Signatures en Télédétection., Val d'lsère, France, ISPRS-CNES.
[122] ESCADAFAL, R. AND HUETE, A. 1991: Etude des propriétés spectrales des sols arides appliquée à l'amélioration des indices de végétation obtenus par télédétection. C. R. Acad. Sci. Paris 312, pp. 1385-1391.
[123] MATHIEU, R., POUGET, M., CERVELLE, B. AND ESCADAFAL, R., 1998: Relationships between satellite-based radiometric indices simulated using laboratory reflectance data and typic soil color of an arid environment. *Remote Sens. Environ. 66* , pp. 17-28
[124] MADEIRA, J., BEDIDI, A., CERVELLE, B., POUGET, M. AND FLAY, N. 1997: Visible spectrometric indices of hematite (Hm) and goethite (Gt) content in lateritic soils: the application of a Thematic Mapper (TM) image for soil-mapping in Brasilia, Brazil. *Int. J. Remote Sens. 18* (13), pp.2835-2852.

Spectroscopic Sensors and Methods for the Estimation of Surface Variables in Drylands

M. Bachmann[a], S. Holzwarth[a] and A. Mueller[a]

[a] DLR, German Remote Sensing Data Center, Muenchnerstr. 20, 82234 Wessling, Germany, email: Martin.Bachmann@dlr.de

ABSTRACT

This paper summarises DLR's hyperspectral remote sensing components in different dry land monitoring projects.

Semiarid and subhumid landscapes have always been under strong ecological pressure, but socio-economic and climatic changes in recent times rapidly change the face of these regions. In order to identify these changes and the underlying driving processes, it is essential to monitor the current state of the environment, and to include this information in land degradation models. Previous studies (like [1], [2], [3]) have shown the potential of remote sensing to monitor and model the degradation status of drylands. A survey by SARMAP [4] shows that potential end-users of remote sensing based information, which are mainly institutions involved in desertification monitoring, are interested in information which is "closely related to variables/parameters specific to or indicators of desertification and impacts of droughts on natural ecosystems and living standards." Among this selection of requirements identified by previous studies (like [5]) are indicators for processes and factors of change at different spatial levels, both static and dynamic, requiring different remote sensing approaches [3]. Standard vegetation indices and basic land cover maps are operationally derived from multispectral sensors, while in-depth information on soil and vegetation properties requires improved spectral resolution. Using a combination of advanced hyperspectral sensors, adequate data pre-processing and new retrieval techniques, bio- and geophysical variables of drylands can be quantified [6].

Keywords: Monitoring, land degradation, hyperspectral remote sensing, ground cover fractions, spectral unmixing.

1 INTRODUCTION

DLR is active in the field of airborne hyperspectral remote sensing in semi-arid regions in Europe since 1996, as shown by European Space Agency (ESA), European Commission- and national-funded flight campaigns and research programs like HySens, ARIDE or DAISEX [7]. During these campaigns, hyperspectral data was acquired over a large number of testsites in the northern part of the Mediterranean, ranging from Portugal to Israel (Fig. 1). In addition, HyMap data for BIOTA observatories in Namibia was also acquired in cooperation with HyVista.

For these campaigns, a suit of different hyperspectral sensors was used (Fig. 1), including the DLR own DAIS 7915, a 79-channel imaging spectrometer covering the VIS, NIR and TIR regions, and ROSIS, covering the wavelength range between 0.4µm and 0.8µm with 115 channels. Together with the Australian company HyVista the 128-channel HyMap sensor, covering the wavelength range between 0.4µm and 2.5µm, is frequently utilised for environmental projects in Europe. Due to the specific spectral layout of the sensors, data acquisition with more than one sensor, especially the combination of DAIS and ROSIS, can result in an additional value for the user, as shown by the results of the HySens campaigns 2000 and 2002 [8]. From the beginning of 2006 onwards, the new ARES sensor will be operational, enabling new applications due to the higher data quality, especially in the thermal wavelength range [9].

Sensor	DAIS 7915	ROSIS	HyMap	ARES
FOV	52°	16°	61.3°	65°
IFOV	3.3 mrad	0.56 mrad	2.09 mrad	2 mrad
Pixel per scanline	512	512	512	816
Scan frequency	6 - 24 Hz	-	6 - 24 Hz	10 – 25 Hz
Ground resolution	5 - 20 m²	1 - 6 m²	3 - 10 m²	2 – 15 m²
No. of channe ls	79	115	126	160
Spectral range	500 nm - 12.6 µm	430 - 860 nm	400 nm - 2.5 µm	400 nm – 11.5 µm
Spectral Sampling	20 nm - 2 µm	4 nm	15 - 20 nm	14 – 140 nm
Radiometric resolution	15 bit	14 bit	16 bit	14 bit
Scan principle	Whiskbroom	Pushbroom	Whiskbroom	Whiskbroom

Figure 1. Left: Hyperspectral sensor suite utilised by DLR. Right: Map of previous hyperspectral overflights in Europe conducted by DLR.

As geometric and atmospheric corrections are prerequisites of thematic evaluation, a fully automated data pre-processing and archiving environment for hyperspectral data is currently in a test phase at DLR, as described in [10] (Fig. 2). The raw hyperspectral data is system corrected to at-sensor-radiance based on calibration coefficients attained during laboratory calibration. The imagery is then geocoded using ORTHO, a parametric approach determining the viewing geometry for each pixel based on sensor-specific parameters, flight parameters such as sensor position and attitude (i.e. roll, pitch, true heading), and additional terrain information from a digital terrain model (DEM). For the atmospheric correction, ATCOR4 is used [11]. This physically-based approach, using the MODTRAN radiative transfer code, corrects for atmospheric effects as well as adjacency scattering, and BRDF compensation in order to derive nadir-normalised ground reflectance. Topographic shade effects are also corrected during terrain correction by integrating a DEM.

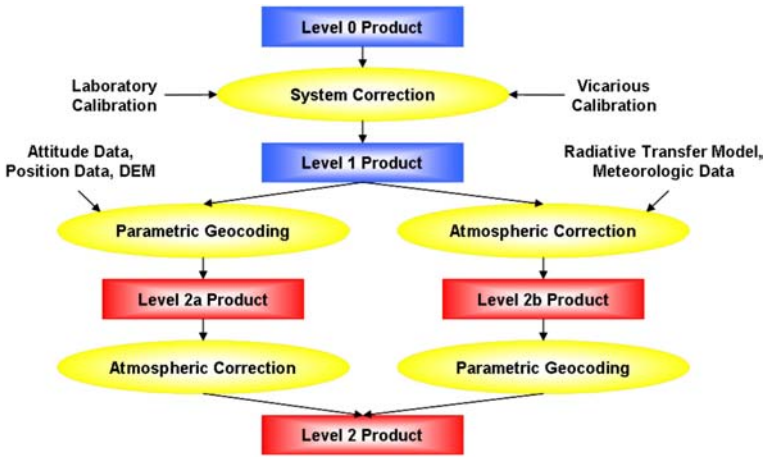

Figure 2. Overview of the automated data processing scheme for hyperspectral data.

This automated processing chain thus allows a fast and cost-effective data pre-processing and reduces the time to thematic evaluation.

Integrated in the automated processing chain, thematic Level 3 products are under development. Examples are automated inversion of radiative transfer models [12] and automated ground cover retrieval, the latter being described in more detail below. Basic land cover classification, standard biophysical indices for chlorophyll, nitrogen, lignin and cellulose content, as well as red edge parameters and other stress indicators can be provided upon request.

2 APPLICATION EXAMPLE: MAPPING GROUND COVER FRACTION IN SEMI-ARID ENVIRONMENTS

In the following, an automated methodology for quantitative ground cover estimates is outlined as an example for automatically generated data products in the framework of the ARES processing chain. First, application examples of ground cover fractions for the Cabo de Gata testsite in Southeast Spain are given. Next, a brief discussion of remote sensing approaches is given, where the focus is set on spectroscopic methods, followed by the description of the proposed unmixing methodology. Finally, preliminary results are presented.

2.1 Test site and data collection

The main study site is located inside the national park 'Cabo de Gata', Province of Almeria, Southeast Spain, and is closer described in e.g. [13],[14],[15]. Climate is typical for the semi-arid Mediterranean, featuring more than 10 arid months and a mean annual temperature of 17.8°C; annual precipitation is below 250 mm with high inter-and intra-annual variation. Vegetation mainly consists of dense arborescent matorral (higher shrubs), tomillares (spare, annual or seasonal dimorphic sub-shrubs), or pasture. Dominant species are tussock grasses (Stipa tenacissima) and annual grasses, intermingled with small bushes (Ziziphus lotus, Periploca laevigata) and small palms (Chamaerops humilis). Together with frequent areas of open soil or rubble, these vegetation patches form a small-scaled mosaic, where the denser vegetation indicates areas with lower grazing intensity, undisturbed soil formation or a more humid microclimate. The terrain is rough, with altitudes ranging from sea level up to 500 m ASL. Dominant soils are Entisols and Aridisols, formed in the northern parts on calcarious material, and in the southern parts on more andesitic substratum [13].

For the testsite Cabo de Gata, an extensive database was compiled. To include data of various phenological states, overflights took place in July 2003, May and August 2004 and June 2005. Data was collected at three different flight altitudes and flight orientations to study the influence of pixel size and bi-directional reflectance function (BRDF) effects. All data was atmospherically and geometrically corrected at DLR to ensure comparability between dates and to allow change detection. During all HyMap overflights, additional field spectroscopic measurements were taken at several locations inside the study area. Using a GER 3700 spectrometer and an ASD FieldSpec Pro, spectra were taken from over 200 soils and plants at different phenological and degradation states. For a thorough description of the field campaigns, please refer [15],[16].

2.2 Relevance of ground cover fractions for land degradation monitoring

For arid Mediterranean ecosystems, climate variations and land use are the main drivers of land degradation. Like many rangelands in the northern Mediterranean, the selected testsite of Cabo de Gata has a long tradition of livestock grazing. Plant community structure, functionality and diversity are therefore effect by grazing intensity, as indicated by a high cover percentage of bare soil and high relative abundance of Stipa tenacissima, and low cover percentage of perennial shrubs. Together with factors like deciduousness or spininess, plant coverage percentage was found to be of great importance in order to differentiate plant functional types and traits within the major life-forms of shrubs, forbs and grasses [14]. Furthermore, the degree and succession stage of plant cover is also related to soil organic matter content and thus soil erodibility, as shown by [13] for the Cabo de Gata area. Ground cover fractions are also frequently used parameters in land degradation models (e.g. [2], [5]), since the type (bare soil or plants), the degree (sparse vs. dense canopies) and the spatial distribution pattern alter the surface runoff and thus the erosion potential.

Thus the mapping of fractional cover of bare soil patches, as well as the cover of dry and green plants is an important input for land degradation models, and has the potential to be used as an indicator for the state of degradation of plants and soils.

2.3 Remote sensing approaches for fractional cover estimates

Vegetation indices like the normalised difference vegetation index (NDVI) have been used as an estimate for ground coverage. Since the NDVI only accounts for photosynthetic active vegetation, it is of limited value when ecosystems are dominated by photosynthetically inactive species or dead annuals during most of the year, as it is the case in semi-arid environments. In addition, even for photosynthetically active vegetation, there is no strong relationship between NDVI and cover percentage ([17]). The similar spectral shape of some soils and senescent plants further complicates the mapping of ground cover fractions, especially when using multispectral sensors. A further problem arises from lichens, because they show chlorophyll absorption and an otherwise similar spectral shape as soils and dry vegetation, requiring high (Fig. 3). Field spectra taken from species in the test area have NDVI values of up to 0.4 units, which is in agreements with previous studies.

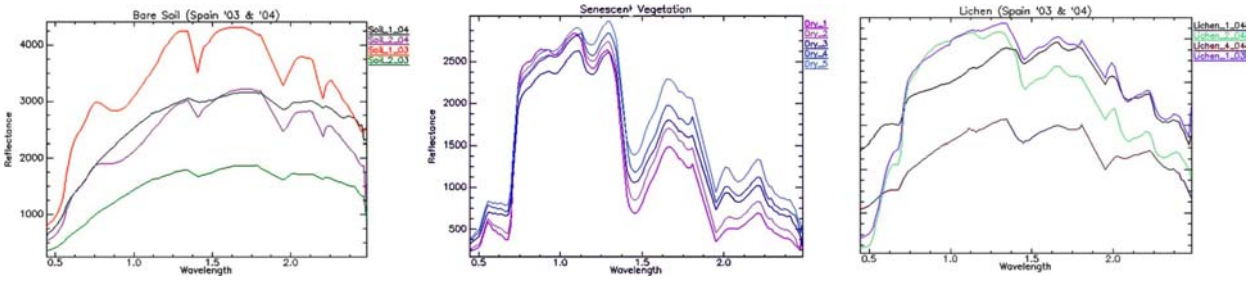

Figure 3. HyMap spectra of bare soil (left), senescent plants (middle) and lichens (right).

To overcome the limitations of simple band indices, approaches based on linear spectral unmixing were successfully applied in many studies, e.g. [3]. A description of the technique and a compilation of recent studies can be found in [17]. Based on the physical relationship between subpixel constituents and sensed signal, the proportion of a material in the signal sensed is assumed to be equal to the actual ground cover fraction of this material in the pixel, thus the surface fraction can be quantitatively derived. In a strict sense, this is only valid for the assumption that a photon interacts with only one ground cover type, i.e. all non-linear effects like multiple scattering in plant canopies are neglected. Nevertheless, as many plants in semi-arid regions are adapted to the harsh environment by thick leaves or wax coating having only little transmittance, the linear mixture model is a valid working hypothesis.

2.4 Proposed Spectral Unmixing Methodology

One mayor disadvantage of standard unmixing approaches is that a fixed set of reference spectra, in the following denoted as Endmember (EM), is used to model the whole image. Since plant species and soil types are normally not constant in one scene, it is unlikely that only one green, dry or soil component can adequately represent the spectral variability of its ground cover class and thus model the entire image. One way to cope with the variety of possible scene components is to include all possible EM in one mixture model, with the mayor drawback that the problem with linear dependent EMs is aggravated, resulting in wrong abundances.

Next, even though the linear mixture model can be solved as long as the number of EMs is less than the number of bands plus one, the intrinsic dimensionality of hyperspectral data is smaller due to the high degree of correlation between bands, preventing this method. A far better approach is to optimise the EM set for each pixel independently. Recent examples for these multiple endmember spectral mixture analysis (MESMA) approaches and applications for semi-arid and arid environments can be found in [18],[19].

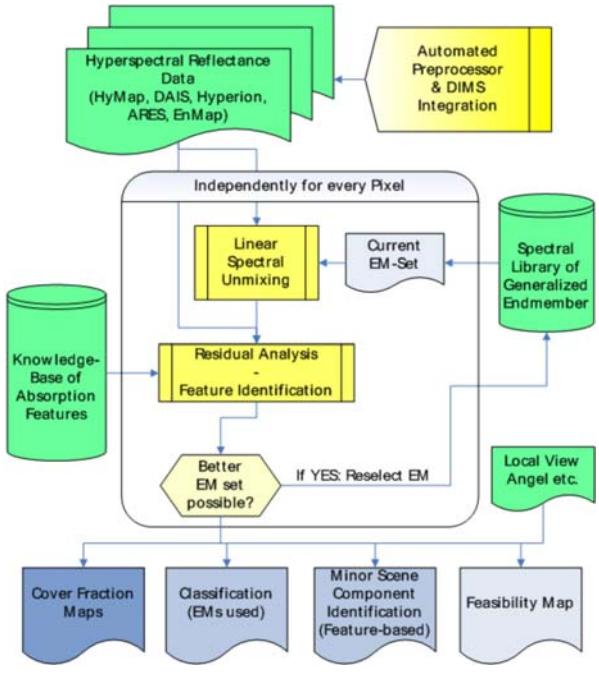

Figure 4. Overview of the automated MESMA unmixing approach.

While most MESMA approaches mainly optimise for total root mean square (RMS) error and abundance constraints, the presented approach (depicted in Fig. 4, and closer described in [15]) also aims to identify which mixture model is meaningful in terms of absorption features of the spectra. Examples are chlorophyll absorption, clay-OH-absorption, and ligno-cellulose absorption among others. After the first unmixing iteration, the measured spectrum and the residual (i.e. the difference between the measured and the modelled spectra of a pixel) are checked for significant features. If this divergence is characteristic and thus can be identified, e.g. an underestimation of iron in a soil, the mixture model for this pixel is adjusted, e.g. a soil with higher iron content is used to model the pixel in the next unmixing iteration. The spectral identification is accomplished using correlation and specified narrow-band absorption features. The model selection criterion is thus based on a combined error score of wavelength-weighted RMS, deviation from constraints, and knowledge-based analysis of features in the residuum and signal sensed. This model selection criterion is also part of a feasibility measure, so that problematic areas can be easily identified and excluded from further analysis.

As a step towards automation, the EM used for unmixing are selected from a spectral library of image-derived EM from existing hyperspectral imagery at DLR (Fig. 1). Based on a large number of scenes from dry-subhumid and semi-arid regions, spectra are selected for the relevant material groups of photosynthetic active vegetation, non-photosynthetic active vegetation (NPV, which includes dry, senescent and dead plants), and bare soils and rocks. All other material groups are not of interest in this study and thus are excluded. After the first unmixing iteration, pixels with high error score are determined and tested if these spectra may represent EMs not included in the starting library. Another improvement of the proposed approach is based on the fact that in nature, small-scaled changes of soil type rarely occur. But when using MESMA without normalisation or shade component, the soil EM is often used to model changes in overall albedo, resulting in a small-scaled mosaic of different soil EMs. Thus it is checked if a pixel can be modelled with the dominant soil EM in a defined neighbourhood without increasing the error score too much, resulting in less patches and more realistic EM abundances.

3 PRELIMINARY RESULTS

Currently, this MESMA approach is evaluated on HyMap imagery of Cabo de Gata In agreement with previous studies ([18], [19]), MESMA can model hyperspectral imagery with a significantly smaller RMS than normal unmixing (Fig. 5), especially when changes in plant or soil type occur (Fig. 6). Outputs of the proposed MESMA approach are ground cover percentage maps for soil, green and dry vegetation, as well as a classification, as depicted in Figure 6. A residual analysis is performed during unmixing to select meaningful EMs in terms of spectral absorption features, and the inclusion of a feasibility measure indicates pixels with low model accuracy.

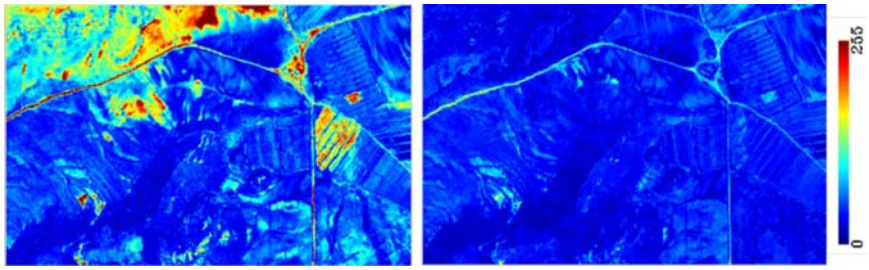

Figure 5. Unmixing RMS for HyMap scene Cabo de Gata (subset) Left: standard unmxing using 3 EM.
Right: MESMA optimised for RMS. Note the area in the northwest with calcareous soils, which can not be modeled with standard unmixing when the fixed soil EM represents the andesitic soils in the southern parts of the image.

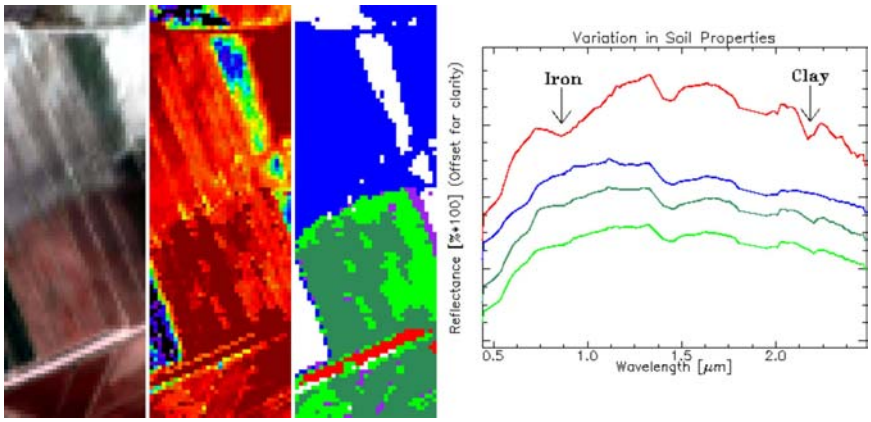

Figure 6. MESMA unmixing results - zoom on a ploughed bare soil area with changing lithology.
Left to right: HyMap image (true colour). Soil ground cover fraction. Soil classification. Corresponding spectra of soil classes (stacked for clarity).

In Order to quantify the accuracy of the proposed approach, simulations are carried out. During the Cabo de Gata field campaigns in close co-operation with GFZ and local project partners ([15],[16]), and during fieldwork by DLR-DFD in the framework of the BIOTA South project in Namibia, comprehensive field spectroscopic measurements were taken. Using these pure spectra of various plants and soils, a large number of synthetic scenes are generated as reference for evaluation. As an example for a test of portability, image-derived EM from the HyMap scene of Cabo de Gata were used to unmix a synthetic scene generated of field spectra from Namibia. In

this simulation, errors were normally well within 10% abundance except for low coverage. In case that no suitable EM is included in the library, errors may raise significantly, indicating the need for an extensive EM library.

In a next step, HyMap overflights for the BIOTA testsites in Namibia are included in the evaluation in order to test the portability of the approach. Using this atmospheric and geometric corrected imagery and corresponding ground truth data, the proposed unmixing methodology will be further evaluated. An example is shown in Fig. 8. Recently, a new study based on spectroscopic data is conducted in different test areas in Namibia. Using HyMap data plant functional types and traits are mapped in different ecosystems. Furthermore, the retrieval of biophysical properties of dryland vegetation by the inversion of radiative transfer models is investigated. These approaches will be integrated in the automated ARES processing environment, and will be tested for portability to spaceborne hyperspectral sensors like the proposed EnMAP.

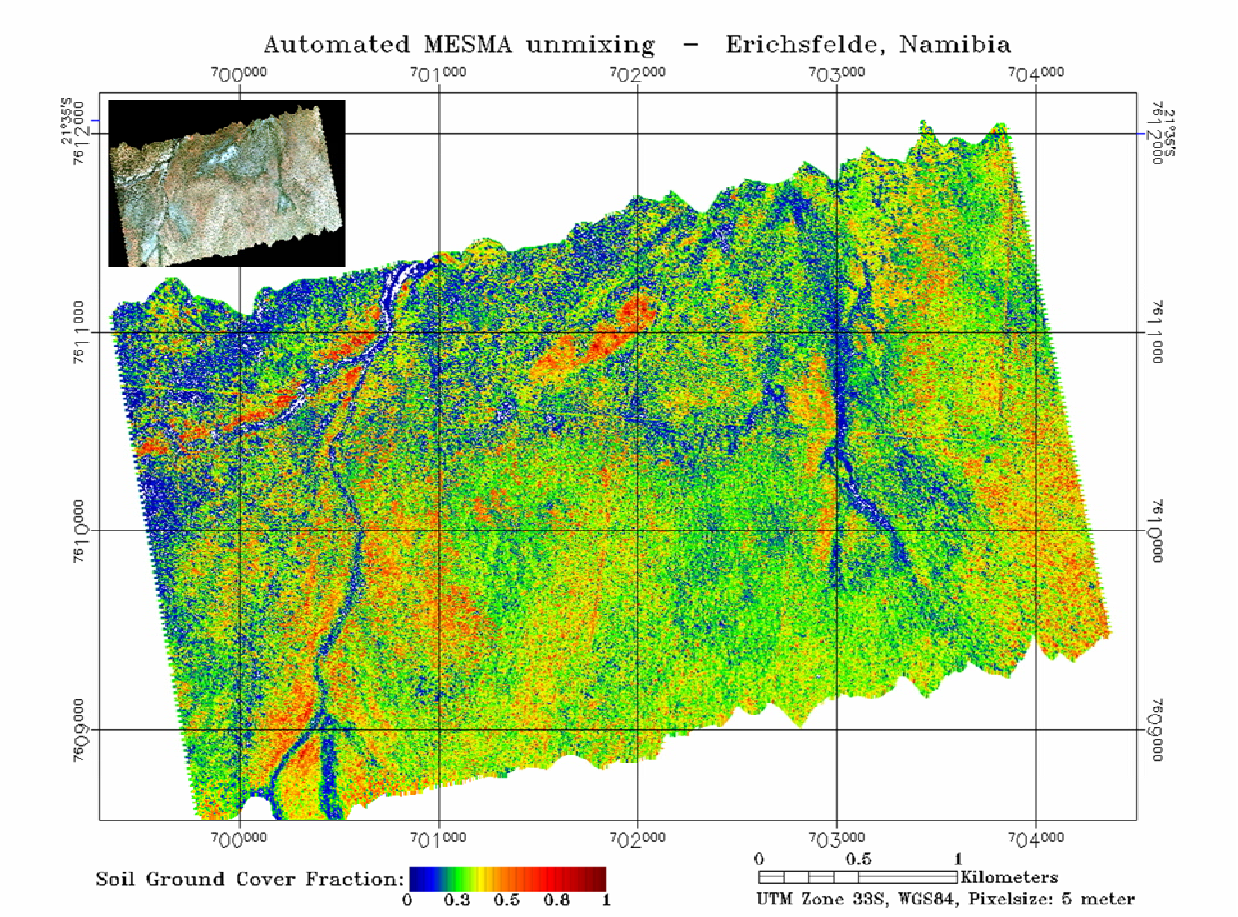

Figure 8. Map of soil ground cover fraction for Erichsfelde, Namibia, based on automated MESMA unmixing of atmospheric and geometric corrected HyMap data.

3 SUMMARY

For the quantitative retrieval of bio- and geophysical variables in drylands, a combination of advanced hyperspectral sensors, adequate data pre-processing and new retrieval techniques is proposed. Being active in the field of airborne hyperspectral remote sensing since 1996, a large number of flight campaigns were conducted by DLR in semi-arid regions in Europe, Israel and Namibia. Based on this experience, a fully automated processing chain for hyperspectral data including geometric and atmospheric correction is developed. Integrated in the automated processing chain, thematic data products for semi-arid regions are under development. For the presented application "automated mapping of ground cover fractions", first results indicate that qualitative and quantitative subpixel information can be derived with improved accuracy, resulting in reliable ground cover estimates and scene classification. As a future perspective, the new airborne ARES sensor will be operational from 2006 onwards, enabling new applications due to higher data quality, especially in the thermal wavelength range. In order to accomplish an operational long term monitoring system with global coverage, the DLR will continue to support initiatives towards the development of hyperspectral satellite instruments like the proposed EnMAP.

ACKNOWLEDGMENTS

The authors are grateful to S. Chabrillat (GFZ Potsdam) for ASD FieldSpec measurements, to C. Oyonarte Gutierrez and P. Escribano (both University of Almeria), and A. Palacios-Orueta (Polytechnic University of Madrid) for plant species discrimination, insights in the ecosystem and assistance during the field campaigns in Cabo de Gata 2003 and '04. Field spectroscopic measurements of Namibian plants and soils were provided by C. Schulz and M. Vogel, BIOTA south project at DLR-DFD and University of Würzburg. The authors would also like to thank HyVista, in particular T. Cocks and P. Hausknecht, for the excellent cooperation during many flight campaigns in the previous years.

REFERENCES

[1] BRANDT, C.J., THORNES, J.B. (ed.), 1996: Mediterranean desertification and land use. John Wiley and Sons. Chichester, New York.

[2] BOER, M., PUIGDEFABREGAS, J., 2003: Predicting potential vegetation index values as a reference for the assessment and monitoring of dryland condition. International Journal of Remote Sensing, 24 (4), 1135-1141.

[3] HILL, J., SOMMER, S., MEHL, W., MEGIER; J., 1996: A conceptual framework for mapping and monitoring the degradation of Mediterranean ecosystems with remote sensing. In: The use of remote sensing for land degradation and desertification monitoring in the Mediterranean basin. European Commission Report EUR 16732 EN

[4] SARMAP, UNIVERSITY OF VALENCIA, EOS.D2C, CHINESE ACADEMY OF FOREST, 2003: Treaty enforcement services using earth observation. Desertification. Final report, ESA/ESRIN.

[5] RUBIO, J.L., BOCHET, E., 1998: Desertification indicators as diagnosis criteria for desertification risk assessment in Europe. Journal of Arid Environments 39, 113-120.

[6] MÜLLER, A., KAUFMANN, H., BRIOTTET, X., PINET, P., HILL, J., DECH, S., 2001: An imaging spectrometer mission for the monitoring of desertification processes. Proc. SPIE 8th Int. Symp. on Remote Sensing, Toulouse, France, 2001.

[7] BERGER, M., RAST, M., WURSTEISEN, P., ATTEMA, E., MORENO, J., MÜLLER, A:, BEISL, U., RICHTER, R., SCHAEPMAN, M., STRUB, G., STOLL, M.P., NERRY, F., LEROY, M., 2000: The DAISEX campaigns in support of a future Land-Surface-Processes mission. ESA Bulletin 105.

[8] HOLZWARTH, S., MÜLLER, A., HABERMEYER, M., RICHTER, R., HAUSOLD, A., THIEMANN, S., STROBL, P. 2001: HySens- DAIS 7915/ROSIS Imaging Spectrometers at DLR. Proc. 3rd EARSeL Workshop on Imaging Spectroscopy, Herrsching, Germany, 2003.

[9] KAUFMANN, H., CHABRILLAT, S., DECH, S., HABERMEYER, M., HOLZWARTH, S., MEHL, H., MÜLLER, A., RICHTER, R., SEGL, K., 2003: Environmental mapping and analysis program based on the use of the ARES airborne reflective emissive spectrometer. Proc. 3rd EARSeL Workshop on Imaging Spectroscopy, Herrsching, Germany, 2003.

[10] HABERMEYER, M., MÜLLER, A., HOLZWARTH, S., RICHTER, R., MÜLLER, R., BACHMANN, M., SEITZ, K.-H., SEIFERT, P., STROBL, P., 2005: Implementation of the automatic processing chain for ARES. Proc. 4rd EARSeL Workshop on Imaging Spectroscopy, Warsaw, Poland, April 27-29 2005. In press.

[11] RICHTER, R., SCHLÄPFER, D., 2002: Geo-Atmospheric Processing of Airborne Imaging Spectrometry Data, Part 2: Atmospheric / Topographic Correction. International Journal of Remote Sensing 23 (13), 2631 –2649.

[12] DORIGO, W., RICHTER, R., MÜLLER, A., 2005: A LUT approach for biophysical parameter retrieval by RT model inversion applied to data from wide field of view sensors. 4rd EARSeL Workshop on Imaging Spectroscopy, Warsaw, Poland, April 27-29 2005. In press.

[13] ARANDA, V., OYONARTE, C., 2005: Effects of vegetation with different evolution degree on soil organic matter in a semi-arid environment (Cabo de Gata - Nijar Natural Park, SE Spain). Journal of Arid Environments 62, 631-647.

[14] NAVARRO, T., ALADOS, C., CABEZUDO, B., 2005: Changes in plant functional types in response to goat and sheep grazing in two semi-arid shrublands of SE Spain.). Journal of Arid Environments. In Press, Available online 1 August 2005.

[15] BACHMANN, M., MÜLLER, A., HABERMEYER, M., DECH, S., 2004: An iterative unmixing approach in support of fractional cover estimation in semi-arid environments. Proc. SPIE 11th Int. Symp. on Remote Sensing, Masplomas, Spain, 2004.

[16] CHABRILLAT, S., KAUFMANN, H., PALACIOS-ORUETA, A., ESCRIBANO, P., MÜLLER; A., 2004: Development of Land Degradation Spectral Indices in the Natural Park Cabo de Gata (Spain). Proc. SPIE 11th Int. Symp. on Remote Sensing, Masplomas, Spain, 2004.

[17] DRAKE, N:, MACKIN, S., SETTLE, J., 1999: Mapping Vegetation, Soils, and Geology in Semiarid Shrublands using Spectral Matching and Mixture Modeling of SWIR AVIRIS Imagery. Remote Sensing of Environment 68, 12 –25.
[18] OKIN, G., ROBERTS, D., MURRAY, B., OKIN, W., 2001: Practical Limits on Hyperspectral Vegetation Discrimination in Arid and Semiarid Environments. Remote Sensing of Environment 77, 212–225.
[19] ASNER, G., LOBELL, D., 2000: A Biogeophysical Approach for Automated SWIR Unmixing of Soils and Vegetation. Remote Sensing of Environment 74, 99–112.

Detecting the structure and composition of induced soil surface change using bi-directional soil spectral reflectance

A. Chappell[a], T. Zobeck[b] and G. Brunner[a]

[a] Centre for Environmental Systems Research, University of Salford, Manchester, M5 4WT, UK, email: a.chappell@salford.ac.uk

[b] USDA, Cropping Systems Research Laboratory, Lubbock, Texas, USA 79415

ABSTRACT

Relatively small changes in the composition and / or structure of the material at, or near, the surface can have a considerable effect on the temporal and spatial variation of soil erosion. There is a requirement for a non-invasive approach that can be used rapidly to characterise soil surface changes frequently over large areas. Spectral reflectance of the soil surface meets these desirable requirements and many workers have acquired spectra with a single direction of illumination and a single viewing angle. However, the reflectance of a soil surface is directional mainly as a consequence of roughness but also because of the preferential orientation of the matter comprising the soil. A bidirectional soil spectral reflectance model was fitted to spectral (450-2450 nm) measurements at many viewing angles with a single illumination angle. The single scattering albedo spectra and the values of the parameters were used to characterise the surface processes during a sequence of rainfall and wind tunnel experiments. The results provided diverse information on the structure and composition of the soil surface and appeared to be important for future work intended to improve the understanding of soil erosion using remote sensing.

Keywords: bi-directional spectral reflectance, soil, erodibility, rainfall simulation, wind tunnel, abrasion, wind erosion, soil crust, rainsplash.

1 INTRODUCTION

Information about the characteristics of a soil surface is important for understanding soil erosion by wind and water. Relatively small changes in the composition and / or structure of the material at, or near, the surface can have a considerable effect on the temporal and spatial variability of soil flux. Measurement of the factors that control soil flux are themselves problematic for at least two important reasons: i) the spatial, temporal and spatio-temporal scale of variation in the factors controlling soil erosion is largely unknown and unlikely to coincide with even the most expensive soil surface sampling campaign; ii) measurements at the soil surface are labour-intensive, time consuming and often so invasive that the measurements may interfere with the results. Thus, there is a requirement for a non-invasive approach that can be used rapidly to assess changes in the composition and structure of the soil surface in space and time. Spectral reflectance of the soil surface appears to meet these desirable requirements. Many workers have used in the field and the laboratory, measurements of this type particularly for classification purposes [1]. More recent research has been conducted that attempts to elucidate the processes of soil surface change due to rainsplash, soil crusting and wind erosion [2]. These recent developments, like earlier work, have acquired spectra with a single direction of illumination and a single viewing angle (e.g., on-nadir). However, the reflectance of a soil surface is anisotropic mainly as a consequence of roughness. Directional reflectance is likely to be even more important for process-based studies of a soil surface especially when the process involves the flux of matter (e.g., eluviation, erosion etc.) in a preferential direction.

The aim here is to demonstrate the information content of directional reflectance and its importance for field and laboratory studies of soil surface processes. More specifically, a model [3] will be used to predict the soil bidirectional reflectance of surfaces modified following a sequence of rainfall and wind tunnel simulations for three soil types. The results will be used to elucidate the geomorphic processes of rainsplash, surface sealing and wind erosion. A comparison with earlier work using the same experiment but from a single illumination direction and only one (on-nadir) viewing direction [2] will be used to consider the implications for future spectroscopic work.

2 DATA AND METHODS

2.1 Directional reflectance model and parameters

Using the fundamental principles of radiative transfer theory an analytical equation was derived [4] for the bi-directional reflectance function of a medium composed of particles. The physical interpretation of the model's parameters has been questioned and a rationalised formulation was provided [3] that required six parameters. The model [3] explains both backward and forward scattering (the specular effect) of light by smooth soils as a consequence of the material it comprises. Thus, the model and its parameters are likely to be useful for characterising the soil surface and changes to it. It is used in this paper and is described below.

The model assumes that a plane surface at z=0 contained irregular and randomly orientated particles that are large compared with the wavelength. The bidirectional reflectance *r* of a surface illuminated with a solar zenith angle *i*, viewed from a zenith angle *e* and normalised with respect to the reflectance of a perfectly reflecting Lambertian surface under the same conditions of illumination and observation is given by:

$$r(i,e,\phi)=\frac{\omega}{4}\frac{1}{\cos i+\cos e}\{[1+B(g)]P(g,g')+H(\cos i)H(\cos e)-1\} \quad \text{, where} \tag{1}$$

$$\cos g=\cos i\cdot\cos e+\sin i\cdot\sin e\cdot\cos\phi\cdot\cos g'=\cos i\cdot\cos e-\sin i\cdot\sin e\cdot\cos\phi \tag{2}$$

$$B(g)=\frac{1}{1+(1/h)\tan(g/2)} \quad , \quad P(g,g')=1+b\cos g+c\frac{3\cos^2 g-1}{2}+b'\cos g'+c'\frac{3\cos^2 g'-1}{2} \quad \text{and} \tag{3)(4}$$

$$H(x)=\frac{1+2x}{1+2\sqrt{1-\omega x}} \tag{5}$$

In equation 1, ϕ is the viewing azimuth relative to the Sun's azimuth, ω is the single scattering albedo (the ratio of the scattered energy to the total energy either scattered or absorbed by the particle), *g* is the phase angle between the incoming and outgoing rays, *g'* is the angle between the specular and the outgoing light directions. The function *B(g)* explains backscattering of light as a function of *g* and a roughness parameter *h* which may be related to the grain size distribution, the porosity of the medium and gradient of compaction with depth [4]. In other words, as h increases the surface appears to become smoother. The type of scattering is related to the surface roughness and the nature of the particles. The phase function *P(g, g')* describes the angular distribution of the light scattered by a terrestrial surface. Three different types of reflections were demonstrated as part of the model derivation [3]: backscattering has values for b and c parameters larger than those for *b'* and *c'*; forward scattering has values for *b'* and *c'* larger than those of *b* and *c*; mixed scattering has similarly large values for *b* and *c* as those for *b'* and *c'*.

2.2 Application of the model

If the radiometric properties of a bare soil surface can be described by equation 1 the interpretation problem consists of finding the values of the six parameters such that the computed value of *r* best approximates the actual observations. Following previous workers [5],[3], a non-linear least square fitting procedure was used to solve the inverse problem:

$$\delta^2=\sum_{k=1}^{n}\left[r_k-r(i_k,e_k,g_k)\right]^2 \tag{6}$$

where r_k is the measured bi-directional reflectance of the surface for the relative geometry of illumination and observation defined by i_k, e_k, g_k, *n* is the total number of measurements, and *r* is the predicted bi-directional reflectance. The problem then reduces to finding the optimal values of the parameters which minimises δ^2 for a set of observations. The performance of the optimisation is judged using the

square root of mean squared difference (RMSE), δ^2/N_f , (7)

where N_f is the number of degrees of freedom, which is the number of independent data points minus the number of parameters estimated by the procedure. This inverse modelling problem was coded in Matlab (using 'lsqnonlin'). It implements either a Gauss-Newton or Levenberg-Marquardt method depending on performance subject to fixed upper and lower bounds on the independent variables using function values alone.

2.3 Directional spectral reflectance measurements

The Analytical Spectral Devices (ASD) spectroradiometer used here had a spectral range of 350–2500nm and spectral sampling of 1.4 nm between 350–1050 nm and 2 nm between 1000–2500 nm. An eight degree field of view was used and illumination was provided by a 1000W Halogen lamp which was held constant at 53 degrees above the horizontal soil plane. A goniometer allowed repeatable and consistent measurements of multi-angular reflectance (including on-nadir) of the soil surface from a constant height (35 cm) and enabled several view zenith and azimuth angles (table 1).

Table 1. Geometries of measurement for directional spectral data

Source		Sensor
i	ϕ	e
53	0	0, -10, -20, -30, -40, -50, +10
53	180	0, +10, +20, +30, +40, +50, -10
53	270	0, +10, +20, +30, +40, +50, -10, -20, -30, -40, -50

In the experiments conducted here a calibrated spectralon panel provided total irradiance information. Two spectralon reflectance reference measurements were made immediately before and after the target measurements under the same conditions as the measurement. Conversion to spectral reflectance was conducted by dividing the radiance spectra of the soil samples by the radiance spectrum of a white spectralon reference panel. The soil surfaces were placed under the sensor at exactly the same location.

Some general results from previous laboratory spectroscopy experiments [6] include several broad and shallow absorption bands in wavelengths smaller than 1000 nm due to iron-oxide phases (goethite and haematite); narrow and well-defined absorption features at 1400 nm, 1900 nm and 2200 nm related to clay minerals (the presence of moisture reduces the overall soil reflectance but strong absorption features at 1400nm and 1900nm remain the same); a decrease in organic matter, iron oxides and the clay fraction produces a soil reflectance increase.

2.4 Soil types and property measurements

Three soil types were used in the experiments and table 2 provides some of their characteristics and their sample locations. The soil types chosen were susceptible to wind erosion on agricultural land that was close to where the experiments were conducted in the vicinity of the United Stated Department of Agriculture (USDA) Agricultural Research Service (ARS) in Lubbock, Texas. The soil types were also used to represent variation in texture; an important factor controlling wind erosion. The first type was an Amarillo fine sand (FS), that was a fine, mixed, superactive, thermic Aridic Paleustalf. The second was an Amarillo fine sandy loam (FSL). The third soil type was a Randall clay loam (CL) which was a fine, smectitic, thermic Ustic Epiaquert. All of the soils were from the Ap horizon. An abrader was used in the wind tunnel experiments and the characteristics of this material and details of the soil measurement procedures can be found elsewhere [2].

Table 2. Some characteristics of the soils used in the experiments (modified from [2]).

Soil type (label)	Soil Munsell Dry Colour	Fe (%)	pH	Organic carbon (%)	Median particle size (µm)	Sand content (%)	Silt content (%)	Clay content (%)
Randall clay loam (CL)	7.5YR 5/2	0.55	7.07± 0.005	1.09± 0.010	43.4	44.9	22.7	32.4
Amarillo fine sandy loam (FSL)	7.5YR 4/4	0.53	7.99± 0.005	0.83± 0.091	88.3	63.4	18.2	18.4
Amarillo fine sand (FS)	7.5YR 5/6	0.26	7.53± 0.034	0.34± 0.008	176.2	89.1	4.0	6.9

2.5 Soil treatment experiments

Straightforward experiments involving a rainfall simulator, drying ovens and a wind tunnel were used to induce changes in the surfaces of each soil type. The experiments were developed to include simulations of natural environmental processes that were known to alter the soil surface condition as part of a larger study. This approach

provided an alternative to the traditional development of a relationship between soil properties and spectral wavebands [6]. An outline of the experimental procedure is included below for brevity. Details of the experiments can be found elsewhere [2].

The soils were passed through a 2 mm mesh and loaded into trays prior to the experiments. The intention was to expose each soil type to simulations of short and long duration of abrasion in the wind tunnel and for high and low intensity rainfall. Unfortunately, operational constraints reduced the experiments that were performed on the CL soil to only high rainfall intensity. Directional reflectance measurements were taken before any experiments were conducted. After the soils were exposed to either low or high intensity rainfall simulation they were placed in drying ovens set at 40ºC for 45 hours to ensure surface layers were dry and then removed and allowed to cool overnight. After drying in the oven directional reflectance was measured and it was also measured after 1 minute and 8 minutes of abrasion.

3 RESULTS

3.1 Bi-directional soil spectral reflectance model

The values of the bi-directional soil spectral reflectance model parameters for each soil type and treatment are shown in figure 1. The open bars represent the primary parameters used in the original model [4]. The filled bars represent the additional parameters [3]. The hatched bars represent the *b* and *b'* parameters whilst the dotted bars represent the *c* and *c'* parameters. The values of the model parameters for each soil type prior to any treatment is shown first (Figure 1) and is used for comparison separately against the values of the model parameters for the same soil type after the treatment with (i) low intensity rainfall and wind tunnel abrasion and (ii) high intensity rainfall and wind tunnel abrasion. Soil CL has the smallest particles and the largest clay, organic matter and Fe content of all soil types (Table 2). Soil CL has values of the roughness parameter *h* that are much smaller than those of the other soil types (Figure 1a). This suggests that optically the surface appears much rougher than the other soils and is caused by small shadows behind individual particles and microaggregates [4],[7]. The value of *h* increased after high intensity rainfall and then it decreased as abrasion continued (Figure 1a). This pattern suggests that the surface decreased its roughness after rainfall and the abrasion increased the roughness. The large magnitude of the values for the *b'* and *c'* parameters suggests that the soil is predominantly forward scattering. After rainfall the forward scattering increased in magnitude presumably as a consequence of the smooth surface. However, the forward scattering decreased during wind tunnel abrasion as the surface returned to a slightly rougher condition (Figure 1a).

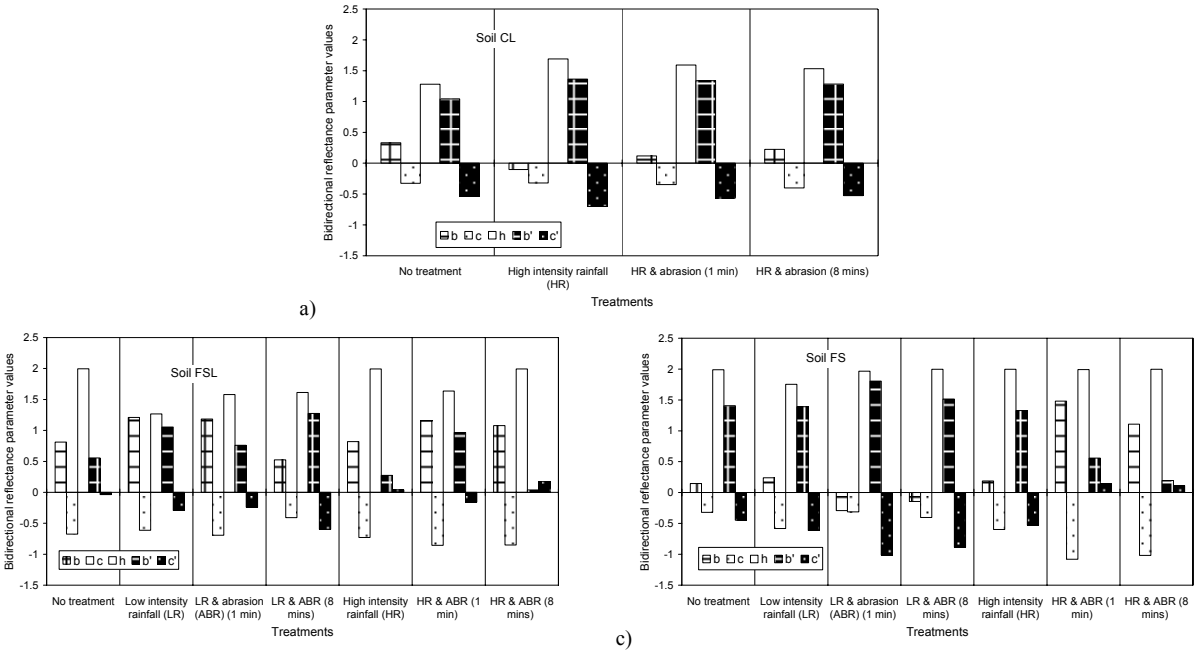

Figure 1. The values of the parameters derived from the soil bi-directional spectral reflectance model for soil CL (a), FSL (b) and FS (c).

Soil FSL had medium-sized particles and intermediate amounts of clay, organic matter and Fe of those soils considered here. Soil FSL showed a considerable decrease in the value of *h* after low intensity rainfall and then an increase after the initial abrasion (Figure 1b). This pattern indicates that the surface became rough after the low intensity rainfall and then decreased its roughness during the abrasion process. Unlike the other soil types the untreated soil FSL was dominated by backward scattering. After the initial abrasion the reflectance increased in backward scattering and then after the longest duration of abrasion the surface reflectance became forward scattering despite the absence of any change in the roughness parameter *h*. After high intensity rainfall the value of *h* for soil FSL was similar to that of the untreated soil. After the initial abrasion it decreased and then increased after the prolonged abrasion (Figure 1b). The surface remained backward scattering in its untreated state and after high intensity rainfall. It remained backward scattering after the initial abrasion and after prolonged exposure.

Soil FS had the coarsest particle size, dominated by sand with very little clay. It also has the smallest amount of organic matter and Fe. The untreated soil FS had a value for *h* which was similar to that of the untreated soil FSL indicating a similarly smooth initial surface (Figure 1c). The value of *h* for soil FS decreased after low intensity rainfall and then increased to approximately the same level as the untreated surface. This pattern indicates that the rainfall caused the surface to increase in roughness and the abrasion caused it to become as smooth as the untreated surface. The large magnitude of the values for the *b'* and *c'* parameters indicated that soil FS is dominated by forward scattering. The forward scattering remained largely unaffected by the low intensity rainfall but the initial abrasion caused an increase in forward scattering. Prolonged exposure to abrasion reduced the forward scattering. It appeared that the initial abrasion after low intensity rainfall did not change the roughness but increased the forward scattering. The same soil FS responded very differently to high intensity rainfall (Figure 1c). The value of *h* remained approximately the same as the untreated value indicating that the surface remained similarly smooth. However, the untreated soil, dominated by forward scattering, changed to one of mixed scattering after the high intensity rainfall. Furthermore, despite the absence of any change in roughness the soil surface became backward scattering after initial abrasion. The dominance of this type of scattering increased with prolonged exposure to abrasion.

3.2 Single scattering albedo

The single scattering albedo for wavelengths between 450 nm and 2450 nm predicted by the model (equation 1) for all soils prior to any treatment are shown in figure 2a. The albedo of soil FS is larger than the other soils in most of the wavelengths. The exceptions are those bands less than 500 nm in the visible (VIS ca. < 1000 nm) region. In this region soil CL has the largest albedo which may be attributed to iron-oxide phases (goethite and haematite). However, for all other wavelengths the albedo of soil CL is approximately 10% smaller than that of soils FS and FSL. The albedo spectra of soil FSL is slightly smaller than that of soil FS between 500 nm and 1410 nm in the near-infrared (NIR ca. 1000 – 1800 nm) region. All soils showed evidence of narrow and well-defined absorption features at 1400 nm and at 1900 nm and 2200 nm in the short-wave infrared (SWIR ca. 1800 – 2450 nm) region related to clay minerals in general and smectite minerals in particular [8]. The presence of moisture reduces the overall soil reflectance but strong absorption features at 1400 nm and 1900 nm remain the same [8].

To minimise common and constant features and therefore enhance differences in the spectra the single scattering albedo spectra for each treatment were divided by their respective spectrum for untreated soil. These ratios are shown in figure 2b-f for all wavebands. Overall, there appears to be substantial differences in the VIS region for most of the soils and their treatments. The exceptions appear to be soil CL exposed to high intensity rainfall and abrasion (Figure 2b) and soil FSL exposed to low intensity rainfall and abrasion (Figure 2c). In both cases there appears to have been a shift in albedo across all wavebands. Soil CL retained large values in the VIS region. The high intensity rainfall applied to soil CL initiated the increased albedo and the wind tunnel abrasion reduced it over time. Wavebands around 600 nm revealed the greatest difference relative to the untreated spectrum however, features at 1900 nm and 2200 nm were also evident.

Low intensity rainfall for soil FSL reduced reflectance overall but wavebands at 1930 nm and 2450 nm revealed the greatest negative change relative to the untreated spectrum (Figure 2c). Abrasion increased the albedo and wavebands around 460 nm revealed the greatest positive change relative to the untreated spectrum. High intensity rainfall affected soil FSL differently and caused changes to the albedo spectra mainly in the VIS region (Figure 2d). The waveband with the greatest positive change relative to the untreated spectrum was evident around 470 nm. Initial abrasion reduced significantly the reflectance across all wavebands so that it was smaller than the untreated spectrum with the exception of values in the region of 450-590 nm. The wavebands with the greatest negative change relative to the untreated spectrum were evident at 1940 nm and 2440 nm. After abrasion the reflectance in all wavebands had increased to approximately the same amount as that after the high intensity rainfall.

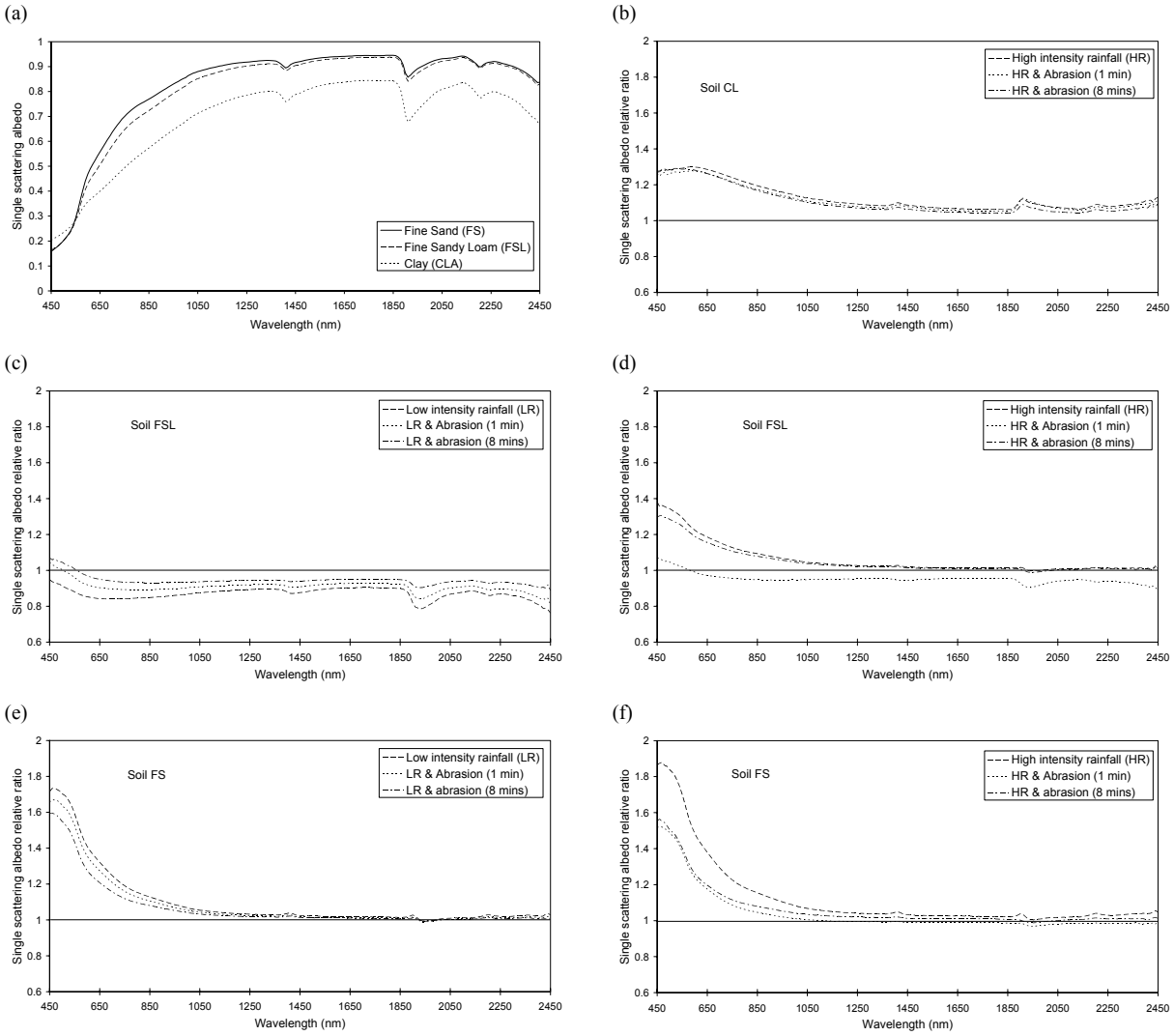

Figure 2. Single scattering albedo for wavelengths 450-2450 nm predicted using a soil bi-directional reflectance model of untreated soils (a), and the ratio of the untreated soil to treatments with high intensity rainfall (b, d & f), low intensity rainfall (c & e) and wind tunnel abrasion, for soil CL (b), soil FSL (c & d) and soil FS (e & f).

The albedo spectra for soil FS also increased after low intensity rainfall but the changes were confined mainly to the VIS region (Figure 2e). Wind tunnel abrasion reduced the albedo spectra in the VIS region over time. The waveband with the greatest positive change relative to the untreated spectrum was evident around 470 nm. This waveband was also the site of the greatest positive change in the spectrum for soil FS after high intensity rainfall (Figure 2f). The greatest change in wavebands after this treatment was also found in the VIS region. Initial wind tunnel abrasion reduced slightly the reflectance in all wavebands and decreased that in the NIR and SWIR wavebands to values smaller than those for the untreated soil. After 8 minutes duration of abrasion the reflectance had increased in all wavebands but with only very small changes in the region between 450-590 nm.

4 DISCUSSION

The development of soil crusts due to rainsplash is reasonably well understood [9]. The surface of a crust usually comprises smaller (clay) particles than those within or beneath the crust. This is a consequence of the preferential movement of particles near the surface resulting in an upperskin seal (crust) and deeper wash-in region [10]. Soil micro-aggregates may also be broken during rainfall. Thus, the orientation of the particles and their distribution over the surface is altered due to rainfall. The extent of crust development and aggregate stability is highly dependent on soil type which itself depends on the organic matter and sand, silt and clay fractions. Abrasion of the

soil surface by the impact of saltating particles is well known to erode material and may either increase or decrease the surface roughness depending on its status e.g., loose erodible material on a crusted surface.

4.1 Soil CL

The forward scattering of the untreated soil was caused by the relatively homogeneous optical properties [4] of this soil. The increase in (the roughness parameter) *h* after the rainfall and the increase in forward scattering showed that the surface has become smoother and the particles at the surface became more similar. In addition, the single scattering albedo of soil CL increased and wavebands around 600 nm, 1900 nm and 2200 nm also changed after high intensity rainfall which is consistent with a decrease in clay (probably haematite or goethite) particle size at the surface [8]. Thus, there is direct evidence for smoothing and sealing of the surface with small clay particles as a consequence of rainsplash. During abrasion the albedo decreased, the roughness parameter *h* decreased and the forward scattering of reflectance decreased. These characteristics are in opposition to those for the development of a surface seal and suggest strongly that the abrasion process has selectively removed material from the seal.

4.2 Soil FSL

The untreated soil was dominated by mixed or isotropic scattering and appeared very smooth relative to soil CL, despite its relatively coarse particle size (Table 2). Mixed scattering is expected from a mixture of particles including opaque spheroids with smooth surfaces, irregular translucent particles and particles with smooth surfaces that reflect light specularly [4]. After low intensity rainfall the roughness parameter decreased, the albedo decreased and the reflectance became backward scattering. Backscattering is caused by particles at the surface that are larger than a wavelength and hide shadows. It is expected from opaque surfaces with fairly rough faces orientated at random [4]. A reduction in the reflectance at waveband 1930 nm and a decrease in that of the VIS region suggested that the clay fraction at the surface decreased. These characteristics suggest that in this soil rainsplash has washed-in the small clay particles coated with iron oxides and replaced the surface with larger particles / aggregates with few iron oxides. The shadows created by the loose erodible material at the surface were observed in an earlier study [2]. After initial abrasion the reflectance became more backward scattering, the albedo increased and the roughness parameter increased. These quantitative results are consistent with the observations made in an earlier study [2]. This pattern is consistent with the preferential removal of some of the coarse material at the surface by the abrasion process exposing the washed-in clay material. It is likely that the development of the backscattering reflectance is a consequence of the poorly sorted nature of the exposed fine material. Surprisingly, the reflectance of the soil surface became forward scattering after 8 minutes of abrasion and the albedo of the wavebands increased to a level similar to that of the untreated soil despite the absence of any change in the roughness parameter. It appears that the prolonged abrasion has progressively eroded into the washed-in layer and exposed at the surface a fine homogeneous material with scattering properties similar to soil CL.

Between its untreated state and that after high intensity rainfall there appeared to be little change in the roughness parameter and the backward scattering of reflectance of soil FSL. However, the treatment caused an increase in albedo mainly in the VIS region which suggests that despite the absence of a change in the roughness parameter there was an increase in the number of similarly sized particles / aggregates at the surface with iron oxide coatings as part of the seal development during the rainsplash process. The high intensity rainfall smoothed the soil surface and created a crust with loose erodible particles upon it. After initial abrasion the roughness parameter decreased, the soil surface remained backward scattering of reflectance and decreased its albedo. In particular, a large reduction relative to the untreated surface in wavebands 1940 nm and 2440 nm signaled a reduction in clay particles at the surface and an increase in particle size. It appeared that the initial abrasion removed those small aggregates brought to the surface during the rainsplash and exposed a mixture of particles with fewer clay coatings. After prolonged abrasion the surface reflectance was strongly backward scattering and the roughness parameter increased to a level similar to that found after the high intensity rainfall. The single scattering albedo spectrum was considerably larger, mainly in the VIS region, than that of the untreated surface and similar to that spectrum found after rainfall. It appears that the prolonged abrasion preferentially removed large darker-coloured particles.

4.3 Soil FS

Low intensity rainfall on this soil produced a similar response to that of soil FSL after high intensity rainfall. The roughness parameter decreased after low intensity rainfall, forward scattering remained largely unaffected from that of the untreated surface and the albedo increased particularly in the VIS region. The suggestion here is that the untreated surface was relatively smooth and that the rainfall increased the roughness by bringing particles / aggregates to the surface with clay coatings which changed the colour and increased the reflectance in the VIS region. Abrasion over time increased the roughness parameter by removing those particles / aggregates with clay coatings. Notably, the forward scattering was reduced suggesting that the surface was preferentially eroded by the

abrasion process and that a more mixed surface has been revealed. This finding is consistent with that of earlier work [2].

Soil FS remained as smooth after high intensity rainfall as the untreated surface, the forward scattering of reflectance remained, but the albedo increased again mainly in the VIS region. This suggests that the high intensity rainfall replaced particles at the untreated surface with those that had a greater reflectance and that this translocation during rainsplash did not affect the roughness parameter or the optical scattering of the surface. Initial abrasion did not change the roughness parameter either but it reduced the albedo in the VIS region and shifted to backward scattering of the reflectance. It appears that the removal of the brighter clay material exposed a darker surface in which the numbers of shadows remained the same but that the size of the particles changed to cause the backward scattering of reflectance. Prolonged abrasion hardly affected the roughness parameter and the scattering of reflectance but the albedo increased, mainly in the VIS region suggesting a tendency for the preferential selection of particles / aggregates with iron-oxide coatings typical of those readily eroded sand-sized particles of this soil type.

5 CONCLUSION

The combination of the single scattering albedo spectra and the bi-directional soil spectral model [3] parameter values enabled the discrimination of geomorphic processes including rainsplash, surface seal development and the preferential erosion of material by wind. The details of that discrimination appeared to be largely consistent with similar previous on-nadir spectroscopic experiments of soil surface change [11]. The soil structure parameters provide additional information to interpret the changes of the soil surface remotely without interfering with natural processes. The directional soil reflectance methodology has much to recommend it for field trial and ultimately its use for identifying and quantifying soil erosion using angular sensors on airborne or satellite platforms.

ACKNOWLEDGMENTS

This work was funded by an award to AC from the UK Natural Environmental Research Council (NER/M/S/2001/00124). The authors are grateful to the United States Department of Agriculture, Agricultural Research Service for making available the spectroradiometer and the rainfall simulator used in these experiments and to Texas Tech University for generously providing access to the wind tunnel. We are also grateful to Dean Holder for constructing the goniometer and for technical assistance with the operation of the wind tunnel.

REFERENCES

[1] BAUMGARDNER, M.F., SILVA, L.F., BIEHL, L.L. AND STONER, E.R., 1985: Reflectance properties of soils. *Advances in Agronomy*, *38*, pp. 1-44.

[2] CHAPPELL, A., ZOBECK, T.M. AND BRUNNER, G., 2005: Induced soil surface change detected using on-nadir spectral reflectance to characterise soil erodibility. *Earth Surface Processes and Landforms*. *30(4),* pp. 489-511.

[3] JACQUEMOUD, S., BATER, F. AND HANOCQ, J.F., 1992: Modeling spectral and bidirectional soil reflectance. *Remote Sensing of Environment, 41*, pp. 123-132.

[4] HAPKE, B.W., 1963: A theoretical photoemetric function for the lunar surface. *Journal of Geophysical Research*. *68(15)*, pp. 4571-4586.

[5] PINTY, B., VERSTRAETE, M.M. AND DICKINSON, R.E., 1990: A physical model for predicting bidirectional reflectances over bare soils. *Remote Sensing Environment*. *27*, pp. 273-288.

[6] LEONE, A.P. AND SOMMER, S., 2000: Multivariate analysis of laboratory spectra for the assessment of soil development and soil degradation in the southern Apennines (Italy). *Remote Sensing of Environment*, *72*, pp. 346-359.

[7] CIERNIEWSKI, J., 1987: A model for soil surface roughness influence on the spectral response of bare soils in the visible and near-infrared range. *Remote Sensing of Environment. 23*, pp. 97-115.

[8] BEN-DOR, E., IRONS, J.R., AND EPEMA, G., 1999: Soil reflectance. In A.N. Renzc (ed.), *Remote Sensing for the Earth Sciences* pp. 111-188, Vol. 3, New York, Wiley.

[9] ZOBECK, T. M., 1991: Soil properties affecting wind erosion. *J. Soil & Water Cons. 46(2)*, pp. 112-118.

[10] MCINTYRE, D.S., 1958: Soil splash and the formation of surface crusts by raindrop impact. *Soil Science*, *85*, pp. 261-266.

[11] BEN-DOR, E., GOLDSHLEGER, N., BENYAMINI, Y., AGASSI, M., BLUMBERG, D.G., 2003: The spectral reflectance properties of soil structural crusts in the 1.2 to 2.5 μm spectral region. *Soil Science Society American Proceedings*, *67*, pp. 289-299.

Estimating land surface energy fluxes in SE Spain using Aster and MODIS data

M. García[a] , S. Contreras[a], F. Domingo[a] and J. Puigdefábregas[a]

[a] Estación Experimental de Zonas Áridas,CSIC, General Segura 1, Almería 04001, Spain, email: monica@eeza.csic.es

ABSTRACT

Land degradation can be associated with decreases in water use efficiency by ecosystems, with impacts on actual evapotranspiration or latent heat. As this should be reflected in the partition of surface energy fluxes, indicators of land degradation based on energy ratios could help to monitor land condition. In this study, we test a simple operational model for calculating energy fluxes in a semiarid region, in mountainous terrain, at two different spatial resolutions (90 m and 1 km), using Aster and MODIS data on 18-07-2004.

Results show that Aster and MODIS results are comparable within reported instrumental errors. However, the lost of detail is remarkable. If the processes of land degradation related with changes in the surface energy balance are explicit at 1 km, which needs further elucidation, MODIS is an adequate tool to perform regional assessments by means of its high temporal and spatial coverage. Comparisons with field data show low net radiation errors (within pyranometer precision) and large errors for sensible heat (using eddy covariance technique) but within the ranges obtained by other authors.

The spatial patterns for the ratio H/Rn (sensible heat to net radiation) proposed as an indicator of land condition are coherent with the surface type. Potentially degraded sites are in the radiation controlled domain at this time of the year, which provides some insight about their energy partition. Preliminary comparisons at 1 km of the rescaled H/Rn index by aridity levels with an independent indicator of land degradation based on Rainfall Use Efficiency (RUE) show promising results. Because, of the limited verification data and dates, the model results are preliminary and need further testing.

Keywords: sensible heat, net radiation, surface fluxes, Aster, MODIS, semi-arid.

1 INTRODUCTION

Currently, there is a lack of standard and operational procedures for monitoring land degradation over large regions [1]. Land degradation processes are the consequence of permanent alterations in the optimum structure and functioning of ecosystems leading to decreases in its resource use efficiency and productive capacity. Some of these changes, mostly human driven, can be related to ecosystem functional indicators based on the hydrologic cycle [2,3] or the surface energy balance. Both types of indicators are connected through the latent heat flux (LE) or evapotranspiration. Calculation of surface energy ratios requires spatially disaggregated estimates of surface energy balance components on monthly and annual scales compatible with the temporal scales of desertification.

The law of conservation of energy states that the available energy reaching a surface is dissipated mainly as latent heat (LE) and sensible heat (H): Rn-G = LE+H . Being, Rn net radiation, G soil heat flux and Rn-G available energy. The algorithms to calculate these energy components use information in the solar and thermal range, being remote sensing the only data source providing radiometric temperature and vegetation cover observations over large extents. This is crucial as explains most of the partition of the available energy into sensible and latent heat [4].

The most vulnerable areas to land degradation are located in arid regions (UNCCD) where the development of an operative system would require data such as MODIS (Moderate Resolution Imaging Spectrometer), available at high temporal resolution but with 1 km pixel size. This questions the validity of models originally designed for agricultural areas or almost ideal conditions when these models are applied over arid regions and heterogeneous sites with sparse vegetation covers [5].

In this study, we test a simple operational model [6,7,8] for calculating energy fluxes in a semi-arid region at two different spatial resolutions (90 m and 1 km). To select an appropriate energy balance indicator, it is important to note the low value of latent heat fluxes during several months in semi-arid areas. For instance in the study region latent heat is within error level of models during several days [9].

For this reason, we explore the H/Rn ratio as an indicator for land degradation. Most authors assume that daily soil heat fluxes (G) are zero [4]. Therefore, the evaporative fraction (EF), defined as the ratio of latent heat (LE) and available energy (Rn-G), can be expressed as EF=LE/Rn; being the H/Rn =1-EF. The reason for not using EF=1-H/Rn as an indicator is twofold: in semiarid areas the contribution of G cannot be neglected [10]; and latent heat is usually within model errors as was pointed out before. We preferred to use the index H/Rn, that should present a wider range of variability than EF and a higher signal-to-noise ratio without making any assumption about G,

We hypothesize that the increase in bare soil due to decreases in vegetation cover taking place as a consequence of land degradation should increase surface temperature and albedo causing increases in H, and decreases in Rn similarly to results presented by [11] in the Sahel. Feedback effects, such as those occuring between albedo and surface temperature might counterbalance some of these impacts. This work pretends to elucidate some of these aspects. The specific objectives are:

(1) Evaluate the performance of a simple energy balance algorithm in a semi-arid region in SE Spain characterized by its land cover heterogeneity, fragmentation and mountainous terrain on a daily basis.

(2) Compare results derived from finer to coarser resolution data. In particular, 1 km MODIS versus 90 m Aster (Advanced Spaceborne Thermal Emission and Reflection Radiometer) to estimate land surface energy fluxes.

Aster is currently, the only sensor collecting multispectral thermal infrared data at high spatial resolution being very appropriate for testing of models and direct ground comparisons [12]. On the other hand, Aster and MODIS are on board the Terra platform, allowing analyses of scale. Recent work has been done to compare both sensors showing good agreement (<1 K) [13]. It is desirable to extend this type of comparisons to other variables and regions.

2 STUDY SITE AND DATA

The study region (Figure 1) located in South East Iberian Peninsula (Almería, Spain) comprises 3600 km^2 (36.95º N, 2.58ºW). This region is characterized by its heterogeneity, due to the abrupt relief changes with altitudinal gradients ranging from sea level up to 2800 m (a.s.l.) in Sierra Nevada mountain. The precipitation and temperature regimes present wide contrasts driven by the orography [14]. Annual precipitation is the lowest in the Tabernas desert, with less than 200 mm, while in the mountains can be enough to sustain forest growth, ranging between 400 mm up to 700 mm.

In the center of the study site, the Gador mountain range covers 552 km^2, composed of shrubland and perennial grassland vegetation, some oak relicts, reforested areas of pine woods, and some semi-abandoned orchards. The study site includes part of the Natural Park of Sierra Nevada including wood of pines, oak relicts, and shrublands. In the northeast is the Tabernas desert with a complex topography comprising an area of badlands. Along the Andarax ephemeral river which flows by Almeria city, there is a mosaic of citrus orchards and vinegrapes. One of the most outstanding features of the scene is the large plastic greenhouse area covering more than 330 km^2. This unique combination allows using this area as a pilot site where to test a simple model for calculating surface energy fluxes that could be extended for use at regional and global scales.

For this study, we have used Aster and MODIS data acquired on July-18th-2004 at 11.00 UTC. The Aster products used were 2AST07 which is Surface reflectance at 15 m (VNIR) and 30 m (SWIR), and 2AST08 Kinetic temperature at 90 m. Two MODIS products were used: the 8 day surface reflectance at 500 m (MOD09) instead of daily, to decrease errors as albedo and vegetation indices can be assumed constant during this time. The other product used was daily land surface temperature product (MOD11). In the case of MODIS, surface temperature errors range from 1 -3 K with no incidences for ASTER, where the reported absolute precision is 1-4 K.

A digital elevation model (DEM) from USGS (United States Geological Survey) available at 30 m resolution and a digital orthophoto (from the Andalusian Regional Government) at 0.5 m were used at different stages of the study.

Instrumental field data are acquired continuously at the Gador Experimental site since 2003 (Figure 1, upper right panel). They were used to compare with model results. The eddy covariance technique was used to measure latent and sensible heat flux using a three dimensional sonic anemometer CSTAT3 and a krypton hygrometer KH20, both from Campbell Scientific Inc., USA. The tower is located in a flat area covered with perennial grasslands and shrubs so that the measurements acquired at that point include an area of 2 km^2, existing several areas with similar vegetation type within the Gador mountain. Net radiation (NR-LITE; Kipp & Zonen, Delft, the Netherlandstemperature), and relative humidity (thermohygrometer HMP 35C, Campbell Scientific, Logan, UT, USA) sonic and soil temperature (SBIB sensors) are also continuously measured at the site. Besides air temperature

measurements at the Gádor Mountain range field site, air temperature was measured from other 10 meteorological stations at the time of the satellite overpass (11.00 UTC).

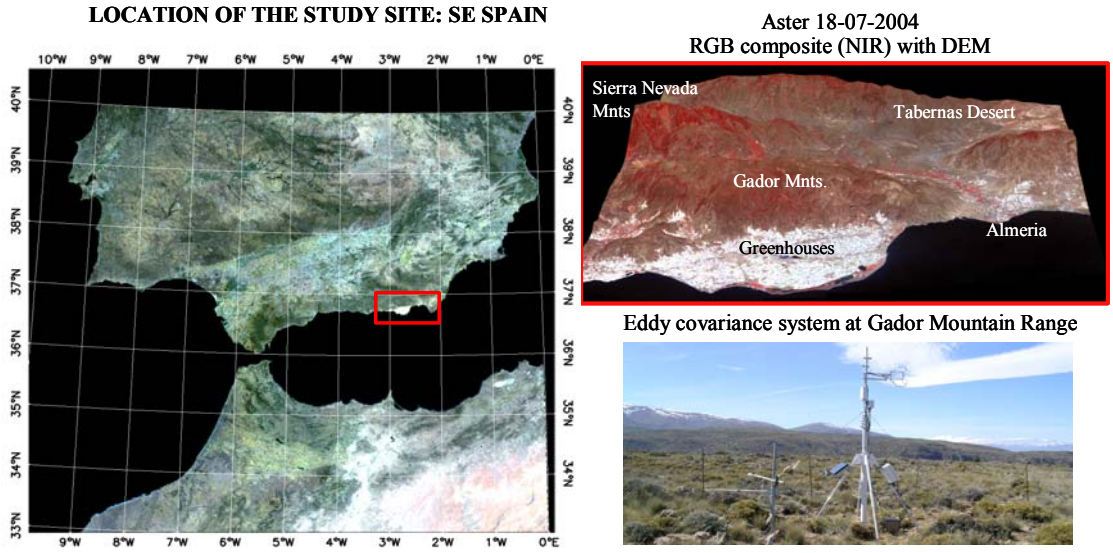

Figure 1. Location of the study site in South East Spain, Almeria province. The upper right panel shows MODIS True Color Composite corresponding to the study site and 18-07-2004. The lower right panel shows the location of the eddy covariance system for sensible and latent heat in a flat area at the Gador Mountain range.

3 METHODS

First, Rn, H and its ratio H/Rn were calculated for Aster and MODIS. In a second step, the results obtained with Aster were linearly aggregated into a 1 km pixel to compare with MODIS. Finally, results of H/Rn at 1 km were rescaled according to aridity levels to compare with an independent land degradation indicator.

3.1 Estimation of Net Radiation

Rn is calculated as the balance between incoming (↓) and outgoing fluxes (↑) of shortwave (Rs) and longwave (Lw) radiation. By agreement, incoming fluxes are positive and outgoing negative. This can be expressed as the sum of Shortwave (Rns) and Longwave net radiation (Lnw)

$$Rn = Rs\uparrow + Rs\downarrow + Lw\downarrow + Lw\uparrow = Rns + Lnw \quad (1)$$

Shortwave Net radiation

The shortwave net radiation using remote sensing is calculated as: $Rns=(1-\alpha)\ Rs\downarrow$. Where α is the broadband surface albedo, estimated according to [15] for 6 Aster and MODIS bands. $Rs\downarrow$ (incoming solar radiation) was estimated using a solar radiation model from [16].

Longwave Net radiation

The longwave energy components are related to surface and atmospheric temperatures through the Stephan-Boltzmann law. The longwave net radiation is calculated as in (2):

$$Lnw = -\varepsilon s \sigma T4s + Lw\downarrow \quad (2)$$

Where broadband emissivity for the surface (ε_s) was estimated based on a logarithmic relationship with NDVI [17] and radiometric surface temperature (Ts) was directly obtained from Aster and MODIS LST (Land Surface Temperature) products calculated with the TES (Temperature Emissivity Separation) algorithm for Aster and the day/night LST algorithm for MODIS. An empirical function is used for the incoming longwave radiation Lw [18].

Air temperature

To avoid relying on meteorological information, air temperature was estimated from the images using the triangle NDVI-Ts proposed by [8]. The apex of the NDVI-ts space (high NDVI and low temperature) should correspond to pixels with high NDVI located at the wet edge of the triangle, and can be assumed to be at the air temperature [19]. Due to the altitudinal gradients it is necessary to apply a correction to air temperature considering as a base or reference altitude that of the pixels at the apex. Afterwards, positive corrections for altitude are made for pixels below the base altitude and vice-versa for pixels above using the rule of thumb of 6.5 ºC each 1000 m. This is better than approaches considering a unique air temperature for the whole area assuming constant meteorological conditions at the blending height [8, 20] and also works better than [21] dry and wet pixel approach, probably more suited for flat areas, evaluated in preliminary tests (results not shown).

3.2 Estimation of Sensible Heat flux

H can be estimated by a model of turbulent transport from the surface to the lower atmosphere based on surface layer similarity of mean profiles of temperature and wind speed using a resistance form:

$$H = \rho \cdot c_p \cdot \frac{(Ts - Tair)}{r_h} \tag{3}$$

Where Ts is land surface temperature, Tair is air temperature, both at the time of image acquisition, r_h is the atmospheric resistance to the transfer of H, ρ and c_p are air density and specific heat at constant pressure respectively. B can be defined as an exchange coefficient to sensible heat transfer [6, 7]: $B=\cdot\rho\cdot c_p\cdot h_a$

Being h_a the turbulent exchange coefficient dependent on wind velocity, aerodynamic roughness length, roughness length for heat transfer and Monin-Obukov length. As having estimates of these variables at large scales is impossible, more operational parameterizations have been proposed. We used the [8] approach which states that the main factor affecting conductance to heat transfer is vegetation cover and establishes a linear relation between the exchange coefficient to sensible heat transfer B and fractional cover.

3.3 Relation of H/Rn at 1 km with land degradation

To provide some preliminary insights of the relation of the H/Rn ratio with potentially degraded areas at 1 km, we compared in the study site the H/Rn ratio at 1 km with a land degradation index based on the concept of RUE (Rainfall Use Efficiency) expressed as NDVI / Precipitation [22].

First, it was necessary to rescale the H/Rn ratio according to the aridity index to make comparisons across different regions (e.g. forest, desert). The aridity index was calculated as the ratio between potential evapotranspiration [22] and average annual precipitation interpolated from the stations at the site.

The assumption below rescaling H/Rn by aridity index levels is that in the scene there is enough variability as to find degraded and non-degraded sites. Therefore, within each aridity index level there is range of variation from optimum levels (low H/Rn) to degraded (high H/Rn). Quantile regression for the 5 % and 95 % were performed to find the enveloping functions.

The rescaled H/Rn is:

$$H/Rn_{resc} = \frac{H/Rn_{obs} - H/Rn_{5\%}}{H/Rn_{95\%} - H/Rn_{5\%}} \tag{4}$$

Where: H/Rn_{obs} is the observed value of H/Rn in the pixel.

$H/Rn_{5\%}$ is the value of H/Rn lower enveloping function for the aridity level corresponding to that pixel.

$H/Rn_{95\%}$ is the value of H/Rn upper enveloping function for the aridity level corresponding to that pixel.

The land degradation index has two dimensions: RUE_{mean} or the average RUE for a four year period, related with annual productivity or biomass, and RUE_{max} or the maximum monthly RUE within that four year period that could be related with maximum productivity. Sites with low RUE_{mean} or low RUE_{max} could be potentially degraded sites. [22] estimated maximum productivity and annual biomass using NDVI on a 1 km pixel level from AVHRR. For comparison with H/Rn the RUE was used in a qualitative way, with low, mean and high classes of both indices: RUE_{mean} and RUE_{max}.

4 RESULTS

4.1 Comparison of air temperature with field data

Eleven meteorological stations were used to evaluate air temperature (Tair) estimations at the time of the Terra satellite overpass (11.00 UTC). First, the temperature of the apex according to [8] was selected (Figure 2). Afterwards, corrections for altitude improved the overall error from to less than 2 ºC (Table 1).

The overall adjustment is good, but Tair estimates are subjected to local errors. One concern is that altitude is not the only factor affecting Tair. Nevertheless, using this approach presents the advantage of relief from using ancillary data. Also any systematic error in Ts estimation will propagate in the Tair; therefore, these errors should cancel out when calculating differences Ts-Tair for estimating sensible heat flux.

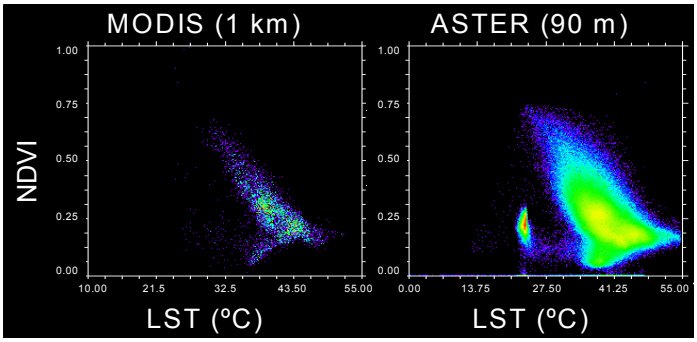

Figure 2. MODIS and ASTER NDVI-LST (Land Surface Temperature) triangle to extract apex temperature values (minimum temperature with higher NDVI) according to [8].

Table 1. Air temperature estimates. "T bias before adjustment" is the absolut average difference of the residuals between estimated air temperature and measured air temperature. "T bias after adjustment" is the absolut average difference of the residuals between estimated air temperature after applying a correction factor by altitude.

	ASTER	**MODIS**
R2 (T air stations and altitude)	0.61	
T bias before adjustment (ºC)	4.31	2.45
T bias after adjustment (ºC)	1.96	1.91
T apex (ºC)	24	28.5
Base altitude (m)	1800	800

4.2 Model performance with MODIS and Aster at the Gador Mountain range field site

At the Gádor Mountain range field site (see Figure 1, lower right panel), Rn and surface energy fluxes were measured and compared with Aster and MODIS estimates (Table 2). The B values obtained at the Gador Mountain range field site are reasonable as they are similar to the fixed value of 0.25 proposed by [7] for dryland and irrigated crops in France and much lower than the fixed value of 0.64 of [6] in irrigated wheat fields in Arizona.

In the Gador mountain range field site, errors are very low for Rn (around 5% compared to field data) and therefore within reported pyranometer errors ($\pm$10 % and directional error of < 25 W m^{-2}). In this site, both Aster and MODIS underestimate H when comparing with eddy covariance measurements. Although errors for Ts are within acceptable quality levels reported for Aster and MODIS, otherwise pixels were masked, it would be necessary to evaluate its influence in H and Rn estimates in future studies. We also have to be aware that the eddy covariance technique is subjected to uncertainty levels of 20-30 % [23]. Moreover, in semi-arid areas with sparse vegetation cover, error in energy fluxes tend to be on the higher side of this range around 30 % [24].

In general, the range of errors reported by other authors in H flux is very variable. [25] consider around 50 Wm^{-2} an acceptable error for H. In the literature, errors in the best cases are around 22 Wm^{-2} [4] and can reach up to 50% even with sophisticated models if parameterizations are not good. Using a fixed value for kB^{-1} in agricultural areas produces errors as high as 150 Wm^{-2} or 43-64 Wm^{-2} [25]. [26] obtained a RMSE of 43.35 W m^{-2} for sensible heat. [27] in the Great Basin desert got errors in H around 40 % similarly to our results.

Table 2. Comparisons between measured and estimated values at the Gádor Mountain range field site. B is the exchange coefficient for heat transfer, Rn is net radiation and H is sensible heat flux.

	Sensor	B	Rn (W m^{-2})	H (W m^{-2})
Values	**Aster**	0.250	189.86	107.65
	MODIS	0.2407	172.73	84.42
	Measured	0.370*	179.72	152.97
Error (differences)	**Aster-Measured**	-0.06	10.14	-45.33
	Modis-Measured	-0.069	-6.99	-68.56
	Modis-Aster	0.0093	-17.13	-23.23
Error (%)	**Aster-Measured**	-24.00	5.34	-42.11
	Modis-Measured	-18.65	-3.89	-44.82
	Modis-Aster	3.72	-9.02	-21.58

**Estimated empirically from field data at Gádor Mountain range field site*

4.3 Analysis of the H/Rn spatial patterns

The assessment of model results cannot be made solely on the basis of a unique, although very representative of the study site, eddy covariance value. To evaluate the spatial coherence of the results obtained with Aster, comparison of values for different land use types has been performed (Figure 3). These sites were selected by photo-interpretation based on field knowledge of the area.

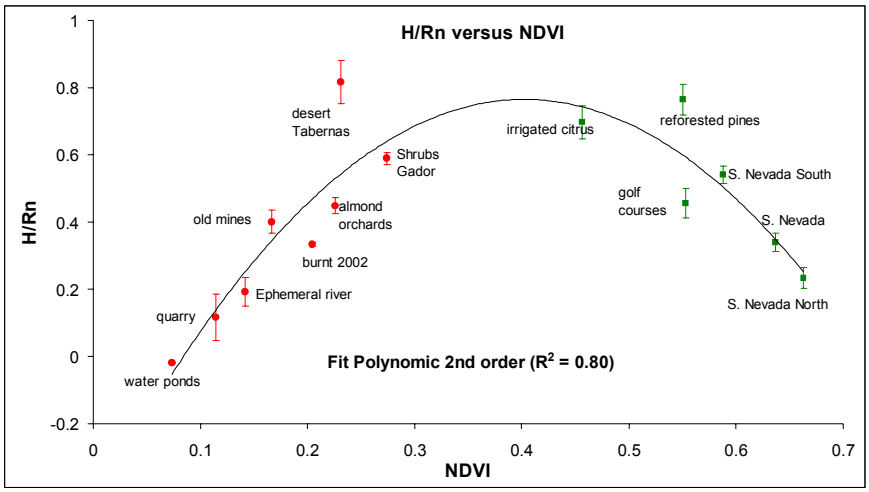

Figure 3. H/Rn versus NDVI for different vegetation types. The surface type legend is close to each value. Error bars represent the confidence interval ($p < 0.05$). 2nd order polynomial fitting for mean values presents an $R^2 = 0.80$. Red dots represent the part of the curve controlled by radiation and green squares by evapotranspiration. There is a threshold for NDVI (0.4). Before the threshold the H/Rn increases with vegetation cover, after it the ratio H/Rn decreases.

In general, H/Rn patterns are consistent and resemble the pattern of a radiation and an evaporation controlled branch related with direct and feedback effects between albedo and surface temperature [20, 21]. At the study site, the highest evaporative surface are the water ponds that can be considered a calibration site with zero values of H/Rn (Figure 3). Then, there is a trend to increase the partition of H to Rn with increasing vegetation cover. These surfaces present high albedo values, e.g. the cement quarry, and in this date the soil is dry, and the increase in vegetation cover tends to increase surface roughness, and in consequence the driving force for H flux [8]. However, this sparse vegetation is not evaporative, being reasonable to expect increases in G. This trend occurs up to a threshold in which either vegetation cover is evaporative (trees with deep roots or the irrigated crops). Then, the H/Rn tends to decrease with increasing vegetation cover responding to a situation in which the surfaces are evaporating water.

It is remarkable the influence of aspect on the surface energy fluxes. Thus, in the Sierra Nevada mountain, those pixels located in northern aspects show lower H/Rn ratio than those at southern or Mediterranean face. The golf courses present H/Rn values similar to almond crops but their LAI is low enough to have a strong soil influence. It is surprising that the irrigated citrus orchards located by the Andarax ephemeral river present higher values than for instance dryland almonds. The reason is the high degree of land fragmentation (parcels are in general smaller than 1 ha) alternating bare soil and citrus orchards.

Figure 3 shows that the H/Rn index captures spatial patterns related with surface energy partition. However, solely this index is not good to discriminate among cover types, and a combination with a vegetation cover index helps to evaluate if the surfaces are in the evaporative or in the radiation controlled domain. On the other hand, the plot albedo-Ts did not show the expected bell-shaped pattern (results not shown) which appears very clearly in the H/Rn –NDVI plot. Potentially degraded sites such as abandoned mines, the cement quarry, or the burnt scar from the 2002 fire (Figure 3) are all in the radiation controlled branch at this time of the year. This provides some insight about their radiation balance.

4.4 Comparison between MODIS and ASTER performance

Comparisons between Aster and MODIS were performed by resampling the Aster pixel size of 90 m using a cubic convolution filter into MODIS 1 km pixel size.

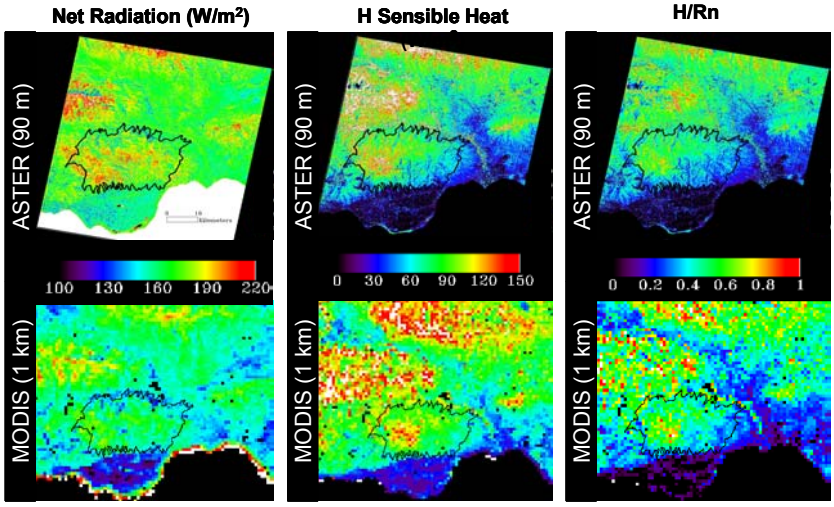

Figure 4. Comparison of spatial patterns of net radiation, sensible heat and H/Rn ratio for ASTER (90 m) and MODIS (1 km) over the study site on 18-07-2004. The Gador mountain range is outlined with a black line.

Results in Table 3 show that for the set of input variables MODIS values tend to be slightly higher than Aster. It is remarkable the RMSE in Ts of almost 2.90 ºC. These differences are translated in the output variables causing underestimations of MODIS with respect to Aster. Most of the input variables present a good R^2, which means that the input variables aggregate linearly at least to explain between 0.63-0.70 of the variance. However, there is a remaining ~30 % of the variance responding to non-linear aggregation effects combined with sensor differences in sensor performance and correction algorithms employed. These differences in input values between MODIS and Aster are amplified in the output values of surface energy fluxes of H, Rn and H/Rn (Table 3).

In any case, both RMSE and mean differences are within reported pyranometer precision for Rn. RMSE results for H are comparable to some closure errors in energy balance using eddy covariance technique [23]. This means that despite some differences between Aster and MODIS sensor performance, combined with the impact of change in spatial resolution, the two sensors provide similar results, for spatial features of 1 km or larger, comparable to repeatability of instrumental data.

VARIABLES		Diff. Mean Value	RMSE	R2
INPUT	**LST (ºC)**	0.277	2.90	0.65
	Broadband Albedo	0.0214	0.0020	0.63
	B (mm/ºC)	-0.009	0.0028	0.74
	Emissivity	0.0047	0.0117	0.70
OUPUT	**H (W m-2)**	-10.08	27.019	0.58
	Rn (W m-2)	-13.37	18.59	0.34
	H/Rn	-0.017	0.025	0.39

Table 3. Input and output variables for MODIS and Aster: LST (Land Surface Temperature), B (exchange coefficient to sensible heat transfer), H (sensible heat flux), Rn (net radiation), RMSE (Root Mean Square Error). Diff. Mean value is the average of differences between MODIS and ASTER, R^2 the Pearson coefficient after aggregation of Aster to 1 km pixel.

Figure 4 shows results for output variables using Aster and MODIS. The gross main structure of the surface fluxes explained by the H/Rn partition is maintained from MODIS to Aster scene, but level of detail is not

comparable. For this reason, features with a spatial resolution lower than 1 km are not resolved (e.g the mosaic of irrigated citrus and bare soil by the Andarax river). Therefore, if the processes of land degradation related with changes in the surface energy balance are explicit at 1 km grains, which needs further elucidation, MODIS can be consider an adequate tool to perform regional assessments by means of its high temporal and spatial coverage.

4.5 Relation of H/Rn at 1 km with land degradation

The H/Rn was rescaled by aridity levels to compare across land cover types, using enveloping functions (Figure 5) polynomic for the lower (5% quantile) and linear for the upper level (95% quantile).

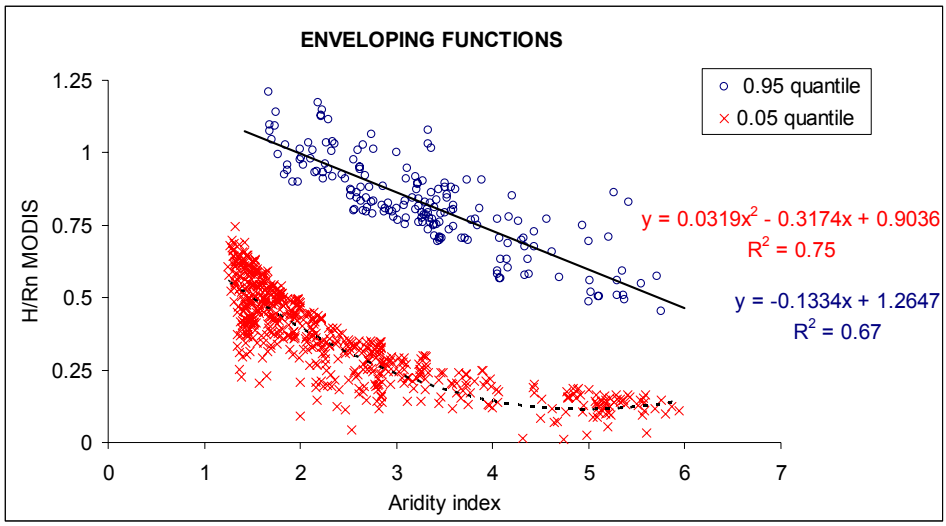

Figure 5. Enveloping functions used to rescale the H/Rn index by aridity levels. They were calculated using quantile regression to find the upper and lower boundaries. For the upper boundary (95 % quantile) a 2nd degree polynomic function was fitted. For the 5 % quantile (lower boundary) a linear regression was fitted.

The H/Rn rescaled presents high values for low RUE_{mean} values and vice-versa. For the mean class of RUE_{mean}, H/Rn is also high (Figure 6). The relations of H/Rn with RUE_{max}, are only apparent when annual productivity (RUE_{mean}) is low or mean showing a decreasing trend along increasing RUE_{max}. This index seems promising in capturing some of the alterations of the energy balance related with potentially degraded sites, being mostly in agreement with the hypothesis regarding the behavior of H/Rn in degraded areas.

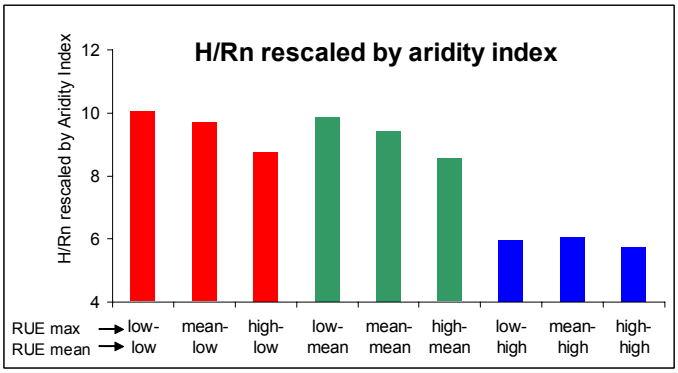

Figure 6. Comparison of the H/Rn ratio rescaled by the aridity index enveloping functions with classes of the RUEmean (Mean Rainfall Use Efficiency) and RUEmax (Maximum Rainfall Use Efficiency) at 1 km over the study site.

5 CONCLUSIONS

Comparison between MODIS and Aster spatial patterns of surface energy balance components on 18-07-2004 reveals that the main structure is maintained from Aster to MODIS. However, the lost of detail is remarkable and features smaller than 1 km are not resolved. Regarding RMSE values between Aster and MODIS, net radiation values are within reported pyranometer precision and sensible heat flux are comparable to closure errors in energy balance using eddy covariance technique [23]. Therefore, if the processes of land degradation related with changes in the surface energy balance are explicit at grains of 1 km, MODIS is an adequate tool to perform regional assessments by means of its high temporal and spatial coverage.

Comparison with field data using eddy covariance technique at the Gador experimental field site shows very low net radiation errors (within pyranometer precision). Sensible heat provides larger errors but within the ranges

obtained by other authors [13,27], being Aster within the threshold of 50 Wm^{-2} proposed by [25]. To decrease errors in sensible heat flux, it will be desirable to improve estimations of the exchange coefficient to sensible heat flux. Air temperature can be extracted from the images using the NDVI-Ts space relationship [8] corrected by altitude with an acceptable overall error (< 2 ºC).

The spatial patterns of Aster H/Rn (sensible heat/net radiation) index are coherent with the type of surface. However, solely this index is not good to discriminate among these cover types, and a combination with a vegetation index helps to evaluate whether surfaces are in the evaporative or in the radiation domain [21].

Potentially degraded sites are in the radiation controlled domain (positive H/Rn-NDVI slope) at this date, which provides some insight about their energy partitioning. In addition, preliminary comparisons at 1 km of the rescaled H/Rn index by aridity levels with an independent indicator of land degradation based on rainfall use efficiency show promising results. However, because of the limited verification data currently available, the model results are preliminary and in need of further testing.

Establishing a robust land degradation index needs additional analysis including several dates to fully understand the interaction between water and energy at different surfaces. Efforts should be devoted to scale daily results to temporal scales compatible to the time scale of land degradation processes. Along this line, a remaining question is the spatial and temporal scales in which alterations of energy balance fluxes related with land degradation are explicit.

ACKNOWLEDGMENTS

This research is within the EU project DeSurvey (A Surveillance System for Assessing and Monitoring of Desertification; FP6-00.950). The authors wish to thank Dr. del Barrio, M. San Juan and Dr. Lazaro for their help.

REFERENCES

[1] PUIGDEFÁBREGAS, J., MENDIZÁBAL, T. 2004: Prospects for desertification impacts in Southern Europe. In A.Marquina (ed): *Environmental challenges in the Mediterranean 2000-2050*, chapter 10, pp 155-172, Kluwer Academic Publisher, Netherlands.

[2] SHARMA, K. D., 1998: The hydrological indicators of desertification. *J. Arid Environ. 39*, pp.121-132.

[3] BOER, M.M. AND PUIGDEFABREGAS, J., 2003: Predicting potential vegetation index values as a reference for the assessment and monitoring of dryland condition. *Int. J. Remote Sens. 24* (5), pp. 1135 – 1141

[4] KUSTAS W.P. Y J.M. NORMAN. 1996: Use of remote sensing for evapotranspiration monitoring over land surfaces. *Hydrolog Sci J*. 41(4), pp. 495-516.

[5] CHEHBOUNI, A.; LOSEEN, D.; NJOKU, E.G.; LHOMME, J.P.; MONTENY, B.; AND KERR,Y.H., 1997: Estimation of sensible heat flux over sparsely vegetated surfaces. *J. Hydrol. 89*(1-4), pp. 855-868.

[6] JACKSON, RD; REGINATO, RJ; IDSO, SB., 1977: Wheat Canopy Temperature: A Practical Tool for Evaluating Water Requirements. *Water Resour. Res. 13 (3),* pp. 651-656,

[7] SEGUIN, B. AND ITIER, B., 1983: Using midday surface temperature to estimate daily evaporation from satellite thermal IR data. *Int. J. Remote Sens. 4*, pp. 37-383.

[8] CARLSON, T.N., CAPEHART, W.J., AND GILLIES, R.R., 1995: A New Look at the Simplified Method for Remote-Sensing of Daily Evapotranspiration. *Remote Sens. Environ. 54*, pp. 161-167.

[9] DOMINGO, F., VILLAGARCÍA, L., BOER, M., ALADOS-ARBOLEDAS, L., PUIGDEFÁBREGAS, J. 2001: Evaluating the long-term water balance of arid zone stream bed vegetation using evapotranspiration modelling and hillslope runoff measurements. *J. Hydrol. 243,* pp. 17 - 30.

[10] WAASSENAAR, T., OLIOSO, A., HASAGER, C., JACOB, F., CHEHBOUNI, A. 2002: Estimation of evapotranspiration on heterogeneous pixels. *Proceedings of the 1st Symposium of Recent advances in Quantitative Remote Sensing. Valencia*, Sept 2002. Sobrino, Ed, pp. 319-328.

[11] DOLMAN A.J., GASH J.H.C., GOUTORBE, J.P., KERR Y, LEBEL T, PRINCE SD, AND STRICKER, J.N.M., 1997: The role of the land surface in Sahelian climate: HAPEX-Sahel results and future research needs. *J. Hydrol. 89* (1-4), pp- 1067-1079.

[12] FRENCH, A. N., JACOB, F., ANDERSON, M. C., KUSTAS, W. P., TIMMERMANS, W., GIESKE, A., SU, B., SU, H., MCCABE, M. F., LI, F., PRUEGER, J. H. AND BRUSNELL, N., 2005: Surface energy fluxes with the Advanced Spaceborne Thermal Emission and Reflection radiometer (ASTER) at the Iowa 2002 SMACEX site (USA). *Rem. Sens. Environ. 99* (1-2), pp. 55-65.

[13] JACOB, F, PETITCOLIN, F.; SCHMUGGE, T.; VERMOTE, E.; FRENCH, A.; OGAWA, K. 2004: Comparison of land surface emissivity and radiometric temperature derived from MODIS and ASTER sensors. *Rem. Sens. Environ. 90(2),* pp. 137-152.

*[14]*LÓPEZ-BERMÚDEZ, F., BOIX-FAYOS, C., SOLÉ-BENET, A., ALBALADEJO, J., BARBERÁ, G.C., DELBARRIO,G., CASTILLO, V., GARCÍA, J., LÁZARO, R., MARTÍNEZ-MENA, M.D., MOSCH, W., NAVARRO-CANO, J.A., PUIGDEFÁBREGAS, J., SANJUÁN,M. 2005: Landscapes and desertification in south-east Spain; overview and field sites. Field Trip Guide A-5. *6th International Conference on Geomorphology. Sociedad Española de Geomorfología.* 40 pp.

[15] WERE, A., 2005: Agregación espacial de la evapotranspiración en clima semiárido. *Ph.D. Thesis* (in Spanish). Universidad de Almeria, Spain. Pp.212

[16] LIANG S., 2000: Narrowband to broadband conversions of land surface albedo I Algorithms. *Rem. Sens. Environ. 76*, pp. 213-238.

[17] FU, P. AND RICH M. 2002: A geometric solar radiation model with applications in agriculture and forestry. *Comput. Electron. Agr.* 37 (2002): 25-35.

[18] VAN DE GRIEND A.A AND OWE M, 1993: On the relationship between thermal emissivity and the normalized difference vegetation index for natural surfaces, *Int. J. Remote Sens. 14(6)*, pp. 1119-1131.

[19] IDSO, S.B., JACKSON, R.D. 1969: Thermal radiation from the atmosphere. *J. Geophys.Res. 74*, pp. 5397–5403.

[20] CZAJKOWSKI, K.P., S.N.GOWARD, T. MULHERN, S.J. GOETZ, A. WALZ, D.SHIREY, S. STADLER, S.D.PRINCE, AND DUBAYAH, R.O., 2000: Estimating environmental variables using thermal remote sensing. In: D. A. Quattrochi and Jeffrey C. Luvall (eds.): *Thermal remote sensing in land surface processes*. CRC Press. Pp. 11-32.

[21] ROERINK, G. J., SU, Z. AND M. MENENTI. 2000: S-SEBI: A Simple Remote Sensing Algorithm to Estimate the Surface Energy Balance. *Phys. Chem. Earth 25,* pp. 147-157.

[22] BASTIAANSSEN, W.G.M., MENENTI, M., FEDDES, R.A., HOLTSLAG, A.A.M., 1998: A remote sensing surface energy balance algorithm for land (SEBAL) 1. Formulation. *J. Hydrol. 212-213* (1-4) pp. 198-212.

[23] DEL BARRIO G., M. SANJUAN, J. PUIGDEFABREGAS, M. BOER AND STELLMES, M., 2005: Assessing land condition through a bi-dimensional index of vegetation Rainfall Use Efficiency: the case of mainland Spain. Remote Sensing and Geoinformation Processing in the Assessment and Monitoring of Land Degradation and Desertification. Trier, September 2005. Abstract book. Pp. 87-88.

[24] BALDOCCHI, D. D., FALGE, E., GU, L., OLSON, R., HOLLINGER, D., RUNNING, S., ANTHONI, P., BERNHOFER, CH., DAVIS, K., FUENTES, J., GOLDSTEIN, A., KATUL, G., LAW, B., LEE, X., MALHI, Y., MEYERS, T., MUNGER, J. W., OECHEL, W., PILEGAARD, K., SCHMID, H. P., VALENTINI, R., VERMA, S., VESALA, T., WILSON K. & WOFSY, S., 2001: FLUXNET: A new tool to study the temporal and spatial variability of ecosystem-scale carbon dioxide, water vapor and energy flux densities. *B. Am. Meteorol. Soc. 82*, pp. 2415 - 2434.

[25] HARGREAVES, G. H. AND Z. A. SAMANI. 1982: Estimating potential evapotranspiration. *J. Irrig. Drain E-ASCE.* 108: 225-230.

[26] SEGUIN, B., BECKER, F., PHULPIN, T., GU, X.F., GUYOT, G., KERR, Y., KING, C., LAGOUARDE, J.P., OTTLE, C., STOLL, M:P:, TABBAGH, A., AND VIDAL, A. 1999: IRSUTE: A Minisatellite Project for Land Surface Heat Flux Estimation form Field to Regional Scale. *Rem. Sens. Environ. 68,* pp. 357-369.

[27] HUMES, K., HARDY, R., KUSTAS, W., PRUEGER, J. AND STARKS, P., 2000: High spatial resolution mapping of surface energy balance components with remotely sensed data. In: D. A. Quattrochi and Jeffrey C. Luvall (eds.): *Thermal remote sensing in land surface processes*. CRC Press. Pp. 110-132.

[28] LAYMON, C, A. AND QUATTROCHI, D.A.., 2000: Estimating spatially-distributed surface fluxes in a semi-arid Great Basin desert using Landsat TM thermal data. In: D. A. Quattrochi and Jeffrey C. Luvall (eds.): *Thermal remote sensing in land surface processes*. CRC Press. Pp. 110-132.

A multiple sensors study for vegetation monitoring in Mediterranean areas

L. Giordano[a], F. Borfecchia[b], C. Trotta[c], L. De Cecco[b]

[a] ENEA – Biotec–DES unit; Via Anguillarese 301, 00060, S.Maria di Galeria (Rome), Italy
ludovica.giordano@casaccia.enea.it
[b] ENEA – CLIM–OSTES unit
[c] Tuscia University, Ecology Department, Via S. Giovanni Decollato 1, 00100, Viterbo, Italy

ABSTRACT

In the last decade lot of knowledge has been gained about vegetation cover/changes through the use of remote sensing techniques. In particular, empirical models have been largely used to quantitatively retrieve important vegetation biophysical parameters. However, most of the studies have concerned relatively homogenous natural or cropped areas and there is a need to extend the results towards more complex and mixed environment. For this purpose, in this study the utility of high spatial resolution satellite data (e.g., IKONOS) for upscaling ground-based measurements of Leaf Area Index (LAI) collected in typical Mediterranean vegetation have been evaluated. In particular, several spectral vegetation indices (VI_s) and a multiple regression approach using all the available channels and the cosine of the illumination angle (accounting for topographical effects) were tested. The latter yielded the best correlations with observations (r^2=0.80, RMSE =0.22, p<.0001) and was used to produce a LAI spatially continuous coverage. Then, such an IKONOS-based LAI map was utilised for establishing a functional relationship (r^2=0.86, RMSE =0.20, p<.0001) with Landsat data which will be used to perform a temporal analysis through a yearly series (1984-2004) of Landsat TM images.

Keywords: Leaf Area Index, Mediterranean vegetation, Vegetation Indices, multiple regression, multiscale analysis

1 INTRODUCTION

Many Mediterranean regions have been experiencing soil and vegetation degradation processes under the stress induced by both climate change and increased human activities. These processes generally result in a substantial change in vegetation patterns and distribution that can be profitably documented through EO data. In particular, previous studies have shown the potential of remotely sensed multispectral images to extensively map important vegetation biophysical parameters, such as biomass density, net primary productivity (NPP), fraction of incident photosynthetically active radiation (FPAR) and Leaf Area Index (LAI; leaves area/ground area). The latter is of paramount interest as it is a key input to many climate [1], hydrological [2] and ecological models [3,4,5].

Since most of the research carried out so far on forest stands concerns relatively homogeneous, mainly conifer, landscape [6, 7, 8, 9, among others] there is an increased need of accurate estimation of this biophysical parameter in different, more heterogeneous, vegetation communities such as those characterising Mediterranean areas. The primary objective of this study was then to develop semiempirical models based on field surveys carried out in Southern Italy (Basilicata region) in order to evaluate the possibility to effectively retrieve the LAI by means of the approach described below.

1.1 Study area

The two study areas, named “Pantano” and “Rotondella” in the following sections, are located both in the southern part of the Province of Matera (South of Italy).

The first site, extending about 500 hectares on a plain coastal strip, was selected for its high naturalistic value. It is the remaining part of a bigger ancient forest which covered 1600 hectares up to last century’s thirties and it is recently become a natural reserve. Here, the vegetation coverage is mainly represented by an hygrofilous forest (*Fraxinus oxycarpa* Bieb*., Populus canescens* L*., Ulmus minor* Miller and *Alnus glutinosa* (L.) Gaertner) and by Mediterranean shrubs (mainly *Phillyrea latifolia* L*., Pistacia lentiscus* L., *Juniperus oxycedrus* L., *Crataegus monogyna* Jacq.). The second site, *Rotondella,* is about 15 kilometres from the coast in an inner, topographically more complex territory with altitudes ranging from 500m to 800m a.s.l. Here, at least three different vegetation

communities can be distinguished: a *Quercus ilex* L. forest, a mixed broadleaf *(Quercus cerris* L*., Q. pubescens* Willd. and *Carpinus orientalis* Miller*)* forest and tall Mediterranean schrubs.

These areas are characterised by typical Mediterranean climate having rainfall concentrated during autumn and winter and decreasing in summer. Minimum and maximum temperatures monthly mean occur in January and in August, respectively. The yearly rain amount (averaged over a thirty-years dataset: 1970-1999) is 535 mm for Pantano and 721 mm for Rotondella, whereas the yearly mean temperature is around 16 °C for both sites.

1.2 Data

Over late June early July 2004 LAI measurements were taken by means of a LAI-2000 (LICOR, Lincoln, NE) Plant Canopy Analyzer [10] in 54 plots previously attributed to different vegetation classes during field surveys. The LAI-2000 unit was programmed to average four observations into a single value, using one reading taken above the canopy and four beneath the canopy in a sampling area of about $12x12m^2$. A mask blocking 1/4 wedge of the sensor view was positioned to intercept direct solar radiation falling on the sensor surface also preventing sensor-operator interference. Moreover, raw data were corrected by excluding the more external sensor ring according to Ref.11. In table 1 the main characteristics of the collected data are summarised.

Table 1. Summary statistics for leaf area index in four vegetation classes.

Vegetation class	n°plots	Mean	StDev	Min	Max
Hygrofilous forest	15	3.96	1.33	1.19	6.20
Quercus ilex forest	11	5.98	0.93	4.72	7.71
Mediterranean shrubs	12	4.80	1.34	2.82	7.10
Mixed broadleaf forest	16	3.30	1.56	1.0	5.44
Tot	54	4.36	1.63	0.84	7.71

The satellite data utilised in this study are multispectral IKONOS and Landsat TM images acquired on the 2nd and on the 30th of August 2004, respectively. The images preprocessing includes orthorectification and atmospheric corrections. The IKONOS images were orthorectified using GCPs derived from a GPS field surveys, from 1:10.000 aerial coloured orthophotos[1] and from a 20m-pixel DEM, achieving a typical accuracy of about 1 pixel. Then, atmospheric corrections were performed using the 6S-*Second Simulation of the Satellite Signal in the Solar Spectrum* radiative transfer code [12]. The 6S was firstly used iteratively for estimating the atmospheric optical thickness at time of satellite overpass from *a-priori* reflectance's knowledge of some *ad hoc* selected targets, measured by an ASD Fieldspec Pro radiometer. Then, it was possible to atmospherically correct the IKONOS images, which were finally used as reference for the Landsat image orthorectification and atmospheric corrections.

2 METHODS

The retrieval of land surface characteristics, such as LAI, from satellite data through semiempirical model calibrated on "point" measurements needs an appropriate density of ground observations. This means that the variability of the deriving products within a single pixel (or a wider area considering also the georeferencing uncertanties) should be accounted for by the adopted sampling scheme [13]. In highly heterogeneous vegetation this implies that an extremely large number of ground observations have to be collected, which is a time consuming, expensive and ultimately not always easy/possible condition to satisfy.

For this reason, in order to optimise the ground observations sampling scheme LAI field measurements were scaled up to Landsat resolution (30m spatial resolution) using very high resolution IKONOS images (4m spatial resolution) to produce an intermediate LAI distribution layer which better account for the high heterogeneity of the typical Mediterranean vegetation growing in the study sites. To this aim, we implemented an approach based on a two-step procedure illustrated in figure 1(a).

Firstly, a multiple regression using LAI ground observations as dependent variable whereas the four IKONOS bands and the cosine of the illumination angle ($\cos\theta$) as independent variables provided the functional relationship to produce the IKONOS-derived LAI map. As no terrain corrections was applied in the image preprocessing, topographic effects are still included in the data and are accounted for in the multiple regression by using $\cos\theta$.

[1] "it2000" Terraitaly-it2000™ - ©CGRSpA – Parma

Atmospherically corrected IKONOS reflectance data were spatially averaged over a 3x3 window (12x12m^2) allowing the sampling area of ground observations to be matched.

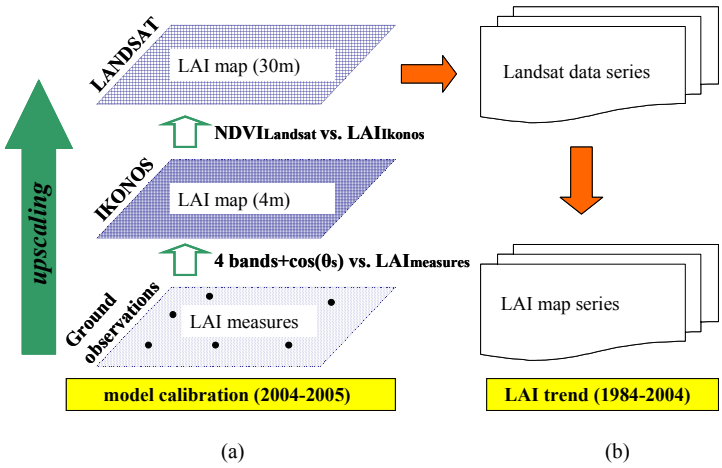

Figure 1. (a) Upscaling from field "point" measurements to Landsat resolution (30m) using higher IKONOS resolution (4m); **(b)** retrospective analysis of vegetation by applying the functional relationship worked out in (a) on Landsat images yearly series.

Secondly, 129 locations were individuated within the overall study area avoiding as much as possible noise effects due to near edge positions in order to establish the empirical relationship between the best performing Landsat-derived VI_s (average values on a 3x3 window, 90x90m^2), and corresponding IKONOS-derived LAI values (avareged on a 23x23 window, 92x92m^2).

In both upscaling steps logarithmic relationships were found to better fit according to a well-known saturation effect [14, among others], which cause additional green biomass having a diminishing effect on canopy reflectance particularly in the red band [15].

Finally, figure 1(b) shows the forthcoming part of this study which will concern a retrospective analysis of vegetation biophysical parameters performed by means of the empirical model calibrated on 2004-2005 field data according to the upscaling procedure described above and applied to a yearly series of Landsat images (1984-2004).

3 RESULTS

Performances and parameters of the multivariate approach used to upscale the LAI ground observations to the IKONOS reflectance data are reported in Table 2. Both results obtained for the pooled data set and the two study sites separately considered are shown. Also, results obtained from the main tested VI_s-based regressions are reported for comparison purposes.

Table 2. Results of LAI measurements upscaling to IKONOS.

model	Dataset	n.	r^2	RMSE	p-value	Equation (reported only for the total dataset)
NDVI	Pantano	15	0.80	0.19	< .0001	
	Rotondella	39	0.54	0.34	"	
	TOT	**54**	**0.60**	**0.31**	"	Ln(LAI)= 8.52*NDVI - 4.68
IPVI	Pantano	15	0.80	0.19	"	
	Rotondella	39	0.54	0.34	"	
	TOT	**54**	**0.60**	**0.31**	"	Ln(LAI)= 17.04*IPVI - 13.20
RVI	Pantano	15	0.73	0.22	"	
	Rotondella	39	0.47	0.37	"	
	TOT	**54**	**0.53**	**0.33**	"	Ln(LAI)= 0.34*RVI - 0.70
OSAVI	Pantano	15	0.65	0.26	<.0002	
	Rotondella	39	0.33	0.42	< .0001	
	TOT	**54**	**0.40**	**0.37**	"	Ln(LAI)= 8.59*OSAVI -2.77
Multivariate	Pantano	15	0.89	0.16	"	
	Rotondella	39	0.79	0.25	"	Ln(LAI)= -38.74*b_1+40.5*b_2-
	TOT	**54**	**0.80**	**0.22**	"	72.76*b_3+2.04*b_4+2.15*cosθ+1.74

A first general outcome was the remarkable differences between the two study sites. Also, single IKONOS band correlations highlighted that nIR band was very poorly correlated whereas the red band had the highest correlation followed by the green one. This partly explained the better results obtained through the multivariate approach with

respect to the various VI_s based on red and nIR reflectances combinations. However, among the tested VI_s the *Normalised Difference Vegetation Index* (NDVI) and the *Infrared Percentage vegetation Index* (IPVI) showed the highest correlation (r^2=0.6 for the pooled dataset; r^2=0.80 for Pantano and r^2=0.54 for Rotondella).

The multivariate regression, using all the available bands and cosθ, significantly improved the results allowing the use of a single equation (r^2=0.8 for the pooled dataset) to produce the LAI distribution map of both test areas on the IKONOS scale. Figure 2 shows the IKONOS-derived LAI maps classified into 4 classes in order to highlight differences in vegetation typologies and conditions.

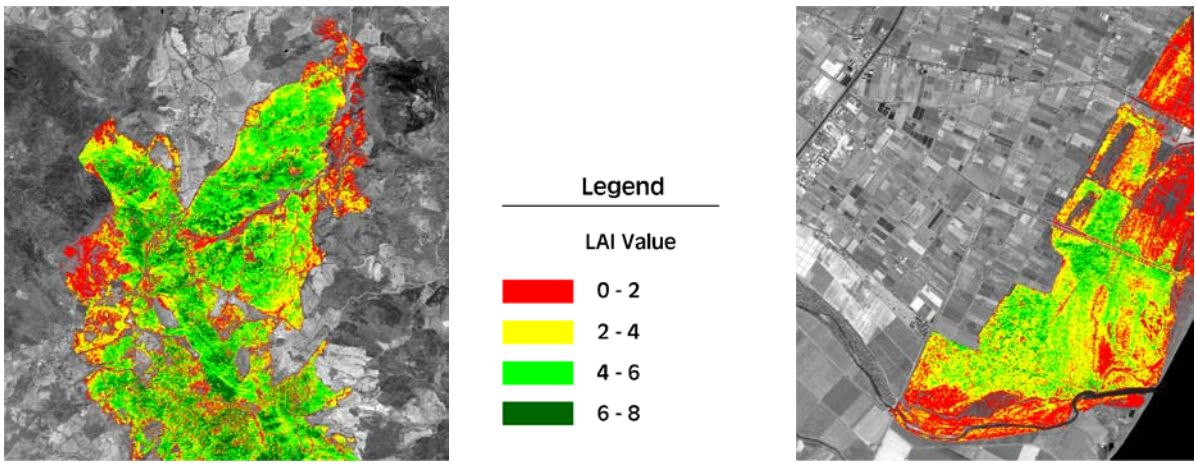

Figure 2. IKONOS-derived LAI map over the two study sites *Pantano* and *Rotondella*.

Of the various Landsat-VIs examined, the best correlations with the IKONOS-based LAI were yielded by the NDVI and IPVI (r^2=0.86, RMSE =0.20, p<.0001) followed by the OSAVI (r^2=0.70,RMSE=0.29, p<.0001) and the NDWI (r^2=0.52, RMSE=0.37, p<.0001). The NDVI was thus selected to produce the Landsat-derived LAI coverage (figure 3). It should be pointed out that all the correlation coefficients directly obtained between Landsat-derived VI_s and LAI ground observations were $r^2 \leq 0.41$ (again maximum values corresponding to NDVI and IPVI; RMSE=0.38, p<.0001).

Finally, the slightly lower values of Landsat-derived LAI estimates can be due to both averages made over a wider area (90x90m vs 12x12m) and the latest date of image acquisition. In fact, August is a very hot and dry month in this region and it is hence characterised by decreasing photosynthetic activity and by likely water-stress, whose intensity also depends on soil and vegetation type.

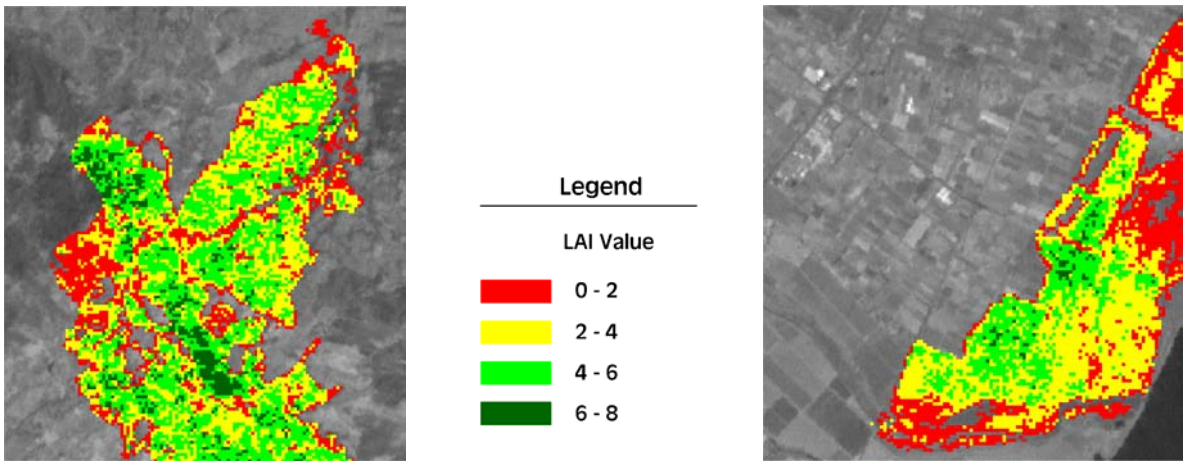

Figure 3. Landsat-derived LAI map over the two study sites *Pantano* and *Rotondella*.

4 OUTLOOK AND CONCLUSIONS

The described approach allowed us to efficiently estimate the LAI distribution in high heterogeneous Mediterranean vegetation from Landsat TM images. The introduction of high resolution satellite data (e.g. IKONOS) as an intermediate processing step between the field measurements and the coarser Landsat resolution, not only allowed the design of a more optimised ground sampling scheme but also appeared a mean to better account for such a complex environment. However, the IKONOS spectral VI_s didn't perform as we expected by reason of its spatial/radiometric resolution and a multiple-variable model, including the topography variable and all the available spectral channels, allowed us to obtain better results. In particular, the IKONOS nIR reflectance poorly explained the ground LAI variability whereas TM-derived spectral VI_s suitably performed in the two study areas.

A further step will test the functional relationship worked out so far on a new dataset from a second LAI field campaign carried out in spring 2005 and corresponding, nearly synchronous, Landsat TM and IKONOS acquisitions. It will allow us to verify the time-independence extent of the model and hence the possibility of using it for a retrospective analysis of vegetation through Landsat TM/ETM images temporal series.

REFERENCES

[1] TIAN Y., WANGA Y., ZHANGA Y., KNYAZIKHINA Y., BOGAERTA J. AND MYNENI R. B., 2002: Radiative transfer based scaling of LAI retrievals from reflectance data of different resolutions. *Remote Sens. of Environ., 84*, pp. 143–159.

[2] D'URSO G:, MENENTI M. AND SANTINI A., 1999: Regional application of one-dimensional water flow models for irrigation management. *Agricultural Water Manag., 40*, pp. 291-302.

[3] GOWER S.T., KUCHARIK C.J, AND NORMAN J.M., 1999: Direct and indirect Estimation of Leaf Area Index, fAPAR, and Net Primary Production of Terrestrial Ecosystems. *Remote Sens. of Environ*., *70*, pp. 29–51.

[4] ASNER, G.P., SCURLOCK J.M.O. AND HICKE J. A, 2003: Global synthesis of leaf area index observations: implications for ecological and remote sensing studies. *Global Ecology & Biogeography*, *12(3)*, pp. 191-205.

[5] GONG P., PU R., BIGING G.S. AND LARRIEU M.R, 2003: Estimation of forest leaf area index using vegetation indices derived from Hyperion Hyperspectral data. *IEEE Trans. on Geoscience and Remote Sensing*, *41(6)*, pp. 1355-1362

[6] CHEN X., VIERLINGA L., ROWELLA E. AND DE FELICE T., 2004: Using lidar and effective LAI data to evaluate IKONOS and Landsat 7 ETM+ vegetation cover estimates in a ponderosa pine forest. *Remote Sens. of Environ, 91*, pp. 14–26.

[7] EKLUNDH L., HARRIEB L. AND KUUSK A., 2001: Investigating relationships between Landsat ETM+ sensor data and leaf area index in a boreal conifer forest. *Remote Sens. of Environ*, *78*, pp. 239-251.

[8] BROWN L., CHEN J.M., LEBLANC S.G.E. AND CIHLAR J., 2000: A Shortwave Infrared Modification to the Simple Ratio for LAI Retrieval in Boreal Forests: An Image and Model Analysis. *Remote Sens. of Environ*., *71*, pp. 16–25.

[9] FASSNACHT K.S., GOWER S.T., MACKENZIE M.D., NORDHEIM E.V. AND LILLESAND T.M., 1997: Estimating the Leaf area Index of North Cantral Wiscounsin Forests using the Landsat Thematic Mapper. *Remote Sens. of Environ*, *61*, pp. 229-245.

[10] WELLES JON M. AND NORMAN J.M., 1991: Instrument for indirect measurement of canopy architecture. *Agronomy Journal*, *83*, pp. 818-825.

[11] CUTINI A., MATTEUCCI G. AND SCARASCIA MUGNOZZA G., 1998: Estimation of leaf area index with the Li-Cor LAI 2000 in deciduous forests. *For. Ecol. Manag*., *105*, pp. 55-65.

[12] VERMOTE E.F., TAN D., DEUZ J.L., HERMAN M. AND MORCRETTE J.-J., 1997: Second Simulation of the Satellite Signal in the Solar Spectrum, 6s: An Overview. *IEEE Trans. on Geoscience and Remote Sensing*., *35(3)*, pp. 675-686.

[13] LIANG S., 2004: Quantitative Remote Sensing, pp. 449-453, John Wiley & Son Inc., Hoboken, New Jersey.

[14] BROGE N.H. AND LEBLANC E., 2000: Comparing prediction power and stability of broadband and hyperspectral vegetation indices for estimation of green leaf area index and canopy chlorophyll density. *Remote Sens. of Environment*, *76*, pp. 156-172.

[15] ANDERSON M.C., NEALE C.M.U., LI F., NORMAN J.M., KUSTAS W.P., JAYANTHI H..J. AND CHAVEZ, 2004: Upscaling ground observations of vegetation water content, canopy height, and leaf area index during SMEX02 using aircraft and Landsat imagery. *Remote Sens. of Environment*, *92*, pp. 447-464.

Potential of long time series of FAPAR products for assessing and monitoring land surfaces changes.

N. Gobron[a], M.M. Verstraete[a], B. Pinty[a], O. Aussedat[a] and M. Taberner[a].

[a] Institute for Environment and Sustainability (IES) of EC-JRC, via E. Fermi, 1, TP 440, I-21020 Ispra (VA), Italy

[b] email: nadine.gobron@jrc.it

ABSTRACT

Earth observation systems have been shown to be high-quality tools to review the state of terrestrial surfaces at the global scale over last decades. In the special context of monitoring land degradation and desertification, long time series of remote sensing products are needed to evaluate the changes in terrestrial surfaces. For example, the vegetation photosynthesis activities on terrestrial environments can be documented from spectral measurements made in space. Advances in the understanding of radiation transfer and the availability of high performance instruments have led to the development of a new generation of geophysical products providing reliable, accurate information on the state and evolution of terrestrial environments. Specifically, a series of optimized algorithms have been developed to estimate the Fraction of Absorbed Photosynthetically Active Radiation (FAPAR) for a suite of recent instruments. Such an approach allows the synergistic use of FAPAR products derived from different sensors and the construction of FAPAR time series independent from the life time of these specific sensors. This paper summarizes the methodology and performance of the FAPAR algorithm and presents various examples of applications showing an analysis of seasonal cycle and maps of vegetation activity anomalies.

Keywords: FAPAR, vegetation activity, remote sensing, seasonal cycle

1 INTRODUCTION

The United Nations (UN) Conference on Desertification (UNCOD) in Nairobi in 1977 was held in part as a response to the severe environmental degradation that affected the Sudano-Sahelian region, itself the combined result of a prolonged drought and of extensive overexploitation of that fragile environment throughout the sixties. These events have been largely reported upon in the media [1]. This conference adopted a 'Plan of Action to Combat Desertification (PACD)', which was intended to propose a comprehensive set of practices to reduce the impact of the incriminating processes and even reverse the degradation by rehabilitating affected lands. Lack of progress along these lines led the UN Conference on Environment and Development (UNCED), held in Rio de Janeiro in 1992, to recommend a renewed interest in and international commitment towards this issue. This initiative materialized in the form of a Convention to Combat Desertification, which entered into force in 1996. The true scope and extent of desertification worldwide has been criticized (e.g., [2]) in the face of repeated claims of progressive and persistent devastation. Nevertheless, even using a somewhat restrictive definition of the process, various European countries suffer from its consequences. The regions concerned are essentially located along the Mediterranean basin, with Spain the most severely affected. Extensive studies, both at the national and European level, have documented the severity and extent of the impact of these processes on the environment and the economy (like the Mediterranean Desertification and Land Use (MEDALUS [3]) project financed by DG-Research) at least at local and regional (sub-national) scales.

Detecting and monitoring the causes and the consequences of the relevant degradation processes remains an overarching goal in all projects dealing with land degradation and desertification as well as any attempt to address the problem. The diverse environmental degradation processes labeled today as 'desertification' have long been experienced throughout the history of humanity and known under a variety of names, including drought, overgrazing, wind and water erosion, salinization (e.g., [1] 4, 5]). In fact, significant efforts have been expended for long periods of time on the definition and generation of desertification indicators, based on field or remote observations (e.g., [6], [7]), as reliable information on the causes and consequences of these processes is deemed essential to mount a rational plan to address the problem as well as to establish the effectiveness of measures and actions undertaken. Space-based remote sensing approaches have long been suggested as suitable solutions to the practical problem of repetitively surveying very large and often remote areas. In this context, the presence and productivity of vegetation plays a critical role, because (1) a vigorous plant cover constitutes a common indicator of

environmental health, (2) its removal or destruction (e.g., by grazing or through the extraction of fuel wood) constitutes a critical precursor for soil erosion by wind and water, and (3) the primary productivity of the vegetation essentially determines the carrying capacity of the land as far as sustainable cattle and human densities are concerned. For these reasons, it is very useful to monitor the actual productivity of the plant cover in space and time. Clearly, the relevance and accuracy of the derived information critically hinges on the performance and reliability of the algorithms used to extract this information from the raw observations (e.g., [7]).

Earth observation systems have been demonstrated to be high-quality tools to review the state of terrestrial surfaces at the global scale since last decades [8]. In the special context of monitoring land degradation and desertification, long time series of remote sensing products are needed to evaluate the changes in terrestrial surfaces. The time scale for studying modifications of landscapes may be longer than the sensor lifetime itself; and therefore the continuity with and synergy between various sensor-derived products are mandatory. Biophysical indicators resulting from different instruments have in this sense a particular interest compared to other proxy, *i.e.* an empirical spectral vegetation index, which depend on the observations conditions, like the spectral characteristics of measurements, the state of atmospheric conditions or the illumination and viewing geometries. To produce a long time series of relevant products, a series of optimized algorithms have been developed to estimate the Fraction of Absorbed Photosynthetically Active Radiation (FAPAR) for various optical instruments [9]. This biophysical indicator has been chosen because it reveals the level of vegetation photosynthesis activity which betrays the amount, state and health of vegetation canopies. This value is derived from the closure of energy balance inside the canopy itself and corresponds to the normalized radiant flux in the Photosynthetic Active Radiation (PAR) region of the solar domain. The concept underpinning these algorithms for deriving optimized vegetation biophysical indicators was proposed by [10] and then applied to multiple sensors including, amongst others, the Medium Resolution Imaging Spectrometer (MERIS) [11] 12] and the Sea-viewing Wide Field-of-view Sensor (SeaWiFS) [13]. Such an approach allows the synergistic use of FAPAR products derived from different sensors and the construction of FAPAR time series much longer than the typical life time of individual sensors. The MERIS FAPAR products have been derived operationally since the launch of the Envisat platform in March 2002 (see, for example, http://envisat.esa.int/). The SeaWiFS FAPAR products are generated at the JRC thanks to a dedicated processing system that was developed to deliver daily, 10-day and monthly composite products at a global scale with spatial resolutions ranging from about 2 km up to 0.5 degrees [14]. Six years of SeaWiFS FAPAR products are available from September 1997 (beginning of the mission) to December 2004. Such a multi-annual global time series is quite suitable for conducting investigations aimed at assessing the performance of this category of FAPAR products over several geographical regions for monitoring land degradation and desertification [16].

The following section summarizes the methodology of optimizing the FAPAR algorithm and evaluates the performances of FAPAR product processed at the European Commission (EC) Joint Research Center (JRC) using 6 years of SeaWiFS data through a comparison with ground estimations over two semi-arid vegetation types. We will then analyze time series of FAPAR over Spain and France through anomalies and seasonal cycle to illustrate and demonstrate the potential of geophysical products in monitoring the land degradation and desertification.

2 JRC-FAPAR PRODUCTS

The generic JRC algorithm aims to derive biophysical indicator from spectral space data, without any *a priori* knowledge on the land cover, to assess the state and health of vegetation surfaces. The products are derived using a physically-based algorithm which has been developed for various optical sensors. This section summarizes the methodology which has been used to derive the FAPAR values from various optical sensor data and describes the JRC-FAPAR products.

Our FAPAR algorithm can be adapted to any sensor acquiring at least three spectral bands in the blue, red and near-infrared regions of the solar spectrum. This algorithm capitalizes on the physics of remote sensing measurements and its development copes with the many operational constraints associated with the systematic processing and analysis of a large amount of data. Basically, the useful information on the presence and state of vegetation is derived from the red and the near-infrared spectral band measurements. The information contained in the blue spectral band, which is very sensitive to aerosol load, is ingested to account for atmospheric effects on these measurements. Our original approach thus consists in analyzing the relationships between measurements in the blue spectral band and those available in the red and near-infrared regions [11]]. Such relationships can indeed be simulated for a variety of environmental conditions with radiation transfer models of the coupled vegetation-atmosphere system. The former are then exploited with polynomial expressions optimized in such a way that top of atmosphere Bidirectional Reflectance Factor (BRF) measurements in the blue are related to those taken at other spectral bands, located at longer wavelengths e.g., in the red and near-infrared regions. This approach aims at decontaminating the BRF from atmospheric effects without performing an explicit retrieval of the ambient

atmospheric properties. The polynomial expressions are also built to simultaneously account for the bulk of the anisotropy effects. The latter are themselves approximated from an extensive set of radiation transfer simulations of the coupled surface-atmosphere system designed to mimick typical vegetation canopy conditions [9]. This same training data set is then used to relate the radiative measurements from each typical vegetation canopy condition to their corresponding FAPAR values. In practice, the generic FAPAR algorithm thus implements a two-step procedure where the spectral BRFs measured in the red and near-infrared bands are, first, rectified in order to ensure their optimal decontamination from atmospheric and angular effects and, second, combined together to estimate at best the instantaneous FAPAR value at the time of acquisition. The most recent versions of the appropriate formulae and coefficients derived from the mathematical optimization are given in [17] for SeaWiFS and [18] for MERIS, respectively.

The SeaWiFS FAPAR products are generated at the JRC thanks to a dedicated processing system that was developed to deliver daily, 10-day and monthly composite products at a global scale with spatial resolutions ranging from about 2 km up to 0.5 degrees [19]. A time composite algorithm of [20] has been applied on the sequence of daily FAPAR products to provide representative values of each time period. Over these selected pixels, time composite algorithms can be applied to eliminate outliers and to limit the impact of uncertainties inherent to the algorithm (e.g. remaining biases due to changing Sun and view geometries and/or un-foreseen atmospheric conditions), intermittent presence of sub-pixel clouds, or any other undesired events such as occasional water or snow during the composite period.

3 PERFORMANCE

The validation of geophysical products, such as FAPAR, derived from remote sensing data is required to evaluate whether the quality of these products is in conformity with the needs of the users and intended applications. Space agencies have therefore developed their own calibration and validation projects on both atmospheric and land surfaces products (see, for example, http://envisat.esa.int/, http://www-misr.jpl.nasa.gov/mission/valid.html and http://landval.gsfc.nasa.gov/MODIS/ among others). In the specific cases of the MOderate Resolution Imaging Spectroradiometer (MODIS) and the Multi-angle Imaging SpectroRadiometer (MISR) sensors operating on board the Terra platform, significant efforts are devoted to the validation of surface products such as the Leaf Area Index (LAI) and FAPAR generated from data acquired by these sensors [21]22, 23]. The science strategy adopted for designing the MODIS and MISR LAI/FAPAR algorithms is such that the LAI product values need to be carefully evaluated since its determination impacts results of the FAPAR algorithm itself [24]. Both LAI (a state variable of the radiation transfer problem) and FAPAR (a normalized radiant flux in the visible region of the solar domain) products correspond to physical quantities that can be measured in the field with different and significant levels of difficulties. Some of the issues associated with the generation of accurate ground-based estimations of FAPAR are addressed in [15].

The verification of the products is made with two examples (Figure 1) which show the time series of the SeaWiFS FAPAR products together with the ground-based estimations available from two experimental sites namely, Dahra North [15° 24' N; 15°26' W] in Senegal and SEVI [34° 2' N; 106° 42' W] in US. The vegetation

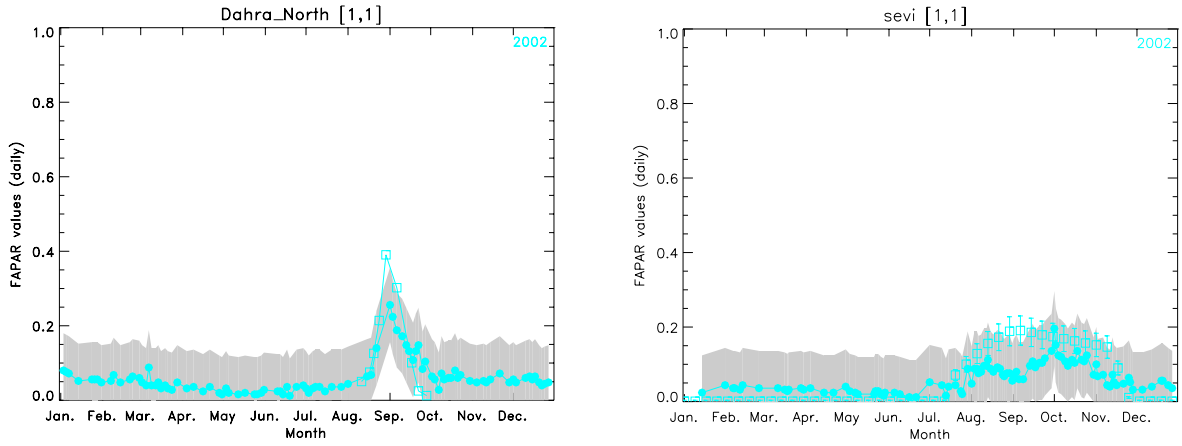

Figure 1. Comparisons of ground-based FAPAR estimations profiles (empty square symbols) and instantaneous daily SeaWiFS FAPAR JRC-products (full circle symbols) over the sites of Dahra **[25]** and SEVI **[26] [15]**. The zone shaded in grey delineates the 0.1 uncertainty range around the FAPAR JRC-products. The vertical bars indicate the uncertainty range around the ground-based estimations.

types covering these sites are made of semi-arid grass savannah (Dahra) and desert grassland (SEVI) (see, [25] 26, 15]). The baseline FAPAR value for these two sites is close to zero and the signature of the different vegetation phenological cycles (both for the growing and decaying periods) are remarkably well identified by both remote sensing and ground-based estimations. Moreover, the amplitudes, both maxima and minima, are in very good agreement with each other.

4 APPLICATION

According to a report published by the European Environmental Agency (EEA) [28], Spain and Portugal seems to be affected by climatic change in the European Union. The average temperatures in Europe have increased approximately 1º more than the average in the rest of the world, and that global warming in Spain and Portugal has been even higher. The report warns of increased drought in southern Spain, more forest fires, wide-spread heat waves and further risks for human health due to the heat.

The impacts of drought on the state and health of land surfaces are illustrated on Figure 2 which exhibits first the maps of anomalies between the monthly FAPAR products for April 1999 (August 2003) and the 6-year average from 1998-2003 over Spain and Portugal (France) (left panels). The regional patterns is clearly visible, with deficits (excesses) in FAPAR values represented in warm (cold) colors, while areas experiencing usual conditions are shown in grey. The right chart of Figure 2 illustrates secondly the seasonal cycle of monthly value of FAPAR spatially averaged over Spain and France for 1999 and 2003. We can notice the level of differences between 1999 and 2003 were less important at the national scale than locally. Spain suffers much more at the beginning of 1999 and France in summer 2003, as was shown in [27].

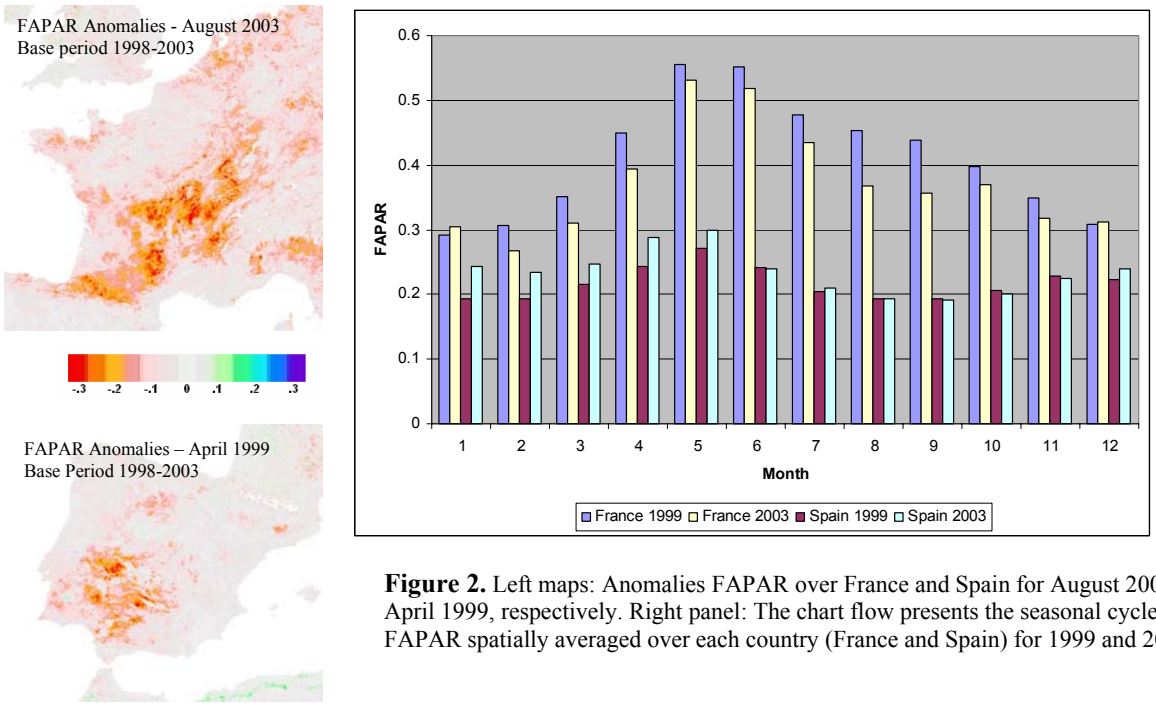

Figure 2. Left maps: Anomalies FAPAR over France and Spain for August 2003 and April 1999, respectively. Right panel: The chart flow presents the seasonal cycle of FAPAR spatially averaged over each country (France and Spain) for 1999 and 2003.

Figure 3 illustrates the impacts on a fire event that occurred in August 2000 in Spain. The Corinne Land Cover map over northern Spain was derived using data acquired in 2000 and published in [29]. The seasonal cycle of FAPAR has been extracted over one of the burned areas (indicated by the arrow) and the values plotted as function of the month from 1998 to 2004. The 2000 profile is colored in green and it can be seen that the vegetation photosynthesis activity decreases in August 2000. The level of FAPAR values following this fire event shows first that the vegetation photosynthesis activity never recovered the previous year level, which means that the land surface has been significantly affected. This example shows that this type of stress impacts can therefore be assessed by using long times series of biophysical indicators derived from space, as was also shown over France for the 2003 drought [27].

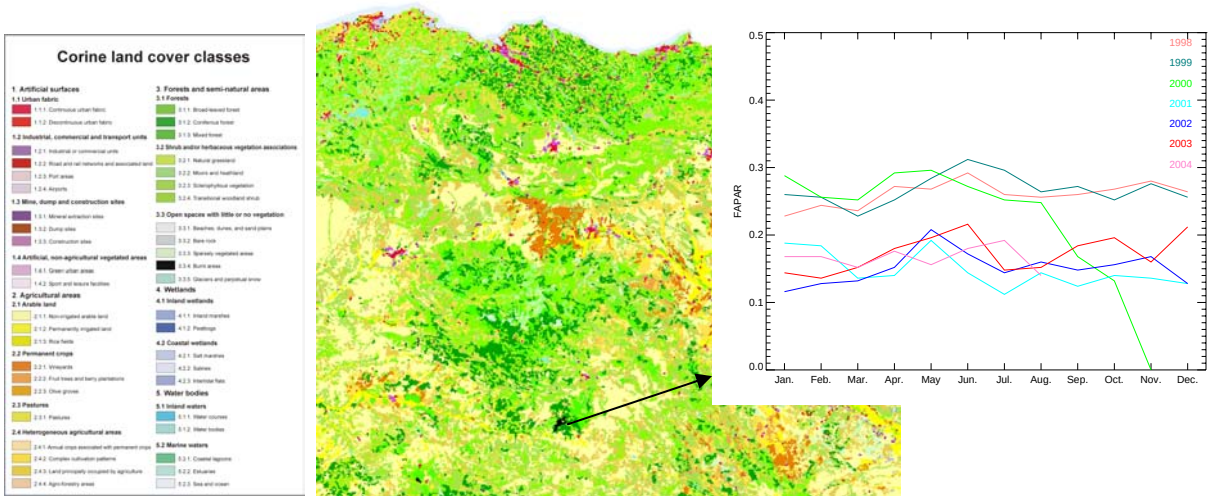

Figure 3. The Corinne Land Cover Map is illustrated over northern Spain (extracted from the original CLC - Source: http://terrestrial.eionet.eu.int/CLC2000). The seasonal cycle of monthly FAPAR products over the 'a burnt area' class is shown from January 98 to August 04. Each year is plotted with different color. (The FAPAR data come from the JRC-FAPAR product remapped at 2km in Lambert Azimuthal Equal Area projection.).

5 CONCLUSION

This paper summarized the methodology for deriving the FAPAR values from various optical sensors to develop a long time series of compatible products. Two results of validation have been shown through the direct comparison against ground-based estimations over semi-arid vegetation sites where field investigations have been carried out. We presented also the potential of using long time series of a biophysical indicator values derived from space, i.e., the SeaWiFS FAPAR JRC-products available from September 1997 up to year 2004, for assessing and monitoring the land change due to land degradation. The spatio-temporal patterns observable in FAPAR products were analyzed to assess the impact of the drought on plant productivity over Spain and France in both 1999 and 2003. This last example illustrated also the potential modification of land cover type by using the seasonal cycle of FAPAR from 1998 to 2004 and the CLC map 2000 after a fire event in August 2000.

ACKNOWLEDGMENTS

The authors are grateful to the SeaWiFS Project (Code 970.2) and the Distributed Active Archive Center (Code 902) at the Goddard Space Flight Center, Greenbelt, MD 20771, for the production and distribution of the SeaWiFS data, respectively. Frédéric Mélin kindly performed the processing of original SeaWiFS data and Monica Robustelli developed the JRC-FAPAR data base from which analyzes have been performed. An IDL and C version of the FAPAR algorithm can be requested from the first author by sending a message to nadine.gobron@jrc.it. The SeaWiFS FAPAR JRC-products are available at the following address: http://fapar.jrc.it/.

REFERENCES

[1] UNITED NATIONS CONFERENCE ON DESERTIFICATION (UNCOD), 1977: Desertification: Its Causes and Consequences, Compiled by the Secretariat of UNCOD, Pergamon Press.
[2] THOMAS, D. AND MIDDLETON, N., 1994: Desertification: Exploding the Myth, J. Wiley & Sons, Chichester.
[3] http://www.medalus.demon.co.uk/
[4] VERSTRAETE, M. M., 1983: Another look at the concept of desertification, In Wells, S. and Haragan, D. (eds.), Origin and Evolution of Deserts, University of New Mexico Press, pp. 213-228.
[5] VERSTRAETE, M. M., 1986: 'Defining desertification: A review'. *Climatic Change, 9*, pp. 5-18.
[6] REINING, P., 1978: Handbook of Desertification Indicators. *American Association for the Advancement of Science,* Washington DC, USA, pp. 141.
[7] PINTY, B., VERSTRAETE, M. M., IAQUINTA, J. AND GOBRON, N., 1996: Advanced modelling and inversion techniques for the quantitative characterization of desertification. In: Hill, J. and Peter, D. (eds.): The Use of remote

sensing for land degradation and desertification monitoring in the Mediterranean basin: State of the art and future research, EUR 16732 EN, pp. 79-93, DG-Science Research and Development, European Commission, Luxemburg.
[8] ESWARAN, H., LAL, R. AND REICH, P.F., 2001: Land degradation: an overview In: Bridges, E.M., Hannam, I.D., Oldeman, L.R., Pening de Vries, F.W.T., Scherr, S.J. and Sompatpanit, S. (eds.). Responses to Land Degradation. Proc. 2nd. International Conference on Land Degradation and Desertification, Khon Kaen, Thailand. Oxford Press, New Delhi, India.
[9] GOBRON, N., PINTY, B., VERSTRAETE, M.M, AND WIDLOWSKI, J.-L., 2000: Advanced Vegetation Indices Optimized for Up-Coming Sensors: Design, Performance, and Applications. *IEEE Transactions on Geoscience and Remote Sensing*, *38*, pp. 2489-2505.
[10] VERSTRAETE, M.M. AND PINTY, B., 1996: Designing Optimal Spectral Indices for Remote Sensing Applications. *IEEE Transactions on Geoscience and Remote Sensing*, *34*, pp. 1254-1265.
[11] GOVAERTS, Y., VERSTRAETE, M.M., PINTY, B. AND GOBRON, N., 1999: Designing Optimal Spectral Indices: A Feasibility and Proof of Concept Study. *International Journal of Remote Sensing*, *20*, pp. 1853-1873.
[12] GOBRON, N., PINTY, B., VERSTRAETE, M.M. AND GOVAERTS Y., 1999: The MERIS Global Vegetation Index (MGVI): Description and Preliminary Application. *International Journal of Remote Sensing*, *20*, pp. 1917-1927.
[13] GOBRON, N., MÉLIN, F., PINTY, B., VERSTRAETE, M.M., WIDLOWSKI, J.-L. AND BUCINI, G., 2001: A Global Vegetation Index for SeaWiFS: Design and Applications. In: Beniston M. and Verstraete M. M. (eds.)**:** Remote Sensing and Climate Modeling: Synergies and Limitations, pp. 5-21 Kluwer Academic, Dordrecht.
[14] MÉLIN, F., STEINICH, C., GOBRON, N., PINTY, B. AND VERSTRAETE, M.M., 2002: Optimal merging of LAC and GAC data from SeaWiFS. *International Journal of Remote Sensing*, *23*, pp. 801-807.
[15] GOBRON, N., PINTY, B., AUSSEDAT, O., CHEN, J., COHEN, W.B., FENSHOLT, R. , GOND, V., HUMMERICH, K.F., LAVERGNE, T., MÉLIN, F. , PRIVETTE, J.L,. SANDHOLT, I., TABERNER, M., TURNER, D.P., VERSTRAETE. M.M. AND WIDLOWSKI J.-L., 2005: Evaluation of FAPAR products for different canopy radiation transfer regimes: Methodology and results using JRC products derived from SeaWiFS against ground-based estimations. *Journal of Geophysical Research*, submitted.
[16] KNORR, W., GOBRON, N., SCHOLZE, M., KAMINSKI, T. AND PINTY, B., 2005: Global-Scale Drought Caused Atmospheric CO_2 Increase. *EOS, Transactions 86(18),* pp.178-181.
[17] GOBRON, N., PINTY, B., MÉLIN, F., TABERNER, M. AND VERSTRAETE, M.M., 2002: Sea Wide Field-of-View Sensor (SeaWiFS) - An Optimized FAPAR Algorithm - Theoretical Basis Document, *Institute for Environment and Sustainability*, EUR Report No. 20148 EN, 20 pp.
[18] GOBRON, N., MÉLIN, F., PINTY, B., TABERNER, M. AND VERSTRAETE, M.M., 2004: MERIS/ENVISAT biophysical land products: Validation and performance. *Advances in Space Research*, in print.
[19] MÉLIN, F., STEINICH, C., GOBRON, N. PINTY, B. AND VERSTRAETE, M.M., 2002: Optimal merging of LAC and GAC data from SeaWiFS. *International Journal of Remote Sensing*, *23*, 801-807.
[20] PINTY, B., GOBRON, N., MÉLIN, F. AND VERSTRAETE, M.M., 2002: A Time Composite Algorithm Theoretical Basis Document, *Institute for Environment and Sustainability*, EUR Report No. 20150 EN, 8 pp.
[21] HUEMMRICH, K.F., PRIVETTE, J.L., MUKELABAI, M., MYNENI, R.B., KNYAZIKHIN, Y., 2005: Time-Series Validation of MODIS land biophysical products in Kalahari woodland, Africa. *International Journal of Remote Sensing*, in press.
[22] WANG, Y., Tuan, Y., Hu, J., KNYAZIKHIN, Y. AND MYNENI, R.B., 2004: Evaluation of the MODIS LAI algorithm at a coniferous forest site in Finland, *Remote Sensing of Environment*, *91*, pp. 114-127.
[23] SHABANOV, N.V., WANG., Y., BUERMANN, W., DONG, J., HOFFMAN, S., SMITH G.R., TIAN, Y., KNYAZIKHIN, Y. AND MYNENI, R.B., 2003: The effect of foliage spatial heterogeneity in the MODIS LAI and FPAR algorithm over broadleaf forests. *Remote Sensing of Environment*, *85*, pp. 410-423.
[24] KNYAZIKHIN, Y., MARTONCHIK, J.V., MYNENI, R.B., DINER, D.J. AND RUNNING S.W., 1998: Synergistic algorithm for estimating vegetation canopy leaf area index and fraction of absorbed photosynthetically active radiation from MODIS and MISR data. *Journal of Geophysical Research, 103*, pp. 32,257-32,276.
[25] FENSHOLT, R., SANDHOLT, I. AND RASMUSSEN, M.S., 2004: Evaluation of MODIS LAI, fAPAR and the relation between fAPAR and NDVI in a semi-arid environment using in situ measurements. *Remote Sensing of Environment, 91*, pp. 490-507.
[26] TURNER, D.P., RITTS, W.D., COHEN, W.B., MAEIRSPERGER, T., GOWER, S.T., KIRSCHBAUM, A., RUNNING, S. W.,ZHAO, M., WOFSY, S., DUNN, A., LAW, B., CAMPBELL, J., OECHEL, W., KWON, H.J. ,MEYERS, T., SMALL, E., KURC, S. AND GAMON, J., 2005: Site-level Evaluation of Satellite-based Global Terrestrial Gross Primary Production and Net Primary Production monitoring. *Global Change Biology*, *11*, pp. 666-684.
[27] GOBRON, N., PINTY, B., MÉLIN, F., TABERNER, M., VERSTRAETE, M.M., BELWARD, A., LAVERGNE, T., WIDLOWSKI, J.-L., 2005: The state of vegetation in Europe following the 2003 drought. *International Journal of Remote Sensing Letters, 26(9)*, pp. 2013-2020.

[28] EUROPEAN ENVIRONMENT AGENCY, 2004: Impacts of Europe's changing climate, An indicator-based assessment, EEA Report No 2/2004.
[29] HTTP://TERRESTRIAL.EIONET.EU.INT/CLC2000

Retrieving Rangeland Vegetation Characteristics through Constrained Inverse Reflectance Modelling of Earth Observation Satellite Imagery

J. Hill[a], W. Mehl[b], A. Röder[a], S. Bärisch[a] and G. Tsiourlis[c]

[a] Remote Sensing Department, University of Trier, D-54286 Trier, Germany, email: hillj@uni-trier.de

[b] European Commission, Joint Research Centre, Institute for Environment and Sustainability (IES), I-21020 Ispra (Va), Italy

[c] Forest Research Institute, NAGREF, Thessaloniki, Greece

ABSTRACT

Rangelands still are an important component of agricultural production systems in the European Mediterranean. The primary task with regard to their sustained use is to find the sometimes delicate balance between their productivity and the corresponding stocking rates, about which substantial expert knowledge is available. However, given the land use change processes of the past decades, it is not sufficient to define average regional stocking rates. The access to rangelands often occurs with such a spatial diversification that environmental degradation might occur although average stocking rates are not exceeded. This not only affects the local carrying capacity, but might impose feedbacks on the hydrological functioning of headwater areas and downstream valleys. For supporting the required spatial management actions resource information in a true spatial diversification is needed. This paper explores options for deriving biophysical variables from earth observation satellite data. Inverse reflectance modelling of Landsat-ETM-data is constrained with fractional cover estimates obtained from very high spatial resolution Quickbird imagery, thereby increasing the possibilities to obtain realistic LAI estimates from open canopies.

Keywords: Rangeland ecology, biophysical parameters, LAI, inverse reflectance modelling

1 INTRODUCTION

As many other fields of vegetation science also rangeland ecology has a need for quantitative vegetation parameters for thoroughly estimating available resources and their change over time. This is not only an important prerequisite for understanding carbon dynamics within these ecosystems, but also assessing adequate stocking rates for sustainable grazing systems. Given the spatial extension of rangelands on one side and the limited human resources on the other, it becomes obvious that the acquisition of these parameters in their spatial diversity is a task that can be facilitated by extrapolating limited field data with support of additional means such as remote sensing. In particular against the background of ongoing degradation and desertification processes in many parts of the world [22], retrospective monitoring approaches which use available remote sensing archives have the potential to reveal important information on whether past management decisions have eventually triggered degradation processes. Standardised remote sensing data interpretation schemes are an important component of an efficient rangeland monitoring.

In the course of research projects[1] on land degradation processes in the European Mediterranean (DeMon-2, GeoRange) dedicated studies were carried out to assess rangeland resources over long time periods in comparison to changing socio-economic boundary conditions. DeMon-2 focussed on the mountainous ecosystem of Central Crete (Greece), a traditional grazing area which, during the past decades, experienced increasing pressure on natural resources through quite excessively expanding grazing activities. These were mainly triggered by an increasing demand in animal products (tourism), agricultural subsidies, and the construction of access roads after Greece joined the European Union in 1981. The GeoRange grazing site (Lagadas County) was located in Northern Greece, in the immediate neighbourhood of the rapidly expanding urban agglomeration of Thessaloniki. In this case the animal statistics did not reveal a substantial increase of stocking rates during the past decades, but the regional authorities nevertheless claimed that range resources had notably deteriorated and action should be taken.

[1] DeMon-2 and GeoRange are RTD projects supported by the DG Research of the European Commission.

Horizontal and vertical canopy densities, as measured by fractional cover and leaf area, represent important indicators which might be directly fed into sustainable range management concepts. Our retrospective monitoring approaches for both project sites were built on spectral mixture analysis (SMA) of atmospherically corrected Landsat imagery. The vegetation abundance estimates could be expected to provide improvements in comparison to empirical relations between proportional cover and various vegetation indices [e.g. 27], and the results in fact proved very useful to unveil the spatial diversity of degradation processes through this consistent indicator [8, 10, 11, 24]. However, besides that non-linear mixing has already some importance for the observation of low plants in arid environments [21], SMA-derived estimates [e.g. 5] only appear to be in good correspondence to ground-measured cover proportions as long as canopy height (i.e., volume) is not too variable. If canopy structure becomes highly variable, SMA-derived abundance estimates rather tend to represent a combination of proportional cover and canopy volume [21].

It is thus advisable to explore additional options for deriving information on the biophysical characteristics of rangelands which can be more directly interfaced with resource assessment and management concepts. Fang et al. [6] have advocated the use of vegetation indices, surface broadband albedo, leaf area index and the fraction of photosynthetically active radiation (FPAR) absorbed by the vegetation. Some of these appear to some extent redundant, but in particular leaf area index is an important state variable with direct relation to biomass as well as exchange of mass and energy. Leaf area is usually derived from empirical relationships to vegetation indices [e.g. 19]. The major disadvantages of these approaches emerge from the difficulty to apply predictive equations in areas where they were not established, or where the available data are not sufficiently standardised and calibrated. There is thus a preference to estimate LAI through the inversion of radiative transfer (RT) models, but the complicated structure of rangelands with their mixture of green and senescent canopy elements, woody components, litter and soil [e.g. 32, 1] impose quite substantial problems.

In this study we were particularly interested in mapping the proportional cover and the leaf area index of woody vegetation communities in Mediterranean rangelands of Northern Greece based on an inversion of the GeoSail reflectance model [12], where the specific objective focussed on combining late summer imagery of the Landsat ETM+ and Quickbird sensors. Although the advantages of reflectance models have been extensively discussed, the inversion of such models is frequently affected by the so-called “ill-posed problem”, i.e. various combinations of biophysical parameters (e.g., “proportional cover” and “leaf area index”) may generate similar or even identical reflectance signatures. In this study, the spectral ambiguity introduced from the combination of horizontal and vertical canopy densities was eliminated by constraining the GeoSail model (inverted on Landsat ETM+ data) with vegetation cover proportions derived from a simple analysis of the very high spatial resolution Quickbird imagery. The approach is justified because the rather expensive Quickbird data were also used for additional important objectives, such as counting and locating sheds for the purpose of modelling cost surfaces for assessing the impact of stocking rates. The results of this study will provide the baseline information to additionally assess palatable herbaceous biomass from corresponding spring/summer imagery.

2 THE STUDY AREA

The test area is characterized by a heterogeneous mosaic of a variety of ecosystems and land uses, which is typical for Mediterranean rangelands [4]. Surrounding the central Mygdonia valley with its two large freshwater lakes, agricultural areas are interwoven with rangelands, which are mainly used for livestock husbandry. Shrublands of varying density are dominating these rangelands, which can be subdivided into three distinctive units: dense (shrub/tree-fraction of 70-100 %), medium dense (shrub/tree-fraction of 40-70 %) and sparse (shrub/tree-fraction of 10-40 %), the latter forming a transition to grasslands. With its resistance to grazing due to its spiny small leaves, its resilience to fires and its competitiveness due to fast resprouting and coppicing abilities, the kermes oak (*Quercus coccifera*) is by far the dominant species. Also *Quercus ilex* is present in high percentages. They are accompanied by characteristic Mediterranean evergreen species such as *Pistacia lentiscus*, *Phillyrea media*, *Olea europaea var. sylvestris*, *Erica arborea*, constituting the association Oleo-Lentiscetum. In the higher altitudes of this zone (300-500 m asl) deciduous Mediterranean shrubs like *Spartium junceum* and *Crataegus monogyna* are also encountered [18]. Herbaceous species are numerous in this area, and the grasses consist of a high number of annual species together with some perennial grasses [20].

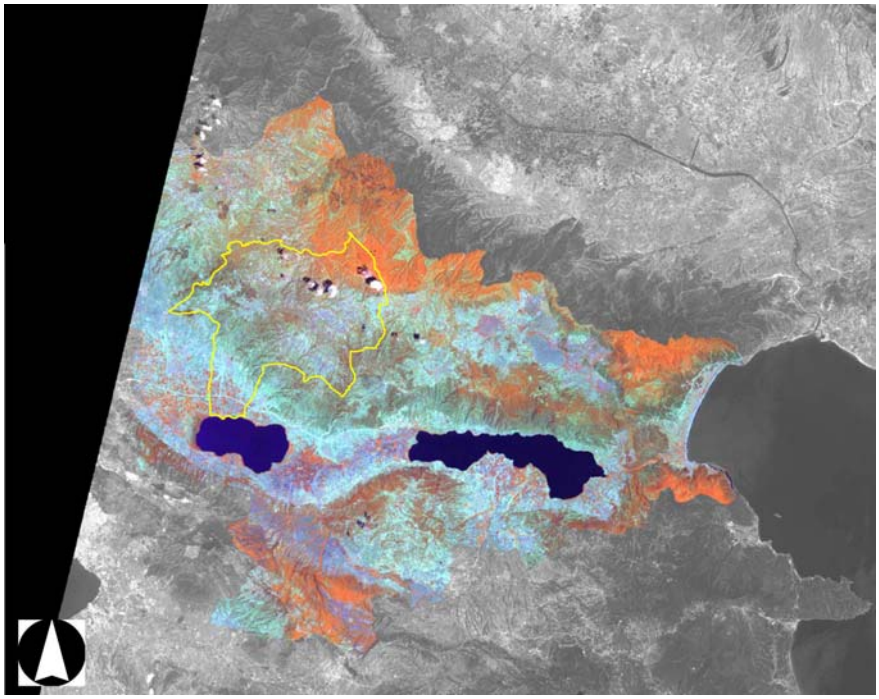

Figure 1. Subset showing Lagadas County (Greece) as depicted by Landsat-5 TM (RGB=TM bands 3, 4, 5). The rangelands extend south and north of the Mygdonia Valley with Lake Volvi (right) and Lake Kouronas (left). The core area mainly addressed in this study is outlined in yellow.

Climate of the area is typical Mediterranean, with precipitation ranging from about 400 mm at lower altitudes to 650 mm at the station of the locality Arnaia at 564 m elevation. Maximum rainfall is received in late spring and autumn, but total amount and distribution are modified by relief and elevation. In the rangeland areas, bedrock is largely dominated by metamorphic rocks, and gneiss as well as quartzite are abundant. Upon these, shallow soils in a rather low development stage can be found. As an exception, accumulation zones are characterized by fertile alluvial soils, which are frequently used for agricultural purposes.

Like in many Mediterranean countries, Greece becoming a member of the European Union in 1981 significantly affected rural activities, and resulted in widespread land abandonment in less accessible rural areas, especially in the higher zones. While in some regions numbers of grazing animals dramatically increased as a result of the European Common Agricultural Policy, the communities of the Lagadas area show a more stable behaviour. Nonetheless, grazing regimes have been reported to have strongly changed towards sedentary livestock keeping and intensification in concentrated areas. In particular, shepherding is now conceived as a daytime profession, with considerable implications for distribution of grazing livestock as opposed to traditional transhumance systems.

3 MATERIAL AND METHODS

A Landsat-5 TM scene acquired on the 24th of July, 2003, formed the basis for the model inversion. After orthorectification, the image was radiometrically corrected using a modified 5S radiative transfer code [28] with published sensor calibration factors [29, 30]. This code was extended to correct terrain-induced illumination variations [7] based on digital elevation data with adequate spatial resolution. In addition, a Quickbird multispectral (3x3m²) and panchromatic (0.64x0.64 m²) scene was acquired on 21st July 2003 and 13th August 2003. Both tiles were orthorectified to the Greek reference system incorporating the accompanying RPC files along with additional field-measured positions and the digital elevation data. After that, the tiles were radiometrically corrected analogous to the approach described before and mosaicked.

The Quickbird multispectral was then used to derive a precise estimate of the proportional cover by shrub and woodlands. This is quite a straightforward task due to the strong contrast between photosynthetic vegetation (shrubs, trees) and all background materials at this time of the year. Based on a simple vegetation index (i.e., NDVI) green woody vegetation cover could be separated from lower (dry) vegetation and non vegetated areas. The high spatial detail of the Quickbird imagery (also the panchromatic band was used for control) confirmed the high accuracy achieved by this approach. Subsequently, this binary image was degraded to the Landsat-TM 5 resolution by applying an appropriate sensor response model. The resulting image in Landsat-TM ground resolution could thus be considered to represent the percentage cover of dense woody vegetation for each 30x30m² pixel.

In order to characterise biochemical properties of typical shrubs found in the test area, leaves from a large number of *Quercus coccifera* shrubs were collected. For each of these, chlorophyll and leaf water content were measured in the laboratory. These were complemented by spectroradiometric measurements of leave stacks. Driving variables for using PROSPECT were derived from this sample by subjecting these leaf spectra to a numerical inversion of this leaf reflectance model (fig. 2).

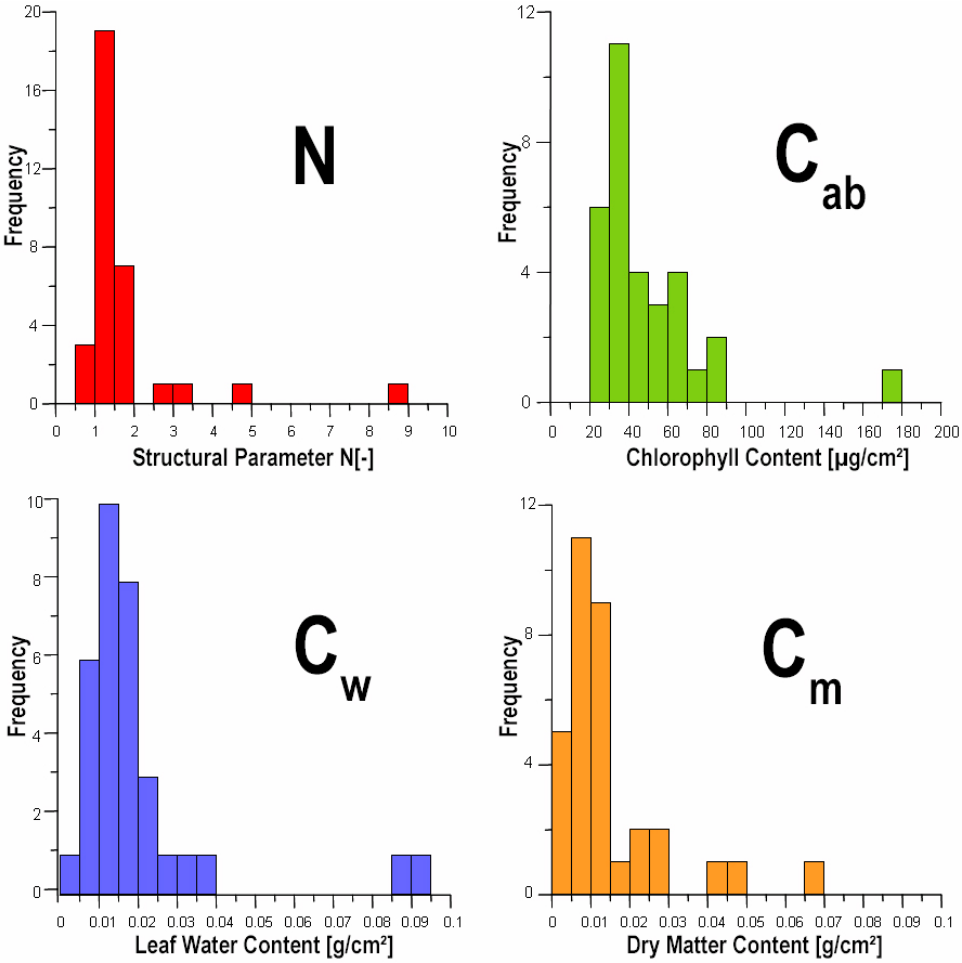

Figure 2. Histograms of the PROSPECT structure parameter N, Chlorophyll ab (Cab), leaf water (Cw) and dry matter content (Cm) as derived from the numerical inversion of PROSPECT for the leaf spectra from the Lagadas ground data collection. Apart from single outliers the retrieved values are well within the expected range for this type of woody vegetation.

LAI data within the study site were collected for 12 plots with varying canopy types, visually delimited on the panchromatic Quickbird image. The plots include a range from closed canopies to sparse woodlands with scattered shrubs, covering a range of LAI values from 1 to 4.5. This preliminary assessment was based on the application of allometric relations between LAI and structure variables which were derived from the analysis of destructive LAI-measurements executed earlier in the same type of vegetation community [23].

4. THE RADIATIVE TRANSFER MODELLING APPROACH

In case of heterogeneous canopies, such as they prevail in the Lagadas rangelands, it is mandatory to use geometrical models [e.g. 14], or hybrid approaches which couple the simulation of three-dimensional canopy elements with leaf and turbid media reflectance models. In this study we have used a modified version of the GeoSail model [12] which is based on the combination of a geometric model [16, 17, 14] to calculate the amount of shadowed and illuminated components in a scene, with an early version of the SAIL model [31] from which the reflectance and transmittance of canopy elements is obtained. Leaf optical properties are injected via the PROSPECT model of Jacquemoud and Baret [13]. The geometric part of GeoSail uses the model developed by Jasinski for the limiting case where the shadows cast by clumps of vegetation are very small relative to the size of the area observed [15, 16, 17]. Scene reflectance is determined in GeoSail by calculating an area-weighted average of three landscape components: illuminated canopy, illuminated background, and shadowed background. The model considers a scene made up of geometric solids scattered over a plane with a Poisson distribution; the solids are identical in size and shape and cast shadows on the background plane, but do not overshadow each other. Its simplicity is a result of the assumption that single values for the reflectance and transmittance of light by canopy clumps are enough to provide a reasonable overall description of scene reflectance and absorption.

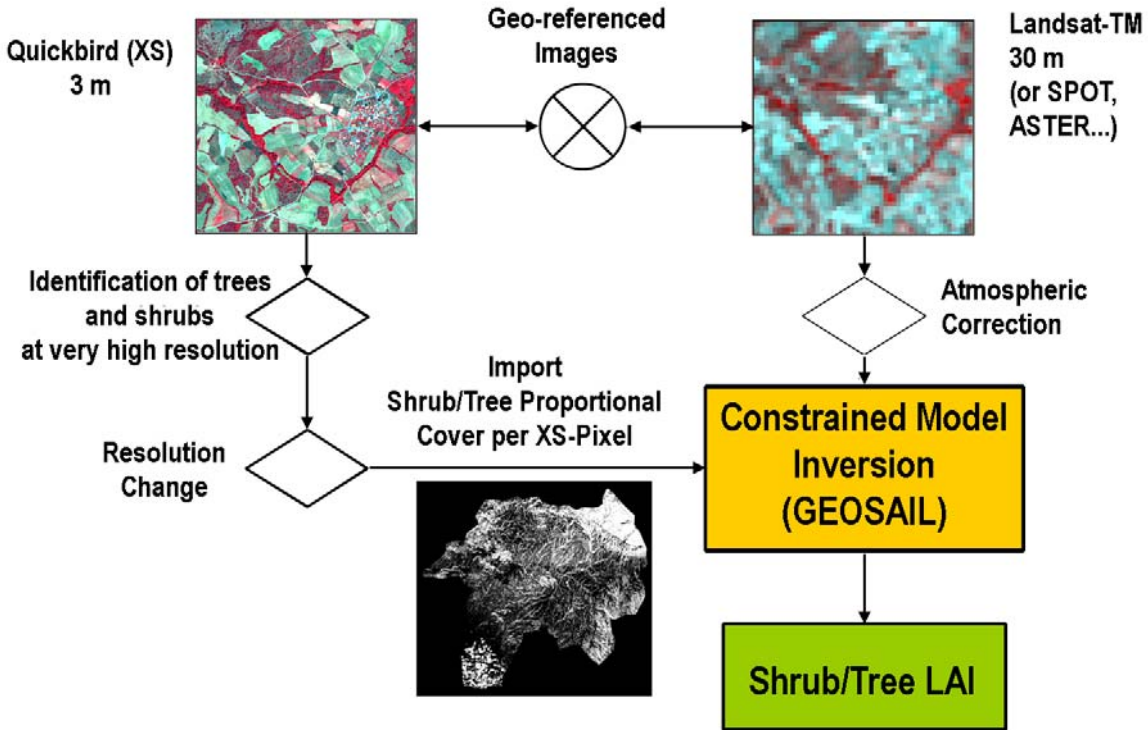

Figure 3. Processing flowchart for using canopy proportional cover estimates derived from very high spatial resolution imagery (Quickbird, resampled to 3 m pixel length) to constrain the GeoSail reflectance model inversion on atmospherically corrected Landsat-TM data.

The reflectance models were coupled in the following way: PROSPECT was parametrised according to the results from the ground data collection on leaf optical properties (section 3); the modelled leaf reflectance was then fed into SAIL to simulate the reflectance properties of turbid canopy components (trees and shrubs of *Quercus coccifera*) with LAI values ranging from 0 to 5 (in step of 0.25); leaf inclination was parametrised according to plagiophile canopy types. Finally, GeoSail was used to produce for each of these canopy spectra the reflectance associated to a suitable range of cover proportions (0 to 1, in steps of 0.05). The shape of the canopy elements was considered to be best approximated as a cylinder with a base/height ratio of 1.5 (i.e., slightly broader than high). To calculate the scene reflectance the GeoSail model weighs the reflectance of each component by its fractional area. The illuminated background reflectance is the same background reflectance used in the SAIL model, the shadow reflectance is the product of the transmittance through the canopy, calculated by the SAIL model, and the background reflectance. This formulation of scene reflectance allows for multiple scattering within tree canopies but assumes no multiple scattering between trees [12]. With regard to the dominant abundance of dry grass at the time of image acquisition, the background and inter-space reflectance was not represented by soil spectra but a typical dry vegetation spectrum available from previous field measurement campaigns with an ASD FieldSpec II instrument. The simulated spectral data base thus includes 400 simulated reflectance spectra at TM resolution.

In order to reduce the ambiguity between the spectral response of canopies with high LAI and low coverage on one hand, and low to medium LAI in high cover situations on the other side, the retrieval of LAI values was constrained by the Quickbird-derived proportional cover estimates (figure 3). This implies that the model inversion for each Landsat pixel only had to consider the simulated LAI-range for the known canopy cover proportion at this position.

5 RESULTS AND DISCUSSION

Figure 3 shows the result obtained from inverting the model on the basis of the Landsat-TM 5 scene acquired 24th July, 2003.

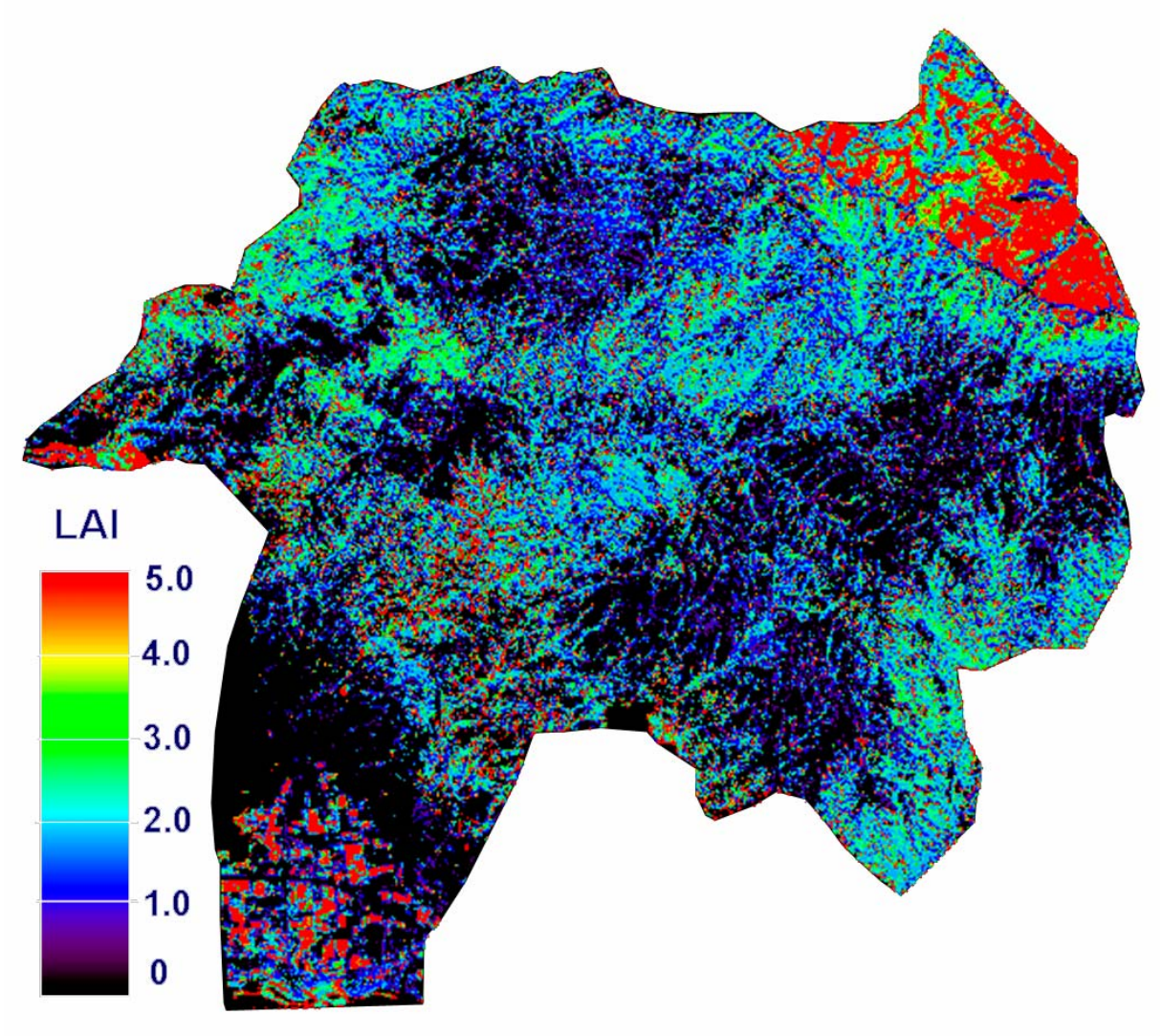

Figure 4. LAI map derived from the constrained inversion of the GeoSail reflectance model.

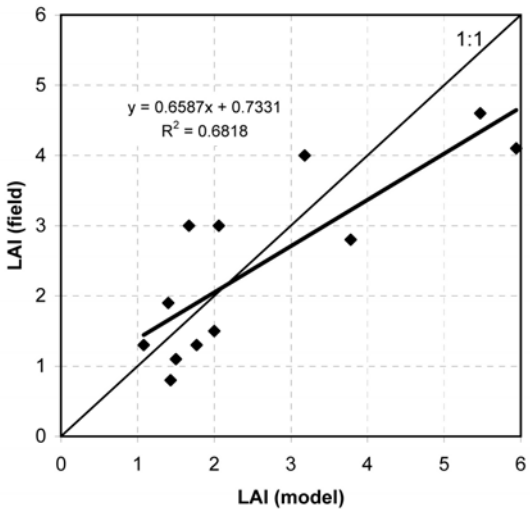

Figure 5. Modelled vs. field-based LAI estimates (further explanation in the text).

The patches with LAI values up to 5, located in the South, relate to the areas used for intensive agriculture in the valley of Mygdonia. Moving north, the heterogeneous pattern of shrublands interwoven with grasslands appears well resolved. In particular, the linear structures showing moderate to high LAI estimates are in accordance with Röder et al. [25]. In the Northeast, the transition zone from dense shrublands to forests is evident. Preliminary validation of the results was based on the field based characterisation of homogenous plots (figure 5).

The estimates derived from model inversion reproduce the LAI range characterised in field using the approach described before, and there is a linear relation with moderate r^2 between the two. However, it must be noted that results are most accurate at rather low LAI ranges, while deviations increase with increasing LAI. Most importantly, the model seems to over-estimate the high LAI range, with values above 5 corresponding to field-based estimates of 4 to 4.5. These preliminary

results underline the validity of the adopted approach and show that the constrained model approach, incorporating different sensors and types of information, works reasonably well in this rather complex, heterogeneous rangeland environment.

The deviations in figure 4 are generally attributed to two complexes. The first relates to model uncertainties, resulting from the presence of different types of woody plants and varying canopy architectures, from approximating the background contribution using a dry vegetation spectrum exclusively, and from fixing some model input parameters with standard parameters obtained from laboratory analyses. On the other hand, a degree of ambiguity is also associated with characterising LAI in field in dependence of biomass estimations. In this respect, forthcoming efforts focus on procuring a calibration function between optical LAI measurements (LI-COR 2000 Plant Canopy Analyzer) and LAI derived from destructive measurements. This will enable the procurement of more accurate and extensive calibration and validation data sets. In addition, the potential of founding the model inversion on the spectral information provided by the Quickbird multispectral image, as the significantly higher spatial resolution is suited to overcome constraints arising from the large IFOV of the Landsat-TM image.

Concluding, the present study shows that constraining the inversion of the GeoSail reflectance model with proportional cover values derived from very high spatial resolution imagery provides LAI estimates which favourably compare to the ground data so far available. This supports the idea of using earth observation systems which include sensors with different spatial and spectral resolution for assessing the state of fragile ecosystems [e.g. 2, 3]. Additional field data are expected to increase our understanding of benefits and limitations of the proposed approach.

ACKNOWLEDGEMENT

The project GeoRange - Geomatics in the Assessment and Sustainable Management of Mediterranean Rangelands - was funded by the European Union, DG Research, within the programme for research, technology development and demonstration adopted by the European Union in the 5th Framework Programme under contract EVK2-CT-2000-00091. This support is gratefully acknowledged.

REFERENCES:

[1] ASNER, G.P. AND HEIDEBRECHT, K. B., 2002: Spectral unmixing of vegetation, soil and dry carbon cover in arid regions: comparing multispectral and hyperspectral observations, International Journal of Remote Sensing, 23, pp. 3939-3958.

[2] BOER, M. AND PUIGDEFABREGAS, J., 2005: Assessment of dryland condition using spatial anomalies of vegetation index values. International Journal of Remote Sensing 26 (18), pp. 4045-4065.

[3] BOER, M., 1999: Assessment of dryland degradation: linking theory and practice through site water balance modelling. Nederlandse Geografische Studies, 251, Utrecht.

[4] DI CASTRI, F., 1981: Mediterranean type shrublands of the world. IN DI CASTRI, F., GOODALL, D.W. AND SPECHT, R.L. (EDS.): Mediterranean-type shrublands, ecosystems of the world, 11, pp. 1-42. Amsterdam, Oxford, New York: Elsevier

[5] ELMORE, A.J., MUSTARD, J.F., MANNING, S.J. AND LOBELL, D.L., 2000: Quantifying vegetation change in semiarid environments: precision and accuracy of spectral mixture analysis and the normalised vegetation index, Remote Sensing of Environment, 73, pp. 87-102.

[6] FANG, H., LIANG, S., MCCLARAN, M.P., VAN LEEUWEN, W.J.D., DRAKE, S., MARSH, S.E., THOMSON, A.M., IZAURRALDE, R.C. AND ROSENBERG, N.J., 2005: Biophysical characterization and management effects on semiarid rangeland observed from Landsat ETM+ data. IEEE Transactions on Geoscience and Remote Sensing 43 (1), pp. 125-134.

[7] HILL, J., MEHL, W., AND RADELOFF, V., 1995: Improved forest mapping by combining corrections of atmospheric and topographic effects. IN ASKNE, J. (ED.): Sensors and environmental applications of remote sensing, pp. 143-151. Proceedings of the 14th EARSeL Symposium, Göteborg, Sweden, 6-8 June 1994. Rotterdam, Brookfield: A.A. Balkema.

[8] HILL, J., HOSTERT, P., TSIOURLIS, G., KASAPIDIS, P., UDELHOVEN, T., AND DIEMER, C., 1998: Monitoring 20 Years of increased grazing impact on the Greek island of Crete with earth observation satellites. Journal of Arid Environment 39, pp. 165-178

[9] HILL, J., HOSTERT, P. AND RÖDER, A., 2003: Observation and long-term monitoring of Mediterranean ecosystems with satellite remote sensing and GIS. Management of Environmental Quality 14 (1), pp. 51-68.

[10] HOSTERT, P., RÖDER, A., HILL, J., UDELHOVEN, T. AND TSIOURLIS, G., 2003, Retrospective studies of grazing-induced land degradation: a case study in central Crete, Greece. International Journal of Remote Sensing 24, 20, pp. 4019-4034.
[11] HOSTERT, P., RÖDER, A. AND HILL, J., 2003: Coupling spectral unmixing and trend analysis for monitoring of long-term vegetation dynamics in Mediterranean rangelands. Remote Sensing of Environment 87, pp. 183-197.
[12] HUEMMRICH, K.F., 2001: The GeoSAIL model: a simple addition to the SAIL model to describe discontinuous canopy reflectance, Remote Sensing of Environment 75 (3), pp. 423-431.
[13] JACQUEMOUD, S, AND F. BARET, 1990: PROSPECT: a model of leaf optical properties spectra, Remote Sensing of Environment 34, pp. 75-91.
[14] JASINSKI, M. F., 1996: Estimation of subpixel vegetation density of natural regions using satellite multispectral imagery, IEEE Trans. Geoscience and Remote Sensing 34 (3), pp. 804-813.
[15] JASINSKI, M.F., 1994: Sensitivity of the normalised difference vegetation index to subpixel canopy cover, soil albedo, and pixel scale, Remote Sensing of Environment 32, pp. 169-187.
[16] JASINSKI, M.F. AND EAGLESON, P.S., 1989: The structure of red-infrared scattergrams of semivegetated landscapes. IEEE Transactions on Geoscience and Remote Sensing 27 (4), pp. 441-451.
[17] JASINSKI, M.F. AND EAGLESON, P.S., 1990: Estimation of subpixel vegetation cover using red-infrared scattergrams, IEEE Trans. Geoscience and Remote Sensing 28 (2), pp. 253-267.
[18] KONSTANTINIDIS, P. AND TSIOURLIS, G., 2003: Description – analysis and mapping of vegetation units (habitats) of Lagadas County (Thessaloniki, Greece). NAGREF – Forest Research Institute, GeoRange project
[19] LACAZE, B., 2005: Remotely-sensed optical and thermal indicators of land degradation, In: Oluic, M. (Ed.): Proc. 24th Symp. EARSeL, Dubrivnik, Croatia, 25-27 May 2004, Millpress: Rotterdam, pp. 211-217.
[20] LIENAU, C., 1989: Griechenland: Geographie eines Staates der europäischen Südperipherie. Wissenschaftliche Länderkunden Band 32. Darmstadt: Wissenschaftliche Buchgesellschaft Darmstadt
[21] RAY, T.W. AND MURRAY, B.C., 1996: Nonlinear spectral mixing in desert vegetation, Remote Sensing of Environment 55, pp. 59-64.
[22] REYNOLDS, J.F. AND STAFFORD-SMITH, M.D., 2002: Global desertification. Do humans cause deserts? Dahlem workshop report 88. Berlin: Dahlem University Press
[23] RÖDER, A., HOSTERT, P., TSIOURLIS, G., KASAPIDIS, P. AND HILL, J., 2001: Resource Assessment to Support the Sustainable Management of Mediterranean Ecosystems. An Approach Integrating Remote Sensing and Ecology. In BELWARD, A., BINAGHI, E., BRIVIO, PA, LANZARONE, GA AND TOSI, G. (EDS.): Proc. Int. Workshop Geo-Spatial Knowledge Processing for Natural Resource Management, 28th-29th June 2001, Varese, Italy, pp. 303-309.
[24] RÖDER, A., 2005: A remote sensing based framework for monitoring and assessing Mediterranean rangelands. PhD Thesis, University of Trier, Germany
[25] RÖDER, A.; KUEMMERLE, T., HILL, J., DEL BARRIO, G., TSIOURLIS, G. AND PAPANASTASIS, V., 2006: Assessing rangeland degradation in heterogeneous Mediterranean environments. A case study in the County of Lagadas/Greece. In: RÖDER, A. AND HILL, J. (EDS.): Proceedings of the 1st International Conference on Remote Sensing and Geoinformation Processing in the Assessment and Monitoring of Land Degradation and Desertification (RGLDD), Trier, 7.-9. Sept, 2005. CD-Rom publication (this issue).
[26] ROSEMA, A., VERHOEF, W., NOORBERGEN, H. AND BORGESIUS, J. J., 1992: A new forest light interaction model in support of forest monitoring. Remote Sensing of Environment, 42, pp. 32-41.
[27] SMITH, M.O., USTIN, S.L., ADAMS, J.B. AND GILLESPIE, A.R., 1990: Vegetation in deserts: I. A regional measure of abundance from multispectral images. Remote Sensing of Environment 31, pp. 1-26.
[28] TANRÉ, D., DEROO, C., DUHAUT, P., HERMAN, J.J., PERBOS, J., AND DESCHAMPS, P.Y., 1990: Description of a computer code to simulate the signal in the solar spectrum – the 5S code. International Journal of Remote Sensing 11(4), pp. 659-668.
[29] THOME, K.J., 2001: Absolute radiometric calibration of Landsat 7 ETM+ using the reflectance-based method. Remote Sensing of Environment 78, pp. 27-38
[30] THOME, K.J., MARKHAM, B., BARKER, J., SLATER, P., AND BIGGAR, S., 1997: Radiometric calibration of Landsat. Photogrammetric Engineering & Remote Sensing 63(7), pp. 853-858.
[31] VERHOEF, W., 1984: Light scattering by leaf layers with application to canopy reflectance modelling: the SAIL model. Remote Sensing of Environment 16, pp. 125-141.
[32] WHITE, M.A., ASNER, G.P., NEMANI, R.R., PRIVETTE, J.L. AND RUNNING, S.W. 2000: Measuring fractional cover and leaf area index in arid ecosystems. Digital camera, radiation transmittance, and laser altimetry methods. Remote Sensing of Environment 74, pp. 45-57.

The use of remote sensing for the assessment of soil inorganic carbon in the Judean Desert (Israel)

T. Jarmer[a], H. Lavée[b], P. Sarah[b] and J. Hill[a]

[a] Remote Sensing Department, University of Trier, D-54286 Trier, Germany,
email: jarmer@uni-trier.de
[b] Department of Geography, Bar-Ilan University, Ramat Gan, Israel

ABSTRACT

A method for spectral detection of carbonate content was generated based on statistical analysis. It allows the prediction of soil inorganic carbon content with a cross-validated r² above 0.95. The established model was then modified to allow its application to Landsat images. Since C.I.E. color coordinates were found to be well suitable parameters for predicting the inorganic carbon content of soils under laboratory conditions, the reflectance values of the Landsat-TM bands were transformed into C.I.E. color coordinates. Subsequently, the C.I.E. based model approach was adopted to a Landsat image with low vegetation cover from July 1998 to predict spatial distribution of the soils inorganic carbon content.

The transfer of the regression model to the satellite image allowed for prediction of the inorganic carbon content. Concentrations obtained from the satellite image are in accordance with the concentration range of the chemical analysis. The predicted soil inorganic carbon concentrations reflect the geographic conditions and show a dependence on the annual rainfall amount. A general trend to increasing concentrations of inorganic carbon can be stated with increasing aridity. Furthermore, local conditions are well reflected by the predicted concentrations.

Keywords: Inorganic carbon, soil properties, reflectance spectra, soil color, spatial analysis, Landsat image.

1 INTRODUCTION

Drylands cover almost one third of the earths surface. Especially the semi-arid ecosystems provide important land resources for adapted land use and livestock farming. But the pressure on arid and semi-arid areas resulting from climatic variability, climate change, demands of increasing stocking rates and population development was probably never as high as nowadays [1]. Since these regions are often considered as risk areas in the context of global climate change and desertification dynamics, a broad monitoring of the status of these areas is of enormous importance. In this context the soils of these ecosystems are of outstanding relevance.

Soil loss resulting from a combination of physiographic and human factors is an important sign of degradation processes. The inorganic carbon content in soils developed on carbonatic parent material in semi-arid and arid environments is one major indicator of soil development. High inorganic carbon contents indicate weakly developed or degraded soils. Since the spatial detection of inorganic carbon has a great importance in the context of monitoring land degradation and sub-recent morphodynamics, it is necessary to develop a remote sensing based approach for spectral determination of inorganic carbon content.

Therefore, the aim of this study is the spatial assessment of the inorganic carbon content of soils. In order to fulfill this objective, an analysis of the relationship between laboratory spectral measurements and inorganic carbon content is accomplished with respect to the characteristic absorption features of carbonate. Based on statistical analysis, a method for spectral detection of inorganic carbon content is generated.

Even with laboratory spectroscopy a spatial detection of soil properties exclusively based on terrestrial inquiry for broader and inaccessible areas is rarely feasible. Operational EOS are in particular suitable for the environmental monitoring of these sensitive ecosystems [2], but they usually only endue a relatively limited number of spectral channels with a comparatively small spectral resolution. Hence, an assessment of soil properties and soil development is only feasible using these few spectral bands or parameters derived from them [3, 4, 5].

The established model for detection of inorganic carbon content based on laboratory reflectance measurements will be modified to allow spatial analysis of the inorganic carbon content of soils based on Landsat images Subsequently, an up-scaling of the model approach will be adopted to a Landsat image in order to predict spatial distribution of the soils inorganic carbon content for the investigated region.

2 THE STUDY SITE

Research was conducted along a transect following a hypsometric rainfall gradient from east of Jerusalem to the Dead Sea covering Mediterranean, semi-arid and mildly-arid climate zones and extending to the east towards the arid area near the Dead Sea (figure 1). The transect shows a strong decrease in elevation, ranging from 650 m a.s.l. in the Judea-Samaria mountains, in the west, to 60 m below sea level in the Judean Desert. Mean annual rainfall decreases on a distance of only 33 km from 620 mm in the west to about 120 mm in the east [6, 7]. According to the amount of rainfall, the soils vary from terra rossa (Mediterranean area) through brown and pale rendzinas (semi-arid and mildly-arid areas) to desert lithosols and bare rocks (arid area). All test sites are located on limestone parent material and soils vary according to the amount of rainfall.

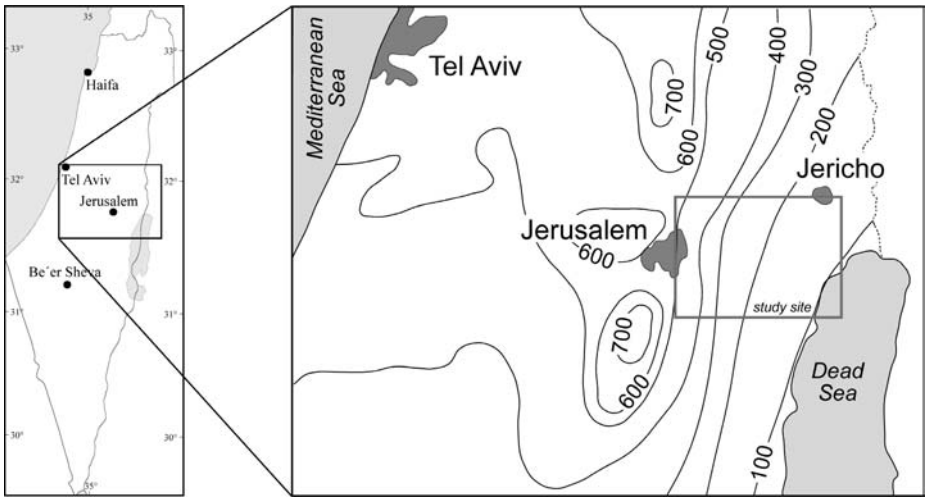

Figure 1. Location of the study site and mean annual rainfall in Israel (modified after [8]).

3 MATERIAL AND METHODS

3.1 Field sampling and chemical analysis

Climatic conditions are modified by physiogeographic factors at meso- microscale level. In this context the relief is of special importance. In dependence of slope and aspect, irradiation is changing both in total and in daily and seasonal distribution. South-oriented slopes show higher irradiation amounts with stronger variations. Water supply is varying due to surface flow between middle slope and top or valley bottom. These different physiogeographic conditions show effects on soil development.

Figure 2. Varying physiogeographic conditions along a sampling transect in the semi-arid part of the study site (left: top of hill; middle: upper slope; right: lower slope).

Within the study site sampling of the soil surface (upper 2 cm) material was conducted along eleven topographical transects covering north- and south- facing slopes and valley bottoms to consider the different physiogeographic conditions. In total 53 samples were collected at the different climatic regions.

The soil samples were air-dried and gently crushed in order to pass a 2mm-sieve. Subsamples were carefully homogenized for an enhancement of spectral features and to allow better reaction with the chemical reagents. For

all samples organic and inorganic carbon content were analyzed by an infrared cell in a high-frequency induction oven (LECO). The content of inorganic carbon varies between 1.57 and 9.24 % with a mean of 5.22 % and a standard deviation of 1.96.

3.2 Laboratory spectral reflectance measurements

The spectral reflectance of soils is affected by the inherent spectral characteristics of varying combinations of mineral components, organic matter and the soil moisture [9]. The relations of spectral reflectance and soil properties, like grain size distribution, soil moisture, iron oxides, carbonate content and organic matter, have been outlined in many studies [5, 10, 11, 12]. Relationships between soil reflectance and carbonate content have been established using statistical methods such as multiple regression analysis [13, 14].

Spectral reflectance measurements of homogenized soil samples were acquired in the laboratory with an ASD FieldSpec II spectroradiometer in 1 nm steps between 350 nm and 2500 nm using a reflectance standard of known reflectivity. The optical head of the spectroradiometer was mounted on a tripod in nadir position with a distance of 10 cm to the sample. A 1000 W quartz-halogen lamp set in a distance of approx. 30 cm and an illumination angle of 30 degrees was used to illuminate reference panel and samples.

Carbonates show diagnostic vibrational absorption bands in the Near Infrared at 2.30 - 2.35 µm and at 2.50 - 2.55 µm. Three weaker bands occur at 1.85 - 1.87 µm, 2.12 - 2.16 µm and at 1.97 - 2.00 µm. The band positions vary with the composition of different carbonates [15, 16]. With increasing content of Mg-carbonate the wavelength position of maximum absorption is shifted to the shorter wavelength [17]. Individual absorption features for the absorption band at 2.30 - 2.35 µm were calculated by continuum removal (figure 3). Derived parameters for this absorption feature are band position, maximum absorption depth, absorption width and area integrals.

Inorganic carbon shows a strong influence to the visible domain of the spectra. Often an increase of reflectance with rising contents of inorganic carbon can be seen (figure 3). Therefore, it was decided to include color information into the further spectral analysis. For the calculation of color parameters, the reflectance measurements were converted into trichromatic specifications, and then expressed in terms of the „Commission Internationale de ´Eclairage [C.I.E.]“ color notation (Y, x, y) from 1931. In this color system the color intensity is characterized by the tristimulus value “Y” (luminance) which represents the brightness of color while “x” and “y” are the chromaticity coordinates [18]. The C.I.E. color coordinates were already found to contain substantial information for spectroradiometric detection of soil properties [10, 12].

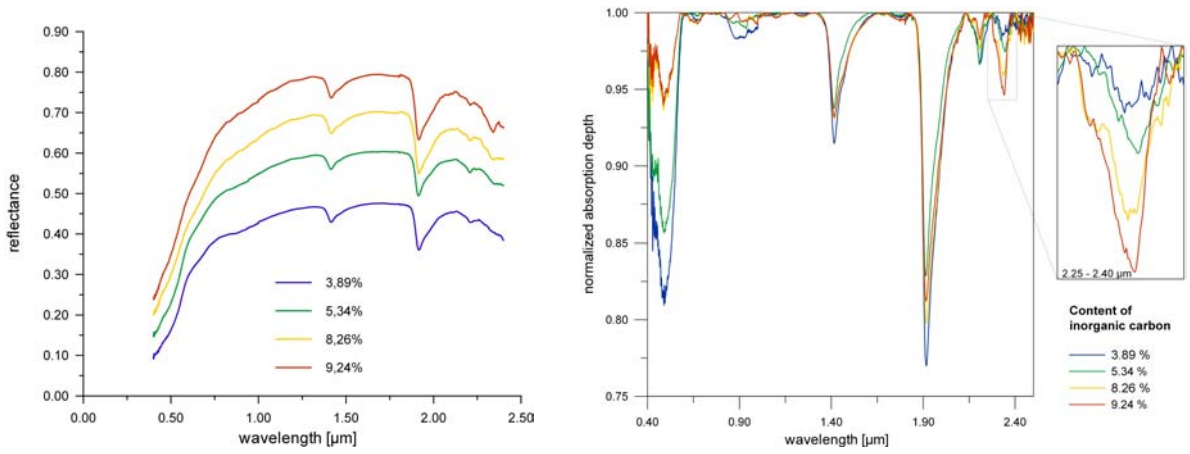

Figure 3. Reflectance spectra (left) and continuum removal normalized reflectance spectra (right) of soil samples with different inorganic carbon content.

Modeling of inorganic carbon content was conducted by multiple regression. Validating of the model results were carried out by cross-validation. Cross-validated statistics were calculated based on estimates derived according to the ‘leave-one-out-method’ which means that each sample is estimated by means of an empirical-statistical model which was calibrated using the remaining (n-1) samples. To assess the cross-validated prediction accuracy of the approach the coefficient of determination (r_{cv}^2) and the root mean square error ($RMSE_{cv}$) were calculated.

3.3 Satellite image pre-processing

One major objective of this study is the spatial analysis of inorganic carbon content in the Judean Desert. The used Landsat-TM 5 image from 27th July 1998 was selected considering available meteorological data. A pronounced dry period prior to image acquisition was mandatory to guarantee optimized conditions for the detection of inorganic carbon. Long dry periods insure minimum vegetation cover in semi-arid and arid regions. Additionally, the influence of varying soil moisture contents on the reflectance signal can be rated as very low.

The satellite image has been geometrically corrected to the New Israeli Grid coordinate system based on the topographic map of the region at scale 1:50,000. The image was corrected for atmospheric effects by applying a radiative transfer model which also accounts for terrain-induced illumination effects [19].

This study is focusing on spatial detection of inorganic carbon. Vegetation cover seriously influences the spectral reflectance signature, by modifying the signal of the litho- and pedological components. Since these components show a different spectral behavior than vegetation, an estimation and elimination of the spectral component of vegetation at the reflectance signal is well feasible by spectral mixture analysis (SMA). Based on SMA, areas with vegetation cover of more than 20 percentage were excluded from further analysis.

4 RESULTS AND DISCUSSION

4.1 Estimation of inorganic carbon from laboratory reflectance spectra

Modeling inorganic carbon content of soil samples requires comparable lithological conditions for soil development, to guarantee that spectral characteristics resulting for carbonate occur due to varying concentrations instead of different chemical composition of the bedrock material. The study site is characterized by relatively homogeneous cretaceous bedrock and the developed soils show a similar soil texture (mostly silt and loam) [15].

To insure that no influence of different carbonates is given the absorption position was determined. Gaffey [16] documented the absorption positions for Calcite (2.333-2.340 µm) and Dolomite (2.312-2.322 µm). The observed absorption position of the investigated soil samples stated that the carbonate exists as calcium carbonate (Calcite) [12]. Since the carbonate absorption is detectable, a relationship between carbonate content and the absorption feature is assumed.

Increasing inorganic carbon contents lead to an increase of the intensity of the carbonate absorption. A strong relationship is observed between the inorganic carbon content and the normalized absorption depth. While this relationship seems to be linear for lower concentrations, it is non-linear when considering all soil samples (figure 4). A similar non-linear relationship is documented for the absorption area of the carbonate absorption feature.

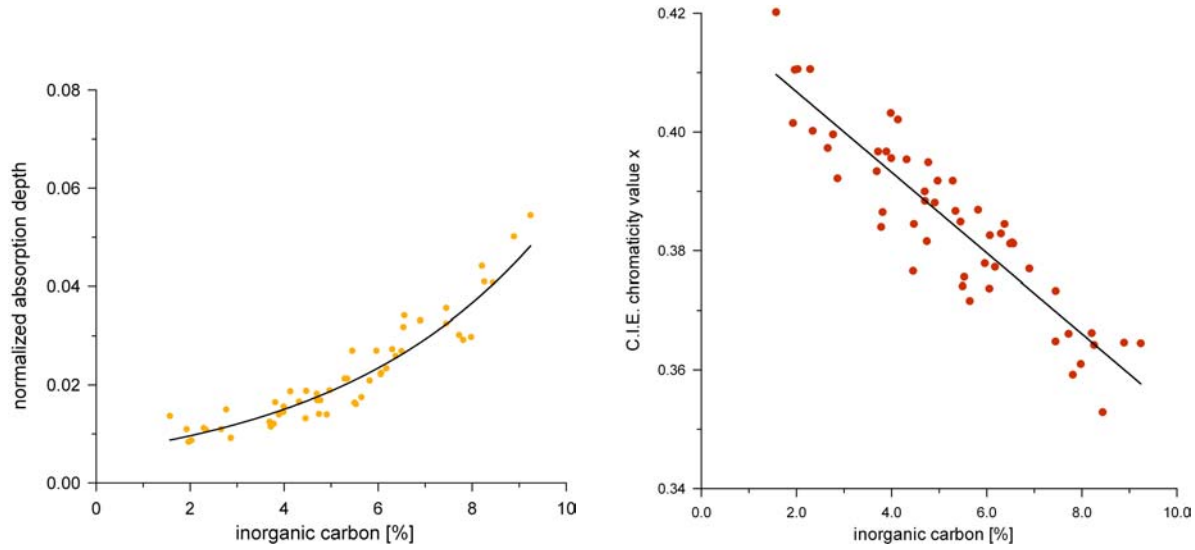

Figure 4. Inorganic carbon vs. normalized absorption depth (left) and vs. C.I.E. chromaticity value x (right).

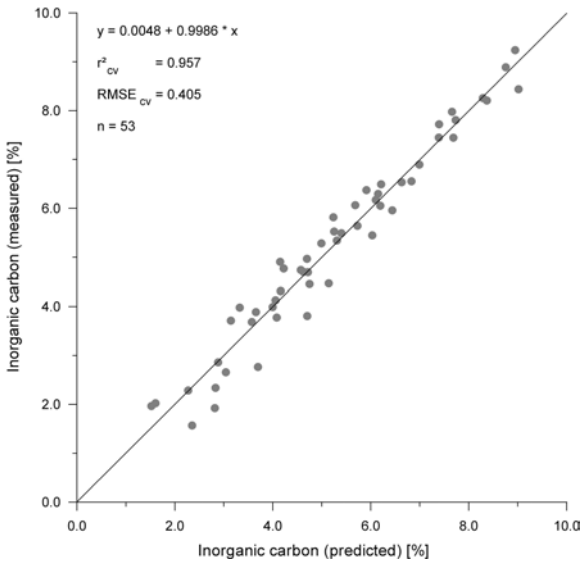

Figure 5. Scatterplot for cross validation of the generated model for predicting the inorganic carbon content.

In a first attempt the inorganic carbon contents in the soil samples were predicted based on derived absorption features. The best result was obtained using the "normalized absorption depth". This approach allowed to estimate inorganic carbon with a cross-validated accuracy of $r_{cv}^2 = 0.876$ ($RMSE_{cv} = 0.674$). This accuracy already shows the potential of spectral determination of inorganic carbon.

The relative amount of carbonate in soils influences soil brightness substantially. Increasing inorganic carbon concentrations result in exponentially higher C.I.E. luminance values Y. Additionally, strong linear relationships were found for the C.I.E. chromaticity values x and y which substantially decrease with higher inorganic carbon concentrations (figure 4).

These findings lead to the integration of C.I.E. color coordinates into the modeling. It was expected that the integration of the luminance "Y" representing the soil brightness would improve the modeling result substantially. However, it was found that the integration of the luminance "Y" did not have a positive effect on the modeling results while the integration of the C.I.E. chromaticity value "x" yielded a significantly higher fit. The final model is based on the variables "normalized absorption depth" and "C.I.E. chromaticity value x" and results in a r_{cv}^2 of 0.957 with a $RMSE_{cv}$ of 0.405 for the cross validation:

$$C_{inorg}\,[\%] = 0.591 * \log(\text{absorption depth}) - 0.446 * \text{C.I.E.-x} \qquad (1)$$

The result of the cross-validation is shown in figure 5. The regression for the cross-validation is very close to the 1:1-line with a gain of almost one and an offset that can be neglected. This supplies evidence for the high accuracy of the model approach.

Table 1. Comparison of predicting inorganic carbon results from laboratory reflectance measurements for the models based on absorption features only, on C.I.E. color coordinates and the combined approach.

C_{inorg} [%]	Absorption feature only	C.I.E. only	Absorption feature + C.I.E.
r^2_{cv}	0.876	0.851	0.957
$RMSE_{cv}$	0.674	0.749	0.405

In table 1 the different predicting results for inorganic carbon from laboratory reflectance measurements are listed. As mentioned above best modeling results were obtained by the combination of absorption features and C.I.E. color information ($r_{cv}^2 = 0.957$; $RMSE_{cv} = 0.405$). It is remarkable that based only on the C.I.E. color coordinates a high predicting accuracy with a r_{cv}^2 of 0.851 ($RMSE_{cv} = 0.749$) is achieved. This is especially important in the context of modeling the spatial distribution of inorganic carbon concentrations using a satellite image, because the C.I.E. color coordinates can be calculated from Landsat-TM channels as described in the following section.

4.2 Mapping the spatial distribution of inorganic carbon from satellite data

The limited spectral resolution of the Landsat image does not allow the exploitation of the carbonate absorption feature at 2.30 - 2.35 µm. Since an estimation of inorganic carbon based on C.I.E. color coordinates showed sound results (see section 4.1), these color coordinates form a suitable alternative for the spatial modeling of inorganic carbon. But to transform the satellite data into the C.I.E. color system some intermediate steps are necessary.

The reflectance values in the Landsat-TM channels TM1, TM2 and TM3 do not correspond to the C.I.E. tristimulus values B, G and R and need to be transformed by empirical relationships. These relationships are depending on the surveyed soils and application to other data sets is limited. While the calculation of C.I.E. color coordinates is done based on the color matching functions, the color information of Landsat-TM is determined by the sensitivity of the detectors (figure 6).

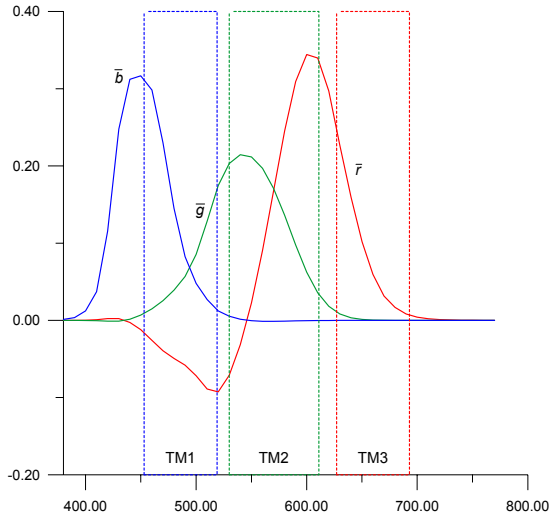

Figure 6. Color matching functions $\bar{b}$, $\bar{g}$ and $\bar{r}$ of the C.I.E. standard observer and the wavelength ranges of the Landsat channels TM1, TM2 and TM3.

The needed empirical equations for transforming the satellite data into C.I.E. color coordinates were determined based on the laboratory spectra. For this the reflectance values of the three Landsat channels were calculated from the continuous reflectance measurements.

Based on this approach the C.I.E. tristimulus values X, Y and Z can be calculated from the satellite data using the following equations [20]:

$$X = 2{,}7659R + 1{,}7519G + 1{,}1302B \quad (2)$$

$$Y = R + 4{,}5909G + 0{,}06012B \quad (3)$$

$$Z = 0{,}0565G + 5{,}5944B \ , \quad (4)$$

which allows the calculation of the C.I.E. chromaticity values x

$$x = X / (X+Y+Z) \quad (5)$$

and y accordingly.

Using the derived C.I.E. color coordinates a model for predicting inorganic carbon concentration from the Landsat-TM image was established:

$$C_{inorg}\,[\%] = -0.509 * \text{C.I.E.-x} + 0.444 * \log(\text{C.I.E.-Y}) \quad (6)$$

The integration of the logarithm of the C.I.E. luminance Y instead of the original value takes into consideration the non-linearity of its relationship with the inorganic carbon concentration. Based on equation 6 the inorganic carbon concentration for the study site was predicted (figure 7).

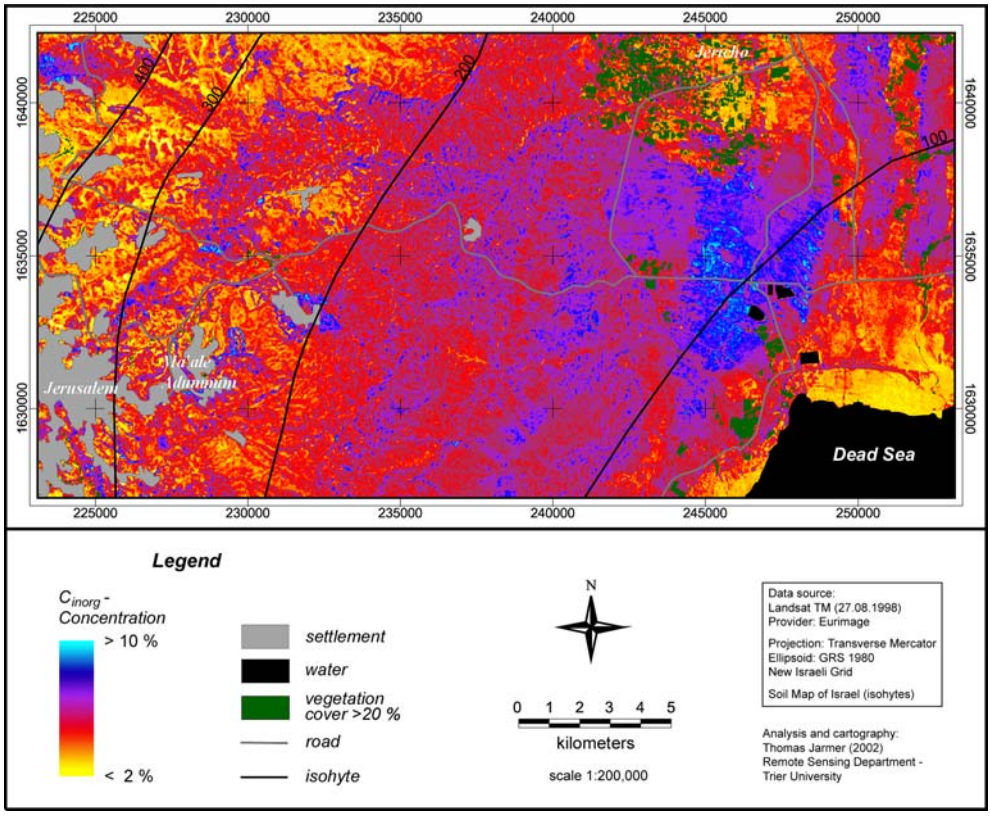

Figure 7. Inorganic carbon contents at the study site derived from Landsat image applying the C.I.E. based model.

The model allows good estimates of inorganic carbon concentrations from the satellite image and represents the spatial dynamics of the study site. The concentration ranges estimated from the image data are in accordance with the concentration range of the chemical analysis (see section 3.1).

The weathering of limestone and the corresponding removal of carbonate is mainly influenced by the available amount of water. This process is accelerated by carbonic acid and organic acids as well as high temperatures. This explains the general trend of increasing inorganic carbon content with decreasing rainfall amount in the study site. This is shows in figure 8, but it has also to be considered that in the eastern part of the study site are quartary sediments (alluvials, Lisan marls) are the bedrock material. In this region (light blue) concentrations of above ten percentages are due to the different bedrock material. A totally different situation is given for the area under agricultural use (south of Jericho and the Jordan valley) where predicted inorganic carbon contents with three to six percentages are relatively low.

Highest concentrations occur apart from the west-east-gradient in new build-up areas where the soil has been removed and the bare bedrock appears at the surface. Such high concentrations are given for the industrial area of Mishor Adummim and the extending settlement of Ma'ale Adummim. In the case of Ma'ale Adummim the newly set up street system is clearly visible (figure 8, left). In these areas in the maximum concentrations between ten and eleven are predicted which are comparable to the inorganic carbon concentrations of pure bedrock samples of around eleven percentages.

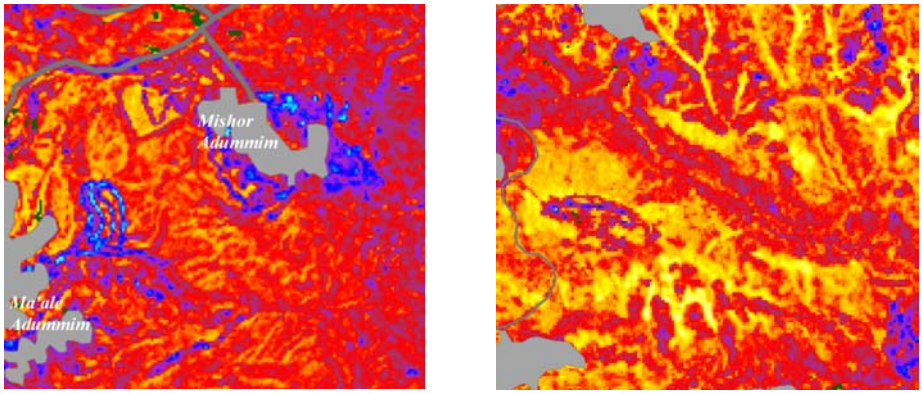

Figure 8. Inorganic carbon contents for a subset showing the settlement of Ma'ale Adummim and the industrial area of Mishor Adummim (left) and the Wadis in the north-western part of the study site (right) (legend see figure 7).

Beside such anthropogenic influenced locations, mainly the mountain ridge and hill tops in the center of the study site are characterized by high to very high estimates. This seems to be contradictory to field survey results because in these positions on top of the hills often the best developed soils were found (compare figure 2). At the same time in these locations a high amount of stones and bedrock outcrops have been observed in these locations, which reaches shares between 45 and 80 %. The bedrock material has the function of a sealed surface and results in a lateral surplus of rainfall which allows higher weathering rates and better soil development. Apart from this, well developed soils areas are very limited as most of the surface is covered by stones and bedrock material. As a consequence the reflectance signal of these areas is dominated by the limestone which results in high estimates of inorganic carbon concentrations of > 8 % maximum.

In the western part of the study site lower to medium concentrations prevail with lowest estimates occurring in the Wadis, sometimes even below 3 %. The reason is the better water supply and the resulting higher soil moisture compared to the slopes, which allows a substantially better soil development in the valleys (figure 8, right).

5 CONCLUSIONS

Inorganic carbon concentrations were predicted with high accuracy from laboratory reflectance measurements (r^2_{cv}>0.95) by combining the normalized absorption depth of the carbonate absorption feature at 2.33 µm and the C.I.E. chromaticity value x. It was found that the adaptation of the regression model to C.I.E. color values only also allows sound estimates of inorganic carbon contents (r^2_{cv}>0.85). The adaptation of the model made an up-scaling to satellite data possible and reflects the spatial pattern in the study site very well. Furthermore, the regression model allows sound estimates of the spatial distribution of inorganic carbon concentrations in the study site. Finally it is

assumed that the introduced approach can also be used for other soil parameters and is applicable to other semi-arid and arid regions with similar physiogeographic conditions.

ACKNOWLEDGMENTS

This work was financially supported through the ERMES-II project (ENV4-CT95-0181), funded by the European Commission and the Forschungsfonds of the University of Trier. The computer code for calculating the C.I.E. colour values was kindly provided by R. Escadafal (Cesbio, France). This support is gratefully acknowledged.

REFERENCES

[1] WHITE, D.H., 2000: Drought policy, monitoring and management in arid lands. *Annals of Arid Zone, 39(2),* pp. 105-129.
[2] HILL, J., 2000: Semiarid land assessment: monitoring dry ecosystems with remote sensing.- Encyclopedia of Analytical Chemistry.- In: Meyers, R.A. (ed.): Encyclopedia of Analytical Chemistry, Chichester, pp. 8769-8794.
[3] PICKUP, G. AND NELSON, D.J., 1984: Use of Landsat radiance parameters to distinguish soil erosion, stability, and deposition in arid central Australia. *RSE, 16*, pp. 195-209.
[4] MADEIRA, J.; BÉDIDI, A.; CERVELLE, B.; POUGET, M. AND FLAY, N., 1997: Visible spectrometric indices of hematite (Hm) and hoethite (Gt) content in lateritic soils: the application of a Thematic Mapper (TM) image for soil-mapping in Brasilia, Brazil. *IJRS, 18(13),* pp. 2835-2852.
[5] HILL, J. AND SCHÜTT, B., 2000: Mapping complex patterns of erosion and stability in dry mediterranean ecosystems. *RSE, 74*, pp. 557-569.
[6] LAVÉE, H.; IMASON, A.C. AND SARAH, P., 1998: The impact of climate change on geomorphology and desertification along a mediterranean-arid transect. *Land degradation & development*, 9, pp. 407-422.
[7] SARAH, P., 2001: Soluble salts dynamics in the soil under different climatic regions. *Catena 43(4),* pp. 307-321
[8] SURVEY OF ISRAEL (eds.), 1985: The Atlas of Israel (3rd ed.) (English-Hebrew). Tel Aviv, New York, London.
[9] BAUMGARDNER, M.F.; SILVA, L.F.; BIEHL, L.L. AND STONER, E.R., 1985: Reflectance properties of soils. *Advances in Agronomy, 38*, pp. 1-44.
[10] JARMER, T. AND SCHÜTT, B., 1998: Analysis of iron contents in carbonate bedrock by spectroradiometric detection based on experimentally designed substrates. In: Schaepmann, M., Schläpfer, D. and Itten, K.(eds.): 1st EARSeL Workshop on Imaging Spectroscopy, pp. 375-382. Zurich.
[11] UDELHOVEN, T.; EMMERLING, C. AND JARMER, T., 2003: Quantitative analysis of soil chemical properties with diffuse reflectance spectrometry and partial-least-square regression:A feasibility study. *Plant and Soil, 251(2)*, pp. 319-329.
[12] JARMER, T., 2005: Der Einsatz von Reflexionsspektrometrie und Satellitenbilddaten zur Erfassung pedochemischer Eigenschaften in semi-ariden und ariden Gebieten Israels. (=Trierer Geographische Studien, 29). Trier.
[13] BEN-DOR, E. AND BANIN, A., 1990: Near-infrared reflectance analysis of carbonate concentration in soils. *Applied Spectroscopy, 44(6),* pp. 1064-1069.
[14] BEN-DOR, E. AND BANIN, A., 1994: Visible and near-infrared (0.4-1.1µm) analysis of arid and semiarid soils. *RSE, 48*, pp. 261-274.
[15] HUNT, G.R. AND SALISBURY J.W., 1971: Visible and near-infrared spectra of minerals and rocks: II. Carbonates. *Modern Geology, 2,* pp. 23-30.
[16] GAFFEY, S.J., 1986. Spectral reflectance of carbonate minerals in the visible and near infrared (0.35-2.55 microns): calcite, aragonite, and dolomite. *American Mineralogist, 71*, pp. 151-162.
[17] CLARK, N., 1999: Spectroscopy of rocks and minerals and principles of spectroscopy.- In: Rencz, A.N. (ed.): Remote Sensing for the Earth Sciences. Manual of Remote Sensing, Volume 3 (3rd Edition), pp. 3-58. New York, Chichester, Weinheim, Brisbane, Singapore.
[18] WYZECKI, G. AND STILES, W.S., 1982: Color science. Concepts and methods, quantitative data and formulas. New York, London, Sidney.
[19] HILL, J., MEHL, W. AND RADELOFF, V., 1995: Improved forest mapping by combining corrections of atmospheric and topographic effects in Landsat TM imagery.- In: Askne, J. (ed.): Sensors and environmental applications in remote sensing, Proceedings of the 14th EARSeL Symposium, Göteborg, Sweden, 6-8 June 1994, pp. 143-151.
[20] ESCADAFAL, R., GIRARD, M.-C., AND COURAULT, D., 1988: Modelling the relationship between Munsell soil color and soil spectral properties. *International Agrophysics, 4(3)*, 249-261.

An operational methodology (VMESMA) to derive biophysical parameters for land degradation processes assessment

B. Martínez[a], A. Verger[a] , F. Camacho-de Coca[a], F.J. García-Haro[a], M.A. Gilabert[a] and J. Meliá[a]
[a] Departament de Termodinámica. Universitat de València
C/Dr. Moliner, 50. 46100 Burjassot. Valencia. Spain

ABSTRACT

New prospective sensor technologies (e.g., VEGETATION, MODIS, SEVIRI) along with the development of operational methodologies provide us a potential tool to assess and monitor land degradation and desertification processes.

In this context, the objective of this work aims at the application of a robust methodology to retrieve vegetation parameters over areas affected by land degradation processes (i.e., *hot spot* areas). The estimation of these parameters relies on an optimised variable and multiple spectral mixture analysis (VMESMA) [1], [2]. This method uses spectral information to derive fraction vegetation cover (FVC) and then applies a semi-empirical relationship to estimate leaf area index (LAI). VMSEMA is a fast and robust algorithm that provides more reliable outcomes when the anisotropy effects have been previously corrected (e.g., using kernel-driven models) [3]. The main improvement comes from the expected higher accuracy and sensitivity to vegetation cover using a variable strategy and also taking advantage of an extended spectral dimensionality [3]. Furthermore, the operability value of this method to extract subpixel vegetation information over semi-arid environments from multispectral datasets has been demonstrated in a variety of studies [2]. Nevertheless, VMESMA is very sensitive to endmembers selection and more investigation is required to optimize the method.

In this work, an early evaluation of potential characteristics and limitations of the VMESMA algorithm is carried out. In particular, our study will be focused on the performance of estimating variations of vegetation activity over land degraded areas. For this purpose, the VMESMA is applied on VEGETATION/SPOT data (http://www.avignon.inra.fr/cyclopes) to retrieve the FVC parameter. This data base consists of a series of normalized monthly BRDF reflectance and LAI/FVC imagery extended over Europe for all the 2003. In a first stage, the analysis is done over the Iberian Peninsula. Then, the VMESMA feasibility approach is evaluated over a hot spot are located in Castilla-La Mancha region, the Barrax site, where FVC ground-truth information was available. The study includes a comparison with the FVC product derived from the CYCLOPES algorithm.

Keywords: Spectral mixture approach, FVC, new sensors, VEGETATION/SPOT, land degradation processes.

1 INTRODUCTION

Desertification is a complex process resulting from several factors such as climate, relief, and the state of the soil and natural vegetation. The vegetation cover reduction and changes in the population of the vegetation cover are sensitive indicators of land degradation that needs to be considered when attempting to measure the extent of desertification [1], [2]. New prospective sensor technologies (e.g., VEGETATION, MODIS, SEVIRI) along with the development of operational methodologies have provided us a potential tool to estimate biophysical vegetation parameters, such as fraction of vegetation cover (FVC) and leaf area index (LAI), in order to assess and monitor land degradation and desertification processes.

In spite of the relevance on desertification treatment, there is a lack of standardized procedures to perform it at operational scales. The DeSURVEY (A Surveillance System for Assessment and Monitoring of Desertification) project offers a contribution to fill this gap by complementing assessment of desertification status with early warning and vulnerability evaluation of the involved land use systems. The project goal is to deliver a compact set of integrated procedures, with application and tutorial examples at the EU and national scales (www.desurvey.net). In this context, our main concern is to develop conceptually new methodological pathways and to explore the potential of prospective sensor technologies to derive existing vegetation parameters with better accuracy over areas affected by land degradation processes (i.e., *hot spot* areas). In semi-arid areas, routine techniques available to estimate parameters of plant canopies from reflectance data of broadband sensors are limited [3], mainly due to the sparse distribution of the plants, coupled with the open canopies means that variability of the soil background will

be very significant in the reflected spectrum in arid regions. This is the case of the vegetation indices which are unsuitable for the accurate measurement of vegetation cover in arid regions due to its high sensitive to changes in soil background [4].

An alternative technique, namely Spectral Mixture Analysis (SMA), has been developed in recent years to extract land-cover information at a sub-pixel level [5]. SMA divides each ground resolution element into its constituent materials using endmembers (EMs), which represent the spectral characteristics of the cover types. With regard to vegetation studies, this modelling approach has been shown to be a valuable remote sensing tool to assess the compositional distribution of vegetation and its change at regional scale [6], [7] and [8].

In this work, the optimised variable and multiple spectral mixture analysis (VMESMA) [9], [10] is applied in order to retrieve the vegetation parameters from spectral information, such as the FVC, which is presented as a suitable magnitude to enable consistent time series for monitoring the vegetation dynamics. The operability value of this method to extract subpixel vegetation information over semi-arid environments from multispectral datasets has been demonstrated in a variety of studies [10], [11]. Nevertheless, VMESMA, as well as the other SMA methods, is very sensitive to endmembers selection. Thus, especial attention of EMs extraction procedure has been given in this work.

Finally, the potential characteristics and limitations of the VMESMA algorithm on the FVC estimates are evaluated in this work. In particular, the VMESMA version 1 FVC product is retrieve from VEGETATION (e.g. VGT) image of July 2003. In a first stage, an early algorithm evaluation is performed over the Iberian Peninsula. Secondly, the study is focused over a hot spot area located on the Castilla-La Mancha region, the Barrax site [12], in order to assess the model performance on land degraded areas. It is a well documented area with large in-situ available dataset, which have been selected in the frame of other EU project on the relevant issues for DeSurvey ([13]; www. eeza.csic.es/surmodes). The study includes a comparison with the FVC product derived from the CYCLOPES version 1 algorithm, which was derived using the Roujean & Lacaze [14] semiempirical method based on a linear relationship with the normalized DVI vegetation index.

2 THEORETICAL BASIN

Different SMA approaches have been developed in the literature, varying in the number or the nature of the components they are capable of resolving, as well as in how the variability is introduced into the scene [15]. The most widely used SMA method consists in employing the same EMs (typically between 2 and 5) on the whole image, and using all available EMs at the same time. Therefore, the EMs used in SMA are the same for each pixel, regardless of whether the materials represented by the EMs are present in the pixel. On the other hand, 2-5 EMs are often insufficient to describe the scene fully and lead to unclear results. In this sense, uncommon materials, which may not merit their own EM, may be poorly modeled by SMA. SMA also does not account for spectral variations present within the same material, since it permits only one EM per material.

In recent years, many authors have proposed the use of a more complex model in which both the number and the set of EMs vary on a per-pixel basis [7]. Roberts et al. [7] refer to this technique as Multiple Endmember Spectral Mixture Analysis (MESMA). The dynamic identification of the optimum EM subset for each image pixel provides a more accurate interpretation of the mixed pixels than SMA, improving the fit of the model. However, modeling a large number of spectra for each pixel reduces the computational efficiency of MESMA and complicates interpretation of the resulting image.

A variable multiple endmember spectral mixture analysis (VMESMA) is introduced in [9], for an improved fulfillment of the unmixing processes. VMESMA employs a variable set of multiples (between 2-4) EMs on a per-pixel basis, and introduces an expert system to select the best submodel, the expert system basically ties together modeling errors and fractional errors, and makes an automated decision to assign each composing material to its optimum EMs subset (see [9] for details). The main improvement comes from the expected higher accuracy and sensitivity to vegetation cover using a variable strategy and also taking advantage of an extended spectral dimensionality [3]. The formulation of VMESMA is briefly described in the next section.

2.1 VMESMA

The main equations of VMESMA are derived from the traditional SMA model, which assumes that the target reflectance is a linear combination of a few macro-components (endmembers) reflectance weighted according to its proportion to the scene. We will refer to n as the dimensionality of the spectral observations and the column vector $\mathbf{r}(r_1,r_2,...,r_n)$ will be the measured spectrum of the mixture. Assuming that there are c composing EMs within the mixture we will order their spectral response in a $n \times c$ matrix, $\mathbf{E}$, with the reflectance of the c EMs in columns. Let

$\mathbf{f}(f_1,f_2,...,f_c)$ be the column vector with the *c* unknown proportions of the EMs in the mixture. The SMA assumes a linear dependence of the theoretical predictions **r** on the unknown parameters **f**:

$$r = E f + \varepsilon \tag{1}$$

where **ε** is the residual vector. This mixing equation is usually accompanied by two constraints. The normalisation constraint says that a pixel is well-defined by its components, for which the proportions or abundances should therefore add up to unity:

$$\sum_{i=1}^{c} f_i = 1 \tag{2}$$

The positivity constraint says that no component of a mixed pixel can make a negative contribution:

$$f_i \geq 0 \qquad i = 1,...,c \tag{3}$$

Let **V**(**r**) denote the error matrix of the observations **r**, namely its covariance matrix. The least-square principle establishes that the unknown parameters are those that minimise the Mahalanobis distance between the pixel **r** and point **E f**:

$$\chi^2 = (r - E f)^T V^{-1} (r - E f) \tag{4}$$

A large number of solution methods exist for this type of linear problem, including least-squares estimation, singular value decomposition and factor analysis [16] and [6]. However, not all solutions are independent. For example, the singular value decomposition is mathematically equivalent to the least squares solution without constraints. In general, solutions that do not constrain the abundances to the normalisation condition produce biased and highly noise-dependent solutions for the abundances [17]. VMESMA uses a partially constrained least-squares solution, which introduces in equation (4) a Lagrange multiplier to impose the sum-to-one constraint. This estimator produces similar results to the numerical methods but is computationally faster [5]. This solution is expressed in a closed form:

$$\hat{f} = C^{-1}G - C^{-1}B^T (B C^{-1}G - 1)/z \tag{5}$$

where **B** denotes a $c \times 1$ vector consisting entirely of ones, and the following abbreviations have been introduced:

$$C = E^T V^{-1} E \qquad G = E^T V^{-1} r \qquad z = B C^{-1} B^T \tag{6}$$

This solution provides a unique and unbiased solution, which is computationally fast due to its matricial form. However, abundances are not constrained to lie between 0 and 1. Thus, noise in the observations and inaccuracies of the model can bring about undesired results. We have preserved negative fractions since they may also convey useful information and provide an additional means of assessing model accuracy. Although numerical methods are available to solve this problem ([8], [16], [17] and [18]), the computational complexity of these methods is often unaffordable on satellite data and moreover they introduce a bias in the solution. A simple approach for dealing with physically unacceptable fractions involves setting any negative fraction to zero and renormalising the positive ones so that they add up to one.

3 EXPERIMENTAL PROCEDURE

3.1 Study Area

Figure 1 shows a RGB color composite of the Iberian Peninsula, which consists of 4, 3 and 2 normalised top of the canopy (TOC) reflectance bands derived from VEGETATION/SPOT data. On the other hand, the selected *hot spot* area can also be observed in figure 1 (e.g. red square). This area is located in Castilla-La Mancha region on the South-Eastern sector of the Iberian plateau. For this site, large in-situ datasets are available existing important experiences and feedbacks. The area covers an extension of 50×50 km^2 and includes the well documented experimental Barrax site [12]. The site shows three main cover types, irrigated land crops (e.g. corn, alfalfa, potato, sugar beet, onion and wheat), soil and dry land (e.g. barley and fallow) and mixed forest.

Until recent decades Castilla-La Mancha was predominantly a dryland farming area. However, exploitation of groundwater resources for irrigation has increased largely and some 20% of the area of the main aquifers system is nowadays subjected to intensive, irrigated agriculture. As a result, the over-exploitation of aquifers and wetland degradation are the main factors that put in danger the sustainability of the agricultural systems in this region. Both

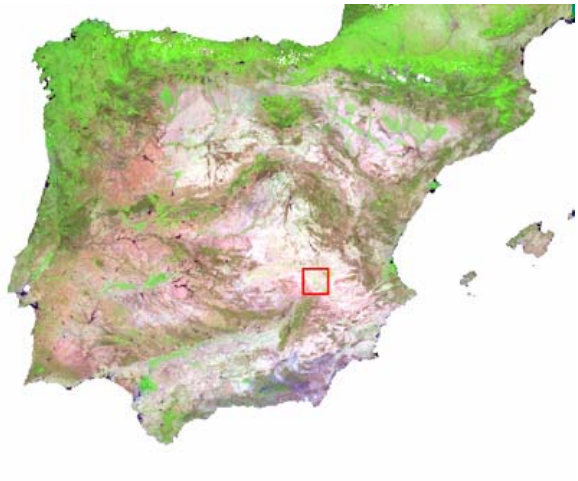

Figure 1. RGB color composite of the 4, 3 and 2 normalised top of the canopy (TOC) reflectance bands derived from VEGETATION data. The selected *hot spot* area is also included (e.g. red square). The image belongs to the ten days composite from 10th to 20th July 2003.

of them are inter-related and can be considered as symptoms of current desertification (www.eeza.csic.es/ surmodes).

3.2 Imagery

In this study, nadir-zenith normalized TOC reflectance represented by the k_0 Roujean's coefficient and provided by CYCLOPES project (http://www.avignon.inra.fr/cyclopes/) are used in order to evaluate the VMESMA algorithm. k_0 dates result from fitting the Roujean et al. [14] parametric model to georeference, atmospherically corrected and cloud-masked VEGETATION/SPOT (VGT) reflectances. Roujean BRDF model can be expressed as [14]:

$$R(\theta_i,\theta_v,\phi;\lambda)=k_0(\lambda)+k_1(\lambda)f_1(\theta_i,\theta_v,\phi)+k_2(\lambda)f_2(\theta_i,\theta_v,\phi) \quad (7)$$

where θ_i and θ_v stands for sun and view zenith angle, ϕ for relative azimuth angle, f_1 and f_2 are "kernels", i.e. known functions of illumination and viewing geometry which describe geometric and volume scattering respectively; and $k_{i=0,1,2}$ are the unknown coefficients to be adjusted to fit observations, which stand, respectively, for an isotropic, roughness and volume scattering contribution to reflectance.

CYCLOPES k_0 datasets over a 30 days temporal window are available every 10 days. In particular, results presented in this paper use VGT data belonging to July 2003. VGT provides information on the reflectance in four spectral channels: B0 (0.43-0.47 μm), B2 (0.61-0.68 μm), B3 (0.78-0.89 μm) and MIR (1.58-1.75 μm), with a spatial resolution of 1 km.

Using k_0 as input of VMESMA solves the main drawback of the SMA approach, which is related to the different acquisition geometry in the data. As it is widely reported, the anisotropic effects on reflectance data due to sun and view geometry should be addressed before applying spectral based methodologies to derive vegetation parameters with better accuracy, especially over areas affected by land degradation processes [19], [20], [21].

3.3 EMs extraction

The key to obtain successful VMESMA results is an appropriate EMs selection. Selecting EMs involves identifying the number of EMs and their corresponding spectral signatures. There are many different methods developed in the literature to deduce the EMs. Some methods extract them simply from the image using known spectral signatures of surface dominant cover types. Other techniques such as principal components analysis enclose the cloud of pixel spectra within a solid geometric figure whose number of vertex is equal to the dimensionality of the basis space**.**

In this study, we use a simple method to extract the vegetation and soil EMs in the image. This method is based on the NDVI and on the exploration of the reflectance triangle, which delimits the domain of variability of NIR and Red of a given vegetation canopy. NDVI provides very good separation for the two endmember types because of its sensitivity to the presence of vegetation. On the one hand, nonvegetated features are distributed in the bidimensional NIR-R space primarily along the soil line which conforms the base of the triangle. The signature variation for bare soils is primarily due to differences in physical composition (changes in soil colour, brightness, humidity, rugosity, etc.). On the other hand, green vegetation is represented in the NIR-R plane in the region located in the upper left part of the soil line.

This way, soil and vegetation endmembers are found in the upper right and upper left vertices of the reflectance triangle, respectively. First, we consider as potential vegetation EMs those surfaces with a NDVI higher than 0.8 and potential soil EMs those ones with a NDVI lower than 0.1 (Figure 2). Second, a study of the spectral distribution of potential vegetation and soil EMs is performed in order to select multiple (2-4) EMs of each class. After a study of sensibility, we concluded that the best VMESMA results (minimum RMS between modelled reflectances and VGT data) were obtained selecting 3 EMs of vegetation and 3 EMs of soil: those ones with the highest, lowest and medium spectral signature in the NIR-R space.

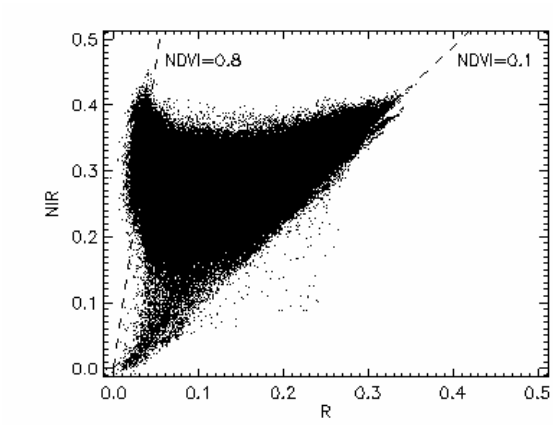

Figure 2. Spectral variation for vegetation and nonvegetation derived from a VGT image collected on July 2003 over the Iberian Peninsula. Dashed lines are NDVI isolines with values of 0.1 and 0.8, which provides good separation for endmembers of soil and vegetation.

3.4. Evaluation of the algorithm

In a first stage, the comparison is done for the Iberian Peninsula by computing different statistical indicators (e.g. mean, stdv, rmse biass, and correlation coefficient) for both FVC products. On the other hand, the evaluation of the algorithm is done over the selected *hot spot* area in order to analyse the performance of the model in the land degradation process detection. The VMSEMA product is compared with a ground-truth FVC product derived from in-situ measurements acquired during the SPARC field camping [22]. The reference map is simultaneous to the VGT data and is obtained from a semi-empirical approach that relates the in-situ measurements with the co-located radiometric SPOT4-HRVIR2 values [23] and [24]. The in-situ measurements are obtained from a method based on the estimation of the gap fraction [25], a directional hemispherical camera [26].

4 RESULTS AND DISCUSSION

Figure 3 shows the VMESMA FVC product (left) along with the histograms corresponding to both CYCLOPES and VMESMA FVC version 1 products over the Iberian Peninsula (right). The VMESMA FVC map clearly reproduces the FVC gradient extended over the Iberian Peninsula from North to South as well as it is possible to detect the *hot spot* area (e.g. red square on figure 3). Both products shows similar means (0.34 and 0.30) and standard deviations (0.24 and 0.21) with differences lower than 10% in terms of the rmse and biass. On the other hand, both histograms provide a similar distribution of FVC values between 0.2 and 0.6 (intermediate cover levels). The main differences from both products refer to very low (FVC<0.2) and very high (FVC>0.6) cover levels. The VMESMA FVC gives a major proportion of FVC low values and reaches FVC values of almost one. Meanwhile, the CYCLOPES FVC product shows a maximum between 0.6 and 0.8 values.

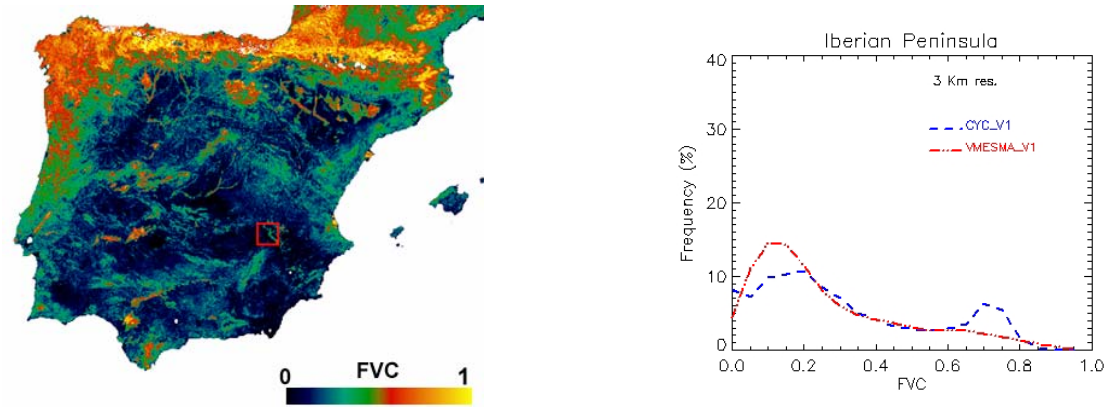

Figure 3. VMESMA FVC map mean and standard deviation for the Iberian Peninsula. Figure on the right shows the histogram distribution of VMESMA (red line) and CYCLOPES FVC (blue line) products.

On the other hand, the model performance in semiarid areas is assessed form an early comparison between the VMESMA FVC product and the ground-truth information over the Barrax site. In the comparison, the CYCLOPES product is also included for this area. Both products are degraded to a spatial resolution of 3 km. Figure 4 shows a RGB composite image belonging to 20 m spatial resolution SPOT4-HRVIR2 image (a), the FVC ground-truth map (b), the VMESMA FVC product (c) and the CYCLOPES FVC product (d) for the *hot spot* area. In a first stage, the three main cover types found in the area, crops (red and yellow colours), soil (blue an black colours) and mixed forest (green colours) can be observed on the products. Although both algorithms provide similar mean values (table 1), the VMESMA product is slightly higher but more correlated (R=0.72) with the ground-truth information than the CYCLOPES product (R=0.34) (table 1 and figure 6). A poor correlation is found for the CYCLOPES product, which not reproduces adequately the fraction cover of this area.

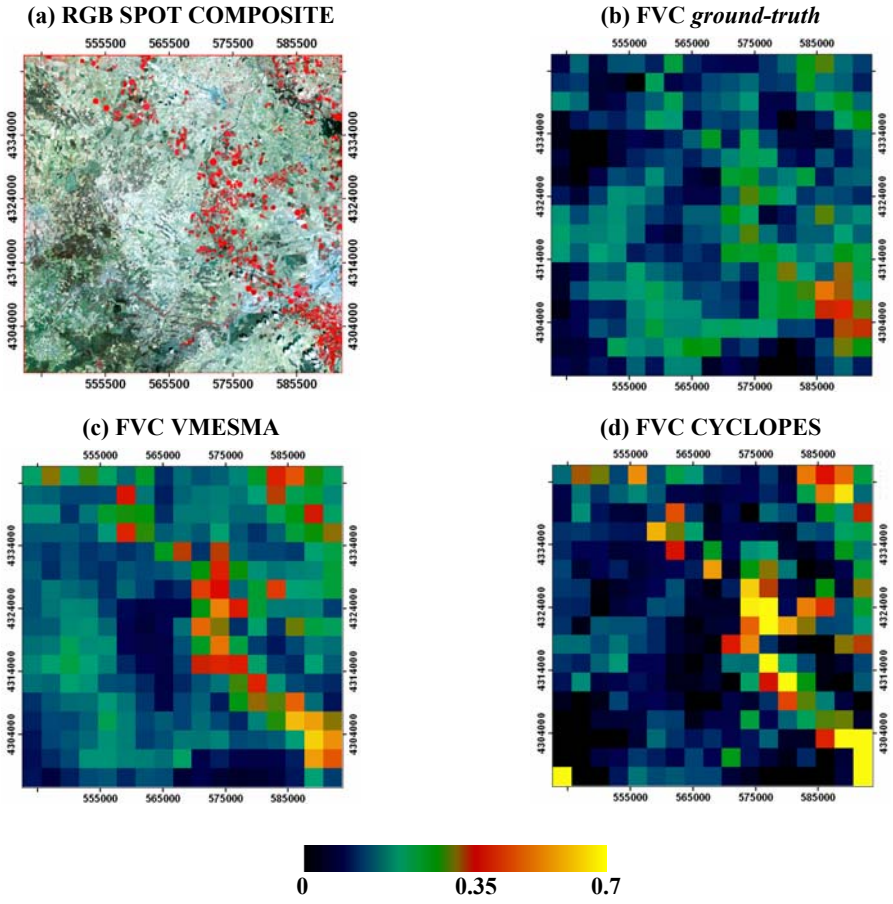

Figure 4. RGB composite image belonging to 20 m spatial resolution SPOT4-HRVIR2 image (a), the FVC ground-truth map (b), the VMESMA FVC product (c) and the CYCLOPES FVC product (d) for the *hot spot* area.

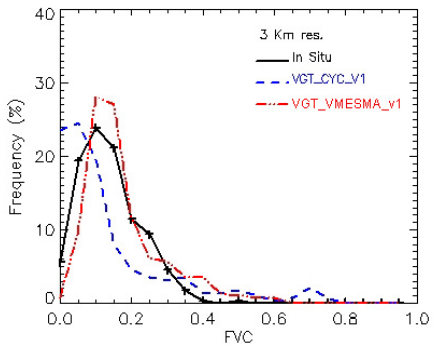

Figure 5. VMESMA and CYCLOPES FVC histograms for the selected *hot spot* area.

Table 1. Mean and stdv corresponding to the ground-truth, VMESMA and CYCLOPES FVC products for the hot spot area of Castilla-La Mancha. The correlation coefficient (R) and rmse for VMESMA and CYCLOPES versus the ground-truth product are also included.

	FVC *Ground truth*	**FVC VGT_ VMESMA_v1**	**FVC VGT_ CYC_v1**
Mean	0.16	0.19	0.16
Stdv	0.09	0.11	0.17
rmse	-	0.086	0.166
R	-	0.72	0.34

Figure 6. Scatter plots for the VMSEMA FVC and CYCLOPES FVC products versus the ground-truth FVC product for the selected *hot spot* area.

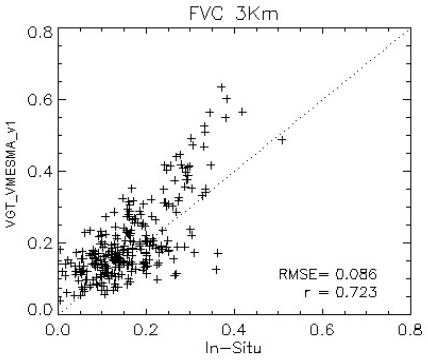

5 CONCLUSIONS

In this work, the optimised variable and multiple spectral mixture analysis (VMESMA) has been applied on VEGETATION/SPOT data in order to retrieve the FVC parameter from spectral information. The main objective has been focused on the performance of the model to retrieve vegetation parameters over areas affected by land degradation processes (i.e., *hot spot* areas).

Special attention has given to describe the model theoretical basin and the different steps required to apply it. The study has included a simple method to extract the vegetation and soil EMs in the image based on the NDVI and on the exploration of the reflectance triangle. The best VMESMA results have been obtained after selecting 3 EMs of vegetation and 3 EMs of soil: those ones with the highest, lowest and medium spectral signature in the NIR-R space. Otherwise, more investigations are under study to develop more a operational EMs extraction method.

Finally, an early evaluation has been carried out over the Iberian Peninsula and a *hot spot* area affected by land degradation processes (Barrax site). The study has included the comparison with the FVC product derived from the CYCLOPES algorithm. The evaluation over the *hot spot* area has included FVC ground-truth information. The results show the VMSEMA as an appropriate approach to reproduce the FVC conditions over the Iberian Peninsula as other currently-used methods. At the *hot spot* area, the high correlation between the VMESMA FVC and ground-truth products shows a high feasibility on the VMESMA algorithm to detect land degraded areas.

6 ACKNOWLEDGMENTS

This work has been supported by DESURVEY, IDEAS (REN2002-01495) and TEDECVA (GV2004-B-191) projects. Special thanks are given to the CYCLOPES project from INRA/Avignon to provide us the VEGETATION/SOPT data base used in this work.

REFERENCES

[1] UNCED, United Nations Conference on Environment and Development (Earth Summit'92), "Managing fragile ecosystems: Combating desertification and drought", 1992.

[2] THOMAS, D.S.G. 1997: Science and the desertification debate. *Journal of Arid Environments*, *37,* pp. 599-608.

[3] ELVIDGE, C.D., CHEN, Z., AND GROENEVELD, D.P., 1993: Detection of trace quantities of green vegetation in 1990 AVIRIS data. *Remote Sensing of Environment. 44*, pp. 271-279.

[4] HUETE, A.R. 1988. A soil-adjusted vegetation index (SAVI). *Remote Sensing and Environment, 25*, pp. 295-309.

[5] GARCÍA-HARO, F.J., GILABERT, M.A. AND MELIÁ, J., 1996: Linear spectral mixture modelling to estimate vegetation amount from optical spectral data. *International Journal of Remote Sensing*, *17(17)*, pp. 3373-3400.

[6] SMITH, M.O., SUSAN, L.U., ADAMS, J.B. AND GILLESPIE, A.R., 1990: Vegetation in deserts: I. A regional measure of abundance from multispectral images. *Remote Sensing of Environment*, *31*, pp. 1-26.

[7] ROBERTS, D.A., GARDNER, M., CHURCH, R., USTIN, S., SCHEER, G. AND GREEN, R.O., 1998: Mapping chaparral in the Santa Monica mountains using multiple endmember spectral mixture models. *Remote Sensing of Environment*, *65*, pp. 267-279.
[8] KLEIN-GEBBINCK, M.S., 1998: Decomposition of mixed pixels in remote sensing images to improve the area estimation of agricultural fields. Ph.D. thesis, University of Nijmegen, Renkum, Holland, 165 pp.
[9] GARCÍA-HARO, F.J, SOMMER, S. AND KEMPER, T., 2005: Variable multiple endmember spectral mixture analysis (VMESMA), *International Journal of Remote Sensing*, *26*, pp. 2135-2162.
[10] CAMACHO-DE COCA, F., GARCÍA-HARO, F.J., GILABERT, M.A., AND MELIÁ, J. 2004: Vegetation cover seasonal changes assessment from a tm imagery in a semiarid landscape. *International Journal of Remote Sensing, 25*, pp. 3451-3476.
[11] ELMORE, J.A., MUSTARD, J.F., MAINNING, S.J., AND LOBELL, D.B., 2000: Quantifying vegetation change in semiarid environments: precision and accuracy of spectral mixture analysis and the Normalized Difference Vegetation Index. *Remote Sensing of Environment, 73*, pp. 87-102.
[12] MORENO, J., CALERA, A., CASELLES, V., CISNEROS, J.M., MARTINEZ-LOZANO, J.A., MELIÁ, J. MONTERO, F. AND SOBRINO, J., 2001: The measurements programme at Barrax. ESA-DAISEX proceedings, ESA SP-499, 43-52.
[13] BOLLE, H.J., ET AL., 1993: EFEDA: European field experiment in a desertification-threatened area. *Annales Geophysical*, pp. 173-189.
[14] ROUJEAN, J.L. AND LACAZE, R., 2002: Global mapping of vegetation parameters from POLDER multiangular measurements for studies of surface-atmosphere interactions: A pragmatic method and its validation. *Journal of Geophysical Research, 107D*, pp. 10129-10145.
[15] ICHOKU, C. AND KARNIELI, A., 1996: A review of mixture modeling techniques for sub-pixel land cover estimation. *Remote Sensing Reviews*, *13*, pp. 161-186.
[16] BOARDMAN, J.W., 1989: Inversion of Imaging Spectrometer Data using Singular Value Decomposition, Proceedings of the IGARRS '89, Twelfth Canadian Symposium on Remote Sensing, vol. 4, pp. 2069-2072.
[17] GARCÍA-HARO, F.J., 1997: Modelización y estimación de parámetros relacionados con la cubierta vegetal en teledetección. Tesis Doctoral. Universitat de València.
[18] SHIMABUKURO, Y.E. AND SMITH, A.J., 1991: The least-squares mixing models to generate fraction images derived from remote sensing multispectral data. *IIEE Transactions of Geoscience and Remote Sensing*, *29*, pp. 16-20.
[19] ROUJEAN, J.-L., LEROY, M., AND DESCHAMPS, P.-Y., 1992: A bidirectional reflectance model of the Earth's surface for the correction of remote sensing data. *Journal of Geophysical Research, 97(D18)*, pp. 20455–20468.
[20] GOWARD, S.N., DYE, D.G., TURNER, S., AND YANG, J., 1993: Objective assessment of the NOAA global vegetation index data product. *International Journal of Remote Sensing, 14*, pp. 3365–3394.
[21] CHOPPING, M.J., RANGO, A., HAVSTAD, K.M., SCHIEBE, F.R., RITCHIE, J.C., SCHMUGGE, T.J., FRENCH, A.N., SU, L., MCKEE, L. AND DAVIS, M. R., 2003: Canopy attributes of desert grassland and transition communities derived from multiangular airborne imagery. *Remote Sensing of Environment*, *85*, pp. 339-354.
[22] MARTÍNEZ, B., BARET, F., CAMACHO-DE COCA, F., GARCÍA-HARO, F.J., VERGER, A. AND MELIÁ, J., 2004: Validation of MSG vegetation products. Part I: Field retrieval of LAI and FVC from hemispherical photographs. *Proceedings of the Remote Sensing for Agriculture, Ecosystem and Hydrology*. SPIE. Gran Canarias. Vol. 5232, pp. 57-68.
[23] BARET, F et al., 2004: VALERI: a network of sites and a methodology for the validation of land satellite products. *Remote Sensing of Environment.* (in press).
[24] MARTÍNEZ, B., CAMACHO-DE COCA, F., AND GARCÍA-HARO, F.J., 2005: Estimación de parámetros biofísicos de la cubierta vegetal a alta resolución a partir de medidas *in-situ* obtenidas en SPARC'03. XI Congreso Nacional de Teledetección, 21-23 septiembre 2005.Puerto de la Cruz. Tenerife.
[25] ROSS, J., 1981: The radiation regime and architecture of plant stands, The Hague, 391 pp.
[26] RICH, P.M., 1990: Characterizing plant canopies with hemispherical photographs. *Remote Sensing Reviews*, *5*, pp. 13–29.

Backscatter Model Inversion Estimation and Geostatistical Characterization of Soil Moisture

A. Merzouki[a], A. Bannari[a], P.M. Teillet[a,b] and D.J. King[c]

[a] Remote Sensing and Geomatics of Environment Laboratory, Geography Department, Ottawa-Carleton Geoscience Centre, University of Ottawa, P.O. Box 450, Ottawa (Ontario), Canada K1N 6N5, email: amerz088@uottawa.ca
[b] Canada Centre for Remote Sensing, 588 Booth Street, Ottawa (Ontario), Canada K1A 0Y7
[c] Department of Geography and Environmental Studies, Carleton University, 1112 Colonel By Drive, Ottawa (Ontario), Canada K1S 5B6

ABSTRACT

This paper reports on a study to evaluate the capability of Radarsat-1 C-band Synthetic Aperture Radar observations to quantify the spatial variability of soil moisture. Radar images were acquired during five different periods over the Roseau River watershed in southern Manitoba, Canada. For validation purposes, ground measurements were carried out at 62 locations simultaneous with satellite data acquisitions. A comparison was made between backscatter coefficient results from simulations using the Integral Equation Model (IEM) and estimates based on SAR image data. A statistically significant improvement in agreement was found using the IEM semi-empirical calibration technique. This calibrated model was then implemented in a simplex inversion routine in order to estimate and map soil moisture. Derived spatial patterns of near-surface moisture content were then examined using an exponential semivariogram model for spatial extents ranging from tens of meters to kilometers. Despite quite different soil proprieties, similarities were found between the semivariogram range results (around 100 m) and those reported in the literature. A significant exponential fit was obtained between the range and the spatial extent of the semivariance analysis, with coefficients of determination R^2 exceeding 0.90.

Keywords: Soil moisture, backscatter models, Radarsat-1, semivariogram, extent analysis.

1 INTRODUCTION

Soil moisture is a key variable in many environmental sciences, including hydrology, climatology and agriculture. Even though it represents a small proportion of the liquid freshwater on Earth (0.15 %), it plays an important role in controlling the partitioning of precipitation into ground water storage and runoff [1]. In addition, it modulates interactions between the land surface and the atmosphere, thereby influencing climate and weather [2]. Experiments undertaken in the 1970s demonstrated the sensitivity of radar backscatter to soil moisture conditions [3]. Recent advances in active microwave remote sensing have confirmed the potential for using satellite data for the generation of soil moisture maps at different scales [4].

A large number of studies have been undertaken in order to establish a relationship between the observed synthetic aperture radar (SAR) response and the soil parameters. From an application perspective, the retrieval of such parameters requires the use of theoretical, empirical or semi-empirical models. In this study, we focus on one of the most widely used models for retrieving soil surface parameters, which is adapted to randomly dielectric rough surfaces [5]: The Integral Equation Model (IEM). In a broad sense, it can be applied to simulate the backscattering behaviour for the wide range of surface roughness values usually encountered in agricultural settings.

This paper reports on an investigation of the potential of Radarsat-1 C-band SAR to provide accurate spatial characterization of soil moisture. Initially, comparison was made between IEM simulation results and SAR responses. In order to reduce the surface roughness effect on radar backscatter behaviour, the empirical calibration technique proposed by Baghdadi *et al.* [6] was implemented for a first dataset covering three SAR image acquisitions. A second dataset was used for validation purposes. Then, a one-dimensional simplex algorithm was applied to experimental data to extract soil moisture maps. Secondly, we used semivariogram analysis to address

the issue of the spatial variability of soil moisture and, in particular, examined the relationship between the semivariogram range and the spatial extent over which the semivariogram was derived.

2 DATASETS

2.1 Study Site

The study site is located in the Canadian part of the Roseau River watershed, which is a part of the Red River basin. This area covers approximately 2400 km^2 in Southern Manitoba; the remainder of the basin is in Minnesota. The Roseau River follows a general north-westerly course covering about 290 km from source to mouth. It crosses the Canada-U.S. boundary at about the midpoint of its course and enters the Red River about 24 km north of the border. Sprague and Pine Creeks, which are located in the eastern headwaters of the watershed, are the only major Roseau River tributaries originating in Canada. Except for a few abrupt elevation changes in the northeast sector, the main valley is flat with few prominent topographic features. As a result, water does not always drain naturally from the land and water-saturated soils are characteristic of the Roseau River basin. As presented in figure 1, a variety of soil types are present throughout the study area, including organic soils, silty loams, sandy soils and clay soils. The western portion is dominated by rich clay soils, ideal for agriculture. Towards the east, the soil gradually changes to silty loams with pockets of sandy soils. The eastern portion consists of silty to clay loams.

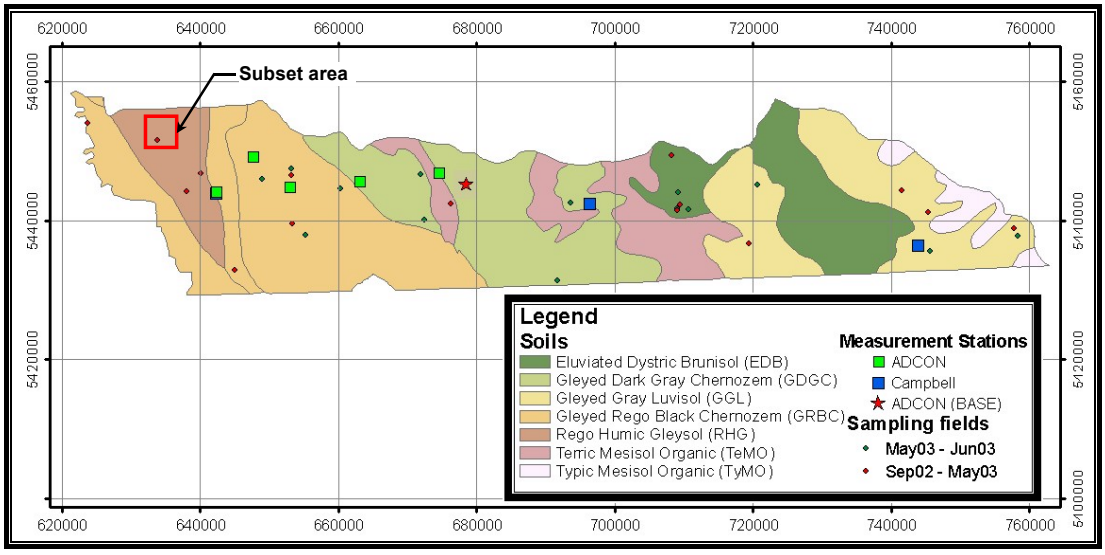

Figure 1: Sampling sites and monitoring station locations in Canadian portion of the Roseau River basin.

In general the climate of south-eastern Manitoba is classified as sub-humid to humid continental with resultant extreme temperature variations. Annually, most of the precipitation is in summer rather than winter. Approximately 75 % of the 50 cm of average annual precipitation occurs from April to September. However, there are weather conditions that periodically promote widespread flooding through the valley [7].

2.2 Data Description

2.2.1 SAR data and image pre-processing

Radarsat-1 is equipped with a SAR operating at 5.3 GHz (C-band) with horizontal-horizontal polarization. The wide beam mode (W1) was selected for this study because its swath covers the full Roseau River basin, with an incidence angle ranging from 20^o to 31^o and a nominal spatial resolution of 30 m. The ascending orbit for Radarsat-1 has an early evening local crossing time and was selected to avoid the effect of early morning dew on the backscatter process. Radar images were acquired during five field campaigns in non-winter months between October 2002 and June 2003 (Table 1). The SAR images were calibrated to backscatter coefficients, σ^o (in Decibels), using Shepherd's method [8]. This procedure was implemented using the Radarsat module included in PCI software, which automatically generates the calibration data. These images were geometrically corrected and georeferenced using a set of 20 ground control points marked on a georeferenced 15 m panchromatic Landast-7 ETM+ image. The control points were evenly distributed and the average root-mean-square (RMS) error was found

to be less than one pixel in both X and Y directions for all SAR images. The image registrations were performed using a second-order polynomial transformation and nearest neighbour resampling.

Table 1. Radarsat-1 SAR image acquisition details for the Roseau River basin study site.

	Acquisition date	Day of year	Acquisition time (UTC)	Scene centre (Lat./Long.)
First dataset	**October 1, 2002**	274	0:01:50	48° 52' N / 95° 56' W
	October 25, 2002	298	0:01:48	48° 54' N / 95° 56' W
	April 11, 2003	101	0:02:44	48° 55' N / 95° 57' W
Second dataset	**May 5, 2003**	125	0:02:44	48° 55' N / 95° 57' W
	June 22, 2003	173	0:02:45	48° 55' N / 95° 57' W

2.2.2 Field selection and ground data acquisition

Apart from soil moisture and surface roughness, radar backscatter from agricultural fields is also affected by vegetation cover, plant water content and crop residue [9-11]. Hence, for this study, only bare fields were selected. The general criteria for field selection were: good distribution across the basin, three to four fields per soil type, and large homogeneous fields with minimal crop residue. Therefore, for the selected fields, soil moisture and surface roughness effects will dominate the backscatter response.

A total of eight measurement stations were installed in September 2002 and remained in their original location until June 2003 (Figure 1). These stations continuously measured soil moisture, soil temperature, air temperature, wind speed, wind direction, snow depth, radiation and precipitation. A Campbell Scientific station was installed in each of the three representative areas. Five Adcon stations plus a base station were deployed in the basin, constituting an autonomous wireless sensorweb prototype [12,13] that sent data in real time to a workstation in Ottawa.

Field measurement campaigns were carried out on SAR data acquisition dates. The measurements included soil moisture content and surface roughness. A total of 22 sampling fields were used in autumn 2002 and 14 fields in spring 2003 (Figure 1). In most cases, the fields selected in September 2002 were bare until May 2003. In the spring, new fields were selected to replace those that had been seeded, had emerging crops, or were overgrown with weeds.

Surface roughness measurements were taken at 62 sites in the selected fields using the SRM-200 surface roughness meter [14]. This instrument consists of a tripod mounted with a camera, flash and projector. The tripod is draped with a shroud to create a portable darkroom. A rectangle of light (50 mm x 100 mm) is projected on the ground when the flash is activated and an oblique photo of the ground is taken. The photograph is subsequently scanned and special software used to extract surface roughness parameters [14] RMS height (s) and correlation length (ℓ). Measurements were taken in the look direction of the radar (74 degrees azimuth with respect to true north). Care was taken to select sampling locations representative of the entire field. Three sampling points were established for each location. The sampling points were a minimum of 5 metres apart. Two measurements were obtained at each sampling point, thus yielding six surface roughness profiles per site.

Near-surface volumetric soil moisture content was measured for the top 6 cm for all sites using a portable Time Domain Reflectometer (TDR). Five sampling points were established along a transect line at each site. The sampling points were at least 5 metres apart. Readings at each point were taken in replicates of three within a one-metre radius. This resulted in a total of 15 soil moisture samples per site. Meteorological constraints were taken into consideration to achieve unbiased sampling results. I.e., soil sampling was not undertaken during periods of intense rainfall, prolonged freezing, or under snow cover. More details on the data collection design can be found in Deschamps [15].

3 ANALYSIS METHODOLOGY

The first step in this analysis was to assess the performance of the IEM in simulating the backscatter coefficients for the selected bare soils. Model simulations were performed using field data as well as Radarsat-1 SAR configuration parameters (frequency, polarization and local incidence angle). The model developed by Peplinski *et al*. [16] was used to obtain the relative soil dielectric constant, which is based on the volumetric water content. According to the literature, this semi-empirical mixing model is the most commonly used. Moreover, it has the widest validity range

in terms of soil properties and radar observation frequencies. In order to improve the performance of IEM, we decided to use the semi-empirical calibration approach proposed by Baghdadi *et al.* [6]. This technique introduces an optimal roughness correlation length (ℓ_{opt}). The performance of the model simulations was investigated using the root mean square error (*RMSE*) index in order to quantify the magnitude of the average errors.

Secondly, we attempted to retrieve near-surface moisture content by inverting the backscatter model. In the inversion procedure, the calibrated IEM was constrained by the experimental radar backscatter coefficients and parameters measured during the field campaigns. Inversion was based on a one-dimension simplex algorithm routine [17]. This technique is widely used for nonlinear optimization, since it requires less a priori information and finds the optimum solution more precisely than other techniques [18]. The implemented direct search algorithm attempts to minimize, in terms of the least squares criterion, a scalar value representing the difference between measured and simulated backscatter coefficients.

The spatial variability of the moisture content of the upper soil layers was investigated using geostatistical tools. Such analysis requires autocorrelation statistics to be obtained for each soil moisture map. For this purpose, experimental semivariograms were calculated for different sample spatial extents using pairs separated by a constant lag (~ 30 m), which represents the nominal cell resolution of Radarsat-1 W1 mode. In most practical applications, the experimental semivariance as a quantification of the spatial correlation structure at a given distance h is given by [19]:

$$\gamma(h) = \frac{1}{2N} \sum_{i=1}^{N} \left[Z(x_i) - Z(x_i + h) \right]^2 \quad (1)$$

where N is the number of pairs separated by the distance h and $Z(x_i)$ is the value of the soil moisture at location x_i. In order to quantify the major spatial features, an exponential model with a nugget component was fitted to the experimental semivariograms. This model is defined as [20]:

$$\gamma(h) = n + c\left[1 - exp(-h/r)\right] \quad (2)$$

where n is the nugget variance at zero distance due to subscale variability and errors, c is the sill where the semivariance reaches a plateau, and r is the practical correlation length that represents the third of the range where the semivariance approaches the sill asymptotically.

4 RESULTS AND DISCUSSION

Two datasets were used in this study. The first was acquired during three different periods from October 2002 to April 2003. The second was obtained within two field campaigns (5 May 2003 - 22 June 2003). In figure 2, roughness RMS heights (s) are plotted against measured correlation lengths (ℓ) for the first dataset. A clear decorrelation between the two roughness parameters is found, which is assumed to be essentially due to the imprecision of the roughness measurement technique and which can affect the accuracy of IEM simulations. Therefore, Baghdadi *et al.* [6] proposed a modeled calibration parameter (ℓ_{opt}) that incorporates the optimum correlation length in backscatter coefficients calculation. This optimum parameter is obtained by forcing the IEM until a good agreement is reached between simulations and SAR image data. These calculations were performed

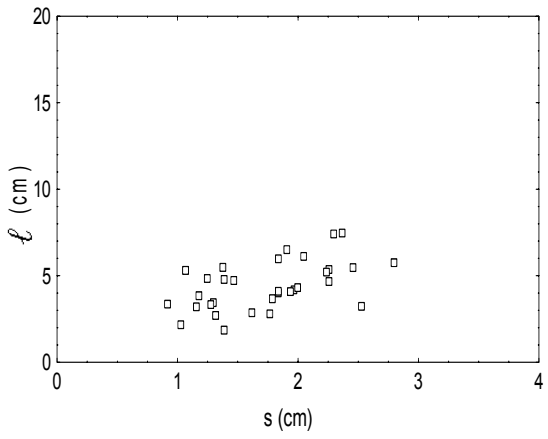

Figure 2. Plot of RMS height (s) versus measured correlation length (ℓ) for the first dataset.

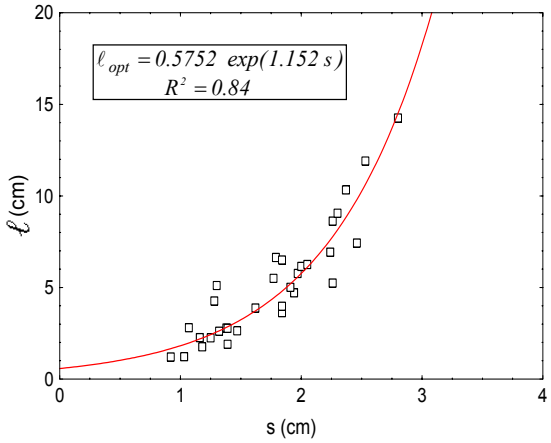

Figure 3. Plot of RMS height (s) versus modeled correlation length (ℓ) for the first dataset. The exponential fit model is superposed.

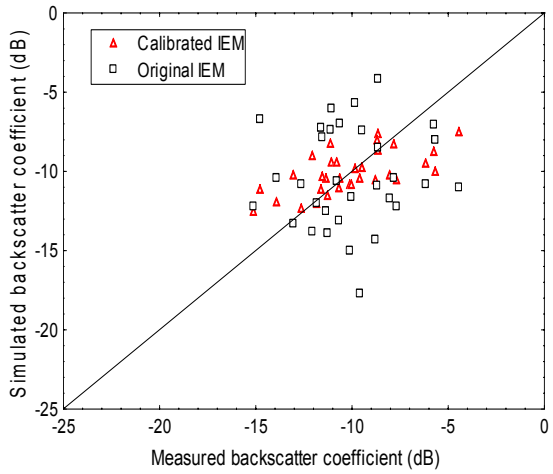

Figure 4. Simulated backscatter coefficient using calibrated and original IEM versions as a function of the measured backscatter coefficient obtained from first dataset SAR images.

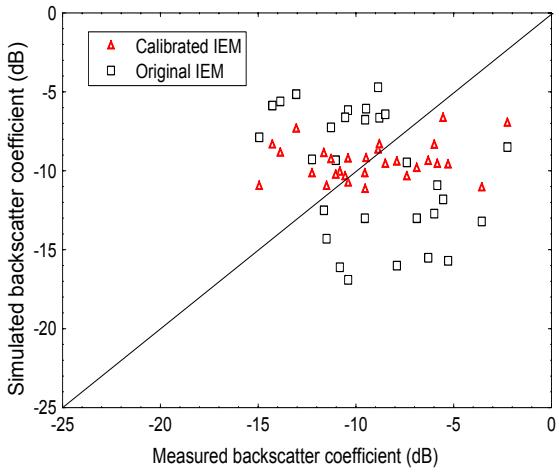

Figure 5. Simulated backscatter coefficient using calibrated and original IEM versions as a function of the measured backscatter coefficient obtained from second dataset SAR images.

involving measured RMS roughness height as well as soil moisture content as ground data input parameters. To quantify the relationship between roughness RMS height and modeled optimal correlation length illustrated in figure 3, an exponential law was fitted empirically, yielding a good coefficient of determination ($R^2 = 0.84$).

Table 2. Summary of *RMSE* (dB) for the calibrated and original IEM simulations for the first and second datasets.

	Model	RMSE (dB)
First dataset	**IEM**	3.85
	Calibrated IEM	1.97
Second dataset	**IEM**	5.85
	Calibrated IEM	3.09

Figure 4 (first dataset) and figure 5 (second dataset), compare the measured and simulated backscatter coefficients for the original IEM, where ℓ values are those measured in each sampling site, and the calibrated version of IEM, where ℓ values are replaced by the optimum values ℓ_{opt}. In order to test the efficiency of the calibration technique, a validation was undertaken using the two datasets acquired over the study site. The associated statistical calculations are summarized in Table 2. Overall, a better agreement was found between the calibrated IEM results and SAR-based backscatter coefficients compared to the original IEM version simulations (Table 2). The results obtained from the calibrated IEM improve the estimation by 49 % and 47 % in terms of agreement for the first and second datasets, respectively. This result is not surprising, since previous studies have

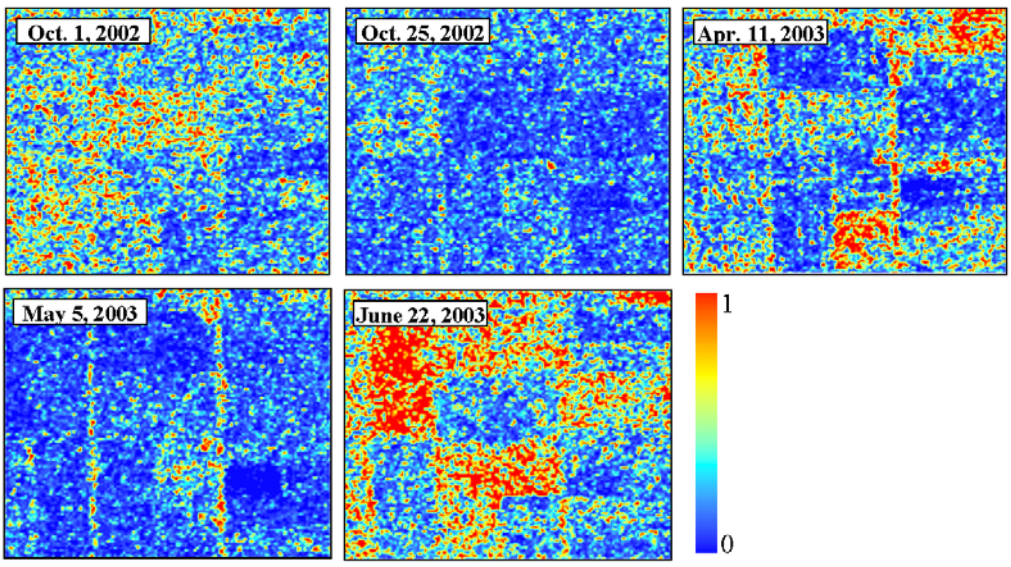

Figure 6. Retrieved soil moisture maps obtained by inverting the calibrated IEM.

shown that correlation length measurements are very sensitive to profile length [21] and relatively short lengths were used in this study (10 m). Baghdadi *et al.* [22] and Oh and Kay [23] have shown that the use of short profiles (< 10 m) yields a low precision in correlation length measurement (between 10 % and 40 %). This could explain the discrepancy between the measured backscatter coefficients and the original IEM simulations results.

Since low incidence angle configurations are better for the estimation of near-surface soil moisture [24], SAR image subsets were selected from the western side of the study site (figure 1). Moreover, soil roughness will contribute less to the backscatter coefficient near the nadir. Soil moisture maps were, then, computed by inversion of the calibrated IEM as illustrated in figure 6. There are clear differences in the spatial variability patterns of soil water content between the obtained maps. High moisture levels were depicted over the considered area during the third (11 April 2003) and the fifth (22 June 2003) acquisition dates, while during the second (25 October 2002) and the fourth (5 May 2003) acquisition periods apparent dry conditions were observed in the landscape with a relatively spatial uniform distribution.

Figure 7 shows the relationship between semivariogram extent and calculated correlation range associated with all the soil moisture maps. Despite quite different soil proprieties and for the same spatial extent of the semivariogram calculations (~ 300 m, which is equivalent to 10 lags), the correlation range results from this study are similar to those reported by previous ground-based investigations [20, 25]. The semivariogram correlation ranges vary between 95 and 140 m, except for the fifth soil moisture map, corresponding to the last radar acquisition, which presents a consistently higher value: ~ 250 m (figure 7). This discrepancy occurs because a highly wet saturated pattern appears within the subset study area. Moreover, it shows that, in this case, the surface soil moisture was not normally distributed, which invalidates the semivariogram method [20]. We examined the relationship between correlation range and sample spatial extent for each soil moisture map. It was possible to discern reliable relationships (figure 7) that can be modeled by an exponential function ($R^2 > 0.90$).

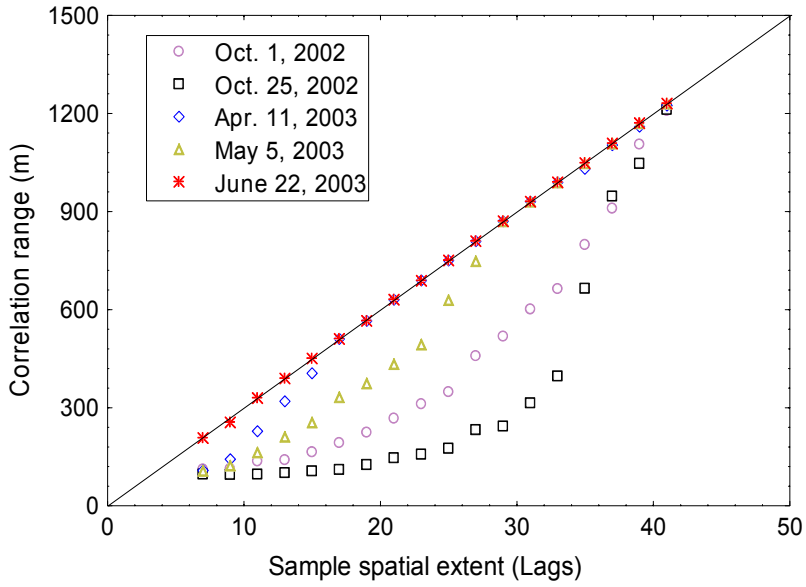

Figure 7. Correlation range versus semivariogram spatial extent (number of lags) for all retrieved soil moisture maps.

5 CONCLUSIONS

In this paper, we presented a methodology to monitor the spatial variability of the near-surface soil moisture over large scales. The adopted retrieval technique consists of inverting the calibrated version of IEM. This model has provided significant improvement in the simulation of backscatter coefficients. By using a second Radarsat-1 SAR dataset for validation, it was possible to confirm the robustness of this semi-empirical calibration.

An inversion algorithm based on the simplex technique was implemented in order to estimate the soil moisture parameter. The near surface moisture distribution over the selected area appears to be very complex, having both a temporal and spatial variability pattern. Nevertheless, during relatively dry periods, analyses based on semivariogram calculations of soil moisture at variable spatial extent were highly consistent. I.e., the correlation

range results were found to be strongly dependent on semivariogram sample spatial extent according to an exponential law. The correlation ranges calculated in this study were found to be similar to those obtained in other investigations (~ 100 m).

REFERENCES

[1] JACKSON, T.J.; SCHMUGGE, J., AND ENGMANN, E.T., 1996: Remote sensing applications to hydrology: Soil moisture. *Hydr. Sc., 41*, pp. 517-530.
[2] ENTEKHABI, D., 1995: Recent Advances in Land-Atmosphere Interaction Research. *Rev. of Geoph., 33*, pp. 995-1004.
[3] ULABY, F.T., CIHLAR, J. AND MOORE, R.K., 1974: Active microwave measurement of soil water content. *Rem. Sens. of Env., 3*, pp. 185-203.
[4] WIGNERON, J.P, CALVET, J.C., PELLARIN, T., VAN DE GRIEND, A.A., BERGER, M. AND FERRAZZOLI, P., 2003: Retrieving near-surface soil moisture from microwave radiometric observations: Current status and future plans. *Rem. Sens. of Env., 85*, pp. 489-506.
[5] FUNG, A.K., LI, Z. AND CHEN, K.S., 1992: Backscatter from a randomly rough dielectric surface. *IEEE Trans. on Geosc. & Rem. Sens., 30*, pp. 356-369.
[6] BAGHDADI, N., GHERBOUDJ, I., ZRIBI, M., SAHEBI, M., KING, C. AND BONN, F., 2004: Semi-Empirical Calibration of the IEM Backscatter Model using Radar Images and Moisture and Roughness Field Measurements. *Int. J. Rem. Sens., 25*, pp. 3593-3623.
[7] OSWALD, T.M., SIMONOVIC, S.P. AND SINCLAIR, J., 1999: A preliminary assessment of the effectiveness of flood damage reduction measures in Canada. Office of Critical Infrastructure Protection and Emergency Preparedness, Environment Canada, Canada, D82-48.
[8] SHEPHERD, N., 2000: Extraction of beta nought and sigma nought from Radarsat CDPF products. ALTRIX Systems Ltd., Ottawa, Ontario, Canada, Report AS97-5001, Rev. 4.
[9] MCNAIRN, H., BROWN, R.J., BRISCO, B., DUGUAY, C., BOISVERT, J.B. AND PULTZ, T.J., 1998: Reviewing the role of radar in mapping soil management practices. In: First International Conference: Geospatial Information in Agriculture and Forestry, Orlando, USA, 6 pp.
[10] DE ROO, R.D., DU, Y., ULABY, F.T. AND DOBSON, M.G., 2001: A Semi-empirical backscatter model at L-band and C-band for a soybean canopy with soil moisture inversion. *IEEE Trans. on Geosc. & Rem. Sens., 39*, pp. 864-872.
[11] ZRIBI, M., LE HÉGARAT-MASCLE, S., OTTLÉ, C., KAMMOUN, B. AND GUERIN, C., 2003: Surface soil moisture estimation from the synergistic use of the (Multi-incidence and multi-resolution) active microwave ERS wind scatterometer and SAR data. *Rem. Sens. of Env., 86*, pp. 30-41.
[12] TEILLET, P.M., GAUTHIER, R.P., FEDOSEJEVS, G., MALOLEY, M., CHICHAGOV, A. AND AINSLEY, G., 2003a: A soil moisture monitoring sensorweb demonstration in the context of integrated Earth sensing. Proc. SPIE Conference 5151 on Sensors, Systems, and Next-Generation Satellites VIII, pp. 63-73.
[13] TEILLET, P.M., GAUTHIER, R.P., PULTZ, T.J., DESCHAMPS, A., FEDOSEJEVS, G., MALOLEY, M., AINSLEY, G. AND CHICHAGOV, A., 2003b: A soil moisture sensorweb for use in flood forecasting applications. Proc. SPIE Conference 5232 on Remote Sensing, pp 467-478.
[14] JOHNSON, F., BRISCO, B. AND BROWN, R.J., 1993: Evaluation of limits to the performance of the surface roughness meter. *Can. J. of Rem. Sens., 19*, pp. 140-145.
[15] DESCHAMPS, A., 2004. Estimation of soil moisture from Radarsat and Envisat data on the Roseau river basin. Canada Centre for Remote Sensing, Earth Sciences Sector, Natural Resources Canada, Canada, Internal Report.
[16] PEPLINSKI, N.R., ULABY, F.T. AND DOBSON, M.C., 1995: Dielectric properties of soils in the 0.3-1.3 GHz range. *IEEE Trans. on Geosc. & Rem. Sens., 33*, pp. 803-807.
[17] NELDER, J.A. AND MEAD, R., 1965: A simplex method for function minimization. *Comp. J., 7*, pp. 308-313.
[18] LAGARIAS, J.C., REEDS, J.A., WRIGHT, M.H. AND WRIGHT, P.E., 1998: Convergence properties of the Nelder-Mead simplex method in low dimensions. *SIAM J. on Opt., 9*, pp. 112-147.
[19] CHILÈS, J.P. AND DELFINER, P., 1999: Geostatistics: Modeling Spatial Uncertainty. Wiley, New York.
[20] ANCTIL, F., MATHIEU, R., PARENT, L-É, VIAU, A.A., SBIH, M. AND HESSAMI, M., 2002: Geostatistics of Near-Surface Moisture in Bare Cultivated Organic Soils. *J. Hydr., 260*, pp. 30-37.
[21] DAVIDSON, M., LE TOAN, T., BORGEAUD, M. AND MANNINEN, N, T., 1998: Measuring the Roughness Characteristics of Natural Surfaces at Pixel Scales: Moving from 1 meter to 25 meter Profiles. Proc. IGARSS'98, pp. 1200-1202.
[22] BAGHDADI, N., PAILLOU, P., DAVIDSON, M., GRANDJEAN, G. AND DUBOIS, P., 2000: Relationship between profile length and roughness parameters for natural surfaces. *Int. J. Rem. Sens., 21*, pp. 3375-3381.

[23] OH, Y. AND KAY, Y., 1998: Condition for precise measurement of soil surface roughness. *IEEE Trans. on Geosc. & Rem. Sens., 36*, pp. 691-695.
[24] SAHEBI, M.R., ANGLES, J. AND BONN, F., 2002: A comparison of multi-polarization and multi-angular approaches for estimating bare soil surface roughness from spaceborne radar data. *Can. J. of Rem. Sens., 28*, pp. 641-652.
[25] WESTERN, A.W., BLÖSCHL, G. AND GRAYSON, R.B., 1998: Geostatistical characterization of soil moisture patterns in the Tarrawarra catchment. *J. Hydr., 205*, pp. 20-37.

Estimation of equivalent water thickness using radial basis function neural networks

D. Riaño[a,b], M.A. Patricio[b], P. Zarco-Tejada[c], C. Rueda[a], L. Usero[b] and S.L. Ustin[a]

[a] Calspace, University of California, 250-N, The Barn, One Shields Avenue
Davis, CA 95616-8527, USA, email: slustin@ucdavis.edu
[b] University of Alcala, Madrid, Spain
[c] Institute of Sustainable Agriculture, Córdoba, Spain

ABSTRACT

This paper presents the estimation of equivalent water thickness (EWT) at leaf and canopy level using radial Artificial Neural Networks (ANN). The ANN trained using real data, and a radiative transfer model "Leaf Optical Properties Spectra" (PROSPECT) with both providing good results (r^2=0.89, 0.91 and 0.92, respectively). We also tested if PROSPECT linked to a canopy radiative transfer model "light scattering by leaf layers with application to canopy reflectance modelling" (SAILH) could be use to predict EWT times Leaf Area Index (LAI). Results on independent random simulations were very good (r^2=0.89).

Keywords: Equivalent water thickness, radial basis function, artificial neural networks, radiative transfer model.

1 INTRODUCTION

Vegetation water content mediates the ability of fire to ignite and propagate [1]. The leaf equivalent water thickness (EWT), water per leaf area unit, is the variable most closely connected to vegetation reflectance [2]. Correspondingly, the spectral response at the canopy level seems to be related to the EWT times Leaf Area Index (LAI) [3]. Initially, vegetation water content was estimated using a statistical approach relating water content measured in the field to reflectance obtained using remote sensing [4]. Radiative transfer models have proven to be good tools to directly estimate water content [5-8]. EWT can be estimated by inverting the model. This method is computationally expensive since all possibilities are tested to identify the minimum error. Different techniques, using for example a merit function, were explored to perform a non-exhaustive search so computational time could be reduced [9]. This reduction still does not make the method applicable to full images. In this work "Leaf Optical Properties Spectra" (PROSPECT) was linked to a canopy radiative transfer model "light scattering by leaf layers with application to canopy reflectance modelling" (SAILH).

The work presented here explores the estimation of EWT using Artificial Neural Networks (ANN). This approach has been successfully applied to estimate LAI or related parameters [10-13]. These cases use only a few input variables. We also follow Fang and Liang [13], training the ANN with a radiative transfer model

2 METHODS

2.1 Analysis at leaf level

LOPEX dataset was produced during an experiment conducted by the Joint Research Center (JRC) of the European Commission (Ispra, Italy) [14]. We selected 49 broad leaf samples from 37 different species, collected over an area within 50 km range of the JRC, in Ispra. Each sample contained 5 fresh leaves from the same individual making a total of 245 leaves. Hosgood et al. [14] measured leaf spectral reflectance and transmittance and different biochemical constituents, including EWT. Spectral measurements were made every 1 nm between 400-2500 nm. Spectral data was interpolated to provide information comparable to the AVRIS sensor (http://aviris.jpl.nasa.gov), relative to its Full-Width Half-Maximum (FWHM). We obtained a total of 210 reflectance and transmittance values, having a total of 420 input variables to resample the spectral data.

We applied ANN to predict EWT on the LOPEX dataset using three different techniques:

- Trained with LOPEX dataset: ANN trained with all LOPEX samples but one each time. That is 48 samples, and a total of 240 leaves. The remaining sample was used for validation (leave one out cross-validation). The process was repeated for each sample performing a cross-validation.

- Trained with PROSPECT [5]: We ran PROPECT in the forward mode using the range of values and steps shown in Table 1 giving a total of 160325 cases. We selected these steps to better cover the entire variation space of the model. We selected randomly 600 cases for ANN training. Validation was performed on the LOPEX dataset.
- Trained with PROSPECT and LOPEX dataset: ANN trained with a sub-sample of 100 PROSPECT cases in the forward mode and all LOPEX samples but one each time. The remaining LOPEX sample was used for validation. The process was repeated for each LOPEX sample performing a cross-validation.

We applied radial basis function (RBF) networks [15] using the Neural Network Toolbox of Matlab 7.0 (The MathWorks, Inc., www.mathworks.com, USA). This type of ANN is trained faster and can work with a large dataset of input variables. RBF networks are structurally simpler with only three layers: an input, hidden and output layer. The hidden layer neurons have a static Gaussian function. The Gaussian function responds only to a small region of the input space where the Gaussian is centered. The key to the Matlab successful implementation of these networks is to find the suitable number of neurons to cover the input space. The final number of neurons is selected automatically when a maximum permitted error is reached.

Table 1. Range and step of input parameters in the PROSPECT model: leaf internal structure (N), chlorophyll a+b content (C_{a+b}), EWT and dry matter content (DM).

	N	**C_{a+b} (μg/cm^2)**	**EWT (g/cm^2)**	**DM (g/cm^2)**
Range	1.0-4.0	10-90	0.001-0.053	0.001-0.018
Step	0.3	20	0.001	0.001

2.2 Analysis at canopy level

RBF networks trained with PROSPECT-SAILH [9] to estimate EWT*LAI. We selected a wide range of input values for the model (Table 2). C_{a+b} was fixed to 40 μg/cm^2, since it has little influence in the estimation of EWT [9]. View zenith and azimuth angles were both set to 0º and sun zenith angle was fixed to 55º. We generated 8000 random cases and selected 600 cases for ANN training and the remaining 7400 for validation. We did not use steps in the range of the different variables of the canopy model.

Table 2. Range of input parameters in the PROSPECT-SAILH model: N, EWT, DM, LAI, leaf inclination density function (LIDF) and soil reflectance (ρ_s).

	N	EWT (g/cm^2)	DM (g/cm^2)	LAI	LIDF	ρ_s
Range	1-2	0.001-0.03	0.001-0.03	1-5	planophile erectophile plagiophile	bright medium dark

3 RESULTS

ANN trained and cross-validated with the LOPEX dataset provided a good fit (r^2=0.89) (Fig. 1). It was also possible for ANN to train with the PROSPECT model and validate it with the LOPEX dataset (r^2=0.91) (Fig. 2). We normalized and applied principal components (PC) in order to be more compatible in the PROSPECT outputs with the LOPEX database, improving the predicting capacity of the ANN. Those PC that explain more than 0.1 % of the variance were retained.

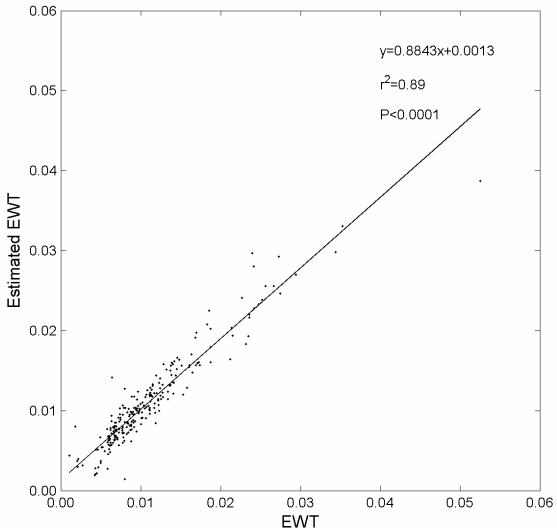

Figure 1. EWT estimation for the LOPEX dataset using ANN training from all LOPEX samples but one each time (n=245).

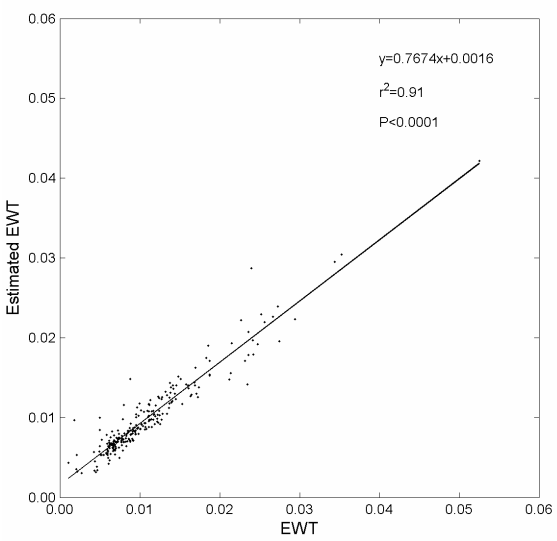

Figure 2. EWT estimation for the LOPEX dataset using ANN training from PROSPECT model (n=245).

PROSPECT model combined with real data, LOPEX, for training ANN slightly improve the results (r^2=0.92) (Fig. 3) of either using independently PROPECT model or real data for training ANN.

EWT*LAI could be estimated accurately using ANN training from different samples generated from the same canopy model (r^2=0.98) (Fig. 4).

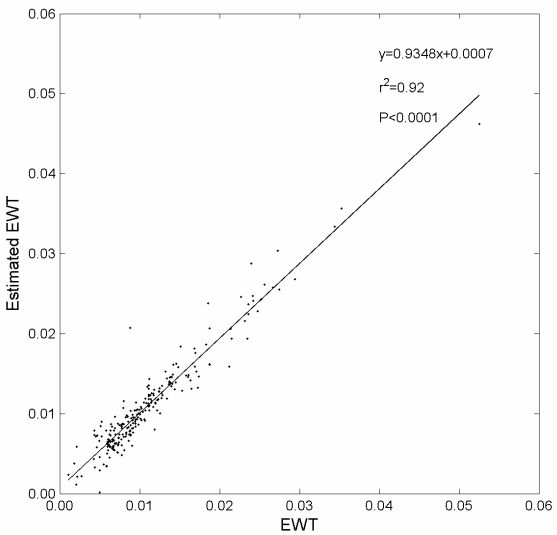

Figure 3. EWT estimation for the LOPEX dataset using ANN training from PROSPECT model and all LOPEX samples but one each time (n=245).

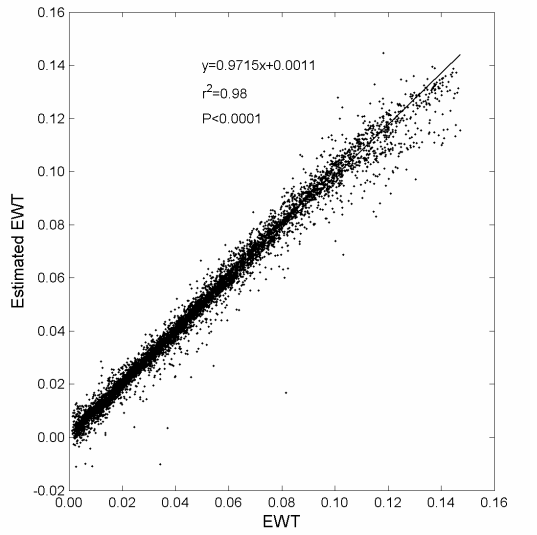

Figure 4. EWT*LAI estimation for samples generated from PROSPECT-SAILH model (n=7400).

4 DICUSSION

Riaño et al. [16] showed that Multilayer Perceptron network can predict leaf EWT using for training samples from the same plant individual (r^2=0.95). This was demonstrated by cross-validation that RBF network can efficiently predict leaf EWT using a large data set of independent real samples from other individuals and species (r^2=0.89). It is also possible that the RBF network can train with the radiative transfer model, PROSPECT. The advantage of using a radiative transfer model in the RBF network training is that is more globally applicable to any dataset. If the

training is correct, results should be at most as good, or as bad, as the inversion of the radiative transfer model itself (r^2=0.94) [8]. Model inversion is much less computationally expensive. Radiative transfer model can also be combined with real data in the RBF network training to improve the accuracy on specific datasets. In our case, combining PROSPECT and LOPEX slightly improve the prediction (r^2=0.92). Further research is needed on how to integrate both datasets in the training process, since normalization and PC did not work well in this case.

RBF networks reproduced PROSPECT-SAILH very well (r^2=0.98), even though it did not use steps in each range to cover the entire variation space. The number of training samples was high. Further research should be conducted with this ANN to test it on real data. Results are expected to be as good or as bad as the inversion but much computationally faster. Therefore this kind of model could be applied to entire remote sensing images.

ACKNOWLEDGMENTS

We wish to acknowledge the NASA project, Global estimation of water content (NNG04GQ42G).

REFERENCES

[1] BURGAN, R. E. and ROTHERMEL, R. C., 1984: "BEHAVE: Fire Behavior Prediction and Fuel Modeling System. Fuel Subsystem," USDA Forest Service, Ogden, Utah GTR INT-167.

[2] USTIN, S. L., JACQUEMOUD, S., ZARCO-TEJADA, P. J., and ASNER, G., 2004: "Remote Sensing of Environmental Processes: State of the Science and New Directions," in *Manual of Remote Sensing Vol. 4. Remote Sensing for Natural Resource Management and Environmental Monitoring*, S. L. Ustin, Ed. New York: ASPRS. John Wiley & Sons, Incorporated, pp. 679-730.

[3] USTIN, S. L., ROBERTS, D. A., PINZON, J., JACQUEMOUD, S., GARDNER, M., SCHEER, G., CASTANEDA, C. M., and PALACIOS-ORUETA, A., 1998: "Estimating canopy water content of chaparral shrubs using optical methods," *Remote Sensing of Environment, 65*, pp. 280-291.

[4] PALTRIDGE, G. W. and BARBER, J., 1988: "Monitoring grassland dryness and fire potential in Australia with NOAA/AVHRR data," *Remote Sensing of Environment, 25*, pp. 381-394.

[5] JACQUEMOUD, S. and BARET, F., 1990: "Prospect - a Model of Leaf Optical-Properties Spectra," *Remote Sensing of Environment, 34*, pp. 75-91.

[6] CECCATO, P., GOBRON, N., FLASSE, S., PINTY, B., and TARANTOLA, S., 2002: "Designing a spectral index to estimate vegetation water content from remote sensing data: Part 1 - Theoretical approach," *Remote Sensing of Environment, 82*, pp. 188-197.

[7] DANSON, F. M. and BOWYER, P., 2004: "Estimating live fuel moisture content from remotely sensed reflectance," *Remote Sensing of Environment, 92*, pp. 309-321.

[8] RIAÑO, D., VAUGHAN, P., CHUVIECO, E., ZARCO-TEJADA, P. J., and USTIN, S. L., 2005: "Estimation of fuel moisture content by inversion of radiative transfer models to simulate equivalent water thickness and dry matter content. Analysis at leaf and canopy level," *IEEE Transactions on Geoscience and Remote Sensing, 43*, pp. 819-826.

[9] ZARCO-TEJADA, P. J., RUEDA, C. A., and USTIN, S. L., 2003: "Water content estimation in vegetation with MODIS reflectance data and model inversion methods," *Remote Sensing of Environment, 85*, pp. 109-124.

[10] BARET, F., CLEVERS, J., and STEVEN, M. D., 1995: "The Robustness Of Canopy Gap Fraction Estimates From Red And Near-Infrared Reflectances - A Comparison Of Approaches," *Remote Sensing Of Environment, 54*, pp. 141-151.

[11] [DANSON, F. M., ROWLAND, C. S., and BARET, F., 2003: "Training a neural network with a canopy reflectance model to estimate crop leaf area index," *International Journal Of Remote Sensing, 24*, pp. 4891-4905.

[12] WEISS, M., BARET, F., LEROY, M., HAUTECOEUR, O., BACOUR, C., PREVOT, L., and BRUGUIER, N., 2002: "Validation of neural net techniques to estimate canopy biophysical variables from remote sensing data," *Agronomie, 22*, pp. 547-553.

[13] [FANG, H. L. and LIANG, S. L., 2003: "Retrieving leaf area index with a neural network method: Simulation and validation," *IEEE Transactions on Geoscience and Remote Sensing, 41*, pp. 2052-2062.

[14] [OSGOOD, B., JACQUEMOUD, S., ANDREOLI, G., VERDEBOUT, J., PEDRINI, A., and SCHMUCK, G., 1994: "The JRC Leaf Optical Properties Experiment (LOPEX'93)," EUROPEAN COMMISSION, Directorate - General XIII, Telecommunications, Information Market and Exploitation of Research, L-2920, Luxembourg. CL-NA-16095-EN-C.

[15] MOODY, J. and DARKEN, C. J., 1989: "Fast learning in networks of locally-tuned processing units," *Neural Computation, 1*, pp. 281-294.

[16] RIAÑO, D., USTIN, S. L., USERO, L., and PATRICIO, M. A., 2005: "Estimation of fuel moisture content using neural networks," *Lecture Notes in Computer Science, 3562*, pp. 489-498.

Preliminary analysis for soil organic carbon determination from spectral reflectance in the frame of the EU project DeSurvey

N. Richter[a], S. Chabrillat[a] and H. Kaufmann[a]

[a] GeoForschungsZentrum Potsdam (GFZ), Section 1.4: Remote Sensing, Telegrafenberg, D-14473 Potsdam, Germany, email: nrichter@gfz-potsdam.de

ABSTRACT

This paper presents the concept of the GFZ hyperspectral remote sensing research project within DeSurvey. First we describe a preliminary analysis of laboratory experiments. These experiments were performed to study the influence of soil organic carbon (SOC) content, roughness and illumination on spectral reflectance. Then we present the design of field experiments that will be further used to test the transferability of reflectance models developed in the laboratory to field and subsequently to remote sensing scale. This work is in its very first stage. Following work includes the evaluation and improvement of the field and laboratory experiments and the investigation of other soil parameters such as soil organic matter and iron content.

Keywords: Hyperspectral remote sensing, DeSurvey, BRDF, soil properties, soil organic carbon

1 INTRODUCTION

The integrated EU project DeSurvey was started in March 2005 with the overall goal to develop a surveillance system for assessing and monitoring of desertification. Five test sites in southern Europe are selected to validate the DeSurvey system, and assess, monitor and forecast desertification and land degradation status. Subsequently, a compact set of integrated procedures for the assessment system will be delivered at EU and national scales. In the framework of the DeSurvey project, advanced remote sensing techniques are developed and tested to derive indicators related to soil surface parameters such as organic matter, organic and inorganic carbon, iron content, roughness status and the presence of biological crusts.

The main focus of the GFZ contribution in the DeSurvey project is to study desertification issues with support of hyperspectral imagery methods [1], [2]. Airborne remote sensing datasets recorded over well documented test areas in the Mediterranean region will be used to develop advanced information extraction procedures that allow the determination of relevant soil parameters (e.g. organic matter content) from hyperspectral data at first step, and extend it to available satellite imagery as a second step.

Our project objectives are:

- Development of a model for extraction of quantitative soil parameters such as soil organic carbon (SOC), iron content etc. from laboratory and field reflectance measurements and hyperspectral data [3], [4], [5].
- Setup of multi-scale field spectral (upscaling) experiments for transfer of models from the laboratory to remote sensing data as basis for the development of enhanced parameter extraction procedures for current and future spaceborne systems.
- Setup of laboratory and field experiments to study BRDF (Bidirectional Reflectance Distribution Function) effects over representative soil samples and selected test areas to obtain their directional spectral properties.

This paper presents the setups of laboratory and field experiments. Preliminary analysis of the laboratory measurements is shown.

2 LABORATORY EXPERIMENTS

2.1 Setup

Laboratory measurements are performed on soil samples from the Guadalentin area in SE-Spain, sampled and geochemically analyzed (organic and inorganic carbon, mineral composition) at the University of Trier. All samples are taken from crop fields representing catenas with different soil development status. Eight soil samples representing different organic carbon contents were chosen to simulate different surface roughness states and measure them under varying illumination angles (Figure 1). It was further attempted to extract the SOC from the spectra. The spectra have been taken with the ASD spectroradiometer *FieldSpec Pro FR* (www.asdi.com) from the University of Trier.

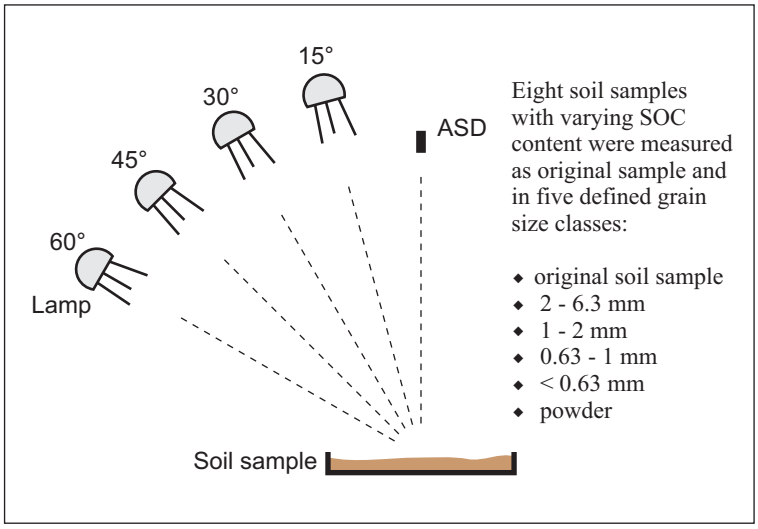

Figure 1. Laboratory experiment settings.

Variation of surface roughness states:

The influence of surface roughness states on reflectance was studied by measuring the spectra of the original sample and five different grain sizes of each soil sample. The grain sizes were retrieved through a sieving process separating the soil fractions starting at fine gravel level (2 – 6.3 mm) and down to homogenized samples in the fine sand level (crushed samples (powder)).

Variation of illumination angle:

The illumination angle of the light source was varied at four positions: 15°, 30°, 45°, 60°. In this laboratory setting the spectral measurements were taken with nadir-looking fiber optic of the ASD spectrometer.

Altogether 24 spectral measurements were taken per soil sample (six different roughness states at four illumination angles each). This results in 192 measurements total for the selected eight soil samples.

2.2 Preliminary analysis

The spectra are analyzed in terms of the influence of varying surface and illumination conditions for the determination of SOC.

The influence of the different surface roughness stages on the spectra is depicted in Figure 2. The surface reflectance of the sieved samples increases with decreasing grain size as can be expected [5]. It was further observed that with decreasing grain size the depth of absorption bands decreases. The high reflectance of the original soil sample might be due to different heights between the sample surface to the lamp and sensor.

The influence of varying illumination conditions is depicted in Figure 3. The variation of the illumination angle at the reflectance plays a major role on reflectance of rough surfaces having lots of shadow, i.e. shadowing is getting strongest with lower illumination. Here, grain size is small, with little shadow, and we observe that spectral reflectances are located at a similar level.

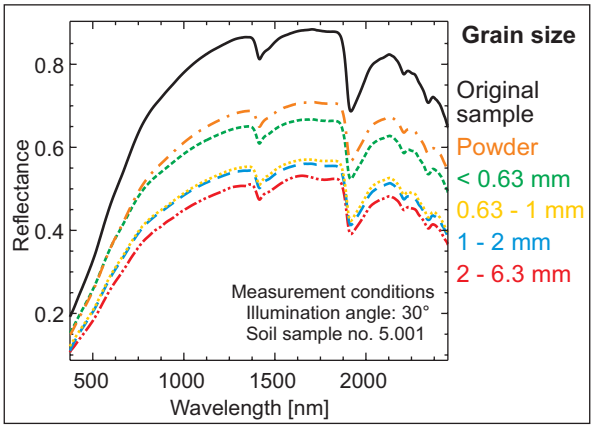

Figure 2. Variation of surface roughness states.

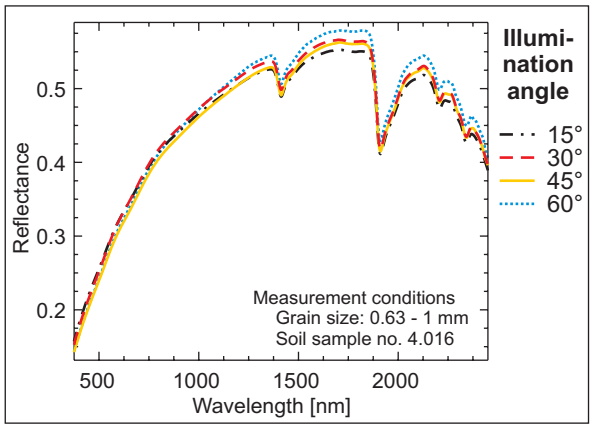

Figure 3. Variation of illumination angle.

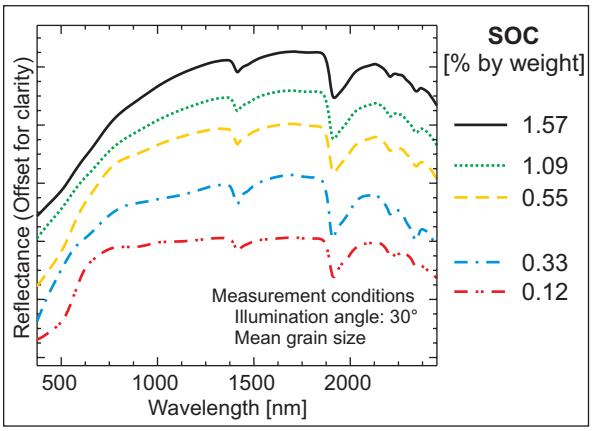

Figure 4. Soil organic carbon content. (The mean grain size spectra were generated by averaging the individual grain size spectra for one sample and illumination angle.)

Figure 4 depicts reflectance spectra of 5 soil samples with different SOC content. The direct extraction of SOC content from these spectra is difficult because of the influence in the same wavelength range of varying iron content. When there is few iron in the samples, the increase of the SOC content is associated with a decrease in the surface reflectance in the VNIR wavelength range and a general flattening of the spectra in this spectral region [5]. Here iron absorption bands at ~900 nm start to appear for samples of low SOC contents Then we observe that the influence of iron absorption bands increases significantly with decreasing SOC.

3 FIELD EXPERIMENTS

A two-weeks field campaign in SE-Spain took place in July and August 2005. Three different types of semi-arid and arid ecosystems associated with the Cabo de Gata region, El Cautivo area, and Sierra de Gador mountains were chosen to perform the planned experiments (Figure 5). The Natural Parc Cabo de Gata – Nijar is geologically characterized by calcareous and volcanic rocks on which two different types of soil developed. El Cautivo is located within the Tabernas desert area. Lichens and different soil crust are typical for the calcareous rich soil in El Cautivo. The soils of the Sierra de Gador Mountains are based on calcareous and phyllitic rocks and show a high content in soil organic carbon.

In general, the whole area is characterized by a warm and very dry climate with average precipitation ranging from 100 to 500 mm and a low potential evapotranspiration.

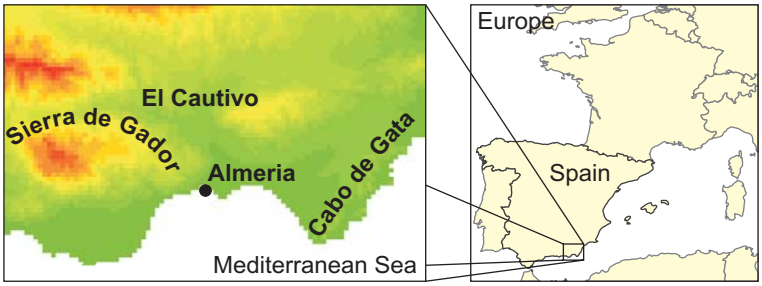

Figure 5. Study site.

3.1 BRDF Experiments

The BRDF experiment comprises spectral reflectance measurements of a 50 x 50 cm test area that are taken with the ASD field spectrometer every 30 min during the diurnal path of the sun (Figure 6). In the initial setup, measurements were acquired with a nadir-looking sensor. In theory, with increasing light angles, the nadir looking sensor records less energy, which will lead to a reduced signal-to-noise ratio and an increased noise in the spectra. This effect was not observed in this laboratory experiment with an artificial light source, but during the field BRDF experiment it was a limiting factor in terms of the daytime of measurements.

Due to technical problems with the field spectrometer during the campaign in SE-Spain, the BRDF experiment was performed in August 2005 in a bio-monitoring recultivation zone in the lignite mine Welzow-Süd near Cottbus, Germany. Undisturbed conditions, an unusual local dry climate and the lack of vegetation make this area ideal for the research on soil parameters. Land degradation processes take place on the area and are accurately measured and controlled throughout the years by different other research projects [6]. Currently, the experiment is re-designed to allow spectral measurements of the surface's forward scattering at different sensor angles in the future.

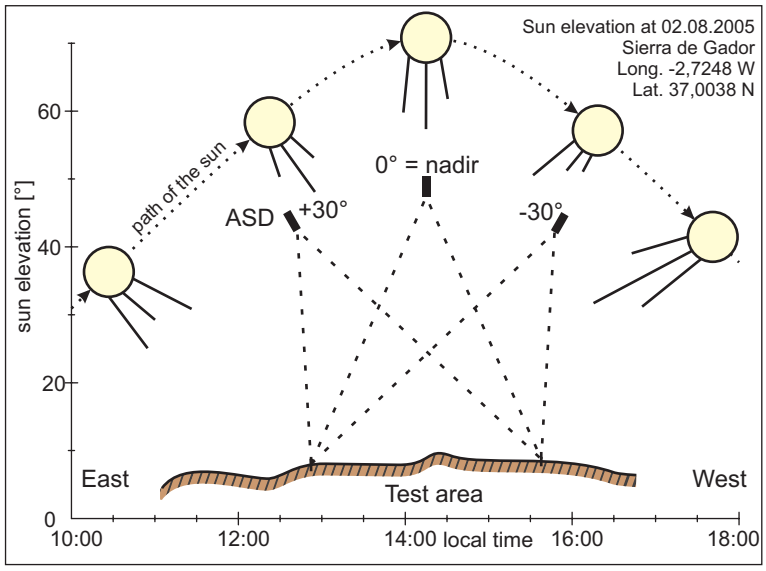

Figure 6. BRDF field experminent settings.

3.2 Upscaling Experiments

The upscaling experiment is designed to test the transferability of the laboratory models to remote sensing data. A 1 x 1m test area is measured with an ASD field spectrometer based on the defined measuring grid (Figure 8). The measurements are taken from 4 different heights to simulate different spatial resolutions (Figure 7). At each height level, the whole test area is measured with a varying number of spectra according to the grid indicated in parenthesis in Figure 7. For example at 30 cm measuring height, 64 spectral measurements are taken to cover the test area (Figure 9). When measuring from 2.50 m height only one spectra is needed (Figure 10). In addition, spectra of the detectable endmembers are recorded in the test area.

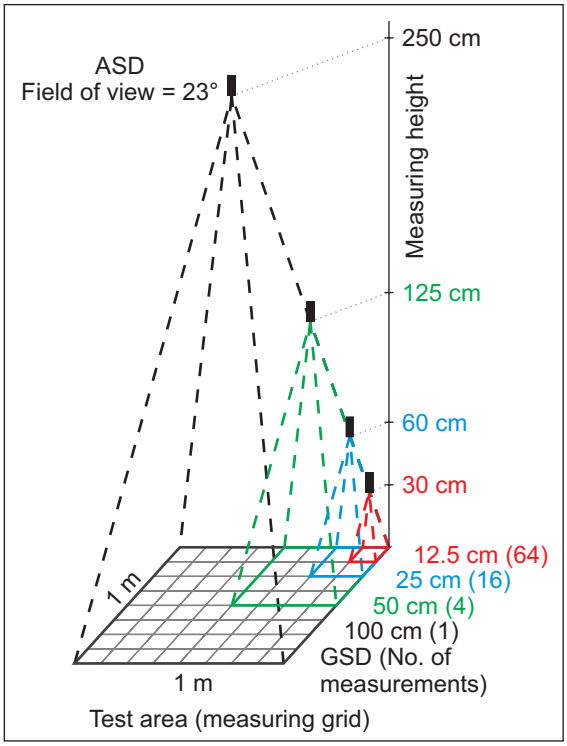

Figure 7. Upscaling field experiment settings.

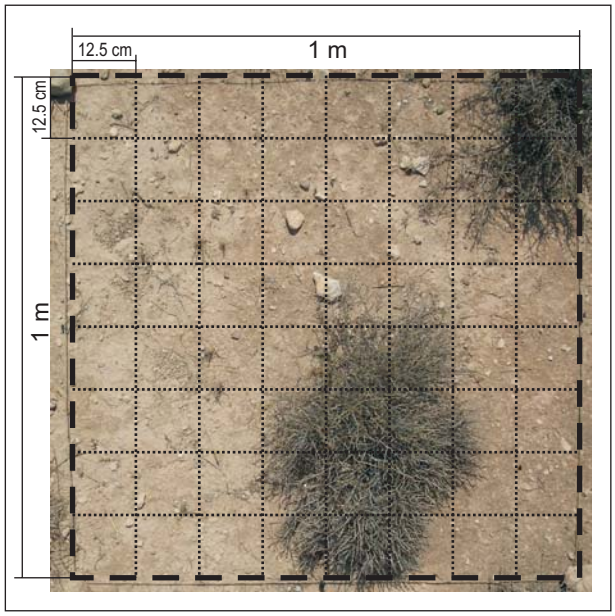

Figure 8. Test area on calcareous-rich soils in Cabo de Gata with indicated measuring grid.

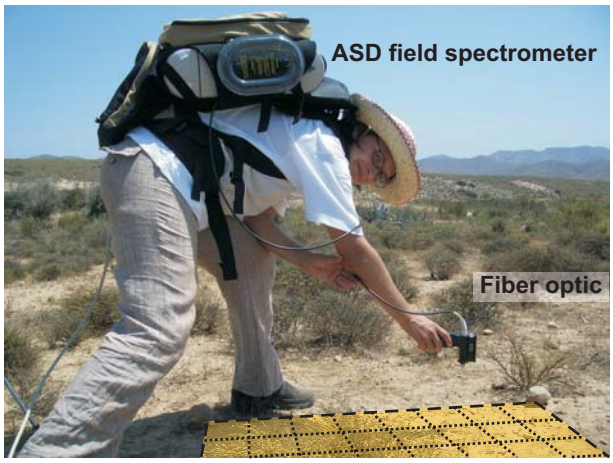

Figure 9. Cabo de Gata - taking spectra at the lowest measuring height (30 cm height -> ~12.5 cm GSD). The measuring grid of the test area is indicated.

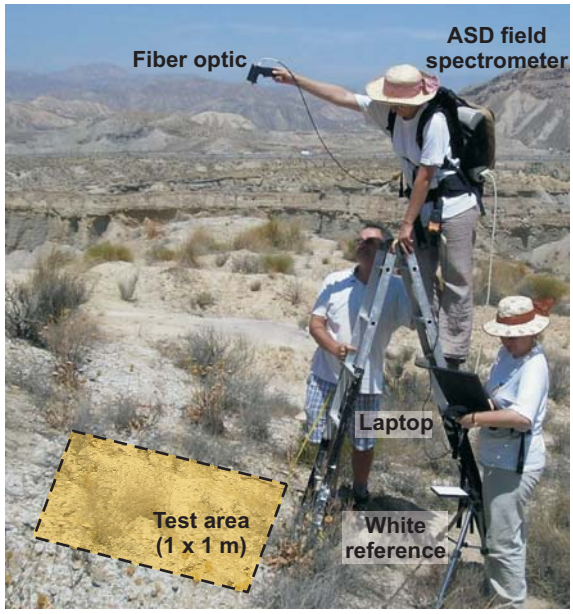

Figure 10. El Cautivo - a ladder is used to aquire spectra at 2.50 m measuring height (~100 cm GSD).

4 SUMMARY AND OUTLOOK

In the frame of the EU integrated project DeSurvey, first field experiments studying BRDF and upscaling effects have been designed and tested. Spectra of a laboratory experiment were analyzed in terms of the influence of roughness and illumination on spectral reflectance of different soil samples with varying SOC content. The strong influence of iron absorption made it difficult to extract SOC content directly from the spectra.

Following work include the evaluation and improvement of laboratory experiments and field experiments. Procedures will be developed to analyze the experiments measurements. Further the combined influence of the SOC and iron content of soil samples in their reflectance spectra will be studied and models are developed.

ACKNOWLEDGMENTS

The authors would like to thank the European Commission for funding the EU integrated project DeSurvey within the 6th Framework Programme: Global Change & Ecosystems (Project Contract N° 003950). Juan Puigdefabregas and DeSurvey participants are gratefully acknowledged for their intensive work toward the successful start of the project. We also would like to thank Thomas Jarmer from the University of Trier for providing us the soil samples, analytical data, laboratory facilities and his support in laboratory reflectance measurements. For their support during the field campaign in Spain this summer, we like to thank Paula Escribano and Cecilio Oyonarte-Gutierrez from the University of Almeria and Mónica García and Roberto Lázaro Suau from the CSIC-EEZA.

REFERENCES

[1] HILL, J., 2000: Semiarid land assessment: monitoring dry ecosystems with remote sensing. Encyclopedia of Analytical Chemistry. In: Meyers, R.A. (ed.): Encyclopedia of Analytical Chemistry, Chichester, pp. 8769-8794.

[2] HOSTERT, P., RÖDER, A., JARMER, T., UDELHOVEN, T. AND HILL, J., 2003: The potential of remote sensing and GIS for desertification monitoring and assessment. *Int. J. Remote Sens. 24 (20)*, pp. 4019-4034.

[3] BEN-DOR, E. AND BANIN, A., 1994: Visible and near-infrared (0.4-1.1µm) analysis of arid and semiarid soils. *Remote Sensing of Environment 48*, pp. 261-274.

[4] UDELHOVEN, T., HILL, J., SCHÜTT, B., IMESON, A. AND CAMMERAAT, L.H., 1998: A neural network approach for the identification of the organic carbon content of soils in a degraded semiarid ecosystem (Guadalentin, SE Spain) based on hyperspectral data from the DAIS 7915 sensor. In: Schaepmann, M., Schläpfer, D. and Itten, K. (eds.): *1st EARSeL Workshop on Imaging Spectroscopy*, pp. 437-444.

[5] BAUMGARDNER, M.F.; SILVA, L.F.; BIEHL, L.L. AND STONER, E.R., 1985: Reflectance properties of soils. *Advances in Agronomy 38*, pp. 1-44.

[6] HAUBROCK, S.; CHABRILLAT, S. AND KAUFMANN, H., 2005: Application of hyperspectral imaging for the Quantification of surface soil moisture in erosion monitoring and modeling. *4th EARSeL Workshop on Imaging Spectroscopy,* in press.

Remote Sensing Techniques for Estimating Leaf Area Index of a Forest Planted in the Desert Transition Zone

M. Sprintsin[a], S. Cohen[b], A. Karnieli[a], P. Berliner[a], E. Rotenberg[c] and D. Yakir[c]

[a] Jacob Blaustein Institute for Desert Research, Ben Gurion University of the Negev, Sede Boker Campus 84990, Israel, email: sprintsi@bgu.ac.il
[b] Institute of Soil, Water and Environmental Sciences, Volcani Center, Bet Dagan, Israel
[C] Weizmann Institute of Science, Rehovot 76100, Israel

ABSTRACT

We present an approach to determining Leaf Area Index (LAI) of a forest located at the desert fringe by using high-spatial resolution imagery and by upscaling values from a moderate spatial but high temporal resolution sensor. A 2-m spatial resolution multi-spectral IKONOS image was acquired under clear sky conditions on March 25, 2004. Normalized Differences Vegetation Index (NDVI) and a linear mixture model were applied to calculate fractional vegetation cover (FVC). LAI was calculated using a non-linear relationship to FVC and then compared with ground truth measurements made in ten 1000 m^2 grids using the Tracing Radiation and Architecture of Canopies (TRAC) canopy analyzer under bright and clear sky conditions during March and April, 2004. Predicted and measured LAI were highly correlated (R^2=0.85, $p<0.0002$). Results were extrapolated to an entire scene producing a LAI map of the forest. Later, the same procedure was applied to the MODIS 250-m resolution surface reflectance product in order to evaluate the applicability of coarse spatial but high temporal resolution sensors for regional LAI assessment. Subsequently, the pixel size of a 2-m resolution LAI image was degraded to that compatible to MODIS (250 m) data. A comparison between both products demonstrates that the latter approach gives a good approximation (R^2=0.5, $p<0.001$) for LAI and thus looks promising for use in determining temporal dynamics, even for regional scale applications.

Keywords: LAI, dry lands forestry, remote sensing, NDVI, IKONOS, MODIS

1 INTRODUCTION

Description of forest stands includes factors related to the eco-physiological processes responsible for forest growth. One of those factors is the stand leaf area index (LAI) defined as the total one-sided area of leaf tissue per unit ground surface area (m^2/m^2) [1]. LAI is a basic canopy parameter highly related to many processes, such as rainfall interception, evapotranspiration, photosynthesis, respiration and leaf litterfall, and is a basic input for various ecosystem models. LAI can be estimated through various direct (contact) and/or optical indirect (non-contact) procedures. Despite their extensive usage, these methods demand considerable amounts of labor and time, and yield information only for the close vicinity of the measured point. Therefore the possibility of remote assessment of LAI is of major interest [2, 3, 4 and 5]. The use of high resolution satellite images, such as those of IKONOS that simultaneously capture 1-metre panchromatic (black & white) and 4-metre multispectral (blue, green, red, near-infrared) digital imagery has recently become popular for providing a relatively new source of data for monitoring various environment parameters; however this source is still comparatively rare and expensive. Thus, in order to carry out research that requires a high number of images for a long period of time, it is more convenient to use higher frequency freely available data. Such information compromises high temporal and moderate spatial resolutions, and therefore requires detailed validation for local implementation. The Moderate Resolution Imaging Spectroradiometer (MODIS) onboard EOS (Earth Observation System) Terra and Aqua satellites provide high temporal (almost twice a day) images in 36 spectral bands ranging from visible (VIS) to short-wave infrared (SWIR) portions of the electromagnetic spectrum, with moderate to low spatial resolution (from 250 to 1000 m.). Our objective was to develop a method for assessing LAI in dry-land forest using high resolution IKONOS data and to downscale this product to coarser MODIS imagery.

2 STUDY AREA

The study was conducted in the Yatir forest (31˚21' N and 35˚02' E, 630 m AMSL) located in the transition zone between semi-arid and sub-humid climatic zones of the northern Negev Desert, Israel. Average annual rainfall is 275 mm, fluctuating annually between 146 and 496 mm. Average monthly maximum and minimum temperatures

are 32.3˚C and 6.9˚C, respectively. The forest lies mostly on Rendzina soil and on lithosols that overlay hard Cenomanian -Turonian chalks. Since the forest was planted by the Jewish National Fund, it is almost even-aged, and is close to being a monoculture dominated by *Pinus halepensis*.

3 MATERIALS AND METHODS

3.1 Ground-truth data collection

Ten randomly distributed grids of 1000 m^2 each (approximately 32 x 32 m) were chosen in order to collect ground truth data (Figure 1). Each grid was divided into seven east-west oriented ~32 m long segments. The measurements were made with the Tracing Radiation and Architecture of Canopies (TRAC) photo-sensor device and software [6], as a series of seven 32 m long transects, one in the middle of each segment, three times a day for different zenith angles during March and April 2004.

3.2 Image processing

A 2-m spatial resolution multispectral IKONOS image was acquired on March 25, 2004 (Figure 1). The image was radiometrically and atmospherically corrected and geo-rectified to the UTM grid. In addition, three MODIS products (also re-projected into the UTM grid), available through the Earth Resources Observation System (EROS) Data Active Archive Center (DAAC), were used: (a) 8-day composites of the 1-kilometer LAI product (MOD15A2) a; (b) 16-day composites of 1-kilometer MODIS/Terra Vegetation Indices product (MOD13Q1) produced from the red, near-infrared, and blue surface reflectance data; and (c) MODIS/Terra Surface Reflectance Daily L2G Global 250m SIN Grid (MOD09GQK) computed from the MODIS Level 1B land red and near-infrared bands.

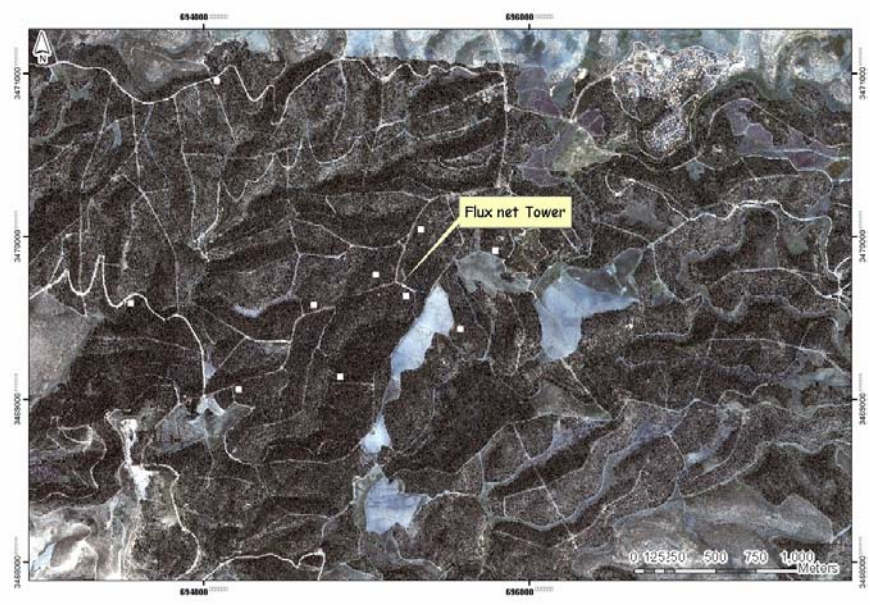

Figure 1. IKONOS of the Yatir forest. Note the location of the grids for ground truth data collection.

3.3 LAI assessment

A Linear Mixture Model (LMM) was implemented for calculating the total surface reflectance measured by the satellite sensor in a specific pixel. The LMM weights the surface reflectances of end-members (e.g., vegetation and soil) by their relative ground cover. The *fractional vegetation cover* (f_c) was calculated from the minimum and maximum Normalized Difference Vegetation Index ($NDVI_{min}$ and $NDVI_{max}$, respectively) values [7]:

$$fc = \frac{NDVI - NDVI_{\min}}{NDVI_{\max} - NDVI_{\min}} \quad (1)$$

A relationship between *fc* and LAI was expressed as [8]:

$$fc = 1 - \exp(-k \cdot LAI) \tag{2}$$

where *k* is an extinction coefficient (a measure of the attenuation of radiation in a canopy), which is a function of wavelength, radiation type, and direction, as well as stand and canopy structure [9 and 10]. Considering only geometrical influences *k* may be expressed as:

$$k = \frac{G(\theta, \alpha)}{\cos(\theta)} \tag{3}$$

where $G(\theta)$ is the foliage projection coefficient (or "shape factor") characterizing the foliage angular distribution (α) [11] and θ is the sensor viewing angle. Eq. 2 was solved for LAI assuming a random angular distribution of leaf area within the canopy, i.e. $G(\theta) = 0.5$

4 RESULTS AND DISCUSSION

Figure 2 shows a map of estimated LAI for the Yatir forest as produced from the IKONOS image following the procedure described above. $NDVI_{min}$ and $NDVI_{max}$ were calculated as 0.01 and 0.75, respectively. A comparison between measured and predicted LAI over the ten grids depicted by Figure 3 shows a high and significant correlation (R^2 = 0.85, p < 0.0002) and prediction accuracy (SE = 0.11). These results demonstrate that the proposed method can be used as a reference for further steps.

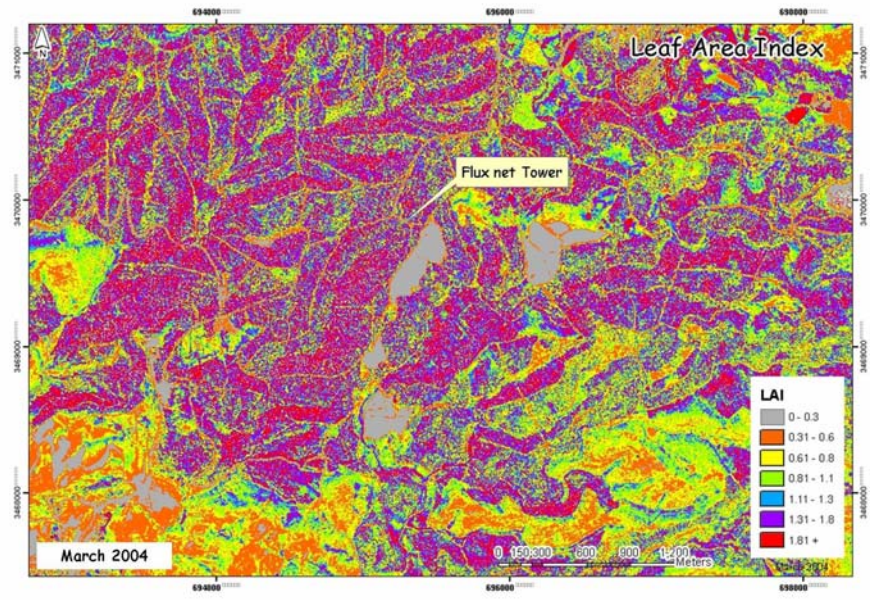

Figure 2. 2-m resolution leaf area index map of Yatir forest for March 2004.

Consequently, the same procedure was applied to MODIS 250-m resolution surface reflectance product solving, and Eq. 2 was inverted to solve for the extinction coefficient. For this solution, the previously-mentioned 1000-m resolution MODIS LAI and VI products were used as a source of data for $f_{c,}$ and LAI as presented by Eq. 4.

$$k = -\frac{\ln(1 - f_{c,MODIS})}{LAI_{MODIS}} \tag{4}$$

The spatial resolution of the resulting image was improved by changing the pixel size from 1-km to 250-m, and was then comparable to the MODIS surface reflectance product. Figure 4 presents an improved map of the extinction coefficient, *k,* with moderate level of extinction coefficient distribution, which is higher for the more mature stands at the north-west section of the forest (average tree age 36 – 37 years). Figure 5 presents a 250-m resolution LAI image produced from MODIS LAI, VI, and surface reflectance products for March 2004 along with

calculated *k*. This figure shows high values of LAI for the more mature stands. Subsequently, the pixel size of a 2-m resolution LAI image was degraded to be comparable to MODIS (250 m) data and a comparison between both sets is presented by Figure 6. The linear relationship indicates that this approach gives a good approximation (R^2=0.50, p<0.001) for LAI.

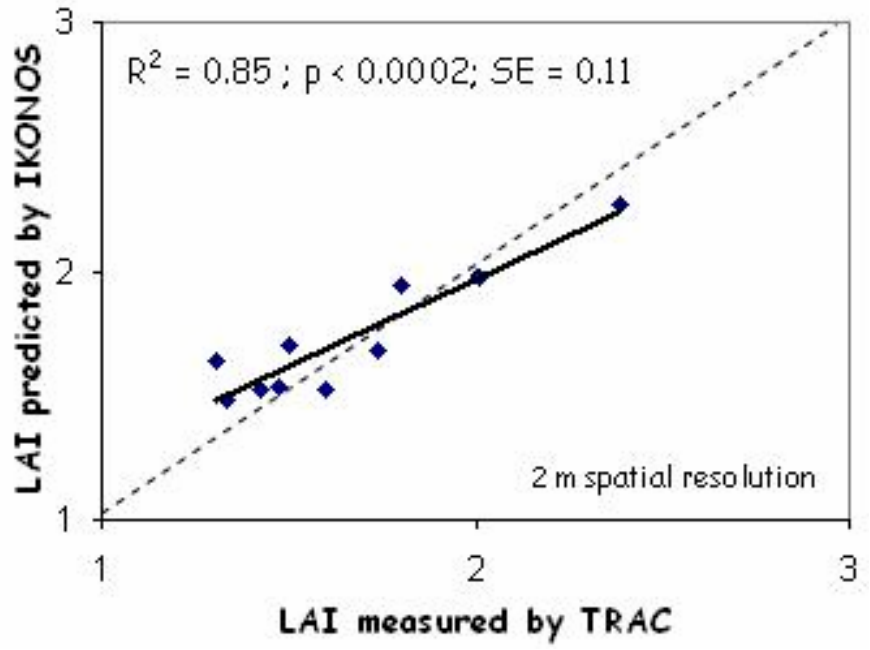

Figure 3. A comparison between measured and predicted LAI values.

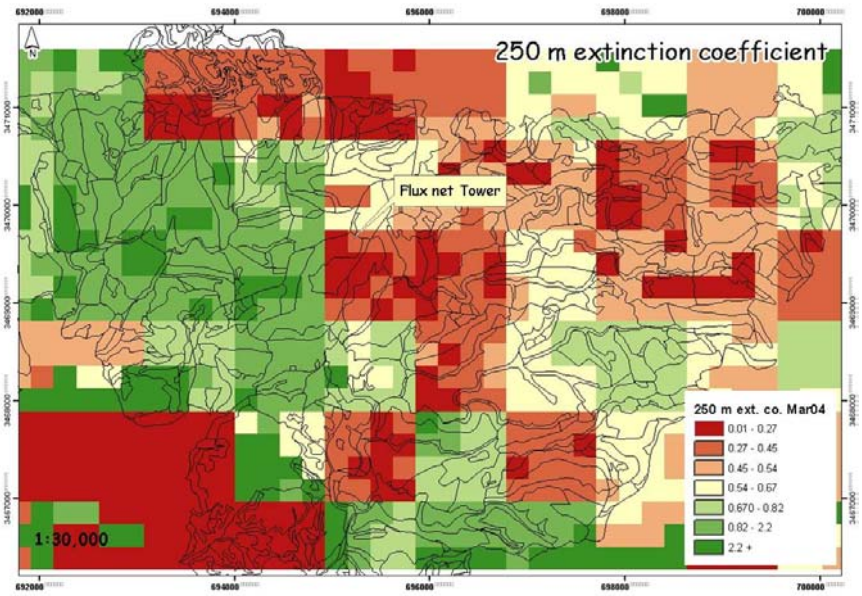

Figure 4. 250-m resolution extinction coefficient map of Yatir forest for March 2004.

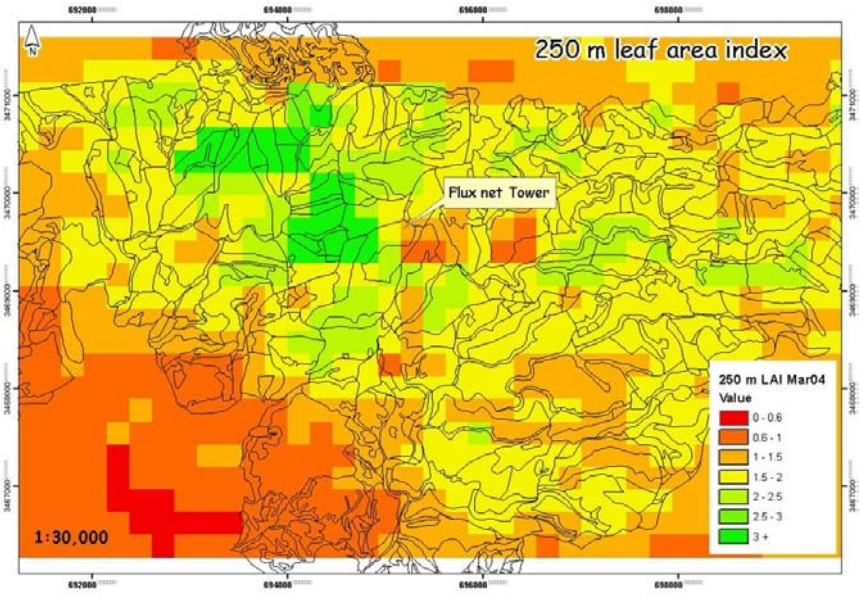

Figure 5. 250-m resolution leaf area index map of Yatir forest for March 2004.

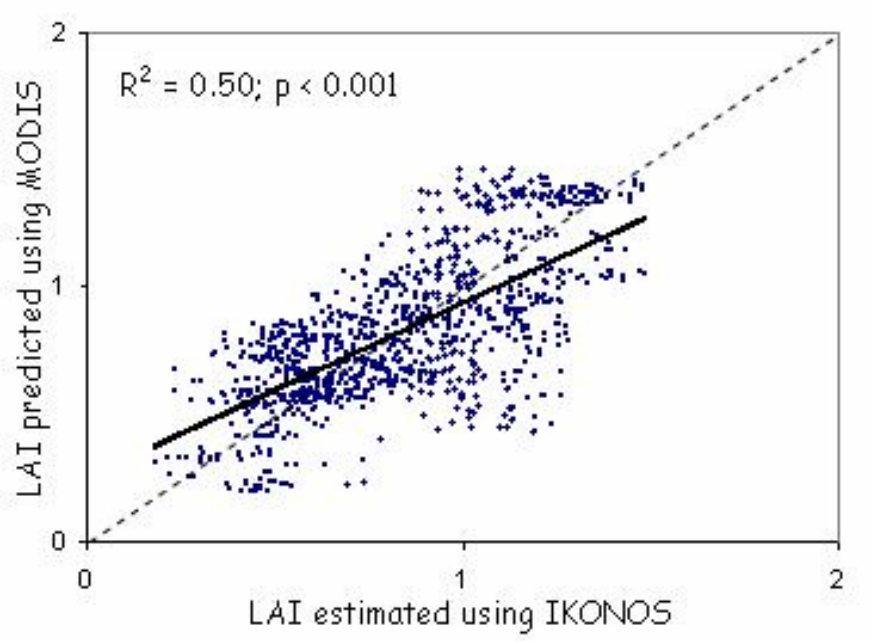

Figure 6. A comparison between LAI values predicted by MODIS and IKONOS.

5 CONCLUSIONS

In the current study we present an approach to determining the Leaf Area Index (LAI) of Yatir forest, located at the desert fringe, by using high-spatial resolution imagery, and for downscaling these values for application to moderate spatial but high temporal resolution imagery. Good accuracy and resolution of LAI was obtained, which is promising for use in evaluating temporal dynamics, even for small (regional) scale applications.

ACKNOWLEDGMENTS

The authors want to thank Mr. A. Goldberg for the help with data collection during the field compaign.

REFERENCES

[1] WATSON, D.J., 1947: Comparative physiological studies in the growth of field crops, I. Variation in net assimilation rate and leaf area between species and varieties, and within and between years. *Annals of Botany, 11*, pp. 41-76

[2] CLEVERS, J.G.P.W., 1997: A simplified approach for yield prediction of sugar beet based on optical remote sensing data. *Remote Sensing of Environment, 61(2)*, pp. 221-228

[3] COLOMBO, R., BELLINGERI, D., FASOLINI, D. AND MARINO, C.M., 2003: Retrieval of leaf area index in different vegetation types using high-resolution satellite data. *Remote Sensing of Environment, 86(1)*, pp. 120-131

[4] ANDERSEN, J., DYBKJAER, G., JENSEN, K.H., REFSGAARD, J.C. AND RASMUSSEN, K., 2002: Use of remotely sensed precipitation and leaf area index in a distributed hydrological model. *Journal of Hydrology, 264(1-4)*, pp. 34-50

[5] WANG, Q., ADIKU, S., TENHUNEN, J., AND GRANIER, A., 2005: On the relationship of NDVI with leaf area index in a deciduous forest site. *Remote Sensing of Environment, 85*, pp. 244-255

[6] CHEN, J.M, AND CIHLAR, J., 1995: Quantifying the effect of canopy architecture on optical measurements of leaf area index using two gap size analysis methods. *IEEE Transactions on Geoscience and Remote Sensing, 33*, pp. 777-787

[7] GOEL, N.S., 1989: Inversion of canopy reflectance models for estimation of biophysical parameters from reflectance data. In: Asrar, G. (ed.): Theory and Application of Optical Remote Sensing, pp. 205-251, John Wiley & Sons.

[8] CHOUDHURY, B.J., AHMED, N.U., IDSO, S.B., REGINATO, R.J. AND DAUGHTRY, C.S.T., 1994: Relations between evaporation coefficients and vegetation indices studied by model simulations. *Remote Sensing of Environment, 50(1)*, pp. 1-17

[9] JARVIS, P.G. AND LAVERENZ, J.W., 1983: Productivity of temperate, deciduous and evergreen forests. In: Lange, O.L., Omond, C.B., and Zeigler, H., (eds.): Physiological Plant Ecology IV, pp. 133-144, New York.

[10] JONES, H.G., 1992: Plant and Microclimate, 2nd ed., Cambrige, UK, Cambrige University Press.

[11] NORMAN, J.M. AND CAMPBELL, G.S., 1989: Crop canopy photosynthesis and conductance from leaf measurements. Workshop prepared for LI-COR, Inc., Lincoln, NE.

Remote Sensing Techniques for long-term Monitoring of Biological Soil Crusts (BSCs) - A Spectral Characterization

B. Weber[a], K. Deutschewitz[a], T. Knerr[a], S. Dojani[a] and B. Büdel[a]

[a] University of Kaiserslautern, Plant Ecology and Systematics, P.O. Box 3049, D – 67653 Kaiserslautern, Germany, email: weberb@rhrk.uni-kl.de

ABSTRACT

According to their dominant components, Biological Soil Crusts (BSCs) were subdivided into cyanobacteria-, lichen- and moss-dominated soil crusts. The reflectance spectra of both cyanobacteria- and lichen-dominated soil crusts showed a reflection minimum around 680 nm (chlorophyll a absorption), which allowed to distinguish them from bare soil. A discrimination of BSCs against phanerogameous plants is easily possible, since the spectral characteristics of higher plants were much more pronounced than those of BSCs (e.g. reflectance maximum around 550 nm, red edge). Upon short-time wettening, the crusts reached their initial spectral rate when they were dry again. Wettening of one day resulted in a local decrease of the spectrum around 680 nm, caused by chl a production. Wettening over ten days resulted in a decrease over the whole visible spectrum, probably due to growth of crust components. Preliminary results on the long term development of spectra during the dry season implied, that already two months after the rainy season the crusts had reached a steady state again. A classification of BSCs according to their chlorophyll content looks feasible, but at this time needs further investigation. The knowledge from the spectral characterization, together with detailed field measurements, should be used to classify hyperspectral data from South Africa.

Keywords: Biological soil crusts, cyanobacteria, reflectance spectra, water, chlorophyll a absorbance, Africa.

1 INTRODUCTION

In the course of the project "BIOTA" (www.biota-africa.org), which includes a network of numerous African and German research projects, the distribution and diversity of Biological Soil Crusts (BSCs) along a transect in southern Africa is studied (Fig.1).

BSCs, which are formed by a close association between soil particles and cyanobacteria, algae, lichens, microfungi, and bryophytes in varying proportions, live within or immediately on top of the uppermost millimeters of soil [1]. They mainly occur in soils of arid and semi-arid regions, which cover 30% of the land surface and are assumed to play a major role as primary producers, as C- and N-sink [2] and as soil stabilizers [3]. BSCs are well known from southern Africa [4]. However, most reports on BSCs either restrict themselves to isolated spots and do not consider the total area covered by BSCs, or they are restricted to a certain taxonomical group [5].

Remote sensing techniques allow to map the distribution of BSCs on a larger scale [6, 7]. The possibility to map the distribution of lichen communities ("upscaling") was first discussed by Wessels and Van Vuuren [8], who could identify the bounds of the lichen fields in the Namib Desert using Landsat imagery. However, up to now, only few attempts to characterize BSCs spectrometrically [9, 10] and to map them [7, 11-13] were made. A universal method to map and classify different types of soil crusts could not be developed up to now.

As an important prerequisite to the classification of BSCs in hyperspectral remote sensing images, the spectra of BSCs with respect to different parameters are studied here in detail and their separability from both bare soils and vegetation of higher plants is analyzed. After a characterization of the spectra of different types of BSCs, the spectral response to different wetting- and drying cycles is investigated. This should bear important information regarding the variation of reflectance characteristics of BSCs in the field in the course of the year. In a third approach, the spectral separability of BSCs with regard to different chlorophyll contents is investigated.

Figure 1. BIOTA-South study area and observatories along the transect through Namibia and South Africa

2 SPECTRAL CHARACTERIZATION OF DIFFERENT CRUST TYPES

Reflectance spectra of the main crust types, bare soil and phanerogameous plants were recorded both to characterize the spectra of the crusts and to analyze their separability against each other. For each type, at least twenty spectra were measured and typical spectra were picked for the following description (Fig. 2). The spectra of cyanobacteria-dominated crusts were characterized by an overall lower reflection than bare soil and low reflection in the blue region. They showed a gradual increase towards the near-infrared region with a reflection minimum around 680 nm due to chlorophyll a (chl a) absorption (chl a content of this sample: 40 mg/m^2). The spectral characteristics and the overall reflectance values of lichen-dominated crusts were similar to those of cyanobacteria-dominated crusts (chl a content: 82 mg/m^2). The moss-dominated crusts (moss: *Riccia* sp.) revealed overall higher reflectance values in the visible region, but despite high chl a contents (this sample: 128 mg/m^2), an absorption feature around 680 nm was hardly visible. The reflectance spectra of flowering plants showed a reflection maximum at 550 nm (VIS green), an absorption maximum in the red region and a distinctive increase at 700 nm (red edge).

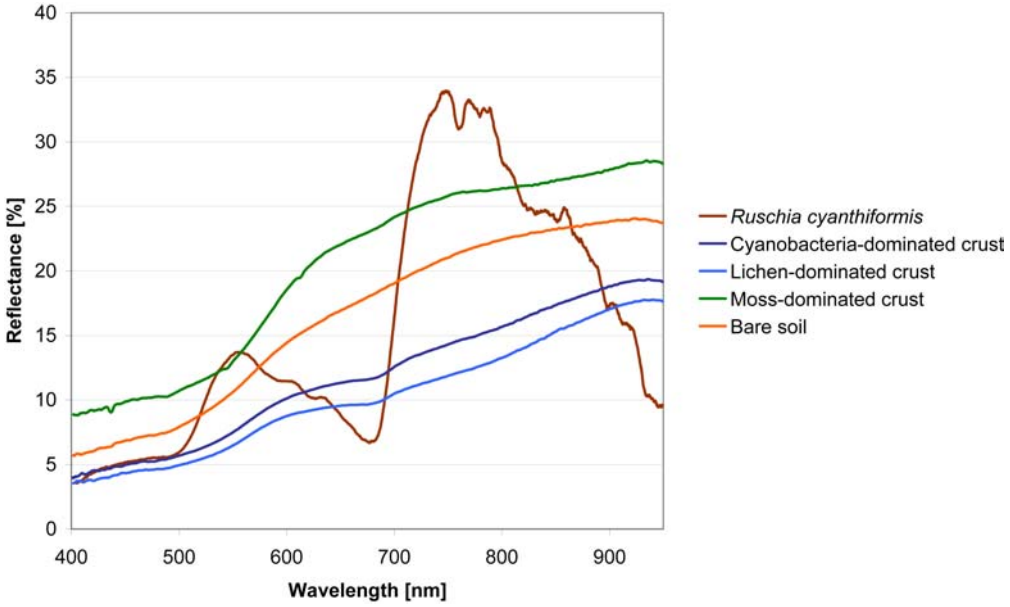

Figure 2. Reflectance spectra of the main crust types, bare soil and phanerogameous plants.

A ratio between the cyanobacteria-dominated crust and the bare soil reflects the similar trends of the spectra, but also a local minimum at 680 nm (arrow), which is universally present (Fig. 3). A ratio between the spectra of flowering plants and cyanobacteria-dominated crusts traces the absorption minimum at 550 nm, the reflection minimum around 680 nm and the strong red edge effect, which are characteristic for phanerogameous plants.

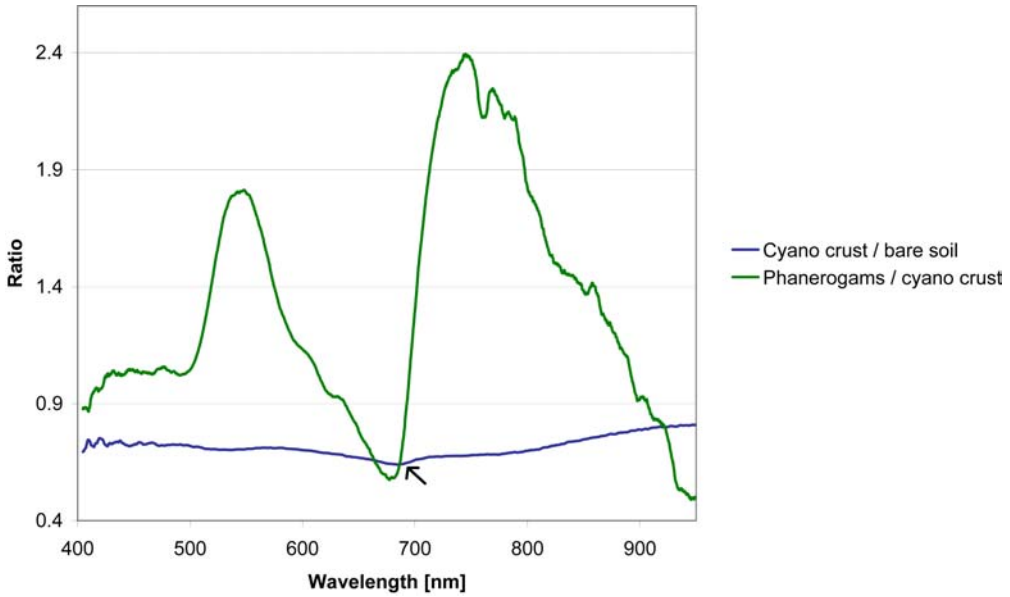

Figure 3. Ratios of the spectra of both bare soil and phanerogameous plants and cyanobacteria-dominated crusts.

3 REACTION OF BSCS TO DIFFERENT WETTING- AND DRYING CYCLES

In different wetting- and drying cycles, the spectral response of cyanobacteria-dominated crusts upon short- and long-time wettening were investigated. When the crusts were only shortly watered, the reflection values decreased evenly over the whole spectrum with a less pronounced decrease between 400 and 500 nm. Upon drying, the crusts reached their initial spectral response again and no chl a production took place.

When the crusts were watered and then were kept wet for 24 hours, the spectra decreased continuously and after 24 hours, a distinct absorption maximum around 680 nm was visible (Fig. 4). After 24 hours of drying, the crusts reached their initial spectral range again. However, due to chl a production the reflection was decreased around 680 nm.

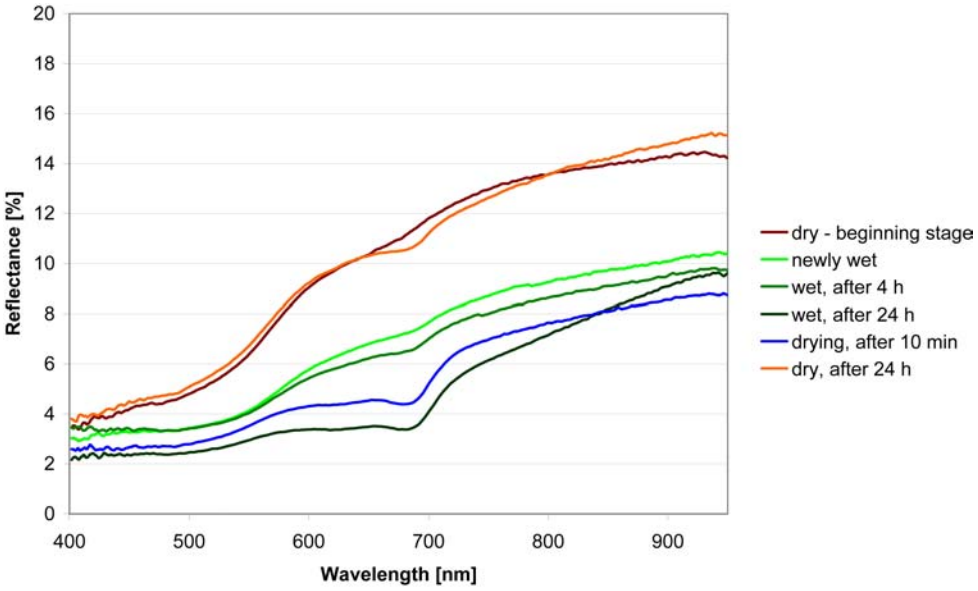

Figure 4. Reflectance spectra of cyanobacteria-dominated crust during a 24 hour wetting- and drying cycle.

After ten days of wettening, the reflectance of the crusts was clearly decreased with a minimum around 680 nm (Fig. 5). After one day of drying, a very pronounced reflection minimum was visible around 680 nm and an increase of the spectrum at 700 nm ressembled the red edge effect of phanerogameous plants. During five subsequent dry weeks, the spectra continuously increased and most of the newly formed chlorophyll was not visible anymore.

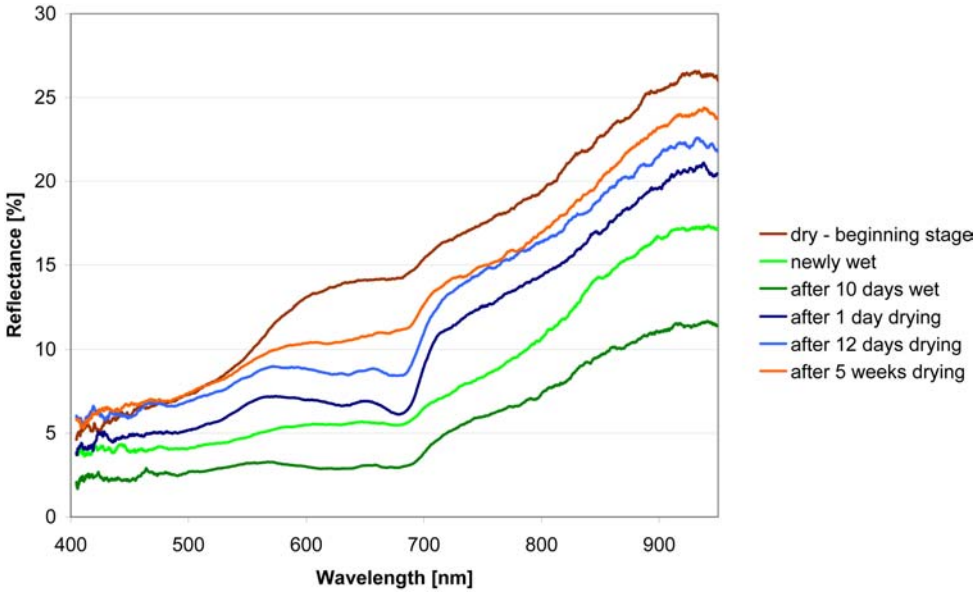

Figure 5. Reflectance spectra of cyanobacteria-dominated crust during a ten-day wettening and five-week drying cycle.

In a fourth approach, samples were collected in the field at the end of the rainy season and kept in the light at 600 – 800 µE * m^{-2} * s^{-1}. During long-term measurements on a monthly basis throughout 11 months, no alteration of the spectrum was visible. The first measurements were taken eight weeks after collection of the samples.

4 SPECTRAL CHARACTERISTICS DEPENDING ON CHLOROPHYLL CONTENT OF BSCS

In order to investigate if BSCs can be classified according to their chlorophyll content, samples of the same crust type but varying chlorophyll content were analyzed spectrometrically and their chorophyll content was determined. In general, crusts with low chlorophyll content tended to have high reflection values throughout the visible spectrum. The chlorophyll a absorption feature was not visibly more pronounced in crusts with high chlorophyll content. The quotients of reflection values at various wavelengths were calculated and tested for possible correlations with the chl a content. However, up to now, the best correlation coefficient was reached between the reflection values at 680 nm and the chlorophyll a content (r = -0.55, n = 91; Fig. 6).

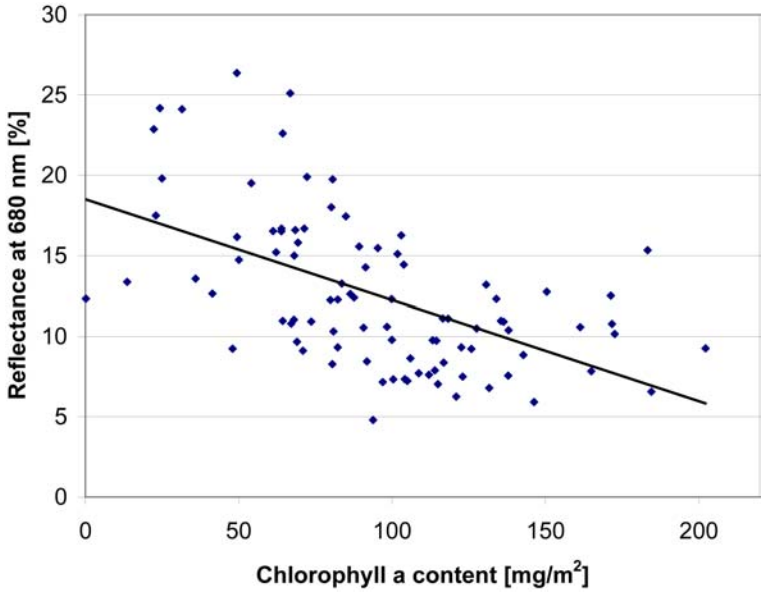

Figure 6. Correlation between chlorophyll a content and spectral response at 680 nm.

5 DISCUSSION

The spectra of cyanobacteria- and lichen-dominated crusts resembled those of bare soil, but showed a minimum around 680 nm (due to chl a), which should allow to discriminate them against the latter. They are similar to those measured by [9, 10, 12] and [14]; however, the characteristics in our crusts are less pronounced than those of [9, 10] and [15]. In concordance with [12], a relatively higher reflectance in the blue region could not be observed by us. The transition between the spectra of cyanobacteria- and lichen-dominated crusts was gradual, so that a spectral discrimination between them doesn't seem easily feasible. The spectrum of moss crusts very closely resembled that of bare soil and lacked a reflectance minimum around 680 nm. This was most probably caused by air-enclosures in the upper epidermis of the *Riccia*-leavlets, which produce a greyish color and elevated reflectance values. A classification of moss-dominated crusts in hyperspectral images therefore doesn't look promising on the basis of the present data. Since the spectral characteristics of higher plants were much more pronounced than those of BSCs (e.g. reflectance maximum around 550 nm), a discrimination of BSCs against phanerogameous plants should easily be possible in hyperspectral images.

In order to establish a monitoring of BSCs on the basis of hyperspectral data, the spectral variability of BSCs in the course of the year has to be known. Therefore, the effects of water and light on the spectral response of BSCs were tested. After a short wet event, the crusts dried out quickly and reached their initial spectral response curve again. After one wet day, the reflectance of crusts was decreased around 680 nm, caused by chlorophyll a production. The fact that ten wet days resulted in a decrease throughout the spectrum of visible light can be

interpreted as growth of the different crust components. Those observations are in concordance with the literature [7, 16]. After five weeks, the spectra of the crusts were still lower than the initial one, but it is not known, if at this stage the samples had reached a new steady state again. The long term development of spectra during the dry season implies, that already two months after the rainy season, the crusts had reached a steady state again, suggesting that monitoring data should be collected at least two months after the last rain event. In the literature, only one study on this topic under semi-arid conditions was found [17], in which the spectral response of BSCs altered continuously throughout the year. In order to get solid results, the long-term study has to be repeated under natural light conditions (1300 - 1500 instead of 600 – 800 $\mu E * m^{-2} * s^{-1}$) and the measurements have to be started right after collection of the samples.

A negative correlation was found between the chl a content and the reflectance of BSCs at 680 nm. In the literature, no data on this topic could be found. By extension of those measurements, a coarse classification of BSCs with respect to their chlorophyll content should be attempted.

In October 2004, hyperspectral CASI and SASI data with a spatial resolution of 1 m were acquired in South Africa. The knowledge from the spectral characterization should be extended and together with detailed field measurements, those data should be used to classify the hyperspectral data.

ACKNOWLEDGMENTS

Christoph Schultz is thanked for preparation of figure 1. The project (BIOTA Southern Africa) was sponsored by the German Federal Ministry of Education and Research under promotion number 01 LC 0024A.

REFERENCES

[1] BELNAP J. AND LANGE O.L., 2001: Biological Soil Crusts: Structure, Function, and Management. *Ecological Studies 150*. Springer-Verlag, Berlin, Heidelberg, New York.
[2] EVANS R.D. AND LANGE O.L., 2001: Biological soil crusts and ecosystem nitrogen and carbon dynamics. *Ecological Studies 150*, pp. 263-279.
[3] BÜDEL B., 2005: Microorganisms of Biological Crusts on Soil Surfaces. *Soil Biology 3*, pp. 307-323.
[4] ULLMANN I. AND BÜDEL B., 2001: Biological soil crusts of Africa. *Ecological Studies 150*, pp. 107-118.
[5] BÜDEL B., 2001: Synopsis: comparative biogeography of soil-crust biota. *Ecological Studies 150*, pp. 141-152.
[6] KARNIELI A., 1997: Development and implementation of spectral crust index over dune sands, *International Journal of Remote Sensing 18 (6)*, pp. 1207-1220.
[7] KARNIELI A., KOKALY, R.F., WEST, N.E. AND CLARK, R.N., 2001 : Remote Sensing of Biological Soil Crusts, *Ecological Studies 150*, pp. 431-455.
[8] WESSELS, D.C.J. AND VAN VUUREN, D.R.J., 1986: Landsat imagery – its possible use in mapping the distribution of major lichen communities in the Namib Desert, South West Africa. *Madoqua 14*, pp. 369-373.
[9] KARNIELI, A. AND TSOAR, H., 1995: Spectral reflectance of biogenic crust developed on desert dune sand along the Israel-Egypt border. *Int. J, Remote Sensing 16 (2)*, pp. 369-374.
[10] KARNIELI, A. AND SARAFIS, V., 1996: Reflectance spectrophotometry of cyanobacteria within soil crusts – a diagnostic tool. *Int. J. Remote Sensing 17 (8)*, pp. 1609-1615.
[11] KARNIELI, A., 1997: Development and implementation of spectral crust index over dune sands. *Int. J. Remote Sensing 18 (6)*, pp. 1207-1220.
[12] CHEN, J., ZHANG, M.Y., WANG, L., SHIMAZAKI, H. AND TAMURA, M., 2005: A new index for mapping lichen-dominated biological soil crusts in desert areas. *Remote Sensing of Environment 96*, pp. 165-175.
[13] HILL, J., UDELHOVEN, T., SCHÜTT, B. AND YAIR, A., 1999: Differentiating Biological Soil Crusts in a sandy arid ecosystem based on multi- and hyperspectral remote sensing data. In: Schaepmann, M. (ed.): 1st EARSEL Workshop on Imaging Spectroscopy – Proceedings, pp. 427-436. University of Zürich, Switzerland.
[14] O'NEILL, A.L., 1994: Reflectance spectra of microphytic soil crusts in semi-arid Australia. *Int. J. Remote Sensing 15 (3)*, pp. 675-681.
[15] KARNIELI, A., SHACHAK, M., TSOAR, H., ZAADY, E., KAUFMAN, Y., DANIN, A. AND PORTER, W., 1996: The effect of microphytes on the spectral reflectance of vegetation in semiarid regions. *Remote Sensing of Environment 57*, pp. 88-96.
[16] KARNIELI, A., KIDRON, G.J., GLAESSER, C. AND BEN-DOR, E., 1999: Spectral characteristics of cyanobacteria soil crust in semiarid environments. *Remote Sensing of Environment 69*, pp. 67-75.
[17] KARNIELI, A., GABAI, C., ICHOKU, C., ZAADY, E. AND SHACHAK, M., 2002: Temporal dynamics of soil and vegetation spectral responses in a semi-arid environment. *Int. J. Remote Sensing 23 (19)*, pp. 4073-4087.

Spatial Variability of Biophysical Parameters in Olive Orchards using High-Spatial Resolution Remote Sensing Imagery

P.J. Zarco-Tejada[a], J. Minas[a], J.A. Gómez[a], M.A. Soriano[b], F.J. Villalobos[a,b] and E. Fereres[a,b]

[a] Instituto de Agricultura Sostenible (IAS), Consejo Superior de Investigaciones Científicas (CSIC), Alameda del Obispo, s/n, 14004, Córdoba, Spain, email: pzarco@ias.csic.es
[b] Dpto. de Agronomía, Universidad de Córdoba, Spain

ABSTRACT

High-spatial resolution multispectral remote sensing imagery was collected in July 2003 and 2004 over two olive orchards in Southern Spain. Airborne imagery was acquired with the Compact Airborne Spectrographic Imager (CASI) in 2003, and with the Airborne Hyperspectral Scanner (AHS) in 2004. In addition, Quickbird satellite imagery were collected over the same areas in winter and summer of each 2003 and 2004 years. The push-broom CASI hyperspectral airborne system used in this project collected 1 m image data in the visible and near infrared wavelength regions (400-950 nm), allowing a selection of band centre locations for calculating specific vegetation indices. The AHS sensor was equipped with 20 channels of 20 nm bandwidth for visible and near infrared, 1 channel of 200 nm bandwidth and 42 channels of 13 nm bandwidth for mid infrared, 7 channels of 300nm bandwidth for short-wave infrared and 10 channels of 400 nm for long-wave infrared, collecting image data at 2 m spatial resolution. Both hyperspectral instruments were used to study the spatial variability of crown leaf area index (LAI) and crown density using remote sensing methods based on specific vegetation indices and automatic crown delineation algorithms. Imagery was processed applying geometric, radiometric and atmospheric corrections with atmospheric optical thickness acquired at the time of image collection. Trees were identified in the field with GPS, and then located in the image after registration. Traditional indices (NDVI, SR, MSR) and new narrow-band indices recently developed to minimize their saturation with high LAI values (RDVI, TVI, MSAVI2) were calculated from the airborne imagery.

Ground data collection consisted of measurements of crown transmittance with a PCA LAI-2000 (Li-Cor, Lincoln, Nebraska), and geometrical measurements of crown projected area, height, and crown cross-section that enabled the estimation of crown leaf area index and crown density for 69 individual trees using gap-fraction relationships. Spatial variations of crown LAI were related to vegetation indices calculated from each crown identified on the imagery, enabling the study of relationships between crown level field measurements and remote sensing indices. Relationships found between the new remote sensing indices and ground data were used to study the spatial variability of crown leaf area index and crown coverage in the field, in turn allowing the mapping of biophysical variables related to the crown intercepted radiation, such as crop yield, canopy fractional cover, and indicators of erosion risk in olive orchards, such as the fraction of intercepted rainfall by the trees. Results emphasize the potential of these new methods for assessing orchard canopy properties, consisting of novel vegetation indices and new algorithms for crown-level biophysical estimates for high resolution imagery, and the applicability of these techniques to Quickbird satellite imagery.

Keywords: crown transmittance, leaf area index, vegetation index, multispectral, Quickbird, CASI, AHS.

1 INTRODUCTION

Accurate estimation of crop biophysical parameters at high spatial resolutions from remote sensing techniques is key for effective management operations using precision agriculture. Leaf biochemical constituents such as chlorophyll a+b, leaf water content, dry matter, and canopy biophysical variables, such as leaf area index can be spatially and temporally estimated by remote sensors placed on satellite and airborne platforms using scaling-up methods and hyperspectral indices [1]-[3]. These crop biophysical parameters, which provide a critically needed quantitative measure of crop status and growth limiting factors, may be estimated by physical models based on the radiative transfer theory from remote sensing data collected in the visible and near infrared spectral regions. The purpose of this research is to investigate narrow-band vegetation indices calculated from high spatial hyperspectral imagery for crown transmittance and plant leaf area index (PLAI), defined as the ratio of the projected leaf area over the projected crown area.

2 MATERIALS AND METHODS

Airborne hyperspectral imagery acquired with the Compact Airborne Spectrographic Imager (CASI) at 1 m pixel size and 8 bands in the 400-950 nm was processed applying geometric, radiometric and atmospheric corrections with atmospheric optical thickness acquired at the time of image collection (figure 1). The olive orchard study sites were located in Córdoba and Alcaudete (Jaén), Southern Spain. A total of 101 trees were identified in the field with GPS, and then located in the image after registration. Ground data collection consisted of measurements of crown transmittance with a PCA LAI-2000 (Li-Cor, Lincoln, Nebraska), and geometrical measurements of crown projected area, height, and crown cross-section that enabled the estimation of crown leaf area index and crown density for each individual tree using gap-fraction relationships [4]. Orchards were selected to comprise a wide range of tree crown densities, projected crown areas, and crown volumes (figure 2). Field measurements from the individual trees showed variations in the crown projected area ranging between 0.9 and 39.9 m^2, with crown volumes between 0.82 and 80.4 m^3.

Spatial variations of crown LAI were related to vegetation indices calculated from each crown identified on the imagery, enabling the study of relationships between crown level field measurements and remote sensing indices. Crown spectral reflectance signatures were extracted from the imagery using spectral un-mixing methods, using an NDVI>0.6 threshold value to separate crown from soil and shadow reflectance, and with a semi-automated tree detection and delineation algorithm TD [5], designed for conditions with regularized tree spacing and consistent crown size canopies (figure 3).

Traditional indices such as NDVI, calculated as

(RNIR - Rred)/(RNIR + Rred) [6], (1)

SR (RNIR/Rred) [7], (2)

MSR as $\frac{R_{NIR}/R_{red}-1}{(R_{NIR}/R_{red})^{0.5}+1}$ [8] (3)

and new narrow-band indices recently developed to minimize their saturation at high LAI values [2] such as

$RDVI = (R_{800}-R_{670})/\sqrt{(R_{800}+R_{670})}$ [9], $TVI = 0.5*[120*(R_{750}-R_{550}) - 200*(R_{670}-R_{550})]$ [10], (4)

were calculated from the airborne imagery for each tree crown (figure 2). Calculated indices were then compared with the crown transmittance and crown leaf area index to study their relationship at the tree level for the wide range of tree size and dimensions found in the olive orchard. Field measurements of the projected crown area for each tree were also compared with the estimated area using the spectral un-mixing and NDVI threshold methods.

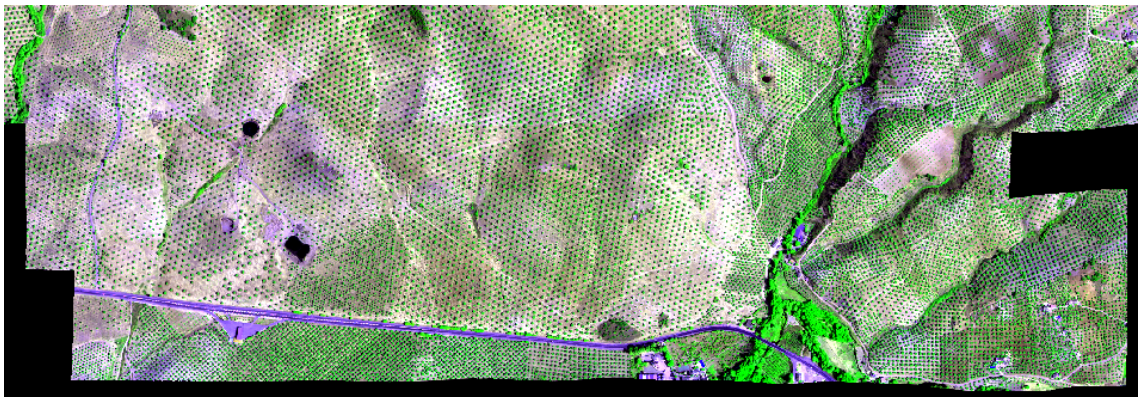

Figure 1. Mosaic image acquired with the CASI sensor at 1 m spatial resolution over one of the study areas used in this research. The image is shown with channels blue (450 nm), green (800 nm) and red (690 nm).

3 RESULTS

Ground truth calculated PLAI values for trees in the area ranged between 0.5 and 4 among the 101 trees used in the study. The best relationship between crown transmittance and image reflectance was found for the RDVI index (r^2=0.72), indicating that the index was sensitive to variations in crown transmittance for the wide range of crowns

used in the study. Correlations between RDVI and PLAI, calculated from crown transmittance, crown volume and projected crown area through gap-fraction relationships showed r^2=0.58 (figure 4), a weaker relationship than that obtained between RDVI and crown transmittance, presumably due to nonlinear effects of crown area and volume on the calculation of PLAI. Nevertheless, these results show that RDVI index is sensitive to variations in crown transmittance and crown leaf area index for a wide range of olive tree crown dimensions and densities.

The successful estimation of the crown projected area at the tree level using the high spatial airborne imagery is shown in figure 4, generating r^2=0.87 when using spectral un-mixing methods (RMSE=6.7 m^2) and NDVI threshold methods (RMSE=5.5 m^2). The relationship found between RDVI and PLAI for the 101 trees was then applied at the image level to map PLAI at the orchard level (figure 5). The mapped PLAI shows the orchard spatial variability which can be used as input for other models intended to predict spatial variations of light interception, yield prediction, and rainfall interception among others, as well as potential management zone classification.

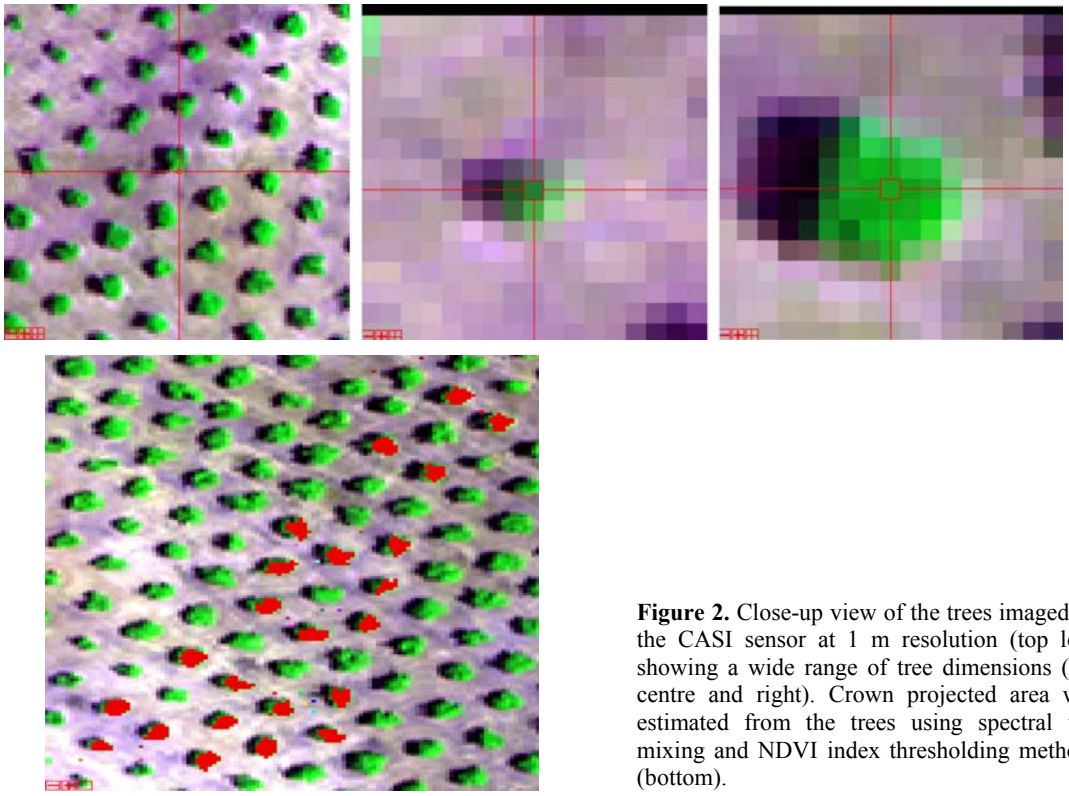

Figure 2. Close-up view of the trees imaged by the CASI sensor at 1 m resolution (top left) showing a wide range of tree dimensions (top centre and right). Crown projected area was estimated from the trees using spectral un-mixing and NDVI index thresholding methods (bottom).

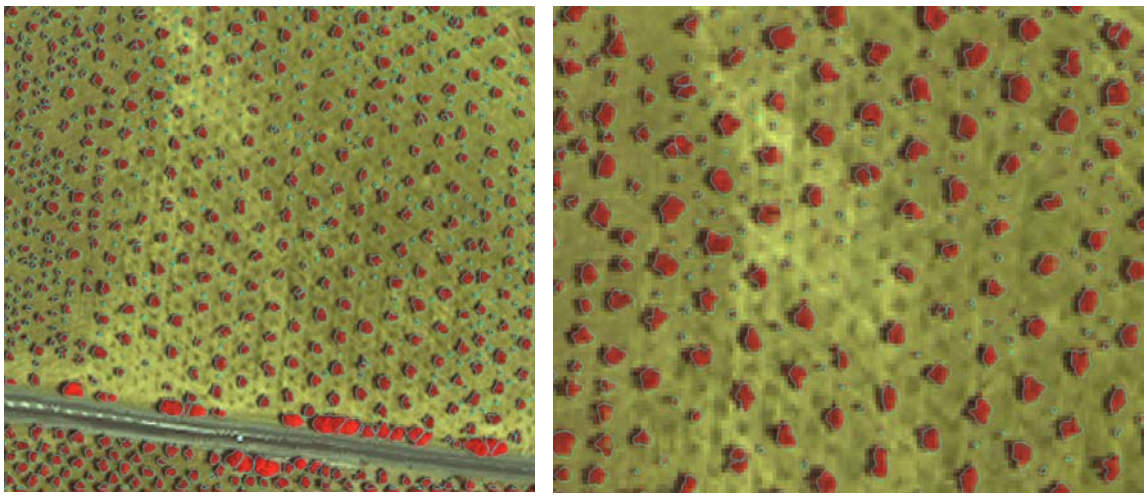

Figure 3. Example of the semi-automated tree detection and delineation algorithm TD output applied to the CASI multispectral image at one of the study sites.

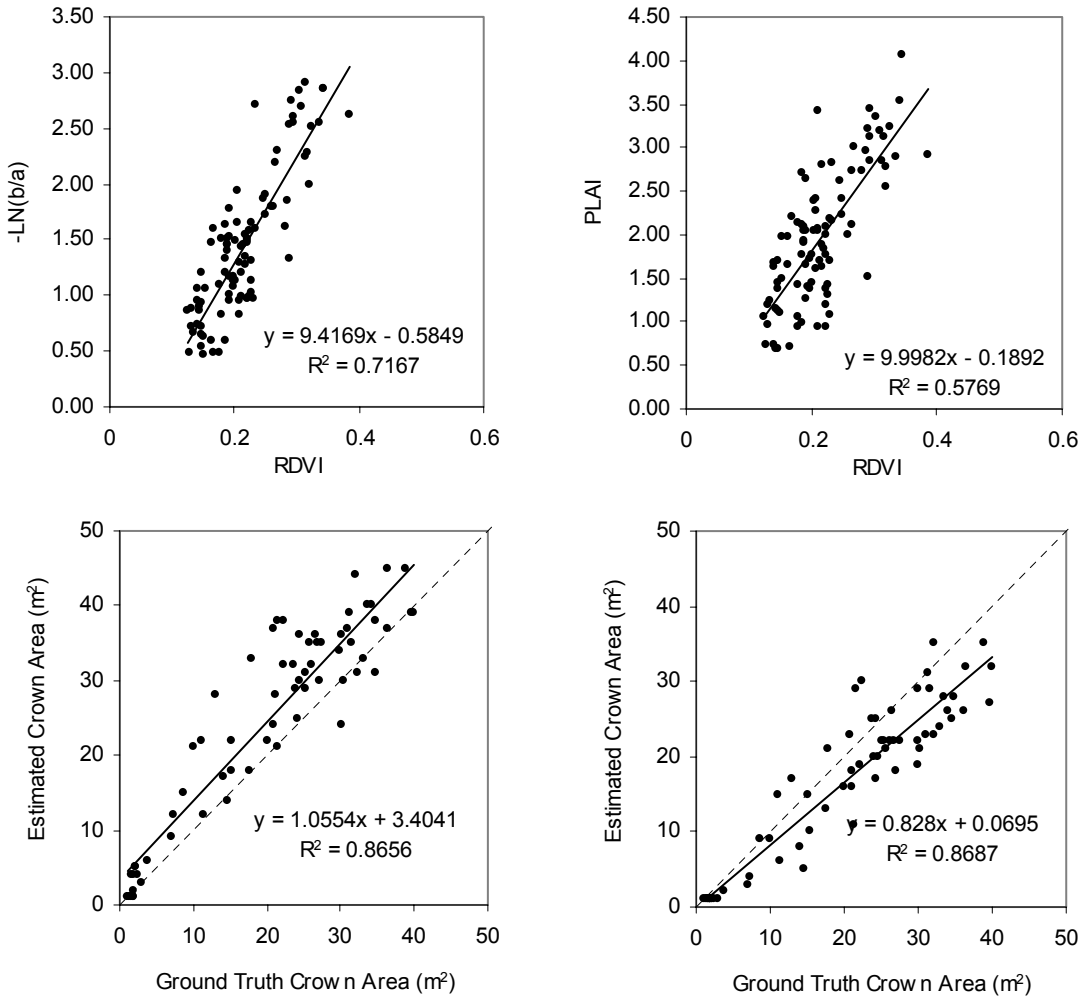

Figure 4. Relationships obtained between RDVI and crown transmittance (shown as –ln b/a) (upper left) and PLAI (upper right). Bottom figures show the relationships between measured and estimated projected crown area using spectral un-mixing methods (left) and NDVI>0.6 threshold (right).

4 CONCLUSIONS

This research shows that high-spatial remote sensing imagery can be used to estimate tree-level biophysical variables using narrow-band indices. Crown transmittance, plant leaf area index, and projected crown area were successfully estimated using the RDVI index, a modification of NDVI to avoid saturation at high LAI values. The relationships between RDVI and crown transmittance (r^2=0.72), PLAI (r^2=0.58), and the successful estimation of the crown projected area (r^2=0.87) suggests that these remote sensing methods can be applied at larger scales when high spatial and narrow band spectral bands are available. These results found between the new remote sensing indices and ground biophysical data enable the study of the spatial variability of crown leaf area index in the field, in turn allowing the mapping of biophysical variables related to the crown intercepted radiation, such as crop yield, canopy fractional cover, and hydrological processes such as rainfall interception and water erosion.

ACKNOWLEDGMENTS

Financial support from the Spanish Ministry of Science and Technology (MCyT) for the project AGL2002-04407-C03, and financial support to P.J. Zarco-Tejada from the Ramón y Cajal (MCyT) and Averroes (JA) programs are gratefully acknowledged. Darren Pouliot is acknowledged for sharing the code and support with the TD algorithm.

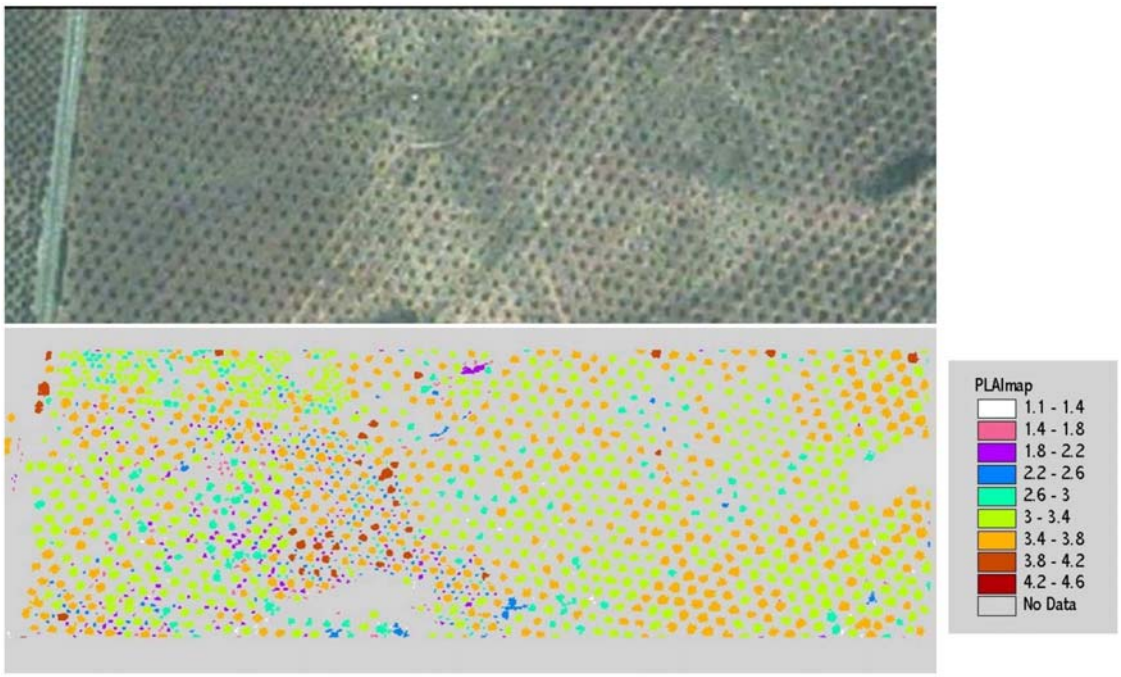

Figure 5. Airborne image of 1 m spatial resolution obtained from one of the study sites (top), and spatial estimation of PLAI using the RDVI index developed at the crown level for 101 trees. Gaps in PLAI map correspond to areas with natural vegetation not included in the analysis

REFERENCES

[1] HABOUDANE, D., MILLER, J.R., TREMBLAY, N, ZARCO-TEJADA, P.J. AND DEXTRAZE, L., 2002: Integration of Hyperspectral Vegetation Indices for Prediction of Crop Chlorophyll Content for Application to Precision Agriculture. *Remote Sens. Environ., 81(2-3)*, pp. 416-426.

[2] HABOUDANE, D., MILLER, J.R., PATTEY, E., ZARCO-TEJADA, P.J., AND STRACHAN, I., 2004: Hyperspectral vegetation indices and novel algorithms for predicting green LAI of crop canopies: modeling and validation in the context of precision agriculture. *Remote Sens. Environ., 90*, pp. 337-352.

[3] ZARCO-TEJADA, P.J., MILLER, J.R., MORALES, A., BERJÓN, A., AND AGÜERA, J., 2004: Hyperspectral Indices and Model Simulation for Chlorophyll Estimation in Open-Canopy Tree Crops. *Remote Sens. Environ, 90(4)*, pp. 463-476.

[4] VILLALOBOS, F.J., ORGAZ, F., AND MATEOS, L., 1995: Non-destructive measurement of leaf area in olive (Olea europaea L.) trees using a gap inversion method. *Agricultural and Forest Meteorology, 73*, pp. 29-42.

[5] [5] POULIOT, D.A., KING, D.J., PITT, D.G., AND BELL, F.W., 2002: Automated tree crown detection and delineation in high-resolution digital camera imagery of coniferous forest regeneration. *Remote Sens. Environ., 82*. pp. 322-334.

[6] ROUSE, J. W., HAAS, R. H., SCHELL, J. A., DEERING, D. W., AND HARLAN, J. C., 1974: Monitoring the vernal advancements and retrogradation of natural vegetation. NASA/GSFC, Final Report, Greenbelt, MD, USA, pp. 1-137.

[7] JORDAN, C.F., 1969: Derivation of leaf area index from quality of light on the forest floor. *Ecology, 50*, pp. 663-666.

[8] CHEN, J., 1996: Evaluation of vegetation indices and modified simple ratio for boreal applications. *Can. J. Remote Sens., 22*. pp. 229-242.

[9] ROUJEAN, J.-L. AND BREON, F.M., 1995: Estimating PAR absorbed by vegetation from bidirectional reflectance measurements. *Remote Sens. Environ., 51*, pp. 375-384.

[10] BROGE, N.H., LEBLANC, E., 2000: Comparing prediction power and stability of broadband and hyperspectral vegetation indices for estimation of green leaf area index and canopy chlorophyll density. *Remote Sens. Environ., 76*, pp. 156-172.